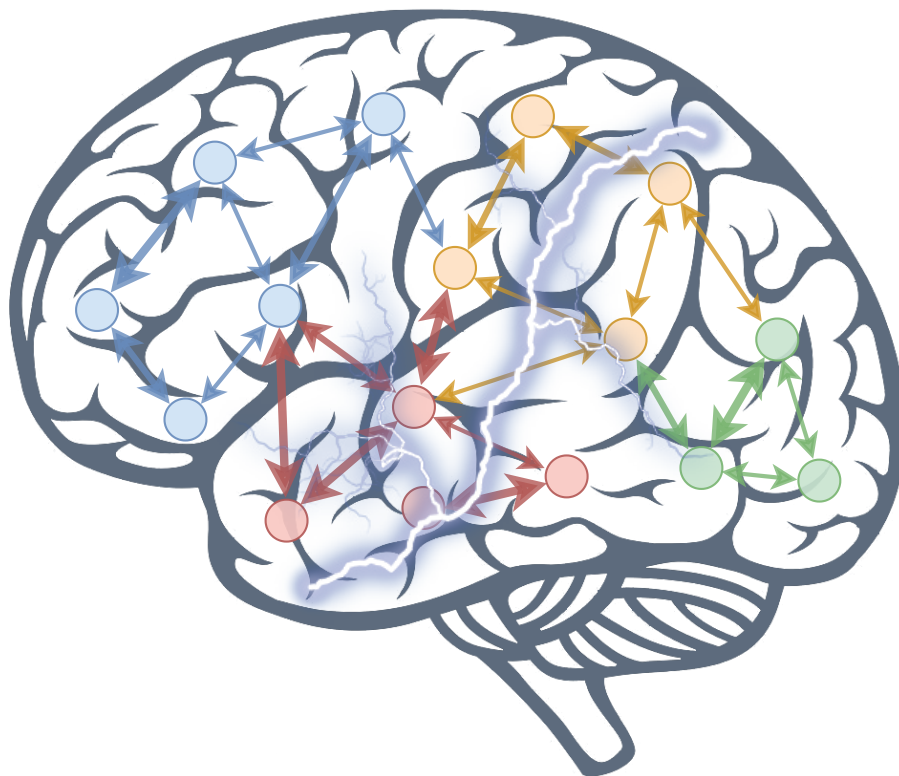


Ye Ren

# Brain Connectivity Analysis in Epilepsy for Epileptogenic Focus Localization

---



JYU DISSERTATIONS 159

---

Ye Ren

# Brain Connectivity Analysis in Epilepsy for Epileptogenic Focus Localization

Esitetään Jyväskylän yliopiston informaatioteknologian tiedekunnan suostumuksella  
julkisesti tarkastettavaksi Agora-rakennuksen Alfa-salissa  
joulukuun 14. päivänä 2019 kello 12.

Academic dissertation to be publicly discussed, by permission of  
the Faculty of Information Technology of the University of Jyväskylä,  
in building Agora, Alfa hall, on December 14, 2019 at 12 o'clock noon.



JYVÄSKYLÄN YLIOPISTO  
UNIVERSITY OF JYVÄSKYLÄ

JYVÄSKYLÄ 2019

Editors

Timo Männikkö

Faculty of Information Technology, University of Jyväskylä

Ville Korkiakangas

Open Science Centre, University of Jyväskylä

Copyright © 2019, by University of Jyväskylä

Permanent link to this publication: <http://urn.fi/URN:ISBN:978-951-39-7954-6>

ISBN 978-951-39-7954-6 (PDF)

URN:ISBN:978-951-39-7954-6

ISSN 2489-9003

## ABSTRACT

Ren, Ye

Brain connectivity analysis in epilepsy for epileptogenic focus localization

Jyväskylä: University of Jyväskylä, 2019, 47 p. (+included articles)

(JYU Dissertations

ISSN 2489-9003; 159)

ISBN 978-951-39-7954-6 (PDF)

Abnormal brain neural activities lead to abnormality and complexity of brain network connectivity in patients with epilepsy. The purpose of this research is to investigate the characteristics of brain connectivity and to explore more accurate localization methods of the epileptogenic foci in drug-resistant epilepsy.

Brain connectivity measures based on synchronization were first evaluated on electroencephalogram data in healthy subjects to find different performance in detecting the synchronization dynamics in the brain network. Spatial and temporal phase-amplitude coupling characteristics between low and high frequency electrocorticogram data were then estimated in patients with temporal lobe epilepsy. The 'fall-max' phase-amplitude coupling pattern appeared in the middle period of seizure was suggested as a reliable biomarker of epileptogenic zone, which provides insight into the underlying neural dynamic between low and high frequency neural activities in the epileptic brain network. Effective connectivity and topology characteristics of the brain network were investigated as well in patients with temporal lobe epilepsy by adopting high temporal resolution effective connectivity measure combined with graph metrics on electrocorticogram data, which describes in detail the strength and direction of information transmission. The transient seizure onset effective connectivity network provides more accurate localization of seizure onset zone and epileptogenic zone. In addition, functional connectivity and source localization were studied on electroencephalogram data of a patients with reflex seizure, which provides insights on generation and propagation of epileptic activities, as well as the local and global topology characteristics on cortical level network.

Overall, this research examined the performance of various brain connectivity measures by analyzing the functional connectivity and effective connectivity in healthy people and epilepsy patients, and explored more accurate methods for localization of epileptogenic foci. It provides insights into the underlying mechanism of epileptic brain network connectivity and an important reference for the preoperative evaluation of clinical epilepsy surgery, which can improve the localization accuracy of epileptogenic foci and reduce the probability of epileptic seizures.

Keywords: brain connectivity, synchronization, epilepsy, epileptogenic focus, localization

## TIIVISTELMÄ (ABSTRACT IN FINNISH)

Ren, Ye

Aivojen konnektiviteettianalyysi epileptogeenisen fokuksen lokalisoinnissa

Jyväskylä: University of Jyväskylä, 2019, 47 p. (+artikkelit)

(JYU Dissertations

ISSN 2489-9003; 159)

ISBN 978-951-39-7954-6 (PDF)

Epilepsiaa sairastavilla potilailla aivojen poikkeavat neuraaliset aktiviteetit aiheuttavat poikkeavuuksia ja kompleksisuutta aivoverkoston konnektiviteetteihin. Tämän väitöskirjan tarkoituksena on tutkia aivojen konnektiviteettien ominaisuuksia ja kehittää tarkempia menetelmiä epileptogeenisen fokuksen paikallistamisessa lääkeresistentissä epilepsiassa.

Synkronointiin perustuvia aivojen konnektiviteettimittauksia evaluoidaan ensimmäiseksi terveiden henkilöiden aivosähkökäyristä (EEG), tavoitteena havaita eroavaisuuksia aivoverkoston synkronian dynamiikassa. Sen jälkeen arvioitiin temporaalieleptisten potilaiden elektokortikografisesta (ECoG) matalan ja korkean taajuuden datasta spatiaalinen ja ajallinen vaihe-amplitudikytkös. Löydettyä nk. 'fall-max' vaihe-amplitudikytköstä, joka ilmeni kohtauksen keskivaiheilla, ehdotetaan luotettavaksi biomarkkeriksi aivojen epileptogeenisellä aluella, mikä havainto lisää ymmärrystä epileptisten potilaiden aivojen matalan ja korkea taajuuden neuraalisten aktiviteettien väliseen dynamiikkaan. Lisäksi tutkittiin näiden potilaiden datasta aivoverkoston efektiivinen konnektiviteetti ja topologia soveltamalla korkeamman aikaresoluution konnektiviteettimittareita yhdistettynä elektokortikografisesta datasta saatuihin graafisiin metriikoihin, jotka kuvaavat yksityiskohtaisesti informaation siirtymisen voimakkuuden ja suunnan. Kohtauksen transientin alkukohdan konnektiviteettiverkosto antaa tarkemman paikannuksen kohtauksen alkukohdalle ja epileptogeeniselle aluella. Lisäksi tutkittiin toiminnallista konnektiviteettia ja paikannusta niiden potilaiden aivosähkökäyristä, joilla havaittiin refleksikohtauksia. Tämä tutkimus lisää ymmärrystä epileptisen aktiviteetin syntyyn ja etenemiseen sekä aivokuoriton verkoston paikalliseen ja globaaliin topologiapiirteisiin.

Kaiken kaikkiaan, tässä väitöskirjassa tutkittiin erilaisten aivoverkoston konnektiviteettien mittaustapojen suosituskykyä analysoimalla terveiden ja epileptisten potilaiden aivojen toiminnallista ja efektiivistä konnektiviteettia, kehittämällä samalla tarkempia menetelmiä epileptogeenisen fokuksen paikallistamiseen. Tutkimus lisää ymmärrystä epileptisen aivoverkon konnektiviteetin mekanismeihin ja tärkeän referenssin pre-operatiiviseen evaluointiin kliinisessä epilepsialeikkauksessa, antaen parannetun paikannustarkkuuden epileptogeeniselle fokukselle ja näin ollen pienentäen epilepsia-kohtausten todennäköisyyttä.

Avainsanat: aivojen konnektiviteetti, synkronointi, epilepsia, epileptogeeninen fokus, paikannus

**Author** Ye Ren  
Faculty of Information Technology  
University of Jyväskylä  
Finland

**Supervisors** Tapani Ristaniemi  
Faculty of Information Technology  
University of Jyväskylä  
Finland

Xiaoli Li  
State Key Laboratory of Cognitive Neuroscience and  
Learning  
Beijing Normal University  
China

Fengyu Cong  
Department of Biomedical Engineering  
Dalian University of Technology  
China

**Reviewers** Jing Jin  
School of Information Science and Engineering  
East China University of Science and Technology  
China

Yu Zhang  
Department of Psychiatry and Behavior Sciences  
Stanford University  
United States

**Opponent** Tarmo Lipping  
Tampere University  
Finland

## ACKNOWLEDGEMENTS

I would like to express my gratitude to many people who helped and supported me during my doctoral study.

First, I would like to thank my main supervisor, Prof. Tapani Ristaniemi. He offered me the opportunity to start my doctoral studies and gave me help during my doctoral study in Jyväskylä. I thank him for providing me great ideas and solving the practical issues in the dissertation, and supporting me in many other ways.

I am very grateful to my second supervisor, Prof. Xiaoli Li, who is also my supervisor during my master's degree, gave me a lot of help, advice, and guidance for my research topics.

I would like to thank my third supervisor, Prof. Fengyu Cong, who introduced me to the doctoral study at the University of Jyväskylä and gave me help and encouragement to continue my doctoral study.

I would also like to thank Dr. Ruihua Zhang, who provides great support for my doctoral study and offered me help and guidance on clinical aspects of my research.

I am grateful for the reviewers of my dissertation, Prof. Jing Jin and Dr. Yu Zhang, and for their comments and valuable suggestions. I am very honored that Prof. Tarmo Lipping can be my opponent on the public defense.

I also express my thanks to my good friends in Finland, Jia Liu, Yongjie Zhu, Deqing Wang, Xueyan Li, Wenya Liu, Lili Tian, Xiulin Wang, Yingying Wang, Biying Wang. They helped me a lot in my study and life and made my life in Jyväskylä more meaningful and colorful.

I also thank Zeqiu Meng. She is a kind and lovely girl. I am grateful to her for being my flatmate in Ristonmma and bringing me a lot of companionship and happiness throughout my doctoral life in Jyväskylä.

Last but not least, I would like to thank my parents for their supports and deep love for me. Finally, I gave my heartfelt gratitude to my boyfriend, Yang Xiao. His companion and support brought me great love and happiness in my life.

Jyväskylä 8.11.2019

Ye Ren

## LIST OF ABBREVIATIONS

ADTF	Adaptive directed transfer function
APDC	Adaptive partial directed coherence
BC	Betweenness centrality
BIS	Bispectral Index
CPL	Charateristic path length
CC	Closeness centrality
C	Clustering coefficient
COR	Cross-correlation
DOA	Depth of anesthesia
DET	Determinism
DTF	Directed transfer function
EC	Effective connectivity
ECS	Electrical cortical stimulation
ECoG	Electrocorticogram
EEG	Electroencephalogram
EZ	Epileptogenic zone
ffADTF	Full-frequency adaptive directed transfer function
FC	Functional connectivity
fMRI	Functional magnetic resonance imaging
GE	Global efficiency
HFOs	High-frequency oscillations
iADTF	Integrated adaptive directed transfer function
IEDs	Interictal epileptiform discharges
LE	Local efficiency
LFOs	Low-frequency oscillations
MRI	Magnetic resonance imaging
MEG	Magnetoencephalogram
mADTF	Masked adaptive directed transfer function
MI	Modulation index
MI	Mutual information
KerMI	Mutual information based on kernel estimation
NI	Nonlinear interdependence
OD	Out-degree
PDC	Partial directed coherence
PCMI	Permutation cross-mutual information
PAC	Phase-amplitude coupling
PLI	Phase lag index
PLV	Phase locking value
PS	Phase synchronization
PS <sub>SE</sub>	Phase synchronization based on Shannon entropy
C <sub>eff</sub>	Propofol effect-site concentration
RR	Recurrence rate
SOZ	Seizure onset zone

TLE Temporal lobe epilepsy  
WTC Wavelet transform coherence

# CONTENTS

ABSTRACT

TIIVISTELMÄ (ABSTRACT IN FINNISH)

ACKNOWLEDGEMENTS

LIST OF ABBREVIATIONS

CONTENTS

LIST OF INCLUDED ARTICLES

1	INTRODUCTION .....	13
1.1	Epilepsy Fact.....	13
1.2	EEG and ECoG in epilepsy.....	14
1.3	Brain connectivity .....	15
1.4	Graph theory of brain network.....	17
1.5	Structure of the dissertation .....	18
2	RESEARCH BACKGROUND AND RESEARCH QUESTIONS.....	19
2.1	Brain connectivity characteristics described using synchronization measures in anesthesia .....	19
2.2	Phase-amplitude coupling of neural oscillations in epilepsy .....	22
2.3	Brain connectivity for epileptogenic focus localization .....	23
2.4	Graph theory for epileptogenic focus localization.....	24
3	OVERVIEW OF INCLUDED ARTICLES .....	26
3.1	Article I: "A comparison of different synchronization measures in electroencephalogram during propofol anesthesia" & Article II: "Synchronization Measures in EEG signals" .....	26
3.2	Article III: "Temporal-spatial characteristics of phase-amplitude coupling in electrocorticogram for human temporal lobe epilepsy" .....	27
3.3	Article IV: "Transient seizure onset network for localization of epileptogenic zone: Effective connectivity and graph theory- based analyses of EcoG data in temporal lobe epilepsy" .....	29
3.4	Article V: " EEG source localization and functional connectivity in a rare patient with cold-induced reflex epilepsy" .....	30
4	DISCUSSION .....	32
4.1	Contributions.....	32
4.2	Limitations and further research.....	34
5	SUMMARY .....	36
	YHTEENVETO (SUMMARY IN FINNISH).....	38

REFERENCES..... 40

INCLUDED ARTICLES

## LIST OF INCLUDED ARTICLES

- I Zhenhu Liang, Ye Ren, Jiaqing Yan, Duan Li, Logan J. Voss, Jamie W. Sleight, Xiaoli Li. (2016). A comparison of different synchronization measures in electroencephalogram during propofol anesthesia. *Journal of clinical monitoring and computing*, 30(4): p. 451-466. DOI: <https://doi.org/10.1007/s10877-015-9738-z>
- II Zhenhu Liang, Yang Bai, Ye Ren, Xiaoli Li. (2016). Synchronization Measures in EEG signals, *In Signal Processing in Neuroscience*, Springer. p. 167-202. DOI: [https://doi.org/10.1007/978-981-10-1822-0\\_9](https://doi.org/10.1007/978-981-10-1822-0_9)
- III Ruihua Zhang, Ye Ren, Chunyan Liu, Na Xu, Xiaoli Li, Fengyu Cong, Tapani Ristaniemi, Yuping Wang. (2017). Temporal-spatial characteristics of phase-amplitude coupling in electrocorticogram for human temporal lobe epilepsy. *Clinical Neurophysiology*, 128(9): p. 1707-1718. DOI: <https://doi.org/10.1016/j.clinph.2017.05.020>
- IV Ye Ren, Fengyu Cong, Tapani Ristaniemi, Yuping Wang, Xiaoli Li, Ruihua Zhang. (2019). Transient seizure onset network for localization of epileptogenic zone: Effective connectivity and graph theory-based analyses of ECoG data in temporal lobe epilepsy. *Journal of Neurology*, 266(4): 844-859. DOI: <https://doi.org/10.1007/s00415-019-09204-4>
- V Ye Ren, Xiaoli Li, Fengyu Cong, Shuying Xiao, Qin Zhang, Ting Ao, Jun Zhang, Yuping Wang, Tapani Ristaniemi, Ruihua Zhang. (2019). EEG source localization and functional connectivity in a rare patient with cold-induced reflex epilepsy. *Epileptic Disorders*, ED-2019-08-0138, Under Review

# 1 INTRODUCTION

This chapter introduces the epilepsy fact, the role of electroencephalogram (EEG) and electrocorticogram (ECoG) in epilepsy, the common brain connectivity techniques, functional brain network characterized by graph theory, and outline of the dissertation's structure.

## 1.1 Epilepsy Fact

Epilepsy is a chronic noncommunicable disease of the brain that affects people of all ages. According to the World Health Organization, around 50 million people worldwide have epilepsy, making it the 4th most common neurological diseases after the migraine, stroke, and Alzheimer's disease (WHO, 2019). Nearly 80% of people with epilepsy live in low- and middle-income countries. In many parts of the world, people with epilepsy and their families suffer from stigma and discrimination.

Characteristics of epileptic seizures vary and depend on where in the brain the disturbance first starts, and how far it spreads. Temporary symptoms occur, such as loss of awareness or consciousness, and disturbances of movement, sensation (including vision, hearing, and taste), mood, or other cognitive functions. People with epilepsy tend to have more physical problems (such as fractures and bruising from injuries related to seizures), as well as higher rates of psychological conditions, including anxiety and depression (WHO, 2019).

Medication is the first choice for epilepsy treatment. For 30% of patients with epilepsy, seizures are not controlled by medication (Dalic & Cook, 2016; Tang, Hartz, & Bauer, 2017). These people who have failed two antiseizure medicine trials are referred to as having drug-resistant seizures (Kwan et al., 2010). Surgical management may be considered and epileptic resection surgery may offer a potential cure or significant improvement to those who are drug-resistant (Jette, Reid, & Wiebe, 2014). However, not all patients with drug-resistant epilepsy can undergo resection surgeries.

Seizures are divided into focal onset seizure (60%), generalized onset seizure (30%), and unknown onset (10%), depending on where they start in the brain (R. S. Fisher et al., 2017). In focal onset seizures, the predominant seizure type, the electrical disruption involves a limited area of the brain. Usually, only the drug-resistant epilepsy patients with focal seizures may consider and implement the resection surgery. On the contrary, in generalized onset seizures, the electrical disruption involves the entire brain, which is not suitable for resection surgery. The remaining 10% of patients experience nonepileptic seizures, which present like epileptic seizures, but aren't associated with the typical electrical discharge found in the brain.

Most patients undergoing epilepsy surgery are patients with temporal lobe epilepsy (TLE) who are refractory to antiepileptic drugs (Spencer & Huh, 2008). The most important aspect of epileptic resection surgery is the localization of the epileptogenic zone (EZ) in the preoperative assessment. At present, neurologist localize the epileptogenic focus mainly through clinical semiology, pathology, video EEG, ECoG, electrical cortical stimulation (ECS), and other neuroimaging options like magnetic resonance imaging (MRI), functional MRI (fMRI), positron emission tomography (PET), and single photo emission computed tomography (SPECT) (Perkins, 2019). Surgical treatment has been shown to be beneficial for the selected patients but fails to provide a seizure-free outcome in 20–30% of TLE patients (Harroud, Bouthillier, Weil, Nguyen, & treatment, 2012). Failure of epilepsy surgery may be caused by wrong localization of the EZ, very widespread EZ, and very limited resection of the suspected EZ (S. Noachtar & Remi, 2009). Also, the localization of the epileptogenic focus and the determination of the extent of surgical resection have a certain degree of subjectivity by epileptologists.

Therefore, it is of great scientific and clinical significance to study the neural mechanism of epileptic seizures in depth and to find more accurate localization methods of epileptogenic focus in drug-resistant epilepsy, so as to improve the accuracy of intraoperative focus resection and improve the postoperative seizure rate in patients with drug-resistant epilepsy.

## 1.2 EEG and ECoG in epilepsy

Neurons work by sending nerve impulses from one cell to another to transfer messages around the brain and the body (Rutecki, 1992). When the brain is working, cells communicate using electrical signals, and when they do this they 'give off' electricity. The electrical signals, sometimes called 'brain waves', can be collected by scalp electrodes and subdural strip or grid electrodes, or depth electrodes, which are known as EEG and ECoG respectively.

EEG and ECoG are the most intuitive ways to interpret what brain activity is happening, which looks for the presence or absence of specific brain activity in specific areas of the brain. They show different types of brain waves, such as delta waves (1-4 Hz), theta waves (4-8 Hz), alpha waves (8-13 Hz), beta waves (13-30

Hz), gamma waves (30-80 Hz), spike waves (Less than 80 milliseconds, i.e., 1/12 of a second), sharp waves (Over 80-200 milliseconds), etc (Teplan, 2002).

Epileptic seizures are a result of excessive electrical discharges in a group of brain cells (Robert S Fisher et al., 2005). Surface EEG recordings provide the best overview and the most efficient way to define the approximate localization of the EZ (S. Noachtar & Remi, 2009). Spike waves, sharp waves, slow spike-wave complexes, etc. are considered interictal epileptiform discharges (IEDs) (S Noachtar et al., 2004), which may occur in patients with epilepsy. The IEDs may provide some useful information about the seizure type (Cascino, 2002). The ictal EEG recording, however, is more sensitive and specific than interictal EEG as a diagnostic tool (Schulz et al., 2000; Steinhoff, So, Lim, & Lüders, 1995) and is considered to be critical in localizing the EZ (Foldvary et al., 2001; S. Noachtar & Remi, 2009). However, many people who do have epilepsy do not have abnormal discharges when the EEG recording is monitoring, while IEDs happen in healthy people who do not have epilepsy (So, 2010). That is why EEG is used alongside other tests and investigations to diagnose epilepsy and localize the EZ.

Invasive ECoG recordings are used to determine the extent of resection in patients in whom the EZ either cannot be localized with noninvasive methods or is anatomically too close to eloquent cortex of which the removal will result in loss of sensory processing or linguistic ability, mostly in partial temporal lobe resections. (Soheyl Noachtar, Borggraefe, & Behavior, 2009). ECoG offers flexible placement of recording and it can be performed before and after each stage of resection to assess the presence or absence of epileptiform activity (Kuruvilla & Flink, 2003; Zumsteg & Wieser, 2000). In addition, it allows identification and localization of eloquent cortex by means of ECS mapping (Brunner et al., 2009), which is important in patients in whom eloquent cortex is adjacent to the EZ and resection surgery has to preserve the eloquent cortex. However, ECoG has some limitations: it has limited acquisition time; spontaneous IEDs and seizures are rarely recorded; both the background activity and epileptiform discharges may be altered by the anesthetics, narcotic analgesics and by the surgery itself (Zumsteg & Wieser, 2000).

### 1.3 Brain connectivity

Brain connectivity can be divided into structural connectivity, functional connectivity (FC), and effective connectivity (EC) (Sakkalis, 2011). Structural connectivity, refers to anatomical connections, usually reflects large-range fiber bundles measured by diffusion tensor MRI (Honey et al., 2009). FC is defined by the correlation or coherence between nodes, does not provide directionality or causality (undirected), while EC is defined as the influence one node exerts over another under a particular network model of causal dynamics, it can evaluate directionality (directed) (Park & Friston, 2013).

FC and EC are estimated on different modalities like blood oxygenation level-dependent fMRI, EEG, ECoG or magnetoencephalogram (MEG) signals acquired during resting state or the task performance. fMRI provides a high spatial resolution but a limited temporal precision, whereas while EEG/ECoG/MEG has a limited spatial resolution but the high temporal precision. Because FC and EC are largely dependent on calculating the correspondence of neural signals over time, modalities such as EEG, ECoG, and MEG, which have excellent temporal resolution, are optimal for calculating such connectivities (Sakkalis, 2011).

FC and EC can be modeled and quantified with a large number of techniques, including correlation and coherence measures, phase synchronization (PS) measures, information-based measures, Granger causality based measures, and so on.

The most well known FC measure is correlation, also called the Pearson correlation coefficient, which calculates the linear correlation between two signals based on the amplitudes of the signals. A variant of this measure is the cross-correlation (COR) which estimates the correlation between two signals that are shifted in time with respect to each other. The magnitude squared coherence calculates the linear correlation between two signals at certain frequencies. Wavelet coherence is an alternative method for calculating coherence (J.-P. Lachaux et al., 2002).

PS measures could investigate the phase relation of two signals. The most commonly used PS measures are the phase locking value (PLV) (J. P. Lachaux, Rodriguez, Martinerie, & Varela, 1999), and phase lag index (PLI) (C. J. Stam, Nolte, & Daffertshofer, 2007) which is robust to the volume conduction.

The most representative measures based on the information theory are mutual information (MI) (Cover & Thomas, 2012) and transfer entropy (Schreiber, 2000). MI quantifies the mutual dependence between the two variables, which is an undirected nonlinear measure. Transfer entropy assesses the amount of directed transfer of information between two random variables.

The Granger causality based measures are usually multivariate measures, which calculate from the coefficients of a multivariate autoregressive model in which the present samples of the signals are predicted using a linear combination of the past samples. The most commonly seen are directed transfer function (DTF) (Kaminski & Blinowska, 1991) and partial directed coherence (PDC) (Baccalá & Sameshima, 2001) which assume the stationarity of signals in a short time window, adaptive DTF (ADTF) (Wilke, Ding, & He, 2007) and adaptive PDC (APDC) (Astolfi et al., 2008) which detect the time-variant connectivity and have a high temporal resolution, and different normalizations of these measures (P. van Mierlo et al., 2011; Pieter Van Mierlo, Coito, Vulliémoz, & Lie, 2016).

The use of different brain connectivity techniques allows the exploration of complex brain network from different perspectives. Although analysis of brain connectivity has evolved significantly during the last decades and a variety of methods addressing both functional and effective connectivity are currently

available, there is no single optimum technique to universally assess brain connectivity (Sakkalis, 2011). The choice of each measure should depend on the measure itself as well as the research questions under consideration.

## 1.4 Graph theory of brain network

Brain network can be represented by a graph which is made up of nodes (also called vertices or points) and connected edges (also called links or lines). It can be investigated using graph theory through the following steps:

(1) Define the brain network nodes. The definition of the nodes (or vertices) for brain graphs is modality-specific. For electrophysiology based modalities, such as EEG, ECoG, and MEG, the nodes are defined as individual electrodes or sensors (Cornelis J Stam & Reijneveld, 2007). However, the signal at each electrode or sensor of EEG and MEG is a mixture of activity from different inner cortical sources, which is a well-known problem called volume conduction (Nunez et al., 1997; van den Broek, Reinders, Donderwinkel, Peters, & neurophysiology, 1998). There are three possible solutions (De Vico Fallani, Richiardi, Chavez, & Achard, 2014): (i) using spatial filters to remove the signal component shared by neighbouring sensors (Bradshaw & Wikswo, 2001), (ii) choosing connectivity measures that can reduce volume conduction effects, such as imaginary coherence or PLI, (iii) using cortical source reconstructions that assign the brain nodes to sources over a realistic cortex model (Schoffelen & Gross, 2009).

(2) Estimate the association between nodes. Usually, a group of signals  $X_1(t), X_2(t), \dots, X_N(t)$  are obtained from  $N$  nodes and the association between nodes  $i$  and  $j$  were estimated to construct a connectivity matrix. The connectivity matrix calculated by either FC or EC measures as mentioned in the previous section are either undirected graphs (symmetric matrix) or directed graphs (asymmetric matrix) respectively. The performance of each connectivity measure depends on the characteristics of both the datasets and the measure itself. A more reasoned approach is selecting the FC or EC measures according to clear scientific goal and well designed experimental protocol (E. Bullmore & Sporns, 2009).

(3) Filter the graph. In the connectivity matrix  $W_{N \times N}$ , the total number of weighted edges is  $N(N - 1)/2$  when using FC measures and  $N(N - 1)$  when using EC measures, excluding self-connectivity. For the matrix  $W_{N \times N}$ , it has been proposed to consider all the information by keeping all the weighted edges (Mikhail Rubinov & Sporns, 2011). Another approach is filtering the matrix and keeping only the significant edges by adding a threshold  $T$  and removing the ones whose weight  $w_{ij}$  is lower than  $T$ . Also, the significant (larger than  $T$ ) and nonsignificant (smaller than  $T$ ) weighted edges can be set to 1 and 0 to transformed into binary matrix, respectively.

(4) Calculate the graph metrics and compare the graphs. Topological properties of brain networks can be measured by a wide variety of graph metrics, some of which will be introduced in a later section. Selecting the appropriate

graph metrics to compare brain graphs depends primarily on the research question and secondly on practical computational requirements (De Vico Fallani et al., 2014). The brain graphs should be compared with the equivalent parameters containing the same number of nodes and edges or called 'density' in order to ensure the most direct mathematical comparability of graph metric values (E. Bullmore & Sporns, 2009; E. T. Bullmore & Bassett, 2011).

The graph theory, the most popular technique in characterizing brain network, can not only describe the brain network topology features but also provide very valuable insights in both structural and functional organization of brain networks.

## **1.5 Structure of the dissertation**

The dissertation consists of a compilation part and five original articles (numbered I-V). In this chapter, we have made an introduction of the problem status, main concepts, common technical methods and analysis procedures related to the topic. The next chapter introduces the research background and proposes the research questions. In Chapter 3, we briefly summarize the objectives, methods, and findings of each included articles. Chapter 4 explains the contributions of the research, discusses the limitations and future research directions. Finally, Chapter 5 summarizes the dissertation.

## **2 RESEARCH BACKGROUND AND RESEARCH QUESTIONS**

This chapter introduces the research background of the dissertation by reviewing the state-of-the-art literature and then proposes the research question.

### **2.1 Brain connectivity characteristics described using synchronization measures in anesthesia**

EEG synchronization is characterized by the coordination of neural activity between the two brain regions, which can be quantified and evaluated using different synchronization measures. Synchronization measures are usually based on time-domain, time-frequency domain, information theory, etc. The characteristics of brain connectivity by synchronization analysis during anesthesia were reviewed as follows.

COR, a traditional synchronization measure, is a measure of similarity of two series that defined in the time domain. The connectivity between frontal and parietal lobes was analyzed by the zero-lag correlation coefficients (Ku, Lee, Noh, Jun, & Mashour, 2011). They found a positive mean value between these two brain regions during general anesthesia but a zero mean value for surrogate data. Lee et al. investigated the network connection of the EEG in multiple channels using COR on awakening and noted that the increase in connection strength was abrupt on wakeup (Lee, Muller, Noh, Choi, & Mashour, 2011). However, it was illustrated that cross-approximate entropy was more suited to detect changes of cortical local field potential than the COR in cortical network during anesthesia period in rats (Kreuzer et al., 2010). COR index was also used to assess changes in neuronal synchronization in frontal-temporal network and found that it had no significant variation in tracking the effect-site drug concentration and cannot estimate anesthetic state of patients (Shalhaf, Behnam, Sleight, Steyn-Ross, & Steyn-Ross, 2015). These previous studies have not confirmed whether COR can

accurately assess the synchronization characteristics during anesthesia and effectively detect the depth of anesthesia (DOA).

Coherence is a time-frequency domain method that can evaluate the synchronization in specific frequency bands. The simplest coherence is based on the Fourier transform. More coherence related analyses in anesthesia used the normal coherence measure or combined the coherence with other measures. Cimenser et al. used the Fourier transform-based global coherence detect strong coordinated  $\alpha$  activity in the occipital lobe in the awake state that shifted to the frontal leads during unconsciousness, but a lack of coordinated  $\delta$  activity during both the awake and unconscious states (Cimenser et al., 2011). Lipping et al. found the magnitude squared coherence of  $\beta$  EEG activity start actually several minutes before the onset of burst suppression and slows down gradually until the burst suppression appears (Lipping et al., 2003). Moreover, the S-estimator was applied to the bi-channel coherence matrix to construct an overall index called the SI which was used to track the overall synchronization changes during anesthesia in sheep (D. Li, Voss, Sleight, & Li, 2013). They found the anesthetic-induced increase in synchrony increased from the waking to the burst-suppression states, and returned to baseline during recovery most in  $\alpha$  and  $\beta$  frequency bands. Bicoherence was used to analyze the nonlinear dynamic of EEG during wakefulness and anesthesia (Hayashi, Mukai, & Sawa, 2014). The  $\alpha$  bicoherence growth is seen in awake state in occipital lobe, and the  $\alpha$  bicoherence peak disappeared in the occipital lobe and appeared in the frontal lobe. However, there are few studies using the coherence based on wavelet transform for investigating the EEG synchronization features in anesthesia. Neuronal synchronization was estimated using wavelet coherence computed from the ERP data in rat (Imas, Ropella, Wood, & Hudetz, 2006). They found a reduction of long-range anterior-posterior coherence in 5–25 Hz and 25–50 Hz frequency bands by isoflurane in a concentration-dependent manner. From previous studies, we do not know whether the coherence based on wavelet transform that was used to evaluate the EEG synchronization feature can better describe the changing DOA in human.

PS is a classical synchronization measure by two signals tend to oscillate with a repeating sequence of relative phase angles and are independent of amplitude. It has been reported that the PS index based on the Hilbert transform in the sub-delta band decreased during the induction and increased during the recovery, while the directions were reversed in the alpha band (Koskinen, Seppanen, Tuukkanen, Yli-Hankala, & Jantti, 2001). More phase synchrony was showed in the unconscious than the conscious state for both gamma and beta passbands in intracranial EEG (Pockett & Holmes, 2009). Rangaprakash et al. found a decreased PS that is based on the correlation between probabilities of recurrence between brain regions during anesthesia on resting state fMRI (Rangaprakash, Hu, & Deshpande, 2013). Not many previous studies have applied PS measure to assess the DOA.

MI is a measure of the mutual dependence between the two variables. Jullitta et al. used the auto MI function to EEG of patients under anesthesia to correctly classify the awake, sedated, anesthetized, and burst suppression states in

the range 61.1%-100% (Julitta et al., 2011). MI combined with complexity was proposed and proven to monitor the DOA accurately and computationally fast (Huang, Yu, Ju, Cheng, & physics, 2003). Moreover, Liang et al. proposed a permutation auto MI method to assess the information coupling of EEG during anesthesia (Liang et al., 2013). They found that the permutation auto MI method had a better performance on tracking drug concentration than traditional MI. The permutation cross-MI (PCMI) could describe the coupling changes of EEG series under isoflurane and remifentanyl anesthesia and distinguish between the consciousness state and anesthesia-induced unconsciousness state (Liang, Liang, Wang, Ouyang, & Li, 2015). Estimation of MI using kernel density estimators was found to be superior to the histogram-based MI (Moon, Rajagopalan, & Lall, 1995), but there is no research using Kernel-density based MI to evaluate the DOA. Previous studies showed that MI-based measures are potential ways to assess DOA.

Nonlinear interdependence (NI) is a measure of generalized synchronization in nonlinear systems, which evaluates the interdependency according to the distance of delay vectors of two time series. It has been applied in nonlinear interactions analysis of EEG data in healthy human (Breakspear & Terry, 2002a, 2002b; Terry, Anderson, & Horne, 2004), Alzheimer's disease (Dauwels, Vialatte, & Cichocki, 2008; Kramer, Chang, Cohen, Hudson, & Szeri, 2007), but mostly in epilepsy patients. NI did not have a good predictive performance of epileptic seizures (Mirowski, Madhavan, LeCun, & Kuzniecky, 2009; Mormann et al., 2005), while it evaluated the interchannel EEG synchronization better than the linear COR during seizures in children (Wallois, Patil, Heberle, & Grebe, 2010). Andrzejak et al. applied NI and other measures to intracranial EEG and suggested EEG signals from epileptogenic brain areas are more nonlinear-dependent compared to signals recorded from non-epileptogenic brain areas (Andrzejak, Schindler, & Rummel, 2012). It was reported that NI was low during interictal period and transient patterns of NI emerged at the initial spread of the seizure, which means that the NI can describe properly the spatio-temporal organization of the seizures and could become a very useful tool to aid the localization of the epileptogenic regions (Le Van Quyen, Adam, Baulac, Martinerie, & Varela, 1998). However, no studies have shown whether NI can assess the synchronization characteristics during anesthesia and whether it can be used to better monitor the DOA.

Recurrence quantification analysis (RQA) is a method of nonlinear data analysis. Common RQA measures are recurrence rate (RR), determinism (DET), laminarity, Shannon entropy, etc. RR was superior to DET and Shannon entropy for detection of burst suppression pattern during anesthesia, with the highest sensitivity of suppression detection 96.49% (Liang et al., 2014). The parameter selected of RR was assessed using EEG data and it was proved that when time lag was larger than 4, the ability to separate consciousness from unconsciousness decreased (Jordan, Stockmanns, Kochs, Pilge, & Schneider, 2008). Shalhaf et al. provided an index named order pattern laminarity, which could estimate anesthetic state at the point of loss of consciousness of patient more efficiently than

the Bispectral Index (BIS) (Shalbab et al., 2015). Moreover, it was found that the DET of EEG between forehead and temple increased gradually with increasing the concentration of sevoflurane (X. Li, Sleight, Voss, & Ouyang, 2007). Becker et al. presented a novel approach based on DET of EEG and demonstrated that it could separate consciousness from unconsciousness during both sevoflurane and propofol anesthesia with an overall prediction probability of more than 85% (Becker et al., 2010). Previous studies have not shown whether RQA measures can effectively detect the recovery of consciousness.

## 2.2 Phase-amplitude coupling of neural oscillations in epilepsy

Abnormal discharge of neurons causes the specificity of the neural oscillations of the cerebral cortex in the epileptic human brain. Complex neural activities in the epileptic cerebral cortex are constituted by simultaneous neural oscillations in different frequency bands.

The interactions between neural oscillations in different frequency bands, termed as cross-frequency coupling, plays an important role in investigating the mechanisms of synchronization of neural oscillations (Jensen & Colgin, 2007). Phase-amplitude coupling (PAC), a form of cross-frequency coupling in which the phase of low-frequency oscillations (LFOs) modulates the amplitude of high-frequency oscillations (HFOs), has become a rising concern in studies of synchronization of neural oscillations in various frequency bands (Tort, Komorowski, Eichenbaum, & Kopell, 2010).

Alvarado-Rojas et al. demonstrated that preictal states can be detected by slow (0.5–3 Hz) modulation of high-frequency gamma activities (40–140 Hz) from patients with partial epilepsy (Alvarado-Rojas et al., 2014). Edakawa et al. also used PAC accurately detected the ictal state from the interictal state, which was characterized by a strong PAC between the phase of  $\beta$  (13–25 Hz) and the amplitude of high  $\gamma$  (80–150 Hz) (Edakawa et al., 2016). Nariai et al. determined that ictal HFOs at 80–200 Hz were coupled tightly to the phase of slow-wave at  $\leq 1$  Hz, whereas interictal HFOs were loosely coupled to the phase of slow-wave at  $\leq 1$  Hz but tightly to that of  $\geq 3$  Hz at the seizure onset zone (SOZ) in 11 children who underwent ECoG recording (Nariai et al., 2011). PAC was also found to be significantly stronger in the SOZ compared to normal regions (Amiri, Frauscher, & Gotman, 2016; Weiss et al., 2016). Moreover, amplitudes of pathological HFOs were found to be most significantly modulated by the phase of  $\alpha$  oscillations in the seizure-onset zone compared to non-epileptic regions. Also, the LFO phase at which HFO amplitudes were maximal was inconsistent at seizure initiation, yet consistently at the trough of the LFOs at seizure termination in ECoG recordings from 17 children (Ibrahim et al., 2014). Recently, Guirgis et al. used modulation index (MI) and eigenvalue decomposition to suggest that delta-modulated HFOs may provide more accurate localization of the EZ in patients with extratemporal lobe epilepsy (Guirgis, Chinvarun, Del Campo, Carlen,

& Bardakjian, 2015). MI was also used to illustrate that epileptogenic HFOs may be coupled with slow-wave 3–4 Hz more preferentially than slow-wave 0.5–1 Hz in focal epilepsy (Nonoda et al., 2016). It was said that MI during interictal recording may provide useful information for the prediction of postoperative seizure outcome (Motoi et al., 2018). Most of the previous studies have shown that increased PAC between HFO amplitude and LFO phase during ictal period may constitute a marker of epileptogenic brain areas and may be relevant for understanding seizure dynamic. However, how the PAC mode between LFOs and HFOs changes at various seizure states has not been studied clearly.

### 2.3 Brain connectivity for epileptogenic focus localization

Abnormal epilepsy discharge leads to brain connectivity disturbances in epileptic brain (Engel et al., 2013; Englot et al., 2017). Abnormal connectivity network makes it difficult for epileptologists to localize the epileptogenic focus in medically intractable epilepsy, which may lead to the failure of resection surgery that causes various degree of postoperative seizures. Accurate localization of epileptogenic focus during preoperative assessment is vital for these patients who undergo the resection surgery.

Over the last decade, considerable effort has been devoted to characterize functional brain connectivity and functional brain connectivity.

DTF-based and PDC-based measures were mostly applied on the brain connectivity studies of ECoG data for epileptogenic focus localization. Wilke et al. used DTF measure on the ictal ECoG recordings of pediatric patients with medically intractable epilepsy and proved that the DTF identified generators of the ictal activity that were highly correlated with the SOZ identified by the epileptologists (Wilke, van Drongelen, Kohrman, & He, 2010). DTF was also calculated for each windowed ictal and resting interictal ECoG dataset over  $\theta$ ,  $\alpha$ ,  $\beta$ , and  $\gamma$  frequency bands and ADTF was calculated for each interictal spike to quantify the network interactions, with  $\gamma$  band activity most closely correlated with improved post-surgical outcome (Wilke, Worrell, & He, 2011). DTF was also used to estimate the EC, which demonstrated that cortical areas with high average outflow values corresponded well with the surgical resection areas identified using electrophysiologic data and conventional neuroimaging modalities (Jung et al., 2011).

Mierlo et al. compared different normalizations of ADTF, i.e., the integrated ADTF (iADTF), the masked ADTF (mADTF) and the full-frequency ADTF (ffADTF), to investigate whether one is more suitable to describe the seizure propagation during an epileptic seizure. They found the ffADTF outperforms the iADTF and mADTF both on simulation data and real ECoG data (P. van Mierlo et al., 2011). They also used spectrum-weighted ADTF improved based on ffADTF to demonstrate the feasibility of correctly localizing the SOZ from ECoG recordings during the first 20 s of ictal rhythmic ECoG activity (P. van Mierlo et

al., 2013). Moreover, generalized PDC was used for ECoG to quantify the EC between brain sites in patients with TLE, which indicates that the PDC measure may lead to an accurate localization of epileptogenic focus in pre-surgical evaluation (Ioannis Vlachos et al., 2013; I. Vlachos et al., 2017). The iADTF, ffADTF, integrated APDC, and full-frequency APDC were later compared by Mierlo et al. in simulations data and in one patient data. They concluded that the integrated and full-frequency variants perform equally well and ADTF is most optimal to localize the SOZ (Pieter Van Mierlo et al., 2016).

DTF-based and PDC-based measures were also applied to the brain connectivity studies of EEG data. ADTF was used to quantify the connectivity strength between pairs of regions, which was effective in detecting the focal regions and in characterizing the dynamics of the spike propagation (Storti et al., 2016) as well as in detecting the EZ in the interictal discharging (Zhang et al., 2017). Also, spectrum-weighted ADTF was employed to quantify the information flow for improving the accuracy of SOZ localization in a non-invasive way in the presurgical evaluation of epilepsy (Martinez-Vargas, Strobbe, Vonck, van Mierlo, & Castellanos-Dominguez, 2017; Staljanssens et al., 2017). Weighted PDC was used to estimate the causal interactions during spike-free resting state EEG epochs and suggest frequency-specific resting-state network alterations underlying focal epilepsy (Coito, Michel, van Mierlo, Vulliemoz, & Plomp, 2016).

In addition, there were some other brain connectivity techniques applied on epileptic EEG data to localize the epileptogenic focus. FC was quantified by lagged PS of EEG in patients with focal epilepsy to find an increased  $\beta$  temporo-frontal connectivity in the hemisphere with predominant seizure focus (Canuet et al., 2011). Klamer et al. used dynamic causal modeling which is a method to non-invasively assess EC between brain regions to indicate that right mesial temporal neuronal activity drives changes in the frontal areas consistently and prove that dynamic causal modeling was able to correctly localize focus and propagation of epileptic activity and thereby characterize the underlying epileptic network (Klamer et al., 2015).

From previous studies, it is unclear how different brain connectivity techniques describe characteristics of epileptic brain networks and localize the epileptogenic focus in various frequency bands during the non-seizure and various seizure periods.

## 2.4 Graph theory for epileptogenic focus localization

Graph theory is the study of graphs, which are used to represent neural networks of communication in neuroscience (Bassett & Sporns, 2017) and are able to explore the topological characteristics of epileptic brain network from many modalities including fMRI, structural MRI, EEG, ECoG, MEG, mouse model, etc (Chiang & Haneef, 2014).

The most common graph metrics that are used to quantitate the brain network topology are out-degree (OD), clustering coefficient (C), characteristic path

length (CPL), closeness centrality (CC), betweenness centrality (BC), local efficiency (LE), global efficiency (GE) (M. Rubinov & Sporns, 2010). High OD identifies nodes output more information to other nodes, which act as sources of information flow. LE and GE act as the alternative graph metrics to the C and CPL respectively, which are robust for networks with disconnected nodes. High LE and high GE represent nodes cluster together with more nearest and long-range neighbors. Nodes with high CC communicate faster with other nodes. Nodes with high BC participate in a larger number of shortest paths and act as hubs in a network.

There are not many studies on the use of the graph metrics to localize the epileptogenic focus. In general, graph metrics are combined with DTF-based and PDC-based connectivity measures for epileptogenic focus localization analysis. It was observed that the brain regions with high OD had a high correlation with cortical areas identified clinically as the generators of the ictal activity (Wilke, Worrell, & He, 2009). High total OD during the first 20 s of ictal ECoG was among the contacts identified by the epileptologist as the seizure onset (P. van Mierlo et al., 2013). Mierlo et al. found in ictal and interictal ECoG data that the ADTF combined with the OD resulted in correct SOZ localization (Pieter Van Mierlo et al., 2016). Epileptogenic focus was also detected prior to the discharge onset by ADTF combined with OD of interictal EEG data, which has been proved that time-varying connectivity analysis and graph topology analysis could not only reveal the underlying neural mechanism of epilepsy, but also function as a useful tool in detecting the epileptogenic focus (Zhang et al., 2017). In addition, Wilke et al. found in ictal and interictal ECoG data that the BC was correlated with the location of the resected cortical regions in patients who were seizure-free following surgical intervention (Wilke et al., 2011). Only high BC values of the ictal ECoG coincided well with the surgical resection areas among various graph metrics such as LE, participation coefficient, and eigenvector centrality on the FC networks constructed by PLV (Kim et al., 2015). Then, the BC was also proved to be a reliable feature for the identification of the EZ on EEG data (Storti et al., 2016).

Most researches of graph theory analysis used OD or BC to localize the focus after DTF-based connectivity analysis, but the accuracy of different graph metric has not been compared. The accuracy of different graph metrics for localization of epileptogenic focus remains an important issue to be studied.

## 3 OVERVIEW OF INCLUDED ARTICLES

### 3.1 Article I: "A comparison of different synchronization measures in electroencephalogram during propofol anesthesia" & Article II: "Synchronization Measures in EEG signals"

Zhenhu Liang, Ye Ren, Jiaqing Yan, Duan Li, Logan J. Voss, Jamie W. Sleight, Xiaoli Li. (2016). A comparison of different synchronization measures in electroencephalogram during propofol anesthesia. *Journal of clinical monitoring and computing*, 30(4): p. 451-466.

Zhenhu Liang, Yang Bai, Ye Ren, Xiaoli Li. (2016). Synchronization Measures in EEG signals, *In Signal Processing in Neuroscience*, Springer. p. 167-202.

#### Objective

The aim of these two studies is to describe the characteristics of EEG synchronization during the whole period of general anesthesia using different synchronization measures, evaluate the performance of the synchronization measures on distinguishing the awake, unconscious, and recovery states, find the effective synchronization measures for monitoring the DOA, and understand the underlying neurophysiological mechanisms of general anesthesia.

#### Methods

Two-channel EEG data from seven volunteers who had undergone a brief standardized propofol anesthesia from a previous study (Williams & Sleight, 1999) were selected. Eight synchronization indexes, i.e., COR, MI based on kernel estimation (KerMI), PCMI, NI, PS based on PLV ( $PS_{PLV}$ ), PS based on Shannon entropy ( $PS_{SE}$ ), DET, wavelet transform coherence (WTC), were calculated and obtained by 10-second sliding windows with an overlap of 7.5 seconds during the whole period of propofol anesthesia. Prediction probability was used to evaluate

the consistency of synchronization indexes, BIS which is one of several technologies used to monitor DOA, and propofol effect-site concentration ( $C_{eff}$ ). The correlation among the synchronization indexes, BIS, and  $C_{eff}$  was calculated by Pearson correlation coefficient. The synchronization indexes in three states (awake state, unconscious state, and recovery state) were compared to assess the ability of different synchronization measures to distinguish different anesthetic states.

## Findings

For consistency with BIS and  $C_{eff}$ , PCMI and DET were more consistent with the BIS and  $C_{eff}$  than the other synchronization measures. Different frequency bands in  $PS_{PLV}$  and  $PS_{SE}$  had no significant difference, while  $\alpha$  and  $\beta$  frequency bands in WTC were more consistent with BIS and  $C_{eff}$  than other frequency bands. In terms of the synchronization change during the anesthetic period, different synchronization measures showed various trends under three anesthetic states. PCMI, NI, and  $PS_{SE}$  in  $\beta$  frequency band decreased significantly in the unconscious state and increased significantly in the recovery state.  $PS_{PLV}$  in  $\delta$ ,  $\theta$ ,  $\alpha$ , and  $\gamma_1$  frequency bands had a significant decreasing trend in the unconscious state, while there is no significant change in the recovery state. In contrast, KerMI, DET, and WTC increased significantly in the unconscious state and decreased significantly in the recovery state. COR increased significantly only in the unconscious state. Moreover, PCMI, NI, and DET correlated closely with each other and had a higher correlation with BIS and  $C_{eff}$  than other synchronization measures.

## Contributions in the articles

Zhenhu Liang and I were responsible for all phases of research. Jiaqing Yan, Duan Li, and Yang Bai helped with the calculation of synchronization measures. Logan J. Voss, Jamie W. Sleight provided information related to the data and revisions to the original manuscript. Xiaoli Li gave overall comments and recommendations.

### 3.2 Article III: "Temporal-spatial characteristics of phase-amplitude coupling in electrocorticogram for human temporal lobe epilepsy"

Ruihua Zhang, Ye Ren, Chunyan Liu, Na Xu, Xiaoli Li, Fengyu Cong, Tapani Ristaniemi, Yuping Wang. (2017). Temporal-spatial characteristics of phase-amplitude coupling in electrocorticogram for human temporal lobe epilepsy. *Clinical Neurophysiology*, 128(9): p. 1707-1718.

## Objective

The aim of this study is to investigate the temporal-spatial characteristics of PAC in TLE, i.e., estimate the PAC strength and PAC pattern between low-frequency phase and high-frequency amplitude in different non-seizure and seizure periods in EZ and normal cortical areas.

## Methods

ECoG data were recorded from the cortical electrode strips placed on temporal lobes and the depth electrode strips implanted in the hippocampus of 12 seizures in seven patients with TLE. The MI based on the Kullback-Leibler distance was adopted to quantify the PAC strength between the phase of LFOs (0.2-10 Hz) and the amplitude of HFOs (11-400 Hz). The coupling strength was presented by the PAC co-modulogram of all channels in the pre-seizure, seizure onset, mid-seizure, seizure-termination, and post-seizure epochs. MI value of seizure-specific frequency bands was compared among five seizure epochs. Channels with high MI values were compared with the seizure onset channels identified by the neurosurgeons and the resection channels in the clinical surgery. The time-varying phase-amplitude modulogram was used to describe the PAC pattern during the period from pre-seizure to post-seizure of all channels. The coupling pattern difference between epileptogenic cortex and normal cortex was elaborated and compared by drawing the low-frequency and high-frequency ECoG signals and their corresponding phase and amplitude.

## Findings

The MI increased significantly in mid-seizure epoch and decreased significantly in seizure termination and post-seizure epochs. High MI was found to appear mainly in the PAC between low-frequency  $\delta$ ,  $\theta$ , and  $\alpha$  oscillations and high-frequency  $\gamma$  and ripple oscillations. MI also varied among channels and almost all channels with high MI values were included in the clinical resection cortical areas. The “fall-max” coupling pattern, i.e., high-frequency amplitudes were largest in the low-frequency phase range  $[-\pi, 0]$  which corresponded to the falling edges of LFOs, emerged in the mid-seizure epoch at the epileptogenic cortex. On the contrary, the largest high-frequency amplitudes distributed evenly in the low-frequency phase range  $[-\pi, \pi]$ , which means that they appeared at the peaks, troughs, rising edges, or falling edges of the LFOs at normal cortex.

## Contributions in the article

Chunyan Liu and Na Xu contributed to the data collection. Ruihua Zhang guided and helped with all clinically related information. I was responsible for all other phases of research. Xiaoli Li, Fengyu Cong, and Tapani Ristaniemi functioned as supervisors. Yuping Wang gave overall revision comments.

### 3.3 Article IV: "Transient seizure onset network for localization of epileptogenic zone: Effective connectivity and graph theory-based analyses of ECoG data in temporal lobe epilepsy"

Ye Ren, Fengyu Cong, Tapani Ristaniemi, Yuping Wang, Xiaoli Li, Ruihua Zhang. (2019). Transient seizure onset network for localization of epileptogenic zone: Effective connectivity and graph theory-based analyses of ECoG data in temporal lobe epilepsy. *Journal of Neurology*, 266(4): 844-859.

#### Objective

The aim of this study is to investigate the characteristics of EC networks in different frequency bands during various non-seizure and seizure periods in patients with TLE, and to compare the performance of different graph theoretical measures for localizing the SOZ and EZ in TLE.

#### Methods

ECoG data from temporal lobe and hippocampus of 14 seizures in seven patients with temporal lobe epilepsy were recorded. ffADTF which is a high temporal resolution measure was adopted to quantify the causal connections among different cortical areas. Five graph metrics, i.e., OD, CC, BC, C, and LE, were used to evaluate the topological properties of the cortical network at the small scale of single regions, i.e., single nodes, and at each cortical area. The ffADTF effective connectivity network and graph-based topological properties were calculated and described in five frequency bands ( $\delta$ ,  $\theta$ ,  $\alpha$ ,  $\beta$ , and  $\gamma$ ) and in five seizure periods (pre-seizure, early seizure, mid-seizure, late seizure, and post-seizure). The cortical areas with the highest values of the graph metric in the transient seizure onset network were compared with the SOZ identified by clinical epileptologists and the resection areas in the surgery. The proportions of the same cortical areas with the highest mean of graph metric as the clinical identified SOZ of each graph metric in three Engel Classes and in five frequency bands were calculated.

#### Findings

Directional connections of the epileptic activities could be observed in the high temporal resolution ffADTF effective connectivity network throughout the entire non-seizure and seizure periods. The seizure-specific transient seizure onset ffADTF networks which remained for approximately 20-50 ms emerged at seizure onset time, with strong connections generated from both SOZ and EZ. The graph metrics in SOZ and EZ were significantly larger than that in the other cortical areas in the transient seizure onset network. The OD and C were more likely to localize the SOZ and EZ than CC, BC, and LE in the transient seizure onset network. More cortical areas with the highest mean of graph metrics were the same as the clinically determined SOZ in low-frequency  $\delta$  and  $\theta$  bands of the

Engel Class I patients than in high-frequency  $\alpha$ ,  $\beta$ , and  $\gamma$  bands of Engel Class II and III patients.

### **Contributions in the article**

Yuping Wang and Ruihua Zhang provided clinically related information. I was responsible for all phases of research. Fengyu Cong, Tapani Ristaniemi, and Xiaoli Li functioned as supervisors.

### **3.4 Article V: " EEG source localization and functional connectivity in a rare patient with cold-induced reflex epilepsy"**

Ye Ren, Xiaoli Li, Fengyu Cong, Shuying Xiao, Qin Zhang, Ting Ao, Jun Zhang, Yuping Wang, Tapani Ristaniemi, Ruihua Zhang. (2019). EEG source localization and functional connectivity in a rare patient with cold-induced reflex epilepsy.

#### **Objective**

The aim of this study is to find the location of the epileptic focus, explore where and how the abnormal epileptic activities originate and propagate during the seizures, and investigate the characteristics of FC network in interictal and ictal stages in a rare patient with cold-induced reflex epilepsy.

#### **Methods**

A 70-year-old male had seizures triggered by the cold sensation of the body. Clinical seizure induction and video-EEG monitoring were implemented on this patient. The EEG data including interictal period and two complete seizures were selected for analysis. Source modeling was used to find the location of epileptic focus on the cortical level and explore the origination and propagation of the seizures. PLI was used to estimate the FC at  $\delta$ ,  $\theta$ ,  $\alpha$ , and  $\beta$  frequency bands in interictal, early ictal, and late ictal stages. Adapted thresholds were set for connectivity network thresholding to ensure that all networks have the same edges or fixed edge density. Graph-based LE and GE were used to quantify the topological properties of the FC network at the local and global level. LE and GE were computed at each network density from 0.05 to 0.95 with a step of 0.01 in four frequency bands and three seizure stages.

#### **Findings**

In the early ictal stage, slow waves of  $\delta$  and  $\theta$  frequency bands were found to appear in the right lateral occipital lobe in the two seizures, and also in the right superior and middle frontal lobes in seizure #2, which were considered as the pathologically epileptic slow waves. In the late or mid-late stages, strong  $\delta$  and  $\theta$

slow waves appeared in the middle temporal and inferior temporal lobes in the two seizures. For the strength of FC, PLI in the late or mid-late ictal stages was significantly larger than that in other stages in the  $\delta$  and  $\theta$  frequency bands, while there were no significant differences between the seizure epochs in  $\alpha$  frequency band in the two seizures. For the  $\beta$  frequency band, late ictal PLI was smaller than the early ictal PLE in the two seizures, and also smaller than the interictal PLI in only one seizure. For the topological properties, two epileptic  $\delta$  and  $\theta$  slow waves caused LE to increase and GE to decrease in the late or mid-late ictal stages.

### **Contributions in the article**

Shuying Xiao, Qin Zhang, Ting Ao, and Jun Zhang contributed to the diagnosis, drug therapy, clinical seizure induction, and data collection. I was responsible for all other phases of research. Xiaoli Li, Fengyu Cong, and Tapani Ristaniemi functioned as supervisors. Yuping Wang and Ruihua Zhang provided overall help and comments.

## 4 DISCUSSION

In this chapter, the contributions of the research are discussed. Also, the limitations and further research ideas are presented.

### 4.1 Contributions

The research provides insights into the localization of EZ in patients with focal epilepsy by investigation and evaluation of the brain connectivity techniques applied on EEG and ECoG data. The specific research contributions are described more detail as follows:

(1) Evaluation of the synchronization characteristics between two brain regions using different brain connectivity measures on EEG data during anesthesia contributes to the understanding of performance of different measures on distinguishing different anesthetic states and on tracking anesthetic drug concentration. Bad performance of COR in correlating with BIS and  $C_{eff}$ , as well as in distinguishing the anesthetic states suggested that it is not suitable for distinguishing brains under different physiological conditions. To calculate the correlation of a certain frequency band, the coherence based on wavelet transform can be used as the first choice rather than based on the Fourier transform. Among the PS measures, the most common PLV was superior to other measures in distinguishing different anesthesia states, indicating that it can still be used as a preferred method for analyzing PS. The best performance of PCMI in both distinguishing anesthetic states and tracking drug concentrate indicated the importance of permutation-based MI in the information theory for describing dynamic synchronization. In addition, the good performance of NI and DET in detecting DOA could also be good tools to investigate the synchronization characteristics in brain network.

(2) Investigation of PAC temporal-spatial characteristics of ECoG data in patients with TLE indicates a reliable biomarker of epileptogenic area, i.e.,

the 'fall-max' pattern between low-frequency phase and high-frequency amplitude that appeared in the middle period of the seizure, which contributes a promising tool for lateralization and localization the EZ in the presurgical evaluation, and provides insight into the underlying neural dynamics between LFOs and HFOs in the epileptic brain. The patient-specific PAC features during the entire period from pre-seizure to post-seizure and the spatial specificity of phase-amplitude modulation were found to be the important neurophysiological characteristic in patients with TLE, which provides meaningful reference for accurate resection of the epileptogenic foci in the clinical surgery.

(3) Study of effective brain network and topological properties of ECoG in patients with TLE proves that the high temporal resolution EC measure ffADTF combined with different graph metrics is able to provide a more precise localization of the SOZ and EZ, which contributes to clinical preoperative assessments and reducing both number of postoperative seizures and the probability of secondary surgeries. The ability to detect and describe dynamic changes of EC at each sample point of the data in specific frequency bands illustrates that the ffADTF is an EC measure that can more accurately describe the intensity and direction of brain information transmission on a time scale. It can not only provide more detailed dynamic brain network connectivity feature during epileptic seizures, but also can be applied to other brain network connectivity research and analysis with high time resolution requirements. The newly discovery biomarker, i.e., approximately 20-50 ms seizure onset EC network emerged at seizure onset time with strong connections generated from both the SOZ and EZ could be an important and promising tool for the localization of SOZ and EZ in the preoperative evaluation. In addition, different graph metrics evaluate the topology characteristics from their own perspectives in the epileptic network, which implies that OD and C are more likely to localize the SOZ and EZ in which areas have a higher correlation with the amount of information output and the degree of clustering with the surrounding cortex when the seizures occur.

(4) Describing the drug treatment process and the effectiveness of each antiepileptic drug provides a valuable reference for clinical drug therapy in patients with the cold-induced reflex epilepsy in the future. Also, source localization and FC analysis of the EEG data reveal the characteristics of the brain functional network of the rare cold-induced epilepsy. The source localization on the cortex level makes it possible to present the abnormal slow waves that are involved in the generation and propagation of the epileptic activities. The volume conduction robust FC measure PLI that are applied on the EEG data indicates a reliable brain connectivity characteristics on the scalp level. In addition, local and global topology characteristics evaluated by LE and GE within a range of densities provides insights on the underlying mechanism of epileptic activities in the functional network.

## 4.2 Limitations and further research

There are some limitations of this research to consider. Not many subjects or patients were recruited in the research, especially the patient involved in the EEG source localization studies is rare. Collection of more EEG or ECoG data including the whole period of anesthesia or spontaneous seizures from more subjects or patients with epilepsy could provide more sufficient and worthy information for the research of brain network connectivity.

Regarding the Article I and II, EEG data from only two brain areas were collected which results in the calculation the brain connectivity between only two channels. The whole-brain EEG acquisition can obtain more comprehensive anesthesia brain connectivity characteristics.

In the research of Article III and IV, the number of seizures involved is not very large and the number of patients in each Engel Class was different. Large-scale data sets from epilepsy patients of Engel Class I are more convincing for giving significant statistical results of the accuracy and consistency of localization of EZ using brain connectivity analysis with clinical identification by epileptologists. In addition, depth electrodes and cortical electrode strips cannot completely ensure coverage of the entire SOZ and EZ. If some EZ located outside the regions are covered by the electrode strips, some locations of EZ would be omitted in both clinical visual analysis and EC analysis. In addition, invasive electrode strips or grids cannot be implanted in healthy individuals, so it is not possible to compare the differences in EC networks between epileptic patients and healthy subjects on cortical level. Furthermore, the data lengths of the ECoG data segments we selected are limited, which only included the data period from pre-seizure to post-seizure for all the patients with TLE. Data of interictal periods, which have longer time interval than that of the seizure period may contain some useful neurophysiological information about the localization of SOZ and EZ. Although the localization of EZ using PAC, ffADTF, and graph metrics might lead to small resection regions, these techniques still need to be further verified in clinical preoperative evaluation and postoperative follow-up results in a large group of epileptic patients before they are applied in clinical practice.

As for Article V, the rare patient with cold-induced reflex epilepsy underwent the seizure induction tests during only one EEG acquisition. Only two seizures with abnormal EEG were obtained. The EEG data were collected before the drug treatment. If we could do EEG collection and induction test after each antiepileptic drug change, the effect of each drug on the functional brain network could be analyzed and compared, which could enhance the understanding of the effects on the neural activity and action mechanism of each antiepileptic drug.

In future work, comparison of different genders, different age group could be considered. High-density EEG recordings could be implemented, which could provide more information on the connectivity features of the whole brain and obtain contrastive connectivity networks from a healthy control group. Other

neuroimaging modalities such as MEG, fMRI, etc. can also be applied and combined for providing information regarding the characteristics of the brain network connectivity. Other recently concerned techniques, such as machine learning, could also be used to investigate the brain connectivity for localization the epileptic focus in epilepsy.

## 5 SUMMARY

In this research, we first considered and compared the brain connectivity measures based on the synchronization to explore the synchronization changes of EEG data between two brain regions during the whole period of general anesthesia and evaluate the performance in tracking the DOA and the ability to distinguish different anesthetic states of the synchronization measures. Each measure presented their own properties on evaluating the synchronization characteristics and different performance in tracking the DOA and drug concentration. Although the experimental data were limited which means that more investigation could be conducted on synchronization characteristics using these brain connectivity measures, we still describe the EEG synchronization dynamics during propofol-induced general anesthesia.

Then, we investigated the temporal and spatial PAC different between LFOs and HFOs of ECoG data collected from patients with TLE and described the characteristics of different low and high neural oscillations during different periods of epileptic seizures on the cortex. The PAC during the entire period from pre-seizure to post-seizure exhibits different features in patients with TLE. The modulation between low-frequency phase and high-frequency amplitude has spatial specificity in different cortical areas. The spatial specificity of phase-amplitude modulation and the newfound 'fall-max' phase-amplitude pattern in the middle period of seizure are the important neurophysiological characteristic and biomarker, respectively, which may be a good tool for the lateralization and localization of the epileptic foci and provide insight into the underlying neural dynamics of the epileptic seizures.

Furthermore, we also investigated the time-varying characteristics of EC in the epileptic brain networks in the same patients with TLE, using the measure of the ffADTF combined with five graph metrics. The EC was evaluated and compared across five frequency bands and five representative seizure periods. The locations of the strong epileptic sources found by using these measures were compared with the SOZ and EZ identified by epileptologists, as well as with the results of epilepsy surgery. Generation and propagation of strong epileptic activities can be observed from the ffADTF effective connectivity networks, and the

location of the SOZ and EZ can be found using the high values of graph metrics in the newfound transient seizure onset effective connectivity network. Different graph metrics reflect the different characteristics of epileptic information communication among the cortical areas. The study proved that the high temporal resolution effective connectivity measure ffADTF combined with different graph metrics is able to provide more precise localization of the SOZ and EZ.

At last, we described the seizure focus and propagation on the cortical level using source modeling, investigated the characteristics of functional connectivity using PLI, and assessed the topological property of the functional network using two graph metrics LE and GE, at three seizure stages of one special reflex epileptic patient induced by the cold sensation. Abnormal slow  $\delta$  and  $\theta$  waves were found to appear mainly in the right occipital lobe and right temporal lobe during the ictal seizure period. The appearance of these two abnormal slow waves make the functional connectivity in the brain areas stronger and allow more information to transmit in the local brain areas rather than in the whole brain in the mid-late and late ictal seizure stages. The study provides a valuable reference for clinical drug therapy in patients with the cold-induced reflex epilepsy and has an important understanding of the brain network characteristics of cold-induced reflex epilepsy.

Overall, we used a variety of brain connectivity techniques to further understand the characteristics of dynamic brain networks in anesthesia and epilepsy brains and to explore reliable brain-connectivity based approaches for EZ localization by analyzing the functional brain connectivity of normal and epilepsy patients, which provides an important reference value for the precise localization and resection of epileptogenic foci in clinically drug-resistant epilepsy.

## YHTEENVETO (SUMMARY IN FINNISH)

Tässä tutkimuksessa keskitytään aluksi synkronointiin pohjautuvaan aivojen konnektiviteetin mittaamiseen, jotta voidaan tutkia EEG datasta mitattuja synkronian muutoksia kahden eri aivoalueen välillä anestesian ajalta sekä evaluoida paikannuksen seurannan tarkkuutta ja kykyä erottaa erilaisia synkronointimitausten anesteettisia tiloja. Jokainen erityyppinen mittaus antoi omanlaisia ominaisuuksia synkronian piirteiden evaluoinnille, erilaisia suorituskykyjä paikannuksen seurannalle ja lääkkeen konsentraatiolle. Vaikka koehenkilöiden määrä oli rajallinen, työssä esitetään silti EEG synkronian dynamiikka yleisen propofoli anestesian aikana.

Työssä tutkittiin sen jälkeen temporaalieleptisten potilaiden elektokortikografisesta (ECoG) matalan ja korkean taajuuden datasta spatiaalinen ja ajallinen vaihe-amplitudikytkös. Löydettyä nk. 'fall-max' vaihe-amplitudikytköstä, joka ilmeni kohtauksen keskivaiheilla, ehdotetaan luotettavaksi biomarkeriksi aivojen epileptogeenisellä aluella, mikä havainto lisää ymmärrystä epileptisten potilaiden aivojen matalan ja korkea taajuuden neuraalisten kvititeettien väliseen dynamiikkaan.

Lisäksi tutkittiin näiden potilaiden datasta aivoverkoston efektiivinen konnektiviteetti ja topologia soveltamalla korkeamman aikaresoluution konnektiviteettimittareita yhdistettynä elektokortikografisesta datasta saatuihin graafisiin metriikoihin, jotka kuvaavat yksityiskohtaisesti informaation siirtymisen voimakkuuden ja suunnan. Efektiivinen konnektiviteetti evaluoitiin ja vertailtiin viiden taajuuskaistan ja kohtausjakson yli. Voimakkaiden epileptisten kohtauksen paikannustulosta verrattiin epileptologin identifioimiin alueisiin ja leikkaustuloksiin. Tutkimus osoitti, että kehitetty korkean aikaresoluution efektiivisen konnektivisuuden mittari ffADTF, kombinoituna eri graafisten metriikoiden kanssa, antoi tarkemman paikannustuloksen kohtauksen alkukohdalle ja epileptogeeniselle aluella.

Lopuksi kuvailtiin kohtauksen fokus ja sen eteneminen aivokuoressa käyttäen lähdemallinnusta, tutkittiin toiminnallisen konnektiviteetin ominaisuuksia vaiheviiveindeksin avulla ja arvioitiin toiminnallisen verkoston topologisia ominaisuuksia käyttäen kahta graafista metriikkaa. Viimeisin arvio kohdistui kolmeen kohtausjaksoon potilaalla, jolla oli kylmän aiheuttama refleksi epilepsia. Tällöin havaittiin poikkeavia delta- ja thetarytmejä oikeassa takaraivolohkossa ja oikeassa ohimolohkossa iktaalisen kohtausjakson aikana. Näiden kahden poikkeavan rytmin ilmeneminen sai aikaan voimakkaamman toiminnallisen konnektiviteetin, joka puolestaan mahdollisti suuremman informaatiosiirron aivoissa enempi paikallisesti kuin globaalisti iktaalisen kohtauksen puolivälissä ja loppuosassa. Tämä tutkimus lisää ymmärrystä epileptisen aktiviteetin syntyyn ja etenemiseen sekä aivokuoritason verkoston paikalliseen ja globaaliin topologiapiirteisiin.

Kaiken kaikkiaan, tässä väitöskirjassa tutkittiin erilaisten aivoverkoston konnektiviteettien mittaustapojen suosituskykyä analysoimalla terveiden ja epi-

leptisten potilaiden aivojen toiminnallista ja efektiivistä konnektiviteettia, kehittäen samalla tarkempia menetelmiä epileptogeenisen fokuksen paikallistamiseen. Tutkimus lisää ymmärrystä epileptisen aivoverkon konnektiviteetin mekanismeihin ja tärkeän referenssin pre-operatiiviseen evaluointiin kliinisessä epilepsialeikkauksessa, antaen parannetun paikannustarkkuuden epileptogeeniselle fokukselle ja näin ollen pienentäen epilepsiakohtausten todennäköisyyttä.

## REFERENCES

- Alvarado-Rojas, C., Valderrama, M., Fouad-Ahmed, A., Feldwisch-Drentrup, H., Ihle, M., Teixeira, C. A., Sales, F., Schulze-Bonhage, A., Adam, C., Dourado, A., Charpier, S., Navarro, V., & Le Van Quyen, M. (2014). Slow modulations of high-frequency activity (40-140-Hz) discriminate preictal changes in human focal epilepsy. *Sci Rep*, 4, 4545.
- Amiri, M., Frauscher, B., & Gotman, J. J. F. i. h. n. (2016). Phase-amplitude coupling is elevated in deep sleep and in the onset zone of focal epileptic seizures. 10, 387.
- Andrzejak, R. G., Schindler, K., & Rummel, C. (2012). Nonrandomness, nonlinear dependence, and nonstationarity of electroencephalographic recordings from epilepsy patients. *Phys Rev E Stat Nonlin Soft Matter Phys*, 86(4 Pt 2), 046206.
- Astolfi, L., Cincotti, F., Mattia, D., Fallani, F. D. V., Tocci, A., Colosimo, A., Salinari, S., Marciani, M. G., Hesse, W., & Witte, H. J. I. T. o. B. E. (2008). Tracking the time-varying cortical connectivity patterns by adaptive multivariate estimators. 55(3), 902-913.
- Baccalá, L. A., & Sameshima, K. J. B. c. (2001). Partial directed coherence: a new concept in neural structure determination. 84(6), 463-474.
- Bassett, D. S., & Sporns, O. (2017). Network neuroscience. *Nat Neurosci*, 20(3), 353-364.
- Becker, K., Schneider, G., Eder, M., Ranft, A., Kochs, E. F., Zieglgansberger, W., & Dodt, H. U. (2010). Anaesthesia monitoring by recurrence quantification analysis of EEG data. *PLoS One*, 5(1), e8876.
- Bradshaw, L. A., & Wikswo, J. P., Jr. (2001). Spatial filter approach for evaluation of the surface Laplacian of the electroencephalogram and magnetoencephalogram. *Ann Biomed Eng*, 29(3), 202-213.
- Breakspear, M., & Terry, J. R. (2002a). Detection and description of non-linear interdependence in normal multichannel human EEG data. *Clin Neurophysiol*, 113(5), 735-753.
- Breakspear, M., & Terry, J. R. (2002b). Topographic organization of nonlinear interdependence in multichannel human EEG. *Neuroimage*, 16(3 Pt 1), 822-835.
- Brunner, P., Ritaccio, A. L., Lynch, T. M., Emrich, J. F., Wilson, J. A., Williams, J. C., Aarnoutse, E. J., Ramsey, N. F., Leuthardt, E. C., Bischof, H. J. E., & Behavior. (2009). A practical procedure for real-time functional mapping of eloquent cortex using electrocorticographic signals in humans. 15(3), 278-286.
- Bullmore, E., & Sporns, O. (2009). Complex brain networks: graph theoretical analysis of structural and functional systems. *Nat Rev Neurosci*, 10(3), 186-198.
- Bullmore, E. T., & Bassett, D. S. (2011). Brain graphs: graphical models of the human brain connectome. *Annu Rev Clin Psychol*, 7, 113-140.

- Canuet, L., Ishii, R., Pascual-Marqui, R. D., Iwase, M., Kurimoto, R., Aoki, Y., Ikeda, S., Takahashi, H., Nakahachi, T., & Takeda, M. (2011). Resting-state EEG source localization and functional connectivity in schizophrenia-like psychosis of epilepsy. *PLoS One*, 6(11), e27863.
- Cascino, G. D. J. E. (2002). Video - EEG monitoring in adults. 43, 80-93.
- Chiang, S., & Haneef, Z. (2014). Graph theory findings in the pathophysiology of temporal lobe epilepsy. *Clin Neurophysiol*, 125(7), 1295-1305.
- Cimenser, A., Purdon, P. L., Pierce, E. T., Walsh, J. L., Salazar-Gomez, A. F., Harrell, P. G., Tavares-Stoeckel, C., Habeeb, K., & Brown, E. N. (2011). Tracking brain states under general anesthesia by using global coherence analysis. *Proc Natl Acad Sci U S A*, 108(21), 8832-8837.
- Coito, A., Michel, C. M., van Mierlo, P., Vulliemoz, S., & Plomp, G. (2016). Directed Functional Brain Connectivity Based on EEG Source Imaging: Methodology and Application to Temporal Lobe Epilepsy. *IEEE Trans Biomed Eng*, 63(12), 2619-2628.
- Cover, T. M., & Thomas, J. A. (2012). *Elements of information theory*: John Wiley & Sons.
- Dalic, L., & Cook, M. J. (2016). Managing drug-resistant epilepsy: challenges and solutions. *Neuropsychiatr Dis Treat*, 12, 2605-2616.
- Dauwels, J., Vialatte, F., & Cichocki, A. (2008). A comparative study of synchrony measures for the early detection of Alzheimer's disease based on EEG. Paper presented at the Neural Information Processing.
- De Vico Fallani, F., Richiardi, J., Chavez, M., & Achard, S. (2014). Graph analysis of functional brain networks: practical issues in translational neuroscience. *Philos Trans R Soc Lond B Biol Sci*, 369(1653).
- Edakawa, K., Yanagisawa, T., Kishima, H., Fukuma, R., Oshino, S., Khoo, H. M., Kobayashi, M., Tanaka, M., & Yoshimine, T. J. S. r. (2016). Detection of epileptic seizures using phase-amplitude coupling in intracranial electroencephalography. 6, 25422.
- Engel, J., Jr., Thompson, P. M., Stern, J. M., Staba, R. J., Bragin, A., & Mody, I. (2013). Connectomics and epilepsy. *Curr Opin Neurol*, 26(2), 186-194.
- Englot, D. J., D'Haese, P. F., Konrad, P. E., Jacobs, M. L., Gore, J. C., Abou-Khalil, B. W., & Morgan, V. L. (2017). Functional connectivity disturbances of the ascending reticular activating system in temporal lobe epilepsy. *J Neurol Neurosurg Psychiatry*, 88(11), 925-932.
- Fisher, R. S., Boas, W. V. E., Blume, W., Elger, C., Genton, P., Lee, P., & Engel Jr, J. J. E. (2005). Epileptic seizures and epilepsy: definitions proposed by the International League Against Epilepsy (ILAE) and the International Bureau for Epilepsy (IBE). 46(4), 470-472.
- Fisher, R. S., Cross, J. H., French, J. A., Higurashi, N., Hirsch, E., Jansen, F. E., Lagae, L., Moshe, S. L., Peltola, J., Roulet Perez, E., Scheffer, I. E., & Zuberi, S. M. (2017). Operational classification of seizure types by the International League Against Epilepsy: Position Paper of the ILAE Commission for Classification and Terminology. *Epilepsia*, 58(4), 522-530.

- Foldvary, N., Klem, G., Hammel, J., Bingaman, W., Najm, I., & Lüders, H. J. N. (2001). The localizing value of ictal EEG in focal epilepsy. *Epilepsia*, 57(11), 2022-2028.
- Guirgis, M., Chinvarun, Y., Del Campo, M., Carlen, P. L., & Bardakjian, B. L. (2015). Defining regions of interest using cross-frequency coupling in extratemporal lobe epilepsy patients. *J Neural Eng*, 12(2), 026011.
- Harroud, A., Bouthillier, A., Weil, A. G., Nguyen, D. K. J. E. r., & treatment. (2012). Temporal lobe epilepsy surgery failures: a review. 2012.
- Hayashi, K., Mukai, N., & Sawa, T. (2014). Simultaneous bicoherence analysis of occipital and frontal electroencephalograms in awake and anesthetized subjects. *Clin Neurophysiol*, 125(1), 194-201.
- Honey, C., Sporns, O., Cammoun, L., Gigandet, X., Thiran, J.-P., Meuli, R., & Hagmann, P. J. P. o. t. N. A. o. S. (2009). Predicting human resting-state functional connectivity from structural connectivity. *PLoS Comput Biol*, 106(6), 2035-2040.
- Huang, L., Yu, P., Ju, F., Cheng, J. J. M. e., & physics. (2003). Prediction of response to incision using the mutual information of electroencephalograms during anaesthesia. *Neurosci Lett*, 25(4), 321-327.
- Ibrahim, G. M., Wong, S. M., Anderson, R. A., Singh-Cadieux, G., Akiyama, T., Ochi, A., Otsubo, H., Okanishi, T., Valiante, T. A., Donner, E., Rutka, J. T., Snead, O. C., 3rd, & Doesburg, S. M. (2014). Dynamic modulation of epileptic high frequency oscillations by the phase of slower cortical rhythms. *Exp Neurol*, 251, 30-38.
- Imas, O. A., Ropella, K. M., Wood, J. D., & Hudetz, A. G. (2006). Isoflurane disrupts antero-posterior phase synchronization of flash-induced field potentials in the rat. *Neurosci Lett*, 402(3), 216-221.
- Jensen, O., & Colgin, L. L. J. T. i. c. s. (2007). Cross-frequency coupling between neuronal oscillations. *Neurosci Lett*, 11(7), 267-269.
- Jette, N., Reid, A. Y., & Wiebe, S. (2014). Surgical management of epilepsy. *CMAJ*, 186(13), 997-1004.
- Jordan, D., Stockmanns, G., Kochs, E. F., Pilge, S., & Schneider, G. (2008). Electroencephalographic order pattern analysis for the separation of consciousness and unconsciousness: an analysis of approximate entropy, permutation entropy, recurrence rate, and phase coupling of order recurrence plots. *Anesthesiology*, 109(6), 1014-1022.
- Julitta, B., Vallverdu, M., Melia, U. S., Tupaika, N., Jospin, M., Jensen, E. W., Struys, M. M., Vereecke, H. E., & Caminal, P. (2011). Auto-mutual information function of the EEG as a measure of depth of anesthesia. *Conf Proc IEEE Eng Med Biol Soc*, 2011, 2574-2577.
- Jung, Y. J., Kang, H. C., Choi, K. O., Lee, J. S., Kim, D. S., Cho, J. H., Kim, S. H., Im, C. H., & Kim, H. D. (2011). Localization of ictal onset zones in Lennox-Gastaut syndrome using directional connectivity analysis of intracranial electroencephalography. *Seizure*, 20(6), 449-457.
- Kaminski, M. J., & Blinowska, K. J. (1991). A new method of the description of the information flow in the brain structures. *Biol Cybern*, 65(3), 203-210.
- Kim, J.-Y., Kang, H.-C., Kim, K., Kim, H. D., Im, C.-H. J. B., & Development. (2015). Localization of epileptogenic zones in Lennox-Gastaut syndrome (LGS)

- using graph theoretical analysis of ictal intracranial EEG: A preliminary investigation. *37(1)*, 29-36.
- Klamer, S., Rona, S., Elshahabi, A., Lerche, H., Braun, C., Honegger, J., Erb, M., & Focke, N. K. (2015). Multimodal effective connectivity analysis reveals seizure focus and propagation in musicogenic epilepsy. *Neuroimage*, *113*, 70-77.
- Koskinen, M., Seppanen, T., Tuukkanen, J., Yli-Hankala, A., & Jantti, V. (2001). Propofol anesthesia induces phase synchronization changes in EEG. *Clin Neurophysiol*, *112(2)*, 386-392.
- Kramer, M. A., Chang, F. L., Cohen, M. E., Hudson, D., & Szeri, A. J. (2007). Synchronization measures of the scalp electroencephalogram can discriminate healthy from Alzheimer's subjects. *Int J Neural Syst*, *17(2)*, 61-69.
- Kreuzer, M., Hentschke, H., Antkowiak, B., Schwarz, C., Kochs, E. F., & Schneider, G. (2010). Cross-approximate entropy of cortical local field potentials quantifies effects of anesthesia--a pilot study in rats. *BMC Neurosci*, *11*, 122.
- Ku, S. W., Lee, U., Noh, G. J., Jun, I. G., & Mashour, G. A. (2011). Preferential inhibition of frontal-to-parietal feedback connectivity is a neurophysiologic correlate of general anesthesia in surgical patients. *PLoS One*, *6(10)*, e25155.
- Kuruvilla, A., & Flink, R. J. S. (2003). Intraoperative electrocorticography in epilepsy surgery: useful or not? , *12(8)*, 577-584.
- Kwan, P., Arzimanoglou, A., Berg, A. T., Brodie, M. J., Allen Hauser, W., Mathern, G., Moshe, S. L., Perucca, E., Wiebe, S., & French, J. (2010). Definition of drug resistant epilepsy: consensus proposal by the ad hoc Task Force of the ILAE Commission on Therapeutic Strategies. *Epilepsia*, *51(6)*, 1069-1077.
- Lachaux, J.-P., Lutz, A., Rudrauf, D., Cosmelli, D., Le Van Quyen, M., Martinerie, J., & Varela, F. J. N. C. C. N. (2002). Estimating the time-course of coherence between single-trial brain signals: an introduction to wavelet coherence. *32(3)*, 157-174.
- Lachaux, J. P., Rodriguez, E., Martinerie, J., & Varela, F. J. (1999). Measuring phase synchrony in brain signals. *Hum Brain Mapp*, *8(4)*, 194-208.
- Le Van Quyen, M., Adam, C., Baulac, M., Martinerie, J., & Varela, F. J. (1998). Nonlinear interdependencies of EEG signals in human intracranially recorded temporal lobe seizures. *Brain Res*, *792(1)*, 24-40.
- Lee, U., Muller, M., Noh, G. J., Choi, B., & Mashour, G. A. (2011). Dissociable network properties of anesthetic state transitions. *Anesthesiology*, *114(4)*, 872-881.
- Li, D., Voss, L. J., Sleight, J. W., & Li, X. (2013). Effects of volatile anesthetic agents on cerebral cortical synchronization in sheep. *Anesthesiology*, *119(1)*, 81-88.
- Li, X., Sleight, J. W., Voss, L. J., & Ouyang, G. (2007). Measure of the electroencephalographic effects of sevoflurane using recurrence dynamics. *Neurosci Lett*, *424(1)*, 47-50.
- Liang, Z., Liang, S., Wang, Y., Ouyang, G., & Li, X. (2015). Tracking the coupling of two electroencephalogram series in the isoflurane and remifentanyl anesthesia. *Clin Neurophysiol*, *126(2)*, 412-422.

- Liang, Z., Wang, Y., Ouyang, G., Voss, L. J., Sleight, J. W., & Li, X. (2013). Permutation auto-mutual information of electroencephalogram in anesthesia. *J Neural Eng*, 10(2), 026004.
- Liang, Z., Wang, Y., Ren, Y., Li, D., Voss, L., Sleight, J., & Li, X. (2014). Detection of burst suppression patterns in EEG using recurrence rate. *ScientificWorldJournal*, 2014, 295070.
- Lipping, T., Ferenets, R., Puumala, P., Suominen, K., Karvonen, E., Sonkajarvi, E., Alahuhta, S., Heikkinen, E., Erola, T., & Baer, G. (2003). EEG independent component and coherence analysis from scalp and depth electrodes during propofol anesthesia. Paper presented at the Proceedings of the 25th Annual International Conference of the IEEE Engineering in Medicine and Biology Society (IEEE Cat. No. 03CH37439).
- Martinez-Vargas, J. D., Strobbe, G., Vonck, K., van Mierlo, P., & Castellanos-Dominguez, G. (2017). Improved Localization of Seizure Onset Zones Using Spatiotemporal Constraints and Time-Varying Source Connectivity. *Front Neurosci*, 11, 156.
- Mirowski, P., Madhavan, D., LeCun, Y., & Kuzniecky, R. (2009). Classification of patterns of EEG synchronization for seizure prediction. *Clin Neurophysiol*, 120(11), 1927-1940.
- Moon, Y. I., Rajagopalan, B., & Lall, U. (1995). Estimation of mutual information using kernel density estimators. *Phys Rev E Stat Phys Plasmas Fluids Relat Interdiscip Topics*, 52(3), 2318-2321.
- Mormann, F., Kreuz, T., Rieke, C., Andrzejak, R. G., Kraskov, A., David, P., Elger, C. E., & Lehnertz, K. (2005). On the predictability of epileptic seizures. *Clin Neurophysiol*, 116(3), 569-587.
- Motoi, H., Miyakoshi, M., Abel, T. J., Jeong, J. W., Nakai, Y., Sugiura, A., Luat, A. F., Agarwal, R., Sood, S., & Asano, E. J. E. (2018). Phase - amplitude coupling between interictal high - frequency activity and slow waves in epilepsy surgery. 59(10), 1954-1965.
- Nariai, H., Matsuzaki, N., Juhasz, C., Nagasawa, T., Sood, S., Chugani, H. T., & Asano, E. (2011). Ictal high-frequency oscillations at 80-200 Hz coupled with delta phase in epileptic spasms. *Epilepsia*, 52(10), e130-134.
- Noachtar, S., Binnie, C., Ebersole, J., Mauguière, F., Sakamoto, A., & Westmoreland, B. J. K. N. (2004). A glossary of terms most commonly used by clinical electroencephalographers and proposal for the report form for the EEG findings. 35(1), 5-21.
- Noachtar, S., Borggraefe, I. J. E., & Behavior. (2009). Epilepsy surgery: a critical review. 15(1), 66-72.
- Noachtar, S., & Remi, J. (2009). The role of EEG in epilepsy: a critical review. *Epilepsy Behav*, 15(1), 22-33.
- Nonoda, Y., Miyakoshi, M., Ojeda, A., Makeig, S., Juhász, C., Sood, S., & Asano, E. J. C. N. (2016). Interictal high-frequency oscillations generated by seizure onset and eloquent areas may be differentially coupled with different slow waves. 127(6), 2489-2499.

- Nunez, P. L., Srinivasan, R., Westdorp, A. F., Wijesinghe, R. S., Tucker, D. M., Silberstein, R. B., Cadusch, P. J. J. E., & neurophysiology, c. (1997). EEG coherency: I: statistics, reference electrode, volume conduction, Laplacians, cortical imaging, and interpretation at multiple scales. *103*(5), 499-515.
- Park, H.-J., & Friston, K. J. S. (2013). Structural and functional brain networks: from connections to cognition. *342*(6158), 1238411.
- Perkins, A. J. N. m. I. E. (2019). Epilepsy: An electrical storm in the brain. *17*(4), 42-50.
- Pockett, S., & Holmes, M. D. (2009). Intracranial EEG power spectra and phase synchrony during consciousness and unconsciousness. *Conscious Cogn*, *18*(4), 1049-1055.
- Rangaprakash, D., Hu, X., & Deshpande, G. (2013). Phase synchronization in brain networks derived from correlation between probabilities of recurrences in functional MRI data. *Int J Neural Syst*, *23*(2), 1350003.
- Rubinov, M., & Sporns, O. (2010). Complex network measures of brain connectivity: uses and interpretations. *Neuroimage*, *52*(3), 1059-1069.
- Rubinov, M., & Sporns, O. J. N. (2011). Weight-conserving characterization of complex functional brain networks. *56*(4), 2068-2079.
- Rutecki, P. A. J. J. o. c. n. o. p. o. t. A. E. S. (1992). Neuronal excitability: voltage-dependent currents and synaptic transmission. *9*(2), 195-211.
- Sakkalis, V. (2011). Review of advanced techniques for the estimation of brain connectivity measured with EEG/MEG. *Comput Biol Med*, *41*(12), 1110-1117.
- Schoffelen, J. M., & Gross, J. (2009). Source connectivity analysis with MEG and EEG. *Hum Brain Mapp*, *30*(6), 1857-1865.
- Schreiber, T. J. P. r. l. (2000). Measuring information transfer. *85*(2), 461.
- Schulz, R., Lüders, H., Hoppe, M., Tuxhorn, I., May, T., & Ebner, A. J. E. (2000). Interictal EEG and ictal scalp EEG propagation are highly predictive of surgical outcome in mesial temporal lobe epilepsy. *41*(5), 564-570.
- Shalhaf, R., Behnam, H., Sleight, J. W., Steyn-Ross, D. A., & Steyn-Ross, M. L. (2015). Frontal-temporal synchronization of EEG signals quantified by order patterns cross recurrence analysis during propofol anesthesia. *IEEE Trans Neural Syst Rehabil Eng*, *23*(3), 468-474.
- So, E. L. J. J. o. C. N. (2010). Interictal epileptiform discharges in persons without a history of seizures: what do they mean? , *27*(4), 229-238.
- Spencer, S., & Huh, L. J. T. L. N. (2008). Outcomes of epilepsy surgery in adults and children. *7*(6), 525-537.
- Staljanssens, W., Strobbe, G., Van Holen, R., Keereman, V., Gadeyne, S., Carrette, E., Meurs, A., Pittau, F., Momjian, S., Seeck, M., Boon, P., Vandenberghe, S., Vulliemoz, S., Vonck, K., & van Mierlo, P. (2017). EEG source connectivity to localize the seizure onset zone in patients with drug resistant epilepsy. *Neuroimage Clin*, *16*, 689-698.
- Stam, C. J., Nolte, G., & Daffertshofer, A. (2007). Phase lag index: assessment of functional connectivity from multi channel EEG and MEG with diminished bias from common sources. *Hum Brain Mapp*, *28*(11), 1178-1193.

- Stam, C. J., & Reijneveld, J. C. J. N. b. p. (2007). Graph theoretical analysis of complex networks in the brain. *1*(1), 3.
- Steinhoff, B. J., So, N. K., Lim, S., & Lüders, H. O. J. N. (1995). Ictal scalp EEG in temporal lobe epilepsy with unitemporal versus bitemporal interictal epileptiform discharges. *45*(5), 889-896.
- Storti, S. F., Galazzo, I. B., Khan, S., Manganotti, P., Menegaz, G. J. I. j. o. b., & informatics, h. (2016). Exploring the epileptic brain network using time-variant effective connectivity and graph theory. *21*(5), 1411-1421.
- Tang, F., Hartz, A. M. S., & Bauer, B. (2017). Drug-Resistant Epilepsy: Multiple Hypotheses, Few Answers. *Front Neurol*, *8*, 301.
- Teplan, M. J. M. s. r. (2002). Fundamentals of EEG measurement. *2*(2), 1-11.
- Terry, J. R., Anderson, C., & Horne, J. A. (2004). Nonlinear analysis of EEG during NREM sleep reveals changes in functional connectivity due to natural aging. *Hum Brain Mapp*, *23*(2), 73-84.
- Tort, A. B., Komorowski, R., Eichenbaum, H., & Kopell, N. (2010). Measuring phase-amplitude coupling between neuronal oscillations of different frequencies. *J Neurophysiol*, *104*(2), 1195-1210.
- van den Broek, S. P., Reinders, F., Donderwinkel, M., Peters, M. J. E., & neurophysiology, c. (1998). Volume conduction effects in EEG and MEG. *106*(6), 522-534.
- van Mierlo, P., Carrette, E., Hallez, H., Raedt, R., Meurs, A., Vandenberghe, S., Van Roost, D., Boon, P., Staelens, S., & Vonck, K. (2013). Ictal-onset localization through connectivity analysis of intracranial EEG signals in patients with refractory epilepsy. *Epilepsia*, *54*(8), 1409-1418.
- van Mierlo, P., Carrette, E., Hallez, H., Vonck, K., Van Roost, D., Boon, P., & Staelens, S. (2011). Accurate epileptogenic focus localization through time-variant functional connectivity analysis of intracranial electroencephalographic signals. *Neuroimage*, *56*(3), 1122-1133.
- Van Mierlo, P., Coito, A., Vulliémoz, S., & Lie, O. (2016). Seizure onset zone localization from many invasive EEG channels using directed functional connectivity. Paper presented at the 2016 24th European Signal Processing Conference (EUSIPCO).
- Vlachos, I., Krishnan, B., Sirven, J., Noe, K., Drazkowski, J., & Iasemidis, L. (2013). Frequency-based connectivity analysis of interictal iEEG to localize the epileptogenic focus. Paper presented at the 2013 29th Southern Biomedical Engineering Conference.
- Vlachos, I., Krishnan, B., Treiman, D. M., Tsakalis, K., Kugiumtzis, D., & Iasemidis, L. D. (2017). The Concept of Effective Inflow: Application to Interictal Localization of the Epileptogenic Focus From iEEG. *IEEE Trans Biomed Eng*, *64*(9), 2241-2252.
- Wallois, F., Patil, A., Heberle, C., & Grebe, R. (2010). EEG-NIRS in epilepsy in children and neonates. *Neurophysiol Clin*, *40*(5-6), 281-292.
- Weiss, S. A., Orosz, I., Salamon, N., Moy, S., Wei, L., Van't Klooster, M. A., Knight, R. T., Harper, R. M., Bragin, A., Fried, I., Engel, J., Jr., & Staba, R. J. (2016).

- Ripples on spikes show increased phase-amplitude coupling in mesial temporal lobe epilepsy seizure-onset zones. *Epilepsia*, 57(11), 1916-1930.
- WHO. (2019). Epilepsy fact sheet. Retrieved from <https://www.who.int/news-room/fact-sheets/detail/epilepsy>
- Wilke, C., Ding, L., & He, B. (2007). An adaptive directed transfer function approach for detecting dynamic causal interactions. *Conf Proc IEEE Eng Med Biol Soc*, 2007, 4949-4952.
- Wilke, C., van Drongelen, W., Kohrman, M., & He, B. (2010). Neocortical seizure foci localization by means of a directed transfer function method. *Epilepsia*, 51(4), 564-572.
- Wilke, C., Worrell, G., & He, B. (2011). Graph analysis of epileptogenic networks in human partial epilepsy. *Epilepsia*, 52(1), 84-93.
- Wilke, C., Worrell, G. A., & He, B. (2009). Analysis of epileptogenic network properties during ictal activity. *Conf Proc IEEE Eng Med Biol Soc*, 2009, 2220-2223.
- Williams, M. L., & Sleight, J. W. (1999). Auditory recall and response to command during recovery from propofol anaesthesia. *Anaesth Intensive Care*, 27(3), 265-268.
- Zhang, L., Liang, Y., Li, F., Sun, H., Peng, W., Du, P., Si, Y., Song, L., Yu, L., & Xu, P. (2017). Time-Varying Networks of Inter-Ictal Discharging Reveal Epileptogenic Zone. *Front Comput Neurosci*, 11, 77.
- Zumsteg, D., & Wieser, H. G. J. E. (2000). Presurgical evaluation: current role of invasive EEG. 41, S55-S60.



## ORIGINAL PAPERS

### I

# A COMPARISON OF DIFFERENT SYNCHRONIZATION MEASURES IN ELECTROENCEPHALOGRAM DURING PROPOFOL ANESTHESIA

by

Zhenhu Liang, Ye Ren, Jiaqing Yan, Duan Li, Logan J. Voss, Jamie W. Sleight &  
Xiaoli Li 2016

Journal of clinical monitoring and computing, 30(4), 451-466

DOI: <https://doi.org/10.1007/s10877-015-9738-z>

Reproduced with kind permission by Springer Nature.

# **A comparison of different synchronization measures in electroencephalogram during propofol anesthesia**

**Authors:** Zhenhu Liang<sup>1,2#</sup>, Ye Ren<sup>1#</sup>, Jiaqing Yan<sup>1</sup>, Duan Li<sup>3</sup>, Logan J. Voss<sup>4</sup>, Jamie W. Sleight<sup>4</sup>, Xiaoli Li<sup>1,2\*</sup>

## **Affiliations:**

<sup>1</sup> Institute of Electric Engineering, Yanshan University, Qinhuangdao 066004, China

<sup>2</sup> Key Laboratory of Industrial Computer Control Engineering of Hebei Province, Yanshan University, Qinhuangdao 066004, China

<sup>3</sup> Institute of Information Science and Engineering, Yanshan University, Qinhuangdao 066004, China

<sup>4</sup> Department of Anaesthesia, Waikato Hospital, Hamilton, New Zealand

# These authors equally contributed to this work.

## **\* Correspondence to:**

Prof. Xiaoli Li

Email: xlli@ysu.edu.cn

## Abstract

**Background:** Electroencephalogram (EEG) synchronization is becoming an essential tool to describe neurophysiological mechanisms of communication between brain regions under general anesthesia. Different synchronization measures have their own properties to reflect the changes of EEG activities during different anesthetic states. However, the performance characteristics and the relations of different synchronization measures in evaluating synchronization changes during propofol-induced anesthesia are not fully elucidated.

**Methods:** Two-channel EEG data from seven volunteers who had undergone a brief standardized propofol anesthesia were then adopted to calculate eight synchronization indexes. We computed the prediction probability ( $P_K$ ) of synchronization indexes with Bispectral Index (BIS) and propofol effect-site concentration ( $C_{eff}$ ) to quantify the ability of the indexes to predict BIS and  $C_{eff}$ . Also, box plots and coefficient of variation (CV) were used to reflect the different synchronization changes and their robustness to noise in awake, unconscious and recovery states, and the Pearson correlation coefficient ( $R$ ) was used for assessing the relationship among synchronization measures, BIS and  $C_{eff}$ .

**Results:** Permutation cross mutual information (PCMI) and determinism (DET) could predict BIS and follow  $C_{eff}$  better than nonlinear interdependence (NI), mutual information based on kernel estimation (KerMI) and cross correlation (COR). Wavelet transform coherence (WTC) in  $\alpha$  and  $\beta$  frequency bands followed BIS and  $C_{eff}$  better than that in other frequency bands. There was a significant decrease in unconscious state and a significant increase in recovery state for PCMI and NI, while the trends were opposite for KerMI, DET and WTC. Phase synchronization based on phase locking value (PS<sub>PLV</sub>) in  $\delta$ ,  $\theta$ ,  $\alpha$  and  $\gamma_1$  frequency bands dropped significantly in unconscious state, whereas it had no significant synchronization in recovery state. Moreover, PCMI, NI, DET correlated closely with each other and they had a better robustness to noise and higher correlation with BIS and  $C_{eff}$  than other synchronization indexes.

**Conclusions:** Propofol caused EEG synchronization changes during the anesthetic period. Different synchronization measures had individual properties in evaluating synchronization changes in differ-

ent anesthetic states, which might be related to various forms of neural activities and neurophysiological mechanisms under general anesthesia.

**Keywords:** electroencephalogram; loss of consciousness; neurophysiological mechanisms; propofol anesthesia; synchronization measures

## 1. Introduction

Understanding the neurophysiological mechanisms of anesthetic drug effect is an important issue for neuroscientists, anesthesiologists, as well as drug researchers [1]. Cognitive binding is thought to be a fundamental mechanism in human consciousness, and a number of recent studies suggest that loss of consciousness (LoC) during general anesthesia is associated with breakdown of long-distance cortical connectivity across multiple brain regions [2-5], especially in the frontal-parietal cortices [5]. Numerous measures, derived from different signal processing methods and statistics, have been proposed for quantifying neuro-synchronization [6-9] and some of the synchronization measures were used to interpret the mechanism of neural synchronization for general anesthesia. However, the performances of these synchronization measures for evaluating brain information integration or connectivity are not fully understood.

Cross correlation is based on the relationship of the magnitude of the electroencephalogram (EEG) signal between two regions, which is defined in the time domain. Lagged cross correlation was used to evaluate the interregional relationships of the blood-oxygen-level dependent signals of depressed people and natural sleep [10, 11]. However, few studies adopted the lagged cross correlation in the monitoring of anesthetic states. Coherence is a time-frequency domain method and it can evaluate the relationship of time series from different brain regions at different frequency bands. Many studies used some methods based on coherence in the coupling analysis during anesthesia. Li et al. combined the magnitude square coherence with S-estimator to analyze the synchronization during sevoflurane anesthesia in sheep and they found that the synchronization increased from the waking to the burst-suppression states and decreased during recovery in the  $\alpha$  and  $\beta$  frequency bands [12]. Hayashi et al. analyzed the bicoherence of frontal and occipital EEGs before and after induction of sevoflurane anesthesia and they found that there were delta and alpha power shift between frontal and occipital EEG with increasing sevoflurane concentration [13].

Phase synchronization analysis is a classical neuronal oscillation analysis method that is independent of the amplitude of the signal. It was sensitive to nonlinear coupling and it was a promising tool for quantifying coupling in multi-channel electroencephalogram or magnetoencephalogram (MEG) re-

cordings [14-16]. Koskinen et al. used the Hilbert transform based phase synchronization indices to investigate the phase coupling during propofol anesthetic induction and recovery periods and they found that the sub-delta band decreased during the induction and increased during the recovery, while the directions were reversed in the alpha band [17]. Nicolaou et al. analyzed how anesthesia affected widespread patterns of phase synchrony and they found anesthesia caused different phase synchronization changes in different frequency bands [18].

Mutual information is an information theory method and it has been widely applied in EEG analysis as a way of estimating information integration between different EEG channels or brain regions for mechanism analysis and neurological disease diagnosis, such as epilepsy seizure, Alzheimer's disease and autism [19-21]. We applied kernel density estimation and permutation entropy to quantify the mutual information. Kernel density estimation which was suggested by Moon et al. [22] was found to be superior to the histogram-based mutual information. However, there is no research using kernel density-based mutual information to evaluate the depth of anesthesia (DoA). On the contrary, permutation mutual information has been proved to be a promising method to tracking EEG dynamics during sevoflurane, isoflurane and remifentanil anesthesia [23, 24].

Nonlinear interdependence is a measure of generalized synchronization in nonlinear systems, which evaluates the interdependency according to the distance of delay vectors of two time series. It was most applied for evaluating the EEG functional connectivity, seizure prediction of epilepsy patients in different brain regions [25, 26]. However, few studies used the NI to characterize the EEG interdependence during anesthesia.

DET in the recurrence quantification analysis is based on the reconstruction of the phase space of the signals. High value of DET means strong synchronization of two time series, and vice versa. Recurrence quantification analysis has been applied to the monitoring of the depth of anesthesia and this technique had been proved that it could separate consciousness from unconsciousness during sevoflurane and propofol anesthesia [27]. Shalhaf et al. proposed the order patterns cross recurrence analysis to assess synchronization changes during propofol anesthesia [28].

Different measures for measuring synchronization rely on certain characteristic features of the dynamical system under investigation. However, the underlying dynamic properties of the synchronization measures applied to the EEG data in different anesthetic states are not completely known. We concentrated on the synchronization changes of two-channel EEG from prefrontal and primary motor cortices during propofol-induced anesthesia. We studied and compared a range of different synchronization measures: cross correlation (COR); magnitude squared coherence based on Fourier transform (FTC) and coherence based on wavelet transform (WTC); phase synchronization (PS) based on phase locking value, Shannon entropy and conditional probability; mutual information (MI) based on kernel density estimation and permutation; nonlinear interdependence (NI) and determinism (DET) in the recurrence quantification analysis (RQA). Using different synchronization measures, we aim to describe their individual properties during the whole period of anesthesia, evaluate performance of distinguishing awake, unconscious and recovery states, find the effective measures for evaluating of clinical anesthetic depth, and help us to understand the underlying neurophysiological mechanisms of anesthesia.

This paper is organized as follows. Section 2 describes each synchronization measure and Section 3 gives the statistical analysis methods. In Section 4, the details of EEG recording, preprocessing and the results of the application of the synchronization measures to the real EEG are presented. Finally, the discussion and conclusion are given in Section 5. The parameter selection of some synchronization measures were discussed in Appendix.

## 2. Synchronization measures

### 2.1 Cross correlation

The cross correlation is one of the most well-known measures for evaluating the linear coupling relationship between two time series. Given two time series  $x(t)$  and  $y(t)$  ( $t=1,2,\dots,N$ ), the cross-correlation function [10, 29] is defined as

$$COR(\tau) = \frac{\text{cov}(x(t+\tau), y(t))}{\sqrt{\text{var}(x(t+\tau)) \text{var}(y(t))}} \quad (1)$$

where  $COR(\tau) = COR(-\tau)$  and it is restricted to the  $[-1,1]$  interval.  $\tau$  is the time lag between two time series. When  $COR$  is positive, it implies that the two time series have strong synchronization relationship. By contrast, the negative  $COR$  represents that the synchronization of two time series is weak.  $\tau=0$  corresponds to zero-order correlation and  $COR(0)$  is used as the synchronization index in our study.

### 2.2 Coherence

Coherence is a frequency domain based method which measures the linear correlations of two time series [30]. In this study, we considered two coherence calculation methods: magnitude squared coherence based on Fourier transform and coherence based on wavelet transform.

Given two time series  $x(t)$  and  $y(t)$  ( $t=1,2,\dots,N$ ), the magnitude squared coherence is defined as a function of the power spectral densities  $P_{xx}(f)$  and  $P_{yy}(f)$ , and the cross power spectral density  $P_{xy}(f)$

$$C_{xy}(f) = \frac{|P_{xy}(f)|^2}{P_{xx}(f)P_{yy}(f)} \quad (2)$$

$C_{xy}(f)$  is a function of frequency with values between 0 and 1, and  $P_{xy}(f) = X(f) \cdot Y^*(f)$  where  $X(f)$  and  $Y(f)$  are the Fourier transforms of  $x(t)$  and  $y(t)$  and  $*$  denotes the complex conjugate.

The wavelet-based coherence function is defined at time  $t$  and frequency  $f$

$$C_{xy}^w(t, f) = \frac{|S_{xy}(t, f)|}{[S_{xx}(t, f)S_{yy}(t, f)]^{1/2}} \quad (3)$$

where  $S_{xy}(t, f)$  is the wavelet cross-spectrum between  $x(t)$  and  $y(t)$ ,

$$S_{xy}(t, f) = \int_{t-\delta/2}^{t+\delta/2} W_x(\tau, f) \cdot W_y^*(\tau, f) d\tau \quad (4)$$

where  $*$  denotes the complex conjugate and  $\delta$  is a scalar that depends on frequency.  $W_x(\tau, f)$  and  $W_y(\tau, f)$  are the wavelet transform of  $x(t)$  and  $y(t)$ , and Morlet wavelet transform(MWT) is employed in this study,

$$W_x(\tau, f) = \frac{1}{\sqrt{f}} \int_{-\infty}^{+\infty} x(t) \psi^* \left( \frac{t-\tau}{f} \right) dt \quad (5)$$

where  $\psi(t) = \pi^{-\frac{1}{4}} e^{i w_0 t} e^{-\frac{1}{2t^2}}$ ,  $w_0$  is the wavelet central angle frequency which is an optional value to adjust the time-frequency resolution, often  $w_0 \geq 6$ . The details are described in [31].

The *WTC* index is used to evaluate synchronization in our study and the *WTC* index at the frequency band  $[f_L, f_H]$  is defined as

$$WTC(t) = \frac{1}{N_w} \sum_{f=f_L}^{f_H} C_{xy}^w(t, f) \quad (6)$$

where  $N_w$  is the number of summands in the summation, *WTC* ranges from 0 to 1 [12].

The *WTC* index is calculated across five frequency bands:  $\delta$  (1-4 Hz),  $\theta$  (4-8 Hz),  $\alpha$  (8-13 Hz),  $\beta$  (13-30 Hz) and  $\gamma$  (30-40 Hz) in our study.

### 2.3 Phase synchronization

Phase synchronization (PS) analysis has been independently proposed by Lachaux et al. [32], Mormann et al. [33] and is applied later by Allefeld and Kurths [34, 35]. This approach is based on the

concept of synchronization of chaotic oscillators studied by Rosenblum et al [36]. There are various estimation methods of phase synchronization. Instantaneous phase estimation and phase coupling quantification are the two fundamental steps in phase synchronization evaluation.

Li et al employed the windowed harmonic wavelet transform (WHWT) to extract the instantaneous phase of brain signals, and shows that WHWT performs better than traditional methods, such as the Hilbert transform (HT) [37]. So we chose WHWT to calculate the instantaneous phase in this study. The algorithm is described as follows:

Given two time series  $x(t)$  and  $y(t)$  ( $t=1,2,\dots,N$ ) and their Fourier transforms are  $X(f)$  and  $Y(f)$  which are used to achieve the corresponding expressions in the frequency domain. Then, multiplying  $X(f)$  by the conjugate of the windowed harmonic wavelet of  $Y(f)$  and denoted as  $A(f) = X(f)Y_w^*(f)$ . Taking the inverse Fourier transform of  $A(f)$  to obtain the signal with WHWT, which is presented by [38]

$$a(t) = u(t) + iH[u(t)] = u(t) + \frac{i}{\pi} \int_{-\infty}^{\infty} \frac{u(\tau)}{t-\tau} d\tau = S(t)e^{i\varphi(t)} \quad (7)$$

where  $H[\cdot]$  stands for Hilbert transform. The magnitude of  $a(t)$  is represented as  $S(t) = \sqrt{(u(t))^2 + (H[u(t)])^2}$  and the instantaneous phase of  $a(t)$  is

$$\varphi(t) = \tan^{-1}\left(\frac{H[u(t)]}{u(t)}\right) = \tan^{-1}\left(\frac{\text{imag}[a(t)]}{\text{real}[a(t)]}\right) \quad (8)$$

The instantaneous phase  $\varphi_x(t)$  and  $\varphi_y(t)$  can be achieved through the WHWT and the phase difference is  $\Delta\varphi_{xy}(t) = \varphi_x(t) - \varphi_y(t)$ .

There are three PS measures considered in this study. The first PS measure uses the phase locking value (PLV) [39], denoted as  $PS_{PLV}$ . The calculation is based on a time window with a specified length  $L$ ,

$$PS_{PLV} = \frac{1}{L} \left| \sum_{t=1}^L e^{i\Delta\varphi_{xy}(t)} \right| \quad (9)$$

where  $PS_{PLV}$  is bound between 0 and 1.

The second PS measure is based on Shannon entropy ( $PS_{SE}$ ) of the distribution of  $\Delta\varphi_{xy}(t)$  [40].

The  $\psi = \Delta\varphi_{xy}(t) \bmod 2\pi$  is divided into  $M$  bins and  $p_k$  is the probability that  $\psi$  is in the bin  $k$ .

Then this PS measure is defined as

$$PS_{SE} = \frac{S_{\max} - S}{S_{\max}} \quad (10)$$

where  $S = -\sum_{k=1}^M p_k \ln p_k$  and  $S_{\max} = \ln M$ . It ranges from 0 for a uniform distribution of  $\Delta\varphi_{xy}(t)$ , to

1 if the distribution is a delta function. The optimum number of  $M$  is found as  $e^{0.626+0.4\ln(L-1)}$  [41], where  $L$  is the number of data points in a time window.

The third PS measure is based on conditional probability ( $PS_{CP}$ ) [40] and it is described as follows:

Dividing the interval  $[0, 2\pi]$  into  $K$  ( $k = 1, 2, \dots, K$ ) bins and binning the phase of time series  $x(t)$  into  $K$  phase bins. The value of  $\varphi_x(t) \bmod 2\pi$  falling into the  $k$ -th bin is denoted as  $\theta_k(t)$  and the number of points within the bin are denoted as  $M_k$ . Then, for all the time points when  $\varphi_x(t) \bmod 2\pi$  belongs to the  $k$ -th bin, we compute the corresponding phase value  $\varphi_y(t) \bmod 2\pi$  of time series  $y(t)$  and denote them as  $\eta_k(t)$ . The PS index is denoted as

$$PS_{CP} = \frac{1}{K} \sum_{k=1}^K |\Lambda_k| \quad (11)$$

where  $\Lambda_k = \frac{1}{M_k} \sum_t e^{i\eta_k(t)}$ .

Each PS index is calculated across the frequency bands  $\delta$ ,  $\theta$ ,  $\alpha$ ,  $\beta$  and  $\gamma$ . We divide the EEG data into a series of time epochs and the discussion of PS indexes at different epoch lengths  $T_e$  is shown in **Appendix A(1)**.

## 2.4 Mutual information based on kernel estimation (KerMI)

The mutual information evaluates the interdependence between variables and is widely used to analyze nonlinear systems. Given two discrete random variables  $X$  and  $Y$ ,  $p_X(x_i)$  ( $i=1,2,\dots,b_X$ ) is the marginal probability of the event  $X = x_i$ ,  $p_Y(y_j)$  ( $j=1,2,\dots,b_Y$ ) is the marginal probability of the event  $Y = y_j$  and  $p_{XY}(x_i, y_j)$  is the joint probability of the event  $X = x_i, Y = y_j$ . Then the mutual information between  $X$  and  $Y$  is defined as

$$I(X, Y) = \sum_{i,j} p_{XY}(x_i, y_j) \log \frac{p_{XY}(x_i, y_j)}{p_X(x_i)p_Y(y_j)} \quad (12)$$

As for the discrete random variables  $X = x(t)$  and  $Y = y(t)$  ( $t=1,2,\dots,N$ ), the most straightforward approach for estimating probabilities is partitioning  $x(t)$  and  $y(t)$  into  $K$  ( $k=1,2,\dots,K$ ) bins of finite size, and counting the numbers of points falling into the each bins. The number of points within the bin are denoted as  $M_X(k)$ ,  $M_Y(k)$  and  $M_{XY}(k)$ . Then, the marginal and joint probabilities can be denoted as  $p_X(k) = \frac{M_X(k)}{N}$ ,  $p_Y(k) = \frac{M_Y(k)}{N}$  and  $p_{XY}(k) = \frac{M_{XY}(k)}{N}$  respectively.

Kernel techniques are an attractive alternative to binning a distribution which is discussed thoroughly in [42]. Rather than simply counting the points, we can determine the distance-dependent weight of each point by using kernel function. Then, the marginal probability density and joint probability density which are estimated by the Gaussian kernel estimator [43] can be denoted as [44, 45],

$$p_X(x(t)) = \frac{1}{N} \frac{1}{\sqrt{2\pi h^2}} \sum_{\tilde{t}=1}^N e^{-\frac{1}{2h^2}(x(t)-x(\tilde{t}))^2}, \quad p_Y(y(t)) = \frac{1}{N} \frac{1}{\sqrt{2\pi h^2}} \sum_{\tilde{t}=1}^N e^{-\frac{1}{2h^2}(y(t)-y(\tilde{t}))^2} \quad (13)$$

$$p_{XY}(x(t), y(t)) = \frac{1}{N} \frac{1}{2\pi h^2} \sum_{\tilde{t}=1}^N e^{-\frac{1}{2h^2}((x(t)-x(\tilde{t}))^2+(y(t)-y(\tilde{t}))^2)} \quad (14)$$

where parameter  $h$  is called window width of the kernels.

Last, we obtain the mutual information based on kernel estimation,

$$KerMI = \sum_{t=1}^N p_{XY}(x(t), y(t)) \log \left[ \frac{p_{XY}(x(t), y(t))}{p_X(x(t))p_Y(y(t))} \right] \quad (15)$$

The approximately optimal window width  $h$  is given by  $h_{opt} \approx \sigma \left( \frac{4}{d+2} \right)^{1/(d+4)} N^{-1/(d+4)}$  with  $d=2$  being the dimension of Gaussian kernel estimation and  $\sigma$  the average marginal SD [42].

## 2.5 Permutation cross mutual information (PCMI)

Order pattern analysis is an important method for studying nonlinear dynamical time series [46]. Calculation of the probability distribution of the order patterns is the core of PCMI calculation. Given the time series  $X = x(t)$  and  $Y = y(t)$  ( $t=1,2,\dots,N$ ), we can obtain the embedding vector

$$\mathbf{x}_i = [x(i), x(i+\tau), \dots, x(i+(m-1)\tau)] \quad \text{and} \quad \mathbf{y}_i = [y(i), y(i+\tau), \dots, y(i+(m-1)\tau)]$$

( $i=1,2,\dots,N-(m-1)\tau$ ) with the embedding dimension  $m$  and time lag  $\tau$ . Then, sorting the elements of vectors  $\mathbf{x}_i$  and  $\mathbf{y}_i$  in ascending order respectively and there are  $m!$  possible order patterns in each vectors, which is also called permutations. Next, counting the number of each order pattern of all vectors  $C_X(k)$  ( $k=1,2,\dots,m!$ ) and  $C_Y(l)$  ( $l=1,2,\dots,m!$ ), and we can obtain the probability of

$$\text{each permutation } p_X(k) = \frac{C_X(k)}{N-(m-1)\tau} \quad \text{and} \quad p_Y(l) = \frac{C_Y(l)}{N-(m-1)\tau}.$$

Based on Shannon information theory, the permutation entropy (PE) of  $X$  and  $Y$  is

$$PE_X = -\sum_{k=1}^{m!} p_X(k) \ln p_X(k), \quad PE_Y = -\sum_{l=1}^{m!} p_Y(l) \ln p_Y(l) \quad (16)$$

The joint permutation entropy of  $X$  and  $Y$  is

$$PE_{XY} = -\sum_{k=1}^{m!} \sum_{l=1}^{m!} p_{XY}(k,l) \ln p_{XY}(k,l) \quad (17)$$

where  $p_{XY}(k,l)$  is the joint probability of permutation of vectors  $\mathbf{x}_i$  and  $\mathbf{y}_i$ .

Then, the PCMI of  $X$  and  $Y$  is defined as

$$PCMI = PE_X + PE_Y - PE_{XY} \quad (18)$$

Previous study found that the parameter selection  $m=6$  and  $\tau=1$  when the sampling rate of data is 100

Hz resulted in the best *PCMI* performance in distinguish different anesthetic state [47]. Therefore, we used  $m=6$  and  $\tau=1$  for the calculation of *PCMI* index in this study.

## 2.6 Nonlinear interdependence

Nonlinear interdependence is an important nonlinear synchronization measure in neural systems [48-51]. The details of the algorithm are described as follows:

Given the time series  $X = x(t)$  and  $Y = y(t)$  ( $t = 1, 2, \dots, N$ ), we can reconstruct delay vectors the embedding vector  $\mathbf{x}_i = [x(i), x(i + \tau), \dots, x(i + (m - 1)\tau)]$  and  $\mathbf{y}_i = [y(i), y(i + \tau), \dots, y(i + (m - 1)\tau)]$  ( $i = 1, 2, \dots, Q$ ,  $Q = N - (m - 1)\tau$ ) with the embedding dimension  $m$  and time lag  $\tau$ . We first denote  $r_{i,j}$  and  $s_{i,j}$ ,  $j = 1, \dots, k$  as the time indices of the  $k$  nearest neighbors of  $\mathbf{x}_i$  and  $\mathbf{y}_i$ , respectively.

For each  $\mathbf{x}_i$ , the mean squared Euclidean distance to its  $k$  neighbors is defined as

$$R(\mathbf{x}_i) = \frac{1}{k} \sum_{j=1}^k (\mathbf{x}_i - \mathbf{x}_{r_{i,j}})^2 \quad (19)$$

The  $y$ -conditioned mean squared Euclidean distance is defined by replacing the nearest neighbors by the equal time partners of the closest neighbors of  $\mathbf{y}_i$

$$R(\mathbf{x}_i | \mathbf{y}_i) = \frac{1}{k} \sum_{j=1}^k (\mathbf{x}_i - \mathbf{x}_{s_{i,j}})^2 \quad (20)$$

We can define the nonlinear interdependence [52]

$$NI(X|Y) = \frac{1}{Q} \sum_{i=1}^Q \frac{R(\mathbf{x}_i)}{R(\mathbf{x}_i | \mathbf{y}_i)} \quad (21)$$

The  $NI(X|Y)$  ranges from 0 if the two time series are independent  $R(\mathbf{x}_i | \mathbf{y}_i) \approx R(X) \gg R(\mathbf{x}_i)$ , to 1 if they are highly correlated  $R(\mathbf{x}_i | \mathbf{y}_i) \approx R(\mathbf{x}_i) \ll R(X)$ , where  $R(X) = 1/Q \sum_{i=1}^Q R(\mathbf{x}_i)$ ,  $k = Q - 1$ .

The selection of three parameters of  $NI$ : embedding dimension  $m$ , time lag  $\tau$  and the number of nearest neighbors  $k$  is discussed in **Appendix A(2)**.

## 2.7 Cross recurrence analysis

The recurrence of states, meaning that states are arbitrarily close after some time, is a fundamental property of dynamical systems [53]. The cross recurrence plot (CRP) which is a bivariate extension of the recurrence plot (RP) is introduced to analyze the dependencies between two different systems [54, 55].

Considering two time series  $x(t)$  and  $y(t)$  ( $t=1,2,\dots,N$ ), we reconstruct the embedding vector

$$\mathbf{x}_k = [x(k), x(k+\tau), \dots, x(k+(m-1)\tau)] \quad \text{and} \quad \mathbf{y}_k = [y(k), y(k+\tau), \dots, y(k+(m-1)\tau)]$$

( $k=1,2,\dots,N-(m-1)\tau$ ) with the embedding dimension  $m$  and time lag  $\tau$ . The cross recurrence matrix which is also called cross recurrence plot is defined by,

$$CR_{i,j} = \Theta(\varepsilon - \|\mathbf{x}_i - \mathbf{y}_j\|) \quad i, j = 1, 2, \dots, Q \quad (22)$$

where  $\varepsilon$  is the threshold distance,  $\Theta(\cdot)$  is the Heaviside function,  $\|\cdot\|$  is the Euclidean norm and  $Q$  is the number of embedding vector.

The recurrence quantification analysis [56, 57] defined several measures based on diagonal oriented lines in RP, such as recurrence rate, determinism (DET), maximal length of diagonal structures, entropy and trend. The determinism is ratio of recurrence points forming diagonal structures (of at least length  $l_{min}$ ) to all recurrence points in CRP. Long diagonal structures show similar phase space behavior of two time series, while stochastic time series cause short diagonals. In our study, we use *DET* to evaluate the synchronization of the two time series,

$$DET = \frac{\sum_{l=l_{min}}^Q lP(l)}{\sum_{l=1}^Q lP(l)} \quad (23)$$

where  $l$  is the length of the diagonal which parallels the main diagonal,  $P(l)$  is the corresponding distribution probability.  $l_{min}$  is the threshold of diagonal length.

The selection of three parameters of *DET*: embedding dimension  $m$ , time lag  $\tau$  and threshold of diagonal length  $l_{min}$  is discussed in **Appendix A(3)**.

### 3. Statistical analysis

The aim of this study is to evaluate the performance of different synchronization measures for tracking synchronization changes during anesthetic period and the ability of distinguish different anesthetic states. We used the prediction probability ( $P_K$ ) [58, 59] to evaluate the ability of predicting BIS and propofol effect-site concentration ( $C_{eff}$ ) (derived from pharmacokinetic/pharmacodynamic (PK/PD) modeling [60]) of all synchronization measures.

Given the BIS or  $C_{eff}$  value  $S(k), k = 1, 2, \dots, N$  and the synchronization index  $I(k), k = 1, 2, \dots, N$ , we choose two data points  $S(i)$  and  $S(j)$  ( $S(i) \neq S(j), i \neq j$ ) randomly. Then, we compare the monotony of  $I(i)$  and  $I(j)$  with the monotony of  $S(i)$  and  $S(j)$ . If  $I(i) = I(j)$ ,  $I(i)$  and  $I(j)$  are considered as an x-only tie. If the monotony of  $I(i)$  and  $I(j)$  is same as the monotony of  $S(i)$  and  $S(j)$ ,  $I(i)$  and  $I(j)$  are considered as a concordance. Otherwise, they are considered as a discordance. We repeat the above steps for 500 times, then the  $P_K$  is defined as

$$P_K = \frac{P_c + P_{tx}/2}{P_c + P_d + P_{tx}} \quad (24)$$

where  $P_c, P_d, P_{tx}$  are the proportions that  $I(i)$  and  $I(j)$  are a concordance, discordance and an x-only tie respectively.  $P_K$  ranges from 0 to 1.  $P_K=1$  means that the synchronization index predicts the BIS or  $C_{eff}$  correctly 100% of the time.  $P_K=0.5$  means that the synchronization index correctly predicts that BIS or  $C_{eff}$  only 50% of the time. The  $P_K$  value is replaced by  $1 - P_K$  when there is a negative monotonic relationship between the synchronization indexes with BIS and  $C_{eff}$ .

Matlab Statistics Toolbox was applied for statistics. Kolmogorov-Smirnov test (*kstest.m*) was used to compare the  $P_K$  values of all synchronization measures to a standard normal distribution. We used the Friedman test (*friedman.m*) and Multiple comparison test (*multcompare.m*) to determine statistical significant difference among the  $P_K$  values of all synchronization indexes with BIS and  $C_{eff}$ . Box plot was adopted to evaluate the performance for distinguishing different anesthetic states of each synchronization index. Kolmogorov-Smirnov test was also used to compare the index values of syn-

chronization measures at awake, unconscious and recovery states of all subjects to a standard normal distribution. Kruskal-Wallis test (*kruskalwallis.m*) and Multiple comparison test were used to determine the significant difference of the index values between awake and unconscious states and between unconscious and recovery states. The coefficient of variation (CV) (the ratio of standard deviation (SD) to mean) was used to evaluate the index stability during propofol-induced anesthesia process [61]. Moreover, in order to gain the relation among different synchronization measures, Bispectral Index (BIS) and  $C_{eff}$ , we calculated the Pearson correlation coefficient  $R$  of all subjects.

## 4. Application to real EEG recordings and results

### 4.1 Subjects and EEG recordings

We studied the EEG data of seven human volunteers from previously published work [60]. With the permission of the Waikato Hospital Ethical Committee, the volunteers (American Society of Anesthesiologists physical status I or II) were recruited to undergo a brief propofol anesthetic and recovered in accordance with normal procedures of the Australian and New Zealand College of Anaesthesia (A.N.Z.C.A) guidelines. All subjects gave written informed consent after obtaining the permission of the hospital ethical committee. The silver-silver chloride scalp electrodes were placed at the position of Fp1-F7 and C3-T3 according to the 10-20 international system to produce bipolar signals (Fig. 1A). The ground electrode was placed at FpZ. The Aspect A-1000 EEG monitor (Aspect Medical Systems, Natick, MA, USA) was used to collect both the raw EEG signal (The sampling frequency is 256 Hz) and the BIS (The sampling frequency is 0.2 Hz).

The experimental sequence diagram is shown in Fig. 1B. The propofol intravenous infusion was 150ml/h (1500mg/h) in an antecubital vein via a syringe driver pump initially, and the BIS and raw EEG data were recorded when the infusion started. Then, a verbal list of dissimilar objects was read to the subject at 30-second intervals who held a syringe filled with water between forefinger and thumb. When the syringe dropped (LoC time), the infusion and the read of the list of dissimilar stopped, and the time was recorded as “syringe-drop time”. The subject was then allowed to awake and given the play of a pre-recorded tape of random numbers and some verbal commands such as “move your right foot”. The verbal commands lasted 5 seconds and they were at 10-second intervals. We recorded the time as “command time” as soon as the subject responded the verbal command correctly (recovery of consciousness (RoC) time). The subject were questioned as to the first number that they could recall and the last object that they could remember during propofol induction, and these two time points were recorded as “number time” and “object time” respectively. The study was terminated about 60 seconds after LoC time. The study four recorded times of all subjects are shown in Table 1.

“Fig. 1”

“Table 1”

## 4.2 EEG preprocessing

Generally, there are three main artifacts in EEG recordings: baseline drift, head movement noise and physiological noise (such as electrooculogram (EOG) and electromyogram (EMG)). For each source of noise we adopted a different artifact-rejection approach. Firstly, baseline drift and head movement noise are usually in the low frequency band ( $<0.5$  Hz) and the function *eegfilt.m* in EEGLAB was used to reduce this noise [62]. Low-pass filter and the mains notch were set at 70 Hz and 50 Hz respectively. Secondly, raw EEG data exceeding an amplitude of  $200 \mu V$  were removed as outlier points. Using statistical mean and standard deviation (SD) methods [63], amplitude values beyond the range  $\text{mean} \pm 2\text{SD}$  were also considered as outliers. Then, EOG artifacts were reduced through a stationary wavelet transform based on an appropriate threshold [61]. Inverse filtering was used to identify transient events in the EEG, and was the method employed to detect and remove EMG and other high-amplitude transient artifacts [64, 65]. Finally, the EEG data were downsampled to 100 Hz by the function *resample.m* in Matlab.

In our study, in order to evaluate the synchronization during the whole experimental period, the EEG data were divided into a series of 10-second epochs, with an overlap of 75% (In particular, the data were divided into different length of time epoch for the calculation of PS indexes.). We used the EEG data in each epochs to calculate the synchronization indexes. Also, we chose three states from the whole period: awake state (the period before “Object time”), unconscious state (the period between LoC time and “Number time”) and recovery state (the period after “command time”) in order to evaluate the ability of different synchronization measures to distinguish different anesthetic states.

## 4.3 Results

We first analyzed the FTC and WTC of the two-channel EEG signals of all subjects to find a better coherence method to quantify the synchronization in frequency domain. The EEG recordings of two channels from one subject and their corresponding time-frequency spectrogram were shown in Fig. 2 A and Fig. 2B. The power in  $\delta$ ,  $\alpha$  and  $\beta$  frequency bands increased with the increasing propofol ef-

fect-site concentration. Fig. 2C and Fig. 2D showed the FTC and WTC spectrums during the whole period. In terms of FTC spectrum, two-channel EEG signals were divided into a series of 10-second epochs with an overlap of 75%. The epochs were windowed using a Hamming window and FFT length was set to be 128. As can be seen from the figure, FTC spectrum could not reflect the changes of coherence during the whole period (Fig. 2C), while the WTC spectrum in the  $\delta$ ,  $\alpha$  and  $\beta$  frequency bands increased obviously during unconscious state (Fig. 2D), which had the similar results as the spectrogram analysis. Therefore, we extracted the WTC index from WTC spectrum to quantify the synchronization during propofol-induced anesthesia period.

We then computed the synchronization indexes of all subjects during the whole anesthetic period. Fig. 3A was the preprocessed EEG signals of one subject from the left prefrontal and left primary motor cortex respectively. Fig. 3B and Fig. 3C were the corresponding BIS and  $C_{eff}$ . Fig. 3D showed the values of all synchronization indexes for the same subject. We computed three PS indexes at frequency bands  $\delta$ ,  $\theta$ ,  $\alpha$ ,  $\beta$  and  $\gamma1$  and we found that the  $PS_{PLV}$  and  $PS_{CP}$  had similar results, which was consistent with previously reported results in [51], and the  $PS_{CP}$  will be not further reported. As can be seen from the Fig. 3D, the  $PCMI$ ,  $NI$ ,  $PS_{PLV}$  ( $\delta$ ,  $\theta$ ,  $\alpha$  and  $\gamma1$ ),  $PS_{SE}$  ( $\delta$ ,  $\beta$ ) saw a decreasing trend with the increasing  $C_{eff}$  value, whereas  $KerMI$ ,  $DET$  and  $WTC$  ( $\delta$ ,  $\theta$  and  $\alpha$ ) showed an increasing trend which were consistent with the  $C_{eff}$ .

“Fig. 2”

“Fig. 3”

To quantify the ability of predicting BIS ( $P_{K\_BIS}$ ) and the relation with  $C_{eff}$  ( $P_{K\_C_{eff}}$ ) of the synchronization measures, we calculated the  $P_K$ . The  $P_K$  values of each synchronization indexes with BIS and  $C_{eff}$  of all subjects and their corresponding box plots were shown in Fig. 4. The median (1st quartile (Q1), 3rd quartile (Q3)) of  $P_K$  values of all measures were displayed in Table 2. It can be seen from Fig. 4 and Table 2 that  $PCMI$  had the highest  $P_K$  value with BIS ( $P_{K\_BIS}=0.855(0.775, 0.875)$ ) and  $C_{eff}$  ( $P_{K\_C_{eff}}=0.794(0.703, 0.842)$ ).  $DET$  ranked second with the value  $P_{K\_BIS}=0.823(0.806, 0.869)$  and  $P_{K\_C_{eff}}=0.781(0.695, 0.816)$ . These figures demonstrated that  $PCMI$  and  $DET$  could best

predict the BIS and follow the  $C_{eff}$ . The  $P_K$  values of NI, KerMI and COR were smaller than PCMI and DET. Kolmogorov-Smirnov test showed that the  $P_K$  values of each index were not normally distributed. The statistical significant difference among the synchronization indexes were marked at the top of Fig. 4A and B, using the notation \*, \*\* and \*\*\* to indicate significant difference at  $p<0.05$ ,  $p<0.01$  and  $p<0.001$  respectively (Friedman test and Multiple comparison test). As for  $PS_{PLV}$  and  $PS_{SE}$ , there was no significant difference among different frequency bands in tracking the BIS and  $C_{eff}$ . By contrast, WTC ( $\alpha$ ) predicted significantly better than WTC ( $\gamma_1$ ) with BIS, and WTC ( $\alpha$ ,  $\beta$ ) predicted significantly better than WTC ( $\gamma_1$ ) with  $C_{eff}$  ( $p<0.01$ ).

“Fig. 4”

“Table 2”

Furthermore, the ability to distinguish different anesthetic states of synchronization measures is essential for DoA monitoring. The synchronization indexes were computed at three anesthetic states (awake, unconscious and recovery) and the boxplots of the index values were shown in Fig. 5. The Kolmogorov-Smirnov test showed that the index value of each measure in each state were not normally distributed, so we adopted the Kruskal-Wallis test and Multiple comparison test to estimate the significant difference among between three states, using the notation \*, \*\* and \*\*\* to indicate significant difference at  $p<0.05$ ,  $p<0.01$  and  $p<0.001$  respectively. It can be seen from Fig. 5 that KerMI, PCMI, NI and DET could significantly distinguish awake and unconscious states as well as unconscious and recovery states ( $p<0.001$ ), whereas COR could only distinguish awake and unconscious states ( $p<0.001$ ). There was an increase in unconscious state and a decrease in recovery state for KerMI and DET, while the trends were opposite for PCMI and NI. In terms of  $PS_{PLV}$ , the phase synchronization dropped significantly in unconscious state for  $PS_{PLV}$  ( $\delta$ ,  $\theta$ ,  $\alpha$  and  $\gamma_1$ ) and had no significant changes in recovery state, while  $PS_{PLV}$  ( $\beta$ ) could not distinguish the three anesthetic states (Fig. 5F-J).  $PS_{SE}$  could only distinguish three states at  $\theta$  and  $\beta$  frequency bands (Fig. 5K-O). As for WTC, there was a significant rise in unconscious state and a significant drop in recovery state for all frequency bands (Fig. 5P-T).

In addition, the stability of the index value during the anesthetic states is important for the reliable DoA monitoring. We calculated the CV of all synchronization indexes of all subjects at awake, un-

conscious and recovery states and the CV values were shown in Table 3. As can be seen from Table 3, PCMI had the low CV in awake state (CV=0.085), unconscious state (CV=0.146) and recovery state (CV=0.105). The CV of NI, PS<sub>PLV</sub>, PS<sub>SE</sub> and DET were lower than COR and KerMI, which were all smaller than WTC in awake and unconscious states. By contrast, the CV of COR, NI, PS<sub>PLV</sub>, PS<sub>SE</sub>, DET gained smaller values than KerMI and WTC in recovery state. These results illustrated that PCMI, NI, PS and DET had a better robustness to noise during the propofol-induced anesthesia.

“Fig. 5”

“Table 3”

To further evaluate the relationship among synchronization measures, BIS and  $C_{eff}$ , we calculated the correlation coefficients  $R$  among different synchronization measures, BIS and  $C_{eff}$  of all subjects and the averaged  $R$  over all subjects were shown in Fig. 6. KerMI, DET, WTC index curves and  $C_{eff}$  during the whole period were reversed when calculating the correlation coefficients. As can be seen from Fig. 6, PCMI had the highest correlation coefficient with BIS ( $R=0.846$ ) and  $C_{eff}$  ( $R=0.739$ ). DET ranked second with BIS ( $R=0.843$ ) and  $C_{eff}$  ( $R=0.703$ ) and NI also had a high value with BIS ( $R=0.729$ ) and  $C_{eff}$  ( $R=0.638$ ). As for PS and WTC, PS<sub>PLV</sub> ( $\delta$ ) and WTC ( $\alpha$ ) correlated with BIS and  $C_{eff}$  higher than that of other frequency bands. In terms of the relation among different synchronization measures, PCMI correlated closely with DET ( $R=0.949$ ) and NI ( $R=0.838$ ). Strong relation was obtained between KerMI and WTC ( $\delta$ ) ( $R=0.833$ ) and between NI and DET ( $R=0.798$ ).

“Fig. 6”

## 5. Discussion and conclusions

Despite the emergence of many DoA monitoring over the last few years, the neurophysiological mechanisms by which anesthetic drugs caused loss of consciousness are still unknown [1]. Many studies suggest that long-range synchronization of neuronal populations is a fundamental principle of cortical processing and communication. Multi-channel EEG is more suited for understanding the mechanisms of anesthetic effect and it could provide a more robust measure of anesthetic depth for clinical application. In this study, we considered ten synchronization measures, including cross correlation, two coherence measures, three phase synchronization measures, two mutual information measures, nonlinear interdependence and cross recurrence analysis. We sought to identify synchronization changes of EEG between two brain regions during different anesthetic states and evaluate the performance in tracking anesthetic drug concentration and the ability of distinguishing different anesthetic states of the synchronization measures.

In our results, COR performed worse in correlating with BIS and  $C_{eff}$  and distinguishing the anesthetic states in this study. We compared the Fourier transform coherence and wavelet transform coherence. The results showed that the coherence based on wavelet transform could reflect the synchronization changes during anesthetic states (Fig. 2C and D) and we used the WTC index which was extracted from WTC spectrum to quantify the synchronization in our study. With increasing WTC in unconscious state and decreasing WTC in recovery state, propofol makes the neural oscillations more synchronous after loss of consciousness, which is consistent with previously reported results in the reference [12]. Furthermore, recent studies using bicoherence [13], global coherence [66] reflected different forms of EEG synchronization in various frequency bands at different brain region under general anesthesia. Therefore, the coherence based synchronization measures are essential and promising for evaluating the communication among brain regions and describe the mechanism of general anesthesia.

The instantaneous phase extraction was based on the WHWT which had been proved that it was better than Hilbert transform [37] and Phase locking and Shannon entropy were used to quantify the phase synchronization. The results showed that propofol caused a decrease phase synchronization in

$\delta$ ,  $\theta$ ,  $\alpha$ ,  $\beta$  and  $\gamma_1$  frequency bands and  $PS_{PLV}$  performed better than  $PS_{SE}$  in distinguishing unconscious state from awake state. However, this finding is not consistent with other studies about phase synchronization changes during anesthesia, which may be due to the different EEG functional connectivity of subjects or patients under different anesthesia procedures.

PCMI is related to the probability distribution of permutation pattern. Our results of decreasing PCMI in unconscious state and increasing PCMI in recovery state revealed that propofol lead to the decrease of permutation pattern of EEG signals, which means that the EEG signal is more regular when anesthetized [67, 68]. Also, PCMI presented a better performance than other indexes in evaluating EEG synchronization changes during anesthesia. It has the highest  $P_K$  and  $R$  values with BIS and  $C_{eff}$  (Fig. 4), strong robustness to noise and it can significantly distinguish awake, unconscious and recovery states (Fig. 5). These results illustrated that PCMI is a meaningful measure for characterizing EEG dynamics during anesthesia. As for KerMI, Gaussian kernel was used to quantify the probability density of mutual information. Our results showed that KerMI increased with increasing depth of anesthesia, which had an opposite trend with PCMI. Maybe it is the regular EEG signals in unconscious state which have small difference between adjacent signals that makes the increasing KerMI in unconscious state.

As for NI, the significant drop of NI in unconscious state in our study demonstrates that propofol weaken the interdependence and lead to the disconnection of two brain regions, which has been previously reported that brain functional integration decreased during propofol-induced loss of consciousness [5, 69]. Also, NI had close relation with BIS and  $C_{eff}$  and the ability to distinguish different anesthetic states. Therefore, as a nonlinear synchronization index, NI is suit for detecting the changes of interdependence of EEG signal during anesthesia.

DET performed good in following the  $C_{eff}$  and had good robustness to noise. Increasing in unconscious states and decreasing in recovery state means that propofol causes the increase of synchronization, which is consistent with the result in the recent study [28]. Accordingly, DET can be effectively evaluate the EEG synchronization changes during anesthesia.

In conclusion, most synchronization measures can detect the EEG dynamics during anesthesia. Each measure has their properties and performance on evaluating synchronization changes because of their own calculating principles, which may reflect different mechanism of anesthesia. Although our experiment data are limited which means that more investigation of these synchronization measures should be conducted for describing the underlying dynamics of these measures, we still characterize the EEG dynamics during propofol-induced anesthesia using different synchronization measures.

## **Conflict of interest**

None declared.

## **Acknowledgments**

This research was supported by National Natural Science Foundation of China (61304247, 61203210, 61273063), China Postdoctoral Science Foundation (2014M551051), Applied basic research project in Hebei province (12966120D) and Natural Science Foundation of Hebei Province of China (F2014203127).

## References

1. Lewis LD, Weiner VS, Mukamel EA, Donoghue JA, Eskandar EN, Madsen JR, Anderson WS, Hochberg LR, Cash SS, Brown EN. Rapid fragmentation of neuronal networks at the onset of propofol-induced unconsciousness. *Proceedings of the National Academy of Sciences* 2012, 109(49).E3377-E3386.
2. Voss L, Sleigh J. Monitoring consciousness: the current status of EEG-based depth of anaesthesia monitors. *Best Practice & Research Clinical Anaesthesiology* 2007, 21(3).313-325.
3. Nallasamy N, Tsao DY. Functional connectivity in the brain: effects of anesthesia. *The Neuroscientist* 2011, 17(1).94-106.
4. Lee U, Mashour GA, Kim S, Noh G-J, Choi B-M. Propofol induction reduces the capacity for neural information integration: implications for the mechanism of consciousness and general anesthesia. *Consciousness and cognition* 2009, 18(1).56-64.
5. Lee U, Kim S, Noh G-J, Choi B-M, Hwang E, Mashour GA. The directionality and functional organization of frontoparietal connectivity during consciousness and anesthesia in humans. *Consciousness and cognition* 2009, 18(4).1069-1078.
6. Pereda E, Quiroga RQ, Bhattacharya J. Nonlinear multivariate analysis of neurophysiological signals. *Progress in neurobiology* 2005, 77(1).1-37.
7. Breakspear M. "Dynamic" connectivity in neural systems. *Neuroinformatics* 2004, 2(2).205-224.
8. Kaminski M, Liang H. Causal influence: advances in neurosignal analysis. *Critical Reviews™ in Biomedical Engineering* 2005, 33(4).
9. Stam CJ. Nonlinear dynamical analysis of EEG and MEG: review of an emerging field. *Clinical Neurophysiology* 2005, 116(10).2266-2301.
10. Siegle GJ, Thompson W, Carter CS, Steinhauer SR, Thase ME. Increased amygdala and decreased dorsolateral prefrontal BOLD responses in unipolar depression: related and independent features. *Biol Psychiatry* 2007, 61(2).198-209.
11. He BJ, Snyder AZ, Zempel JM, Smyth MD, Raichle ME. Electrophysiological correlates of the brain's intrinsic large-scale functional architecture. *Proc Natl Acad Sci U S A* 2008, 105(41).16039-16044.
12. Li D, Voss LJ, Sleigh JW, Li X. Effects of volatile anesthetic agents on cerebral cortical synchronization in sheep. *Anesthesiology* 2013, 119(1).81-88.
13. Hayashi K, Mukai N, Sawa T. Simultaneous bicoherence analysis of occipital and frontal electroencephalograms in awake and anesthetized subjects. *Clin Neurophysiol* 2014, 125(1).194-201.
14. David O, Cosmelli D, Friston KJ. Evaluation of different measures of functional connectivity using a neural mass model. *Neuroimage* 2004, 21(2).659-673.
15. Engel AK, Fries P, Singer W. Dynamic predictions: oscillations and synchrony in top-down processing. *Nature Reviews Neuroscience* 2001, 2(10).704-716.
16. David O, Friston KJ. A neural mass model for meg/eeg: coupling and neuronal dynamics. *Neuroimage* 2003, 20(3).1743-1755.
17. Koskinen M, Seppanen T, Tuukkanen J, Yli-Hankala A, Jantti V. Propofol anesthesia induces phase synchronization changes in EEG. *Clin Neurophysiol* 2001, 112(2).386-392.
18. Nicolaou N, Georgiou J. Spatial Analytic Phase Difference of EEG activity during anesthetic-induced unconsciousness. *Clin Neurophysiol* 2014, 125(10).2122-2131.
19. Abásolo D, Escudero J, Hornero R, Gómez C, Espino P. Approximate entropy and auto mutual information analysis of the electroencephalogram in Alzheimer's disease patients. *Medical & biological engineering & computing* 2008, 46(10).1019-1028.

20. Hall Jr CW, Sarkar A. Mutual information in natural position order of electroencephalogram is significantly increased at seizure onset. *Medical & biological engineering & computing* 2011, 49(2).133-141.
21. Langen M, Schnack HG, Nederveen H, Bos D, Lahuis BE, de Jonge MV, van Engeland H, Durston S. Changes in the developmental trajectories of striatum in autism. *Biological psychiatry* 2009, 66(4).327-333.
22. Moon Y-I, Rajagopalan B, Lall U. Estimation of mutual information using kernel density estimators. *Physical Review E* 1995, 52(3).2318.
23. Liang Z, Wang Y, Ouyang G, Voss LJ, Sleight JW, Li X. Permutation auto-mutual information of electroencephalogram in anesthesia. *J Neural Eng* 2013, 10(2).026004.
24. Liang Z, Liang S, Wang Y, Ouyang G, Li X. Tracking the coupling of two electroencephalogram series in the isoflurane and remifentanyl anesthesia. *Clin Neurophysiol* 2014.
25. Andrzejak RG, Schindler K, Rummel C. Nonrandomness, nonlinear dependence, and nonstationarity of electroencephalographic recordings from epilepsy patients. *Phys Rev E Stat Nonlin Soft Matter Phys* 2012, 86(4 Pt 2).046206.
26. Rabbi AF, Azinfar L, Fazel-Rezai R. Seizure prediction using adaptive neuro-fuzzy inference system. *Conf Proc IEEE Eng Med Biol Soc* 2013, 2013.2100-2103.
27. Becker K, Schneider G, Eder M, Ranft A, Kochs EF, Zieglansberger W, Dodt HU. Anaesthesia monitoring by recurrence quantification analysis of EEG data. *PLoS One* 2010, 5(1).e8876.
28. Shalhaf R, Behnam H, Sleight JW, Steyn-Ross DA, Steyn-Ross ML. Frontal-Temporal Synchronization of EEG Signals Quantified by Order Patterns Cross Recurrence Analysis During Propofol Anesthesia. *IEEE Trans Neural Syst Rehabil Eng* 2014.
29. Zhou D, Thompson WK, Siegle G. MATLAB toolbox for functional connectivity. *Neuroimage* 2009, 47(4).1590-1607.
30. Nunez PL. *Electric fields of the brain: the neurophysics of EEG*. Oxford University Press; 2006.
31. Li X, Yao X, Fox J, Jefferys JG. Interaction dynamics of neuronal oscillations analysed using wavelet transforms. *Journal of neuroscience methods* 2007, 160(1).178-185.
32. Lachaux JP, Rodriguez E, Martinerie J, Varela FJ. Measuring phase synchrony in brain signals. *Hum Brain Mapp* 1999, 8(4).194-208.
33. Mormann F, Lehnertz K, David P, Elger C. Mean phase coherence as a measure for phase synchronization and its application to the EEG of epilepsy patients. *Physica D: Nonlinear Phenomena* 2000, 144(3).358-369.
34. Allefeld C, Kurths J. Multivariate phase synchronization analysis of EEG data. *IEICE Transactions on Fundamentals of Electronics, Communications and Computer Sciences* 2003, 86(9).2218-2221.
35. Allefeld C, Kurths J. An approach to multivariate phase synchronization analysis and its application to event-related potentials. *International Journal of Bifurcation and Chaos* 2004, 14(02).417-426.
36. Rosenblum MG, Pikovsky AS, Kurths J. Phase synchronization of chaotic oscillators. *Physical Review Letters* 1996, 76(11).1804.
37. Li D, Li X, Cui D, Li Z. Phase synchronization with harmonic wavelet transform with application to neuronal populations. *Neurocomputing* 2011, 74(17).3389-3403.
38. Park H, Kim D-S. Evaluation of the dispersive phase and group velocities using harmonic wavelet transform. *NDT & E International* 2001, 34(7).457-467.
39. Lachaux J-P, Rodriguez E, Le van Quyen M, Lutz A, Martinerie J, Varela FJ. Studying single-trials of phase synchronous activity in the brain. *International Journal of Bifurcation and Chaos* 2000, 10(10).2429-2439.
40. Tass P, Rosenblum M, Weule J, Kurths J, Pikovsky A, Volkman J, Schnitzler A, Freund H-J. Detection of n:m phase locking from noisy data: application to magnetoencephalography. *Physical Review Letters* 1998, 81(15).3291.

41. Otnes RK, Enochson L. Digital time series analysis. John Wiley & Sons, Inc.; 1972.
42. Silverman BW. Density estimation for statistics and data analysis. Volume 26. CRC press; 1986.
43. Beirlant J, Dudewicz EJ, Györfi L, Van der Meulen EC. Nonparametric entropy estimation: An overview. *International Journal of Mathematical and Statistical Sciences* 1997, 6.17-40.
44. Steuer R, Kurths J, Daub CO, Weise J, Selbig J. The mutual information: detecting and evaluating dependencies between variables. *Bioinformatics* 2002, 18 Suppl 2.S231-240.
45. Qiu P, Gentles AJ, Plevritis SK. Fast calculation of pairwise mutual information for gene regulatory network reconstruction. *Comput Methods Programs Biomed* 2009, 94(2).177-180.
46. Bandt C, Pompe B. Permutation entropy: a natural complexity measure for time series. *Phys Rev Lett* 2002, 88(17).174102.
47. Liang Z, Wang Y, Ouyang G, Voss LJ, Sleight JW, Li X. Permutation auto-mutual information of electroencephalogram in anesthesia. *Journal of neural engineering* 2013, 10(2).026004.
48. Quiroga RQ, Arnhold J, Grassberger P. Learning driver-response relationships from synchronization patterns. *Physical Review E* 2000, 61(5).5142.
49. Breakspear M, Terry J. Topographic organization of nonlinear interdependence in multichannel human EEG. *Neuroimage* 2002, 16(3).822-835.
50. Breakspear M, Terry J. Nonlinear interdependence in neural systems: motivation, theory, and relevance. *International Journal of Neuroscience* 2002, 112(10).1263-1284.
51. Quiroga RQ, Kraskov A, Kreuz T, Grassberger P. Performance of different synchronization measures in real data: a case study on electroencephalographic signals. *Physical Review E* 2002, 65(4).041903.
52. Arnhold J, Grassberger P, Lehnertz K, Elger C. A robust method for detecting interdependences: application to intracranially recorded EEG. *Physica D: Nonlinear Phenomena* 1999, 134(4).419-430.
53. Eckmann J-P, Kamphorst SO, Ruelle D. Recurrence plots of dynamical systems. *Europhys Lett* 1987, 4(9).973-977.
54. Zbilut JP, Giuliani A, Webber CL. Detecting deterministic signals in exceptionally noisy environments using cross-recurrence quantification. *Physics Letters A* 1998, 246(1).122-128.
55. Marwan N, Kurths J. Nonlinear analysis of bivariate data with cross recurrence plots. *Physics Letters A* 2002, 302(5).299-307.
56. Webber Jr CL, Zbilut JP. Dynamical assessment of physiological systems and states using recurrence plot strategies. *Journal of Applied Physiology* 1994, 76(2).965-973.
57. Zbilut JP, Webber Jr CL. Embeddings and delays as derived from quantification of recurrence plots. *Physics Letters A* 1992, 171(3).199-203.
58. Smith WD, Dutton RC, Smith NT. Measuring the performance of anesthetic depth indicators. *Anesthesiology* 1996, 84(1).38-51.
59. Shalhaf R, Behnam H, Sleight J, Voss L. Using the Hilbert–Huang transform to measure the electroencephalographic effect of propofol. *Physiological Measurement* 2012, 33(2).271.
60. Williams M, Sleight J. Auditory recall and response to command during recovery from propofol anaesthesia. *Anaesthesia and intensive care* 1999, 27(3).265.
61. Li X, Li D, Liang Z, Voss L, Sleight J. Analysis of depth of anesthesia with Hilbert-Huang spectral entropy. *Clinical Neurophysiology* 2008, 119(11).2465-2475.
62. Delorme A, Makeig S. EEGLAB: an open source toolbox for analysis of single-trial EEG dynamics including independent component analysis. *Journal of neuroscience methods* 2004, 134(1).9-21.
63. Seo S. A review and comparison of methods for detecting outliers in univariate data sets. University of Pittsburgh; 2006.

64. Fatourechhi M, Bashashati A, Ward RK, Birch GE. EMG and EOG artifacts in brain computer interface systems: A survey. *Clinical Neurophysiology* 2007, 118(3).480-494.
65. Schlögl A. The electroencephalogram and the adaptive autoregressive model: theory and applications. Shaker Germany; 2000.
66. Cimenser A, Purdon PL, Pierce ET, Walsh JL, Salazar-Gomez AF, Harrell PG, Tavares-Stoeckel C, Habeeb K, Brown EN. Tracking brain states under general anesthesia by using global coherence analysis. *Proc Natl Acad Sci U S A* 2011, 108(21).8832-8837.
67. Sleight JW, Donovan J. Comparison of bispectral index, 95% spectral edge frequency and approximate entropy of the EEG, with changes in heart rate variability during induction of general anaesthesia. *Br J Anaesth* 1999, 82(5).666-671.
68. Vakkuri A, Yli-Hankala A, Talja P, Mustola S, Tolvanen-Laakso H, Sampson T, Viertio-Oja H. Time-frequency balanced spectral entropy as a measure of anesthetic drug effect in central nervous system during sevoflurane, propofol, and thiopental anesthesia. *Acta Anaesthesiol Scand* 2004, 48(2).145-153.
69. Schrouff J, Perlberg V, Boly M, Marrelec G, Boveroux P, Vanhaudenhuyse A, Bruno MA, Laureys S, Phillips C, Pelegrini-Issac M, Maquet P, Benali H. Brain functional integration decreases during propofol-induced loss of consciousness. *Neuroimage* 2011, 57(1).198-205.

## Appendix A

In order to evaluate the synchronization changes in different anesthetic states efficiently, we discussed the parameter selections of PS, NI and DET. We calculated these synchronization indexes under different parameters of all subjects and chose three datasets from each synchronization index in awake, unconscious and recovery states which were according to the time points of each subjects. The values of synchronization indexes under different parameters were shown in Fig. S1-S4. All values were given by median (Q1, Q3).

### 1. PS

Fig. S1 and Fig. S2 showed the  $PS_{PLV}(\delta, \theta, \alpha, \beta \text{ and } \gamma_1)$  and  $PS_{SE}(\delta, \theta, \alpha, \beta \text{ and } \gamma_1)$  values at different epoch length  $T_e$  in awake state (red), unconscious state (green) and recovery state (blue) of all subjects. It can be seen from Fig. S1 that the  $PS_{PLV}$  values of all frequency bands decreased with increasing  $T_e$ . The difference between awake and unconscious states of  $PS_{PLV}(\delta)$  were larger than  $PS_{PLV}$  in other frequency bands, which was also could be seen from Fig. 4F. By contrast,  $PS_{SE}$  had some fluctuation at different  $T_e$  (Fig. S2).  $T_e=20$  was used in our study.

“Fig. S1”

“Fig. S2”

### 2. NI

Fig. S3A showed the NI values with time lag  $\tau=1$ , nearest neighbors  $k=20$  in different embedding dimension  $m$  in awake state (red), unconscious state (green) and recovery state (blue) of all subjects. The NI values with  $\tau=2$ ,  $k=20$  in different  $m$  were shown in Fig. S3B. As can be seen from these two figures, NI increased monotonically with increasing  $m$  and the difference of NI values between awake, unconscious and recovery states became wider with increasing  $m$ . Therefore,  $m=5$  was selected in terms of calculation complexity. Fig. S3C showed NI values with  $m=5$ ,  $k=20$  in different  $\tau$ . The NI difference between awake and unconscious states became smaller with increasing  $\tau$ , so we chose  $\tau=1$ . The NI values with  $m=5$ ,  $\tau=1$  in different nearest neighbors  $k$  were shown in Fig. S3D and we selected  $k=20$ .

“Fig. S3”

### 3. DET

Fig. S4A, Fig. S4B and Fig. S4C showed DET values with embedding dimension  $m=3$ ,  $m=4$  and  $m=5$  respectively in threshold of diagonal length  $l_{min}=2$  in different time lag  $\tau$  in awake state (red), unconscious state (green) and recovery state (blue) of all subjects.  $m=3$ ,  $\tau=2$  were selected because of the great DET difference between awake and unconscious states. DET values with  $m=3$ ,  $\tau=2$  in different  $l_{min}$  were shown in Fig. S4D and  $l_{min}=2$  was selected.

“Fig. S4”

## Appendix B

We used the MATLAB programs *lagged.m* to compute COR, which can be downloaded from the Functional Connectivity Toolbox (<https://sites.google.com/site/functionalconnectivitytoolbox/>). The MATLAB programs of PS<sub>SE</sub> and PS<sub>CP</sub> (*nbt\_n\_m\_detection.m*) can be downloaded from the Neurophysiological Biomarker Toolbox ([https://www.nbtwiki.net/doku.php?id=tutorial:phase\\_locking\\_value#.VWm2zmgyG1B](https://www.nbtwiki.net/doku.php?id=tutorial:phase_locking_value#.VWm2zmgyG1B)). The MATLAB programs of KerMI (*FastPairMI.m*) can be downloaded from <http://pengqiu.gatech.edu/software/FastPairMI/index.htm>. The MATLAB program of NI (*synchro.m*) can be downloaded from <https://vis.caltech.edu/~rodri/software.htm>. The MATLAB programs of PCMI, PS<sub>PLV</sub>, DET and WTC are available by contacting the corresponding author.

# Figures

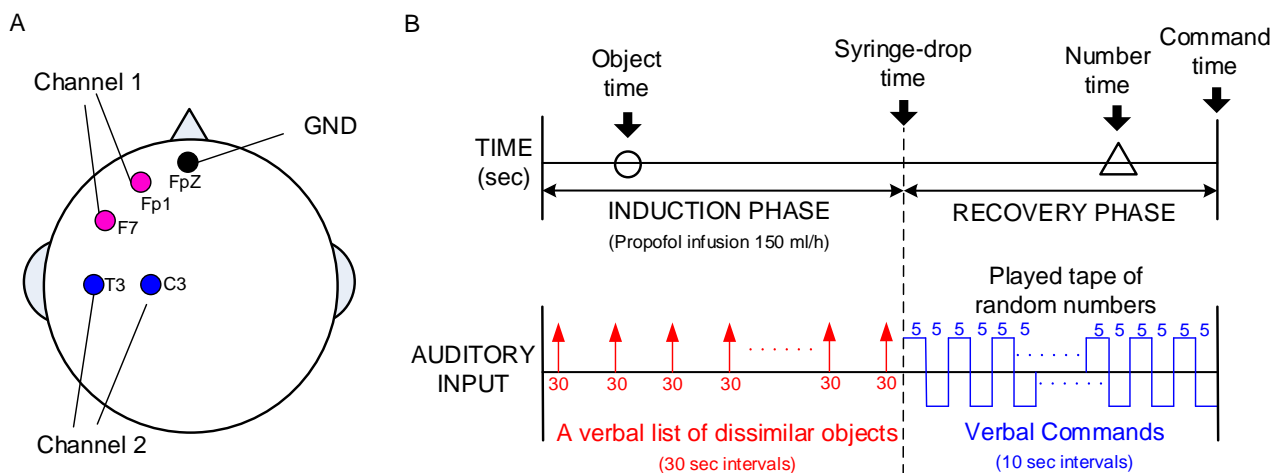


Fig. 1 (A) Positions of scalp electrodes at Fp1-F7 and C3-T3. (B) The diagram of experimental sequence. The “Object time” (circle), “Syringe-drop time”, “Number time” (triangle) and “Command time” were marked in the diagram. A verbal list of dissimilar objects was executed in 30-second intervals in the induction phase. The tape of random numbers was played and verbal commands were given in 10-second intervals in the recovery phase.

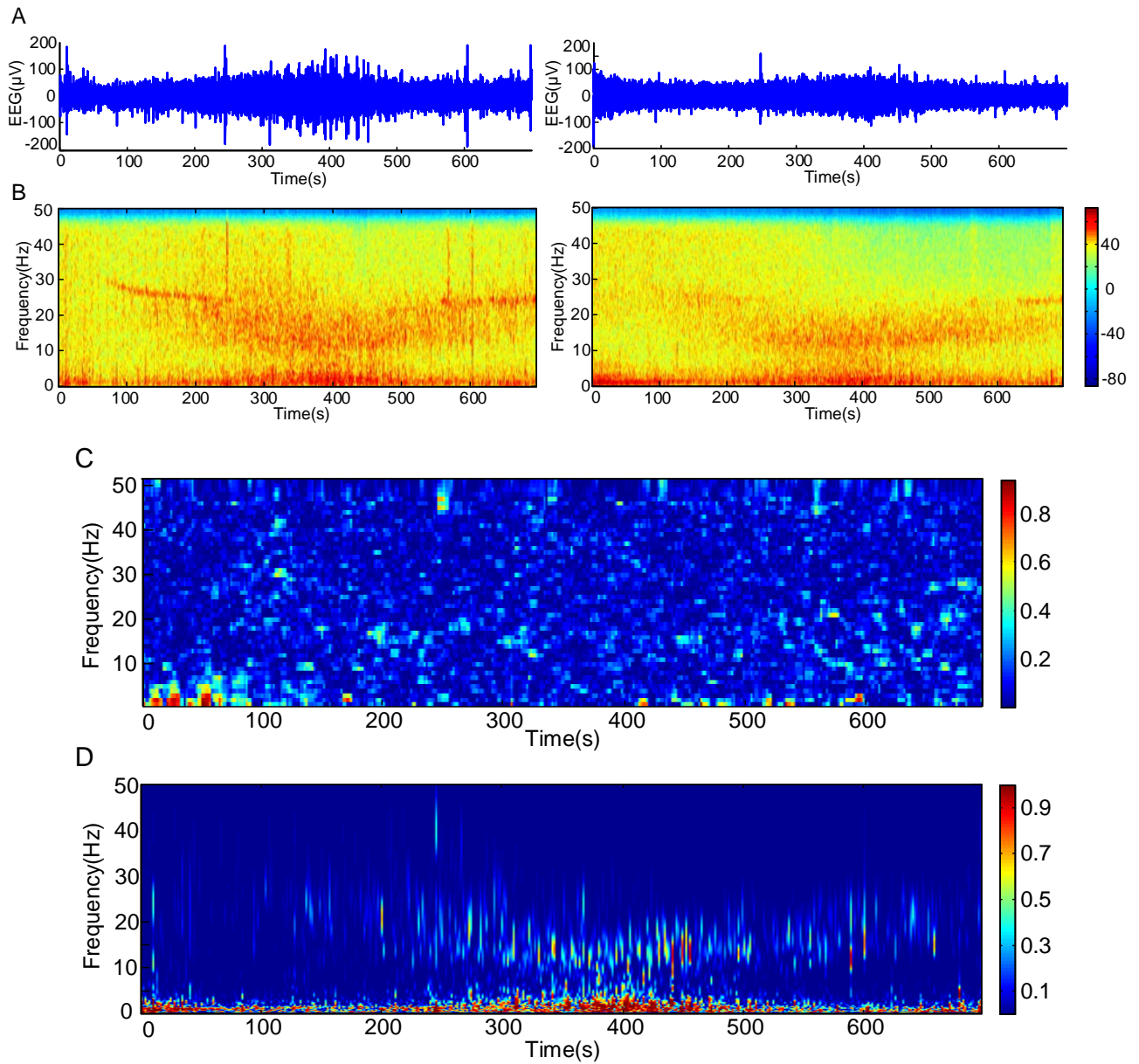


Fig. 2 (A) Two-channel preprocessed EEG recordings of one subject over the whole experiment period. (B) The spectrograms of the EEG recordings computed by a short-time Fourier transform. (C) The FTC spectrum of the two EEG recordings. (D) The WTC spectrum of the two EEG recordings.

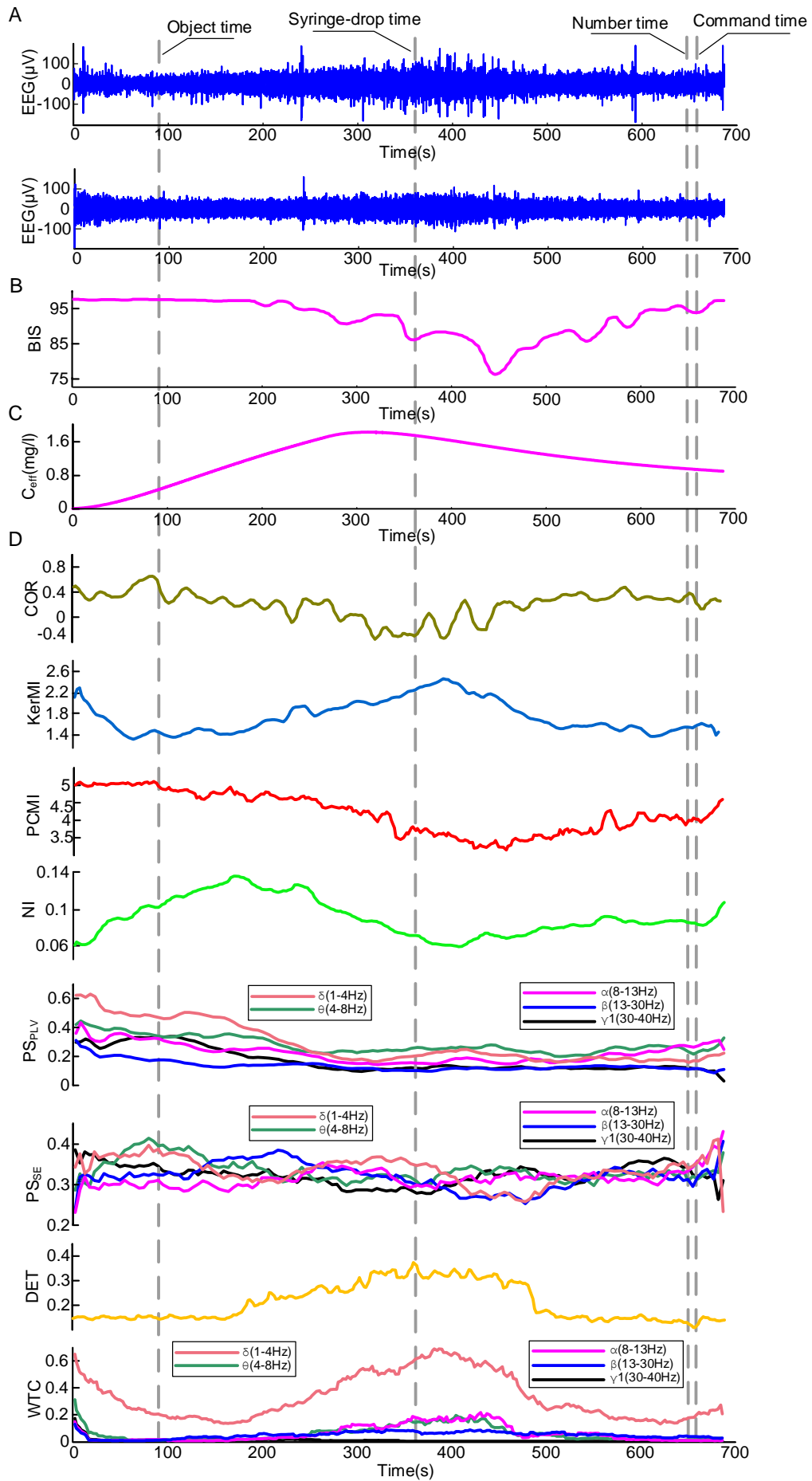


Fig. 3 (A) Two-channel preprocessed EEG recordings of one subject over the whole experiment period. (B) BIS value of the same subject. (C)  $C_{eff}$  value of the same subject. (D) The synchronization index values of the same subject. Four dashed gray lines denoted the four time points in the experiment.

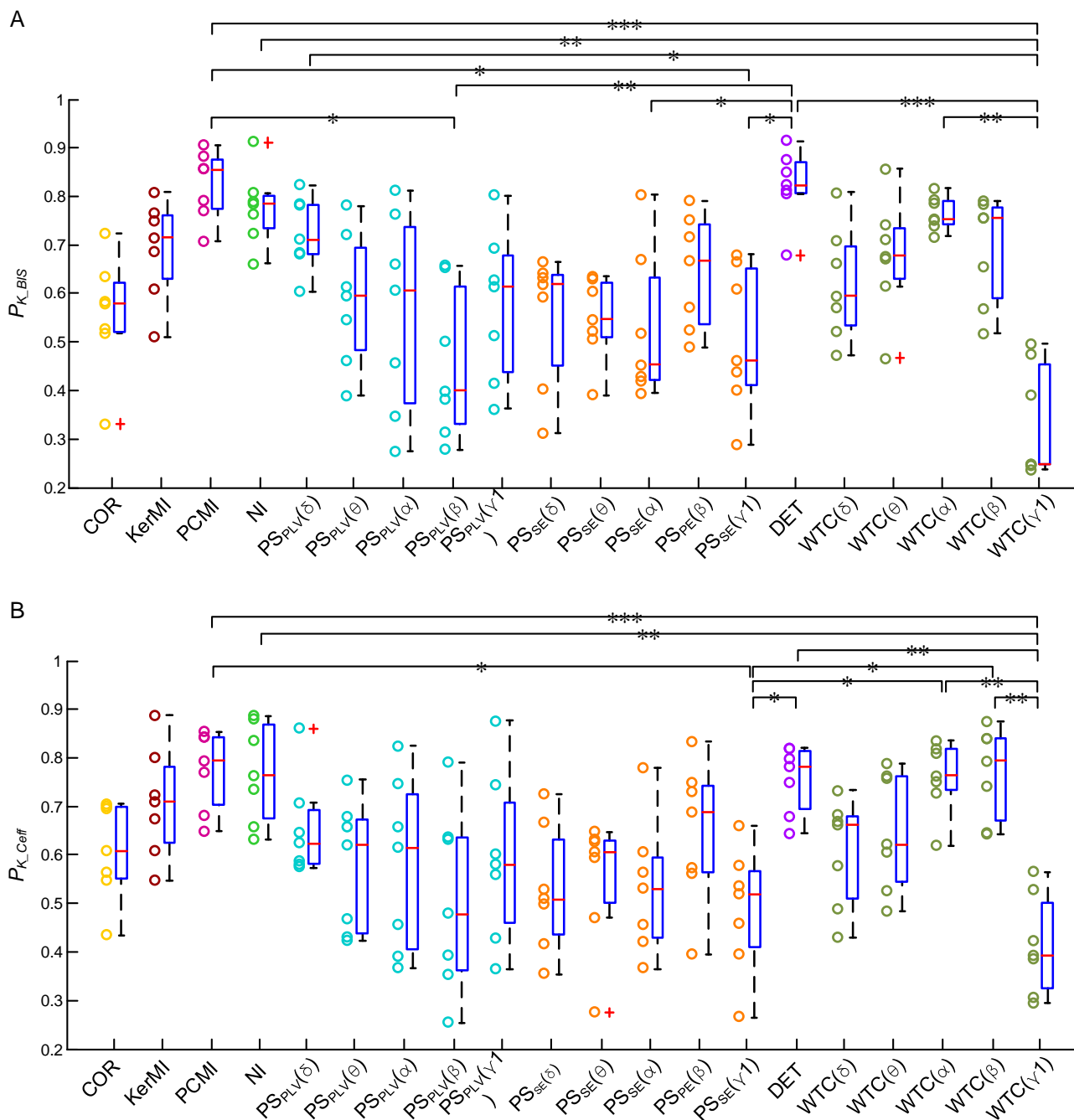


Fig. 4 (A) Prediction probability  $P_K$  values of synchronization indexes with BIS of all subjects. (B) The  $P_K$  values of synchronization indexes with  $C_{eff}$  of all subjects. The notation \*, \*\* and \*\*\* indicate significant difference at  $p < 0.05$ ,  $p < 0.01$  and  $p < 0.001$  respectively, through Friedman test and Multiple comparison test.

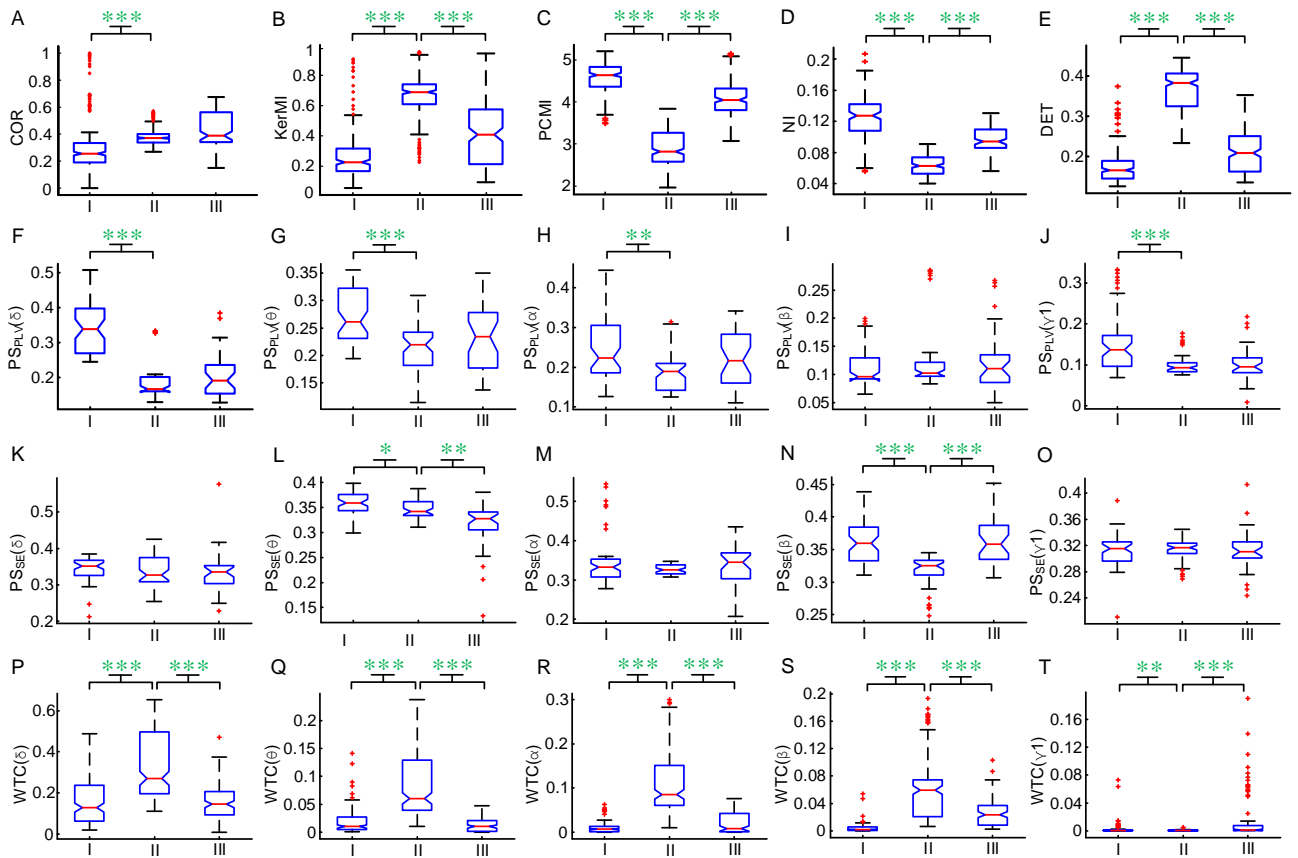


Fig. 5 Box plots of synchronization indexes in different studied periods (I: awake state, II: unconscious state, III: recovery state). The notation \*, \*\* and \*\*\* indicate significant difference at  $p < 0.05$ ,  $p < 0.01$  and  $p < 0.001$  respectively, through Kruskal-Wallis test and Multiple comparison test.

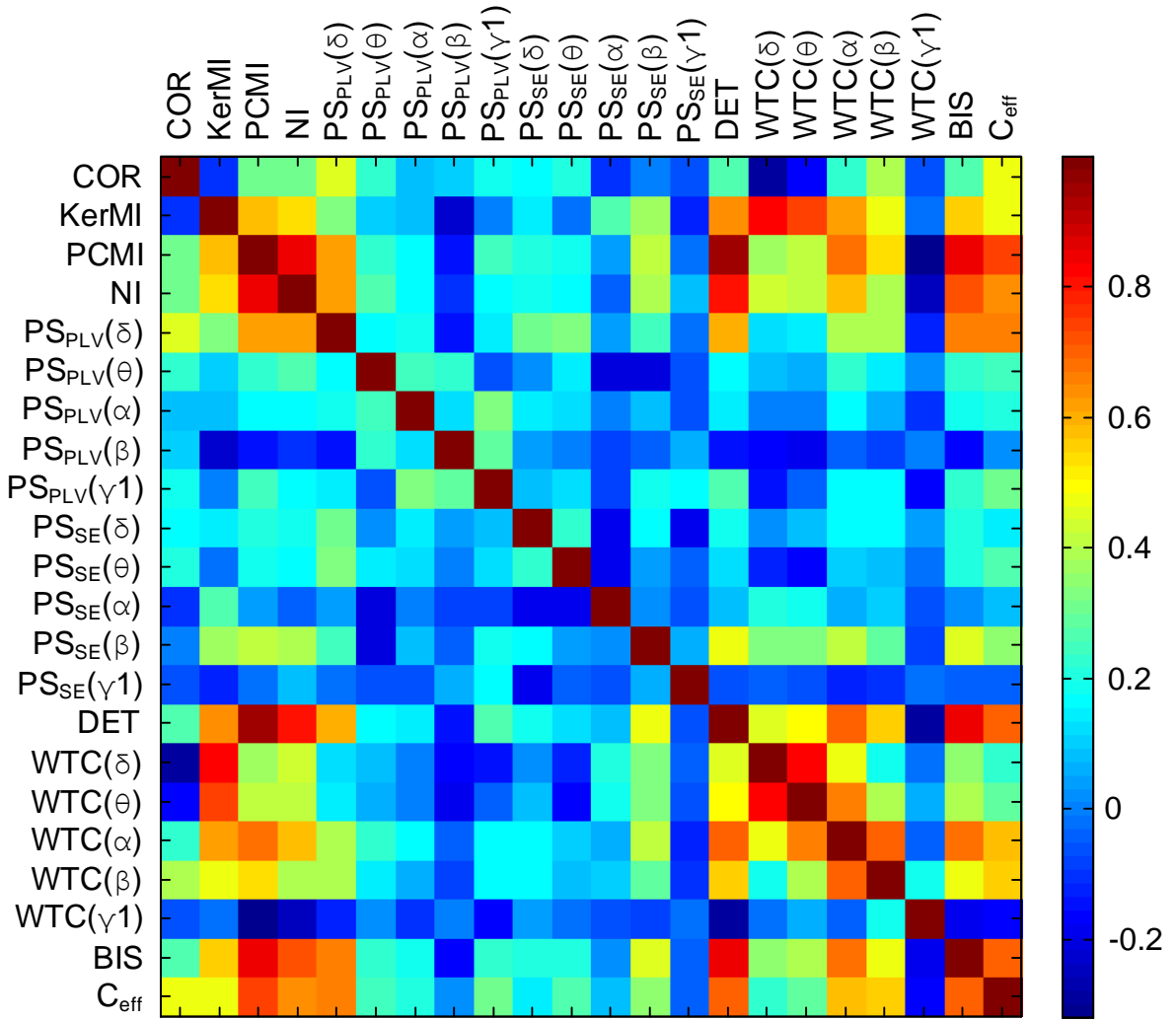


Fig. 6 Correlation coefficient  $R$  among synchronization indexes, BIS and  $C_{eff}$  averaged over all subjects.

## Tables

Table 1 The event times for each subject

Subject	“Object time” (s)	“Syringe-drop time”(s)	“Number time” (s)	“Command time” (s)
#1	180	283	435	475
#2	90	357	639	649
#3	90	421	792	802
#4	30	454	*	650
#5	90	202	*	545
#6	30	401	822	832
#7	90	355	560	570

“Object time” = the time point of the last object remembered for the subject during the induction phase.

“Syringe-drop time” = the time point that the subject dropped the syringe, denoting the end the induction and loss of consciousness.

“Number time” = the time point of the first number remembered during recovery.

\* Subjects who did not remember any number until responding to verbal command.

“Command time” = the time point corresponding to the subject’s correct response to verbal command.

Table 2 Median, Q1 and Q3 of  $P_K$  of different synchronization indexes with BIS and  $C_{eff}$

		COR	KerMI	PCMI	NI	PS <sub>PLV</sub> ( $\delta$ )	PS <sub>PLV</sub> ( $\theta$ )	PS <sub>PLV</sub> ( $\alpha$ )	PS <sub>PLV</sub> ( $\beta$ )	PS <sub>PLV</sub> ( $\gamma_1$ )	PS <sub>SE</sub> ( $\delta$ )
BIS	median	0.579	0.714	0.855	0.783	0.711	0.595	0.605	0.399	0.613	0.619
	Q1	0.519	0.629	0.775	0.734	0.681	0.482	0.373	0.331	0.438	0.450
	Q3	0.621	0.760	0.875	0.802	0.783	0.694	0.737	0.614	0.677	0.639
$C_{eff}$	median	0.607	0.709	0.794	0.764	0.624	0.621	0.615	0.479	0.580	0.509
	Q1	0.552	0.625	0.703	0.676	0.582	0.440	0.408	0.363	0.460	0.437
	Q3	0.699	0.781	0.842	0.868	0.692	0.672	0.725	0.636	0.708	0.633
		PS <sub>SE</sub> ( $\theta$ )	PS <sub>SE</sub> ( $\alpha$ )	PS <sub>SE</sub> ( $\beta$ )	PS <sub>SE</sub> ( $\gamma_1$ )	DET	WTC( $\delta$ )	WTC( $\theta$ )	WTC( $\alpha$ )	WTC( $\beta$ )	WTC( $\gamma_1$ )
BIS	median	0.545	0.453	0.667	0.460	0.823	0.594	0.677	0.753	0.755	0.248
	Q1	0.510	0.420	0.536	0.409	0.806	0.534	0.628	0.742	0.590	0.246
	Q3	0.622	0.632	0.743	0.650	0.869	0.697	0.734	0.790	0.777	0.453
$C_{eff}$	median	0.605	0.530	0.688	0.520	0.781	0.662	0.621	0.763	0.794	0.393
	Q1	0.502	0.430	0.561	0.411	0.695	0.511	0.546	0.733	0.670	0.327
	Q3	0.630	0.595	0.743	0.568	0.816	0.679	0.762	0.817	0.840	0.503

COR = cross correlation;

KerMI = mutual information based on kernel estimation;

PCMI = permutation cross mutual information;

NI = nonlinear interdependence;

PS<sub>PLV</sub> = phase synchronization based on phase locking value;

PS<sub>SE</sub> = phase synchronization based on Shannon entropy;

DET = determinism;

WTC = coherence based on wavelet transformation;

Table 3 CV (SD/mean) of the studied indexes at different anesthetic states

	Awake	Unconscious	Recovery
COR	0.1933/0.3056 $\approx$ 0.633	0.0711/0.3819 $\approx$ 0.186	0.1309/0.4375 $\approx$ 0.299
KerMI	0.1661/0.2654 $\approx$ 0.627	0.1547/0.6831 $\approx$ 0.227	0.2229/0.4071 $\approx$ 0.548
PCMI	0.3910/4.5818 $\approx$ 0.085	0.4223/2.9029 $\approx$ 0.146	0.4286/4.0663 $\approx$ 0.105
NI	0.0271/0.1231 $\approx$ 0.220	0.0105/0.0634 $\approx$ 0.165	0.0203/0.0971 $\approx$ 0.209
PS <sub>PLV</sub> ( $\delta$ )	0.0835/0.3444 $\approx$ 0.243	0.0527/0.1881 $\approx$ 0.280	0.0666/0.2065 $\approx$ 0.323
PS <sub>PLV</sub> ( $\theta$ )	0.0490/0.2684 $\approx$ 0.183	0.0560/0.2133 $\approx$ 0.263	0.0612/0.2334 $\approx$ 0.262
PS <sub>PLV</sub> ( $\alpha$ )	0.0857/0.2448 $\approx$ 0.350	0.0552/0.1905 $\approx$ 0.290	0.0682/0.2210 $\approx$ 0.309
PS <sub>PLV</sub> ( $\beta$ )	0.0369/0.1131 $\approx$ 0.326	0.0627/0.1279 $\approx$ 0.490	0.0584/0.1217 $\approx$ 0.480
PS <sub>PLV</sub> ( $\gamma_1$ )	0.0735/0.1495 $\approx$ 0.491	0.0258/0.1011 $\approx$ 0.255	0.0438/0.1025 $\approx$ 0.427
PS <sub>SE</sub> ( $\delta$ )	0.0326/0.3436 $\approx$ 0.095	0.0477/0.3378 $\approx$ 0.141	0.0620/0.3356 $\approx$ 0.185
PS <sub>SE</sub> ( $\theta$ )	0.0230/0.3598 $\approx$ 0.064	0.0206/0.3475 $\approx$ 0.059	0.0548/0.3098 $\approx$ 0.177
PS <sub>SE</sub> ( $\alpha$ )	0.0622/0.3453 $\approx$ 0.180	0.0125/0.3260 $\approx$ 0.038	0.0521/0.3362 $\approx$ 0.155
PS <sub>SE</sub> ( $\beta$ )	0.0322/0.3604 $\approx$ 0.089	0.0250/0.3173 $\approx$ 0.079	0.0348/0.3623 $\approx$ 0.096
PS <sub>SE</sub> ( $\gamma_1$ )	0.0256/0.3116 $\approx$ 0.082	0.0181/0.3133 $\approx$ 0.058	0.0324/0.3139 $\approx$ 0.103
DET	0.0398/0.1758 $\approx$ 0.226	0.0503/0.3651 $\approx$ 0.138	0.0570/0.2115 $\approx$ 0.269
WTC( $\delta$ )	0.1119/0.1637 $\approx$ 0.684	0.1568/0.3272 $\approx$ 0.479	0.0958/0.1506 $\approx$ 0.636
WTC( $\theta$ )	0.0211/0.0175 $\approx$ 1.206	0.0617/0.0830 $\approx$ 0.743	0.0128/0.0131 $\approx$ 0.981
WTC( $\alpha$ )	0.0146/0.0109 $\approx$ 1.334	0.0751/0.1065 $\approx$ 0.705	0.0230/0.0206 $\approx$ 1.118
WTC( $\beta$ )	0.0063/0.0039 $\approx$ 1.595	0.0437/0.0595 $\approx$ 0.733	0.0228/0.0278 $\approx$ 0.822
WTC( $\gamma_1$ )	0.0080/0.0028 $\approx$ 2.89	0.0009/0.0007 $\approx$ 1.356	0.0317/0.0153 $\approx$ 2.077

The meaning of the indexes refers to the legend of Table 2



## II

### **SYNCHRONIZATION MEASURES IN EEG SIGNALS**

by

Zhenhu Liang, Yang Bai & Ye Ren 2016

In Signal Processing in Neuroscience, Springer, 167-202

DOI: [https://doi.org/10.1007/978-981-10-1822-0\\_9](https://doi.org/10.1007/978-981-10-1822-0_9)

Reproduced with kind permission by Springer Nature.

## Chapter 9 Synchronization Measures in EEG Signals

Zhenhu Liang<sup>1,2</sup>, Yang Bai<sup>1,2</sup>, Ye Ren<sup>1,2</sup>, Logan J. Voss<sup>3</sup>, Jamie W. Sleight<sup>3</sup>, Xiaoli Li<sup>4,5</sup>

### **Affiliations:**

<sup>1</sup> Institute of Electric Engineering, Yanshan University, Qinhuangdao 066004, China

<sup>2</sup> Key Laboratory of Industrial Computer Control Engineering of Hebei Province, Yanshan University, Qinhuangdao 066004, China

<sup>3</sup> Department of Anaesthesia, Waikato Hospital, Hamilton, New Zealand

<sup>4</sup> State Key Laboratory of Cognitive Neuroscience and Learning & IDG/McGovern Institute for Brain Research, Beijing Normal University, Beijing, China

<sup>5</sup> Center for Collaboration and Innovation in Brain and Learning Sciences, Beijing Normal University, Beijing, China

## 9.1 Introduction

Synchronization measures have been widely used in many scientific and technical disciplines. Particularly, Synchronization phenomena has become an important feature in understanding mechanism of normal <sup>[1-3]</sup> or abnormal <sup>[4]</sup> brain functions. And it is found that synchronization between neuronal populations plays a key role in information processing in the brain <sup>[5-8]</sup>.

So far, there exist many synchronization detection methods, such as cross correlation, coherence, mutual information, phase synchronization and event synchronization, and they have been proposed to quantify the degree of synchronization in different neural system. These synchronization measures have been proved effective in epileptic seizure prediction, detection <sup>[9-11]</sup>, Alzheimer <sup>[12, 13]</sup> and autism <sup>[14]</sup> detection and assessment. Also, synchronization measures were used to explore consciousness state related mechanisms, such as sleep <sup>[15, 16]</sup> and anesthesia <sup>[17, 18]</sup>.

The theoretical foundations are different for different synchronization methods. When investigate different brain function or attempt to understand mechanisms of different brain disease, it was difficult to give an unified criteria for synchronization methods selection. In this chapter, we gave an example of using different synchronization measures to understand mechanism of anesthesia effect on the brain. And evaluated performance of these synchronization measures in distinguishing the state of anesthesia.

How general anesthetic agents induce unconsciousness in the central nervous system may provide a direction for future rational anesthetic drug design and improved

intraoperative monitoring <sup>[19]</sup>. Over the last decade, many theories have been proposed to explain the mechanism of consciousness, such as the cognitive binding. A number of recent studies gave evidence that breakdown of long-distance cortical connectivity across multiple brain regions in particular frontal-parietal cortices may play an critical role in loss of consciousness (LoC) <sup>[20-23]</sup>. At the same time, many different signal processing methods based on different information theories have been proposed to quantify neuro-synchrony <sup>[24-27]</sup>.

In this chapter, we systematically investigate changes in electroencephalogram (EEG) synchrony during anesthesia induced by propofol, using a range of different synchrony measures. The aim is to evaluate various information coupling measures for separating different anesthesia states. Some novel synchrony measures, and several methods proposed in our previous work, are used. Among these, cross correlation (COR) is probably the most commonly applied method. Coherence and phase synchronization (PS) are based on the frequency domain, while wavelet coherence (WTC) is based on time-frequency domain. Mutual information (MI) is based on information theory. Nonlinear interdependence (NI) and cross recurrence analysis are based on state space theory.

Any future practical monitor of anesthesia must be quick, robust and operable. Therefore, unlike most studies which incorporate many channels <sup>[28]</sup>, we only considered synchronization and information coupling between two channels of EEG. In this chapter, we concentrated on the coupling between prefrontal and primary motor cortices. In order to compare their properties within the same context, we

applied the synchronization methods to the same EEG data set with a range of depth of anesthesia states: awake, unconsciousness and recovery of consciousness (RoC). To validate the relative effectiveness of these synchronization algorithms, we evaluated performance of each algorithm on modeling pharmacokinetic/pharmacodynamic (PK/PD) drug effects. We quantified the correlation coefficients ( $R_{ij}$ ) between each synchrony measure and the Bispectral Index (BIS), the prediction probability ( $P_k$ ) of each measure with the BIS and with effect-site propofol concentration (ESPC). Our goal is to demonstrate the most effective measure in clinical anesthetic depth evaluation, and to further our understanding the underlying neurophysiological mechanisms of anesthesia.

Different approaches for measuring synchronization rely on certain characteristic features of the dynamical system under investigation. However, the underlying dynamic properties of the experimental data are usually not completely known. Therefore, it is important to validate the measures against model systems where the synchrony of the underlying dynamics are known and can be artificially manipulated [29]. Therefore, we adopted three coupled model systems with different properties to evaluate the performance of each method for tracking coupling strength.

This chapter is organized as follows. Section 2 describes each synchronization measure and its parameters selection. Section 3 gives simulation model and the EEG recording, preprocessing and evaluation methods, as well the results of the applications of the synchronization measures to the model and real EEG. Finally, the conclusions are given in Sect. 4.

## 9.2 Synchronization measures

### 9.2.1 Cross correlation

The cross correlation is a classical and simple measure of the interdependence between two time series. It can be used to evaluate the linear relationship between two variables  $X$  and  $Y$  based on a delay time  $\tau$ , which may reflect a causal relationship between the signals. The calculation of the cross correlation is described in the following. Given two time series, if  $x(t)$  and  $y(t)$  are signals normalized to have zero mean and unit variance, their cross-correlation function is:

$$C_{xy}(\tau) = \frac{1}{N - \tau} \sum_{t=1}^{N-\tau} x(t + \tau)y(t) \quad (1)$$

where  $N$  is the total number of samples and  $\tau$  is the time lag between the signals.

The details of this method can be found in [30]. There are two parameters that affect the value: data length  $N$  and delay time  $\tau$ . Because of the lack of evaluation criteria, it is very difficult to select appropriate parameters in practical applications and many are based on experiments. In this chapter, for the parameters selection process refer to **Appendix A**.

### 9.2.2 Cross coherence

Coherence is a popular method for detecting neuronal sources that are working together in a spatially distributed network and to determine how strongly they collaborate [31]. It is a frequency domain based method which measures the linear correlations of two time series [32]. We considered two coherence calculation methods: coherence based on Fourier transformation (FTC) and wavelet transformation.

Given two time series  $x$  and  $y$ , subdivide into  $M$  segments of equal length  $L$ .

The basic coherence function is computed by averaging over these segments. The coherence function with magnitude square  $C_{xy}(f)$  is described by

$$C_{xy}(f) = \frac{\left| \langle X(f)Y^*(f) \rangle \right|^2}{\langle X(f) \rangle \langle Y(f) \rangle} \quad (2)$$

where  $X(f)$ ,  $Y(f)$  are the Fourier transforms of time series  $x$  and  $y$  respectively.  $Y^*$  denotes the complex conjugate of  $Y$ ,  $\langle X(f) \rangle$  is the average of  $X(f)$  computed over the  $M$  segments, similar to  $\langle Y(f) \rangle$  and  $\langle X(f)Y^*(f) \rangle$ .  $|Y|$  stands for the magnitude of  $Y$ .

Similar to FTC, the Wavelet coherence function calculates the ratio of the cross spectrum to the product of the auto-spectrum of the two series  $x$  and  $y$ , which is defined as

$$(C^w(s, \tau))^2 = \frac{|S_{xy}^w(s, \tau)|^2}{S_{xx}^w(s, \tau)S_{yy}^w(s, \tau)} \quad (3)$$

where  $S_{xy}^w(s, \tau)$  is the localized power spectrum, it is

$$S_{xy}^w(s, \tau) = \frac{1}{s \int_T W_x(s, \tau)W_y^*(s, \tau)d\tau}, T = [\tau - \Delta\tau, \tau + \Delta\tau] \quad (4)$$

Here  $T$  is selected based on the time resolution desired in the coherence map. And the auto-spectrum  $S_{xx}^w(s, \tau)$  and  $S_{yy}^w(s, \tau)$  are defined similar to  $S_{xy}^w(s, \tau)$ .

The power spectrum is calculated based on the Morlet wavelet transform (MWT). The details are described in [33]. The normalized average synchronization based on the coherence of signals  $x$  and  $y$  at a frequency band  $[f_L, f_H]$  is defined by

$$d_{xy} = \frac{1}{N_w} \sum_{w=f_L}^{f_H} H_{xy}(f) \quad (5)$$

where  $H_{xy}(f)$  could be replaced by the  $C_{xy}(f)$  or  $C^w(s, \tau)$ .  $N_w$  is the number of

summands in the summation, so the synchronization value of  $d_{xy}$  is between 0 and 1<sup>[34]</sup>.

The WTC index was calculated across five frequency bands:  $\delta(1-4Hz)$ ,  $\theta(4-8Hz)$ ,  $\alpha(8-13Hz)$ ,  $\beta(13-30Hz)$  and  $\gamma(30-40Hz)$ .

### 9.2.3 Phase synchronization

Phase synchrony analysis has been independently proposed by Lachaux et al.<sup>[35]</sup> and Mormann et al.<sup>[36]</sup> and applied later by Allefeld and Kurths<sup>[37, 38]</sup>. This approach is based on the concept of synchronization of chaotic oscillators studied by Rosenblum et al.<sup>[39]</sup>. Phase synchronization is sensitive to nonlinear coupling<sup>[40]</sup> and is a promising tool for quantifying coupling in multi-channel electroencephalogram or magnetoencephalogram (MEG) recordings<sup>[40-42]</sup> and may be helpful for understanding communication mechanisms in the brain<sup>[33, 43, 44]</sup>.

There are various PS estimation methods, however two steps are fundamental: instantaneous phase estimation and phase locking quantification. Li et al employed the windowed harmonic wavelet transform (WHWT) to extract the instantaneous phase of brain signals, and shows that WHWT performs better than traditional methods, such as the Hilbert transform (HT)<sup>[45]</sup>. So we chose WHWT to calculate the instantaneous phase in this study. The algorithm is described as follows.

Consider two time series  $x(t)$  and  $y(t)$ , the Fourier transform is used to achieve the corresponding expressions in the frequency domain,  $X(f)$  and  $Y(f)$ . Then, multiply  $X(f)$  by the conjugate of the windowed harmonic wavelet  $W_w(f)$  denoted as  $A(f) = X(f)W_w^*(f)$ . Take the inverse Fourier transform of  $A(f)$  to

obtain the signal with WHWT denoted by  $a(t)$ , as presented by <sup>[46]</sup>

$$a(t) = u(t) + jH[u(t)] = u(t) + \frac{j}{\pi} \int_{-\infty}^{\infty} \frac{u(\tau)}{t - \tau} d\tau = S(t)e^{j\phi(t)} \quad (6)$$

where  $H[\cdot]$  stands for the operation of Hilbert transform. The magnitude is represented as  $S(t) = \sqrt{(u(t))^2 + (H[u(t)])^2}$ , and the instantaneous phase of  $a(t)$  is

$$\phi(t) = \tan^{-1}\left(\frac{H[u(t)]}{u(t)}\right) = \tan^{-1}\left(\frac{\text{imag}[a(t)]}{\text{real}[a(t)]}\right) \quad (7)$$

The phase difference can be defined with the instantaneous phase  $\varphi_x(t)$  and  $\varphi_y(t)$  (achieved through the WHWT of the scalar observations  $x(t)$  and  $y(t)$ ):

$$\Delta\varphi_{xy}(t) = \varphi_x(t) - \varphi_y(t) \quad (8)$$

There are mainly three PS calculation methods used. Among them, phase locking value (PLV) <sup>[47]</sup> is based on time windows with a specified length  $N$ . Here, we denote it as PS\_PLV:

$$PS\_PLV = \frac{1}{N} \left| \sum_{t=1}^N e^{j\Delta\varphi_{xy}} \right| \quad (9)$$

where the PS\_PLV is bound between 0 and 1.

Another method is based on Shannon entropy (PS\_SE). It can be defined as:

$$PS\_SE = \frac{S_{\max} - S}{S_{\max}} \quad (10)$$

where  $S = -\sum_{k=0}^N p_k \ln p_k$  is the entropy of the distribution of the cyclic relative phase  $\Psi = \Delta\varphi_{xy} \bmod 2\pi$ . And  $S_{\max} = \ln N$ , where  $N$  is the number of bins used for the distribution. The optimum of bins ( $N$ ) is set as  $e^{0.626+0.41\ln(L-1)}$ , where  $L$  is the number of data points. The range of  $PS\_SE$  is between 0 and 1.

The third PS measure is based on conditional probability (PS\_CP) and is described as follows:

Divide the interval  $[0, 2\pi]$  into  $n$  bins and denote the values of  $\varphi_x \bmod 2\pi$  falling into the  $l$ -th bin as  $\theta_l$  and the number of points within this bin as  $M_l$ . Then, compute the  $M_l$  corresponding values  $\eta_{ij} = \varphi_y \bmod 2\pi |_{\varphi_x \bmod 2\pi = \theta}$ , where  $i = 1 \cdots M_l$ . Last, we average over all  $n$  bins  $\Lambda_l = 1/M_l \sum_{i=1}^{M_l} e^{i\eta_{l,i}}$  and get the synchronization index

$$PS\_CP = 1/n \sum_{l=1}^n |\Lambda_l| \quad (11)$$

In this study, we divide the EEG data into five frequency bands:  $\delta$ ,  $\theta$ ,  $\alpha$ ,  $\beta$  and  $\gamma$ . The PS indices were calculated in each frequency bands with time epochs ( $T_e$ ). Appendix B gives the discussion of the effect of epoch lengths on each PS indexes.

#### 9.2.4 Mutual information based on kernel estimation (KerMI)

The mutual information is a widely used nonlinear measure with calculating the interdependence between variables.

The mutual information between two discrete random variables  $x(t)$  and  $y(t)$  ( $t = 1, 2, \dots, N$ ) calculated with marginal probabilities  $p_x(x)$  and  $p_y(y)$ , and joint probability  $p_{xy}(x, y)$ , which is defined as

$$I(x, y) = \sum_{x, y} p_{xy}(x, y) \log \frac{p_{xy}(x, y)}{p_x(x)p_y(y)} \quad (12)$$

The most straightforward approach for estimating probability is partitioning  $x(t)$  and  $y(t)$  into  $K$  ( $k = 1, 2, \dots, K$ ) bins of finite size, and counting the numbers of points falling into the each bins. The number of points within the bin are denoted as  $Q_x(k)$ ,  $Q_y(k)$  and  $Q_{xy}(k)$ . Then, the probabilities can be denoted as

$$p_x = \frac{Q_x(k)}{N}, p_y = \frac{Q_y(k)}{N} \text{ and } p_{xy} = \frac{Q_{xy}(k)}{N}.$$

Kernel techniques is an attractive alternative to binning a distribution which is discussed thoroughly in [48]. Rather than simply counting the points, we can determine the distance-dependent weight of each point by using kernel function. Then, the marginal probability density and joint probability density which are estimated by the Gaussian kernel estimator [49] can be denoted as [50],

$$p_x(x) = \frac{1}{N} \frac{1}{\sqrt{2\pi h^2}} \sum_{t=1}^N e^{-\frac{1}{2h^2}(x-x_t)^2}, \quad p_y(y) = \frac{1}{N} \frac{1}{\sqrt{2\pi h^2}} \sum_{t=1}^N e^{-\frac{1}{2h^2}(y-y_t)^2} \quad (13)$$

$$p_{xy}(x, y) = \frac{1}{N} \frac{1}{2\pi h^2} \sum_{t=1}^N e^{-\frac{1}{2h^2}((x-x_t)^2+(y-y_t)^2)} \quad (14)$$

where parameter  $h$  is called window width of the kernels.

Last, we obtain the mutual information based on kernel estimation,

$$KerMI = \frac{1}{N} \sum_{t=1}^N \log \left[ \frac{p_{xy}(x, y)}{p_x(x)p_y(y)} \right] \quad (15)$$

The approximately optimal window width  $h$  is given by  $h_{opt} \approx \sigma \left( \frac{4}{d+2} \right)^{1/(d+4)} N^{-1/(d+4)}$

with  $d=2$  being the dimension of Gaussian kernel estimation and  $\sigma$  the average marginal SD [48].

### 9.2.5 Permutation cross mutual information (PCMI)

Recently, the permutation analysis and conditional mutual information were integrated to estimate the coupling direction between two cardiorespiratory series [51].

Then PCMI was proposed with integration of permutation analysis and cross mutual information.

Given a time series  $x_t$  ( $t = 1, 2, \dots$ ), form the embedding vector  $X_t[x_t, x_{t+\tau}, \dots, x_{t+m\tau}]$  with the embedding dimension  $m$  and lag  $\tau$ . Then, arrange the vector  $X_t$  in an increasing order as a symbol of vectors:  $[x_{t+(j_1-1)\tau} \leq x_{t+(j_2-1)\tau} \leq \dots \leq x_{t+(j_m-1)\tau}]$ . For  $m$  dimensions, there will be  $m!$  permutations and each vector  $X_t$  in  $m$ -dimensional

space can be mapped to one of the  $m!$  permutations. Next, the probability distribution of permutations in the symbol sequences can be calculated, denoted  $p_1, p_2, \dots, p_k$ , where  $k \leq m!$ .

Based on the permutation probability distribution of  $X$  and  $Y$ , the permutation entropy  $H(X)$  and  $H(Y)$  can be calculated. And the joint entropy of  $H(X, Y)$  from the cross-probability distribution is described as

$$H(X, Y) = - \sum_{x \in X} \sum_{y \in Y} p(x, y) \log p(x, y) \quad (16)$$

where  $p(x, y)$  is the joint probability distribution of  $X$  and  $Y$ .

The PCMI requires three parameters to be defined before application: the embedded dimension  $m$ , the lag  $\tau$ , and the epoch length. Previous studies found that at a sample rate of 100 Hz,  $m = 6$ ,  $\tau = 1$  and epoch length of 1000 resulted in the best PCMI performance <sup>[52]</sup>. Therefore we use  $m = 6$ ,  $\tau = 1$ , epoch=1000 for calculation of PCMI in this study.

### 9.2.6 Nonlinear interdependence

Nonlinear interdependence provides a measure of generalized synchronization in nonlinear systems, namely the interdependence according to the distance of delay vectors in bivariate data. It was demonstrated that nonlinear interdependence can not only compute the coupling strength but also indicate the coupling direction <sup>[53-55]</sup>.

In the study of <sup>[56]</sup>, nonlinear interdependence was used to disclose the coupling information of two EEG recordings in rats. The details of the algorithm are described as follows:

Two time series are treated as two systems  $X$  and  $Y$ , with embedding dimension

$m$  and time lag  $\tau$ . Then reconstruct the delay vectors  $X_n = (x_n, \dots, x_{n-(m-1)\tau})$  and  $Y_n = (y_n, \dots, y_{n-(m-1)\tau})$ . Defining  $r_{n,j}$  and  $s_{n,j}$ ,  $j = 1, \dots, k$  as the time indices of the  $k$  nearest neighbors of  $X_n$  and  $Y_n$ , respectively.

The mean squared Euclidean distance to its  $k$  neighbors for each  $X_n$  is defined as

$$R_n^{(k)}(X) = \frac{1}{k} \sum_{j=1}^k (X_n - X_{r_{n,j}})^2 \quad (17)$$

The Y-conditioned mean squared Euclidean distance is defined using the time partners of the closest neighbors of  $Y_n$  replacing the nearest neighbors' indices,

$$R_n^{(k)}(X|Y) = \frac{1}{k} \sum_{j=1}^k (X_n - X_{s_{n,j}})^2 \quad (18)$$

There are three interdependence measures defined in the Refs<sup>[53, 56]</sup>. The first is  $S^{(k)}(X|Y)$ , described as

$$S^{(k)}(X|Y) = \frac{1}{N} \sum_{n=1}^N \frac{R_n^{(k)}(X)}{R_n^{(k)}(X|Y)} \quad (19)$$

When the elements in  $X_n$  have an average squared radius, then  $R(X) = 1/N \sum_{n=1}^N R_n^{(N-1)}(X)$ . If the systems are highly correlated, we get  $R_n^{(k)}(X|Y) \approx R_n^{(k)}(X) \leq R(X)$ . While  $R_n^{(k)}(X|Y) \approx R(X) \geq R_n^{(k)}(X)$ , if they are independent. Since  $R_n^{(k)}(X|Y) \geq R_n^{(k)}(X)$  by construction, we have  $0 < S^{(k)}(X|Y) \leq 1$ .

A low value of  $S^{(k)}(X|Y)$  indicates the two series are independent, while high value indicates the two series are synchronous.

The second interdependence measure  $H^{(k)}(X|Y)$  is defined as

$$H^{(k)}(X|Y) = \frac{1}{N} \sum \log \frac{R_n(X)}{R_n^{(k)}(X|Y)} \quad (20)$$

The third interdependence measure is the normalized method, defined as

$$N^{(k)}(X|Y) = \frac{1}{N} \sum_{n=1}^N \frac{R_n(X) - R_n^{(k)}(X|Y)}{R_n(X)} \quad (21)$$

In this study, the  $S^{(k)}(X|Y)$ ,  $H^{(k)}(X|Y)$ ,  $N^{(k)}(X|Y)$  indices were calculated, and the parameter selection is discussed in **Appendix C**.

### 9.2.7 Cross recurrence analysis

Cross recurrence analysis was introduced to examine the intricate recurrent structuring between paired signals which were also time delayed and embedded in higher dimensional space <sup>[57]</sup>.

Considering two time series  $x(t)$  and  $y(t)$ , the cross recurrence plot (CRP), which is a bivariate extension of the recurrence plot (RP), is introduced to analyze the dependencies between two different systems <sup>[58, 59]</sup>. Similar to the RP, the cross recurrence matrix is defined by

$$CR_{i,j}^{\vec{x},\vec{y}}(\varepsilon) = \Theta(\varepsilon - \|\vec{x}_i - \vec{y}_j\|), i = 1, \dots, N, j = 1, \dots, N \quad (22)$$

where  $N$  is the number of measured points  $\vec{x}_i$  or  $\vec{y}_j$ ,  $\varepsilon$  is a threshold distance.  $\Theta(\cdot)$  is the Heaviside function ( i.e.  $\Theta(x) = 0$ , if  $x < 0$ , and  $\Theta(x) = 1$  otherwise) and  $\|\cdot\|$  is a norm function.

There are various ways of quantifying the RP, such as recurrence rate, determinism (DET), Laminarity and Entropy of diagonal length (ENTR). In this study, the DET index was used to evaluate the synchronization of the two systems.

Stochastic behavior causes none or short diagonals, whereas deterministic behavior causes longer diagonals and fewer single, isolated recurrence points. The DET calculates the ratio of recurrence points that form diagonal structures (of at least

length  $l$  min) to all recurrence points, which can characterize the behavior of the nonlinear system, and is defined by

$$DET = \frac{\sum_{l=l_{\min}}^l IP(l)}{\sum_{l=1}^l IP(l)} \quad (23)$$

where  $P(l)$  is the frequency distribution of the lengths of the diagonal structures in the CRP.  $l_{\min}$  is the threshold, which excludes the diagonal lines which are formed by the tangential motion of the phase space trajectory. For  $l_{\min} = 1$ , the determinism is one.

The selection of the parameters for DET is detailed in **Appendix D**.

## 9.3 Simulation and Results

### 9.3.1 Simulation Model and real EEG recordings

In our analysis, we used the time series  $x_1$  and  $y_1$  (length of 4096) generated from three coupled model systems to compare the synchronization measures.

The first model system consisted of two coupled Hénon maps, as proposed in <sup>[60]</sup>. The equations of motion for the driver and the responder are:

$$\begin{aligned} x_{1,n+1} &= 1.4 - x_{1,n}^2 + b_x x_{2,n} \\ x_{2,n+1} &= x_{1,n} \\ y_{1,n+1} &= 1.4 - (C x_{1,n} y_{1,n} + (1 - C) y_{1,n}^2) + b_y y_{2,n} \\ y_{2,n+1} &= y_{1,n} \end{aligned} \quad (24)$$

The parameters were set to  $b_x = b_y = 0.3$  to yield identical systems with a sampling interval of 1. The coupling strength  $C$  was varied from 0 to 0.8 in steps of 0.01.

The second system employed two coupled Rössler systems <sup>[61]</sup>. The equations of motion of this coupling model are:

$$\begin{aligned}
\dot{x}_1 &= -w_x x_2 - x_3 \\
\dot{x}_2 &= w_x x_1 + 0.15 x_2 \\
\dot{x}_3 &= 0.2 + x_3(x_1 - 10) \\
\dot{y}_1 &= -w_y y_2 - y_3 + C(x_1 - y_1) \\
\dot{y}_2 &= w_y y_1 + 0.15 y_2 \\
\dot{y}_3 &= 0.2 + y_3(y_1 - 10)
\end{aligned} \tag{25}$$

The equations were integrated using Runge-Kutta 4th order with a sampling interval of 0.3. A parameter mismatch between the two systems was introduced by setting  $w_x = 0.95$  and  $w_y = 1.05$ . The coupling strength  $C$  was varied from 0 to 2 in steps of 0.025.

The third system adopted two Lorenz systems <sup>[29]</sup>. The equations of motion of this coupling model are:

$$\begin{aligned}
\dot{x}_1 &= 10(x_2 - x_1) \\
\dot{x}_2 &= x_1(28 - x_3) - x_2 \\
\dot{x}_3 &= x_1 x_2 - \frac{8}{3} x_3 \\
\dot{y}_1 &= 10(y_2 - y_1) \\
\dot{y}_2 &= y_1(28.001 - y_3) - y_2 \\
\dot{y}_3 &= y_1 y_2 - \frac{8}{3} y_3 + C(x_3 - y_3)
\end{aligned} \tag{26}$$

The equations were integrated using Runge-Kutta 4th order with a sampling interval of 0.01. The coupling strength  $C$  was varied from 0 to 2 in steps of 0.025.

### 9.3.2 Real EEG recordings and preprocessing

Following the previously published work <sup>[62]</sup> we studied the EEG data recording from seven human volunteers with the permission of the Waikato Hospital Ethical Committee. During the recording, the volunteers (American Society of Anesthesiologists physical status I or II) were recruited to undergo a brief propofol anesthetic and recovered in accordance with normal procedures of the Australian and

New Zealand College of Anaesthesia (A.N.Z.C.A) guidelines. Before the experiment, all subjects gave written informed consent after obtaining the permission of the hospital ethical committee. In order to record credible EEG recordings, the silver-silver chloride scalp electrodes were placed at the position of Fp1-F7 and C3-T3 with the ground electrode placed at FpZ according to the 10-20 international system to produce bipolar signals (Fig. 1 (A)). The raw EEG and the BIS values were recorded with the Aspect A-1000 EEG monitor (Aspect Medical Systems, Natick, MA, USA) with the sampling frequency 256 Hz and 0.2Hz respectively.

Fig. 1 (B) illustrates the whole experimental sequence diagram. The propofol intravenous infusion was 150ml/h (1500mg/h) in an antecubital vein via a syringe driver pump initially, and the BIS and raw EEG data were recorded when the infusion started. Then, a verbal list of dissimilar objects was read to the subject at 30-second intervals who held a syringe filled with water between forefinger and thumb. When the syringe dropped (LoC time), the infusion and the read of the list of dissimilar stopped, and the time was recorded as “syringe-drop time”. The subject was then allowed to awake and given the play of a pre-recorded tape of random numbers and some verbal commands such as “move your right foot”. The verbal commands lasted 5 seconds and they were at 10-second intervals. We recorded the time as “command time” as soon as the subject responded the verbal command correctly (recovery of consciousness (RoC) time). The subject were questioned as to the first number that they could recall and the last object that they could remember during propofol induction, and these two time points were recorded as “object time” and “number

time” respectively. The study was terminated about 60 seconds after LoC time. Table 1 shows the four recorded times of all subjects

“Fig. 1”

“Table 1”

In the EEG preprocessing, we mainly focused on three type artifacts: baseline drift, head movement noise and physiological noise (such as electrooculogram (EOG) and electromyogram (EMG)). And different kinds of artifact were processed with different artifact-rejection approach. Firstly, baseline drift and head movement noise are usually in the low frequency band (<0.5 Hz) and the function `eegfilt.m` in EEGLAB was used to reduce this noise <sup>[63]</sup>. Using statistical mean and standard deviation (SD) methods <sup>[64]</sup> amplitude values beyond the range  $\text{mean} \pm 2\text{SD}$  or the raw data with amplitude larger than  $200 \mu\text{V}$  were rejected as considered as outliers. EOG artifacts were reduced through a stationary wavelet transform based on an appropriate threshold <sup>[65]</sup>. Finally, inverse filtering was used to identify transient events in the EEG, and was employed to detect and remove EMG and other high-amplitude transient artifacts <sup>[66, 67]</sup>.

In practice, the EEG data were divided into a series of 10-second epochs, with an overlap of 75% (In particular, the data were divided into different length of time epoch for the calculation of PS indexes.) All epochs were used to calculate the synchronization indexes. In order to evaluate the synchronization in consciousness detecting, we chose three states from the whole period: awake state (the period before “Object time”), unconscious state (the period between LoC time and “Number time”) and recovery state (the period after “command time”). Then the efficacy of the indexes were evaluated by the ability of different synchronization measures to distinguish different anesthetic states.

## 9.4 Evaluation Criteria and Statistics

### 9.4.1 Criteria for measures evaluation in model

We assume that an increase of coupling strength necessarily leads to an increase of synchronization. To compare the different synchronization measures in terms of their capability to reflect different degrees of coupling, we used the degree of monotonicity [29] to evaluate the dependence on the coupling strength  $C$  of the synchronization measures.

Each synchronization index is computed at  $r=81$  monotonously increasing coupling strengths for each model system, resulting in values  $s_i, i=1,2,\dots,r$ . If  $s$  depends monotonically on the coupling strength  $C$ , the  $s_i \leq s_j, i \leq j$ . The degree of monotonicity is defined as,

$$DoM = \frac{2}{r(r-1)} \sum_{i=1}^{r-1} \sum_{j=i+1}^r \text{sign}(s_j - s_i) \quad (27)$$

The DoM=1 if the sequence  $s_1, s_2, \dots, s_r$  has a strictly monotonous increasing trend, while DoM=-1 if it has a monotonically decreasing trend.

### 9.4.2 Statistical analysis

We did this by comparing the strength of association of each synchrony measure with the BIS index and propofol effect site concentration (derived from pharmacokinetic/pharmacodynamic (PK/PD) modeling)<sup>[62]</sup>; and also the ability of each measure to separate the wakeful from unresponsive behavioral states in the subjects. For each subject, the strength of association between the various synchrony measures and the Bispectral Index (BIS) or effect-site propofol concentration (ESPC)  $C_{eff}$  was assessed using prediction probability ( $P_k$ ). A  $P_k$  value of 1 means that the synchrony measure index is perfectly concordant with the BIS or  $C_{eff}$ . A value of 0.5

means that the synchrony measure is not superior to that expected by chance. We also used box plots to visualize and evaluate the performance of each index for distinguishing different anesthesia states. The relative coefficient of variation (CV) (the ratio of standard deviation (SD) to mean) was used to evaluate the index stability during awake and its sensitivity to the induction process<sup>[68]</sup>. Further, the  $R_{ij}$  was used to assess the correlation of different synchrony measures and BIS with each other. For all tests,  $P < 0.05$  was considered significant.

## 9.5 Results

### 9.5.1 Model simulation results

Fig. 2 A-D showed the attractors of the responder ( $y_1(t)$  and  $y_2(t)$ ) of Hénon maps at four coupling strengths  $C=0$ ,  $C=0.6$ ,  $C=0.7$  and  $C=0.8$ , while Fig. 2E-H showed the plot of the first component of the driver ( $x_1(t)$ ) versus the first component of the responder ( $y_1(t)$ ) at corresponding coupling strengths  $C$ . The attractor of the responder looked the same for  $C=0$  (Fig. 2A) and  $C=0.8$  (Fig. 2D). By contrast, the driver and responder were completely independent when  $C=0$  (Fig. 2E) and identical synchronization between driver and responder could be observed when  $C=0.8$  (Fig. 2H). Between  $C=0$  and  $C=0.8$ , a rather sharp transition to a synchronized state took place around  $C=0.7$  (Fig. 2G). The coupled Rössler systems at four coupling strengths  $C=0$ ,  $C=0.5$ ,  $C=1$  and  $C=2$  were shown in Fig. 3. Fig. 3A-D showed the attractors of the responder ( $y_1(t)$  and  $y_2(t)$ ) and a clear tendency towards the identity of driver ( $x_1(t)$ ) and responder ( $y_1(t)$ ) could be observed in Fig. 3E-H. Fig. 4A-D showed the attractors of the responder ( $y_1(t)$  and  $y_3(t)$ ) of coupled Lorenz systems at four coupling strengths  $C=0$ ,  $C=0.4$ ,  $C=1.15$  and  $C=2$ , whereas Fig. 4E-H showed the plot of the driver ( $x_1(t)$ ) and the responder ( $y_1(t)$ ) at corresponding coupling strengths  $C$ .

The transition towards the synchronized state took place around  $C=1.15$  (Fig. 4G).

“Fig. 2”

“Fig. 3”

“Fig. 4”

We used the simulated data  $x_1$  and  $y_1$  of three coupled model systems to calculate the synchronization indexes mentioned in Section 2 at different coupling strength. The index value at increasing coupling strength  $C$  for the Hénon, Rössler and Lorenz systems were shown in Fig. 5-7.

Different model systems exhibited different behaviors with increasing coupling strength. In Fig. 5, the value of synchronization indexes, with the exception of DET and WTC, showed a rising trend with increasing coupling strength  $C$  and they had a steep rise at a coupling strength  $C=0.7$ . It can be seen from Fig. 5A that the COR, KerMI, PCMI, NI and FTC values started at zero when  $C=0$  and showed less fluctuations. The PCMI rose more gradually, while the NI exhibited a sharp increase at higher  $C$ . In terms of  $PS_{PLV}$ ,  $PS_{SE}$  and  $PS_{CP}$ , high values were obtained for uncoupled or weakly coupled Hénon systems and more fluctuations could be observed (Fig. 5B). DET and WTC decreased slightly when the coupling strength was weak and increased after  $C=0.45$ . They stayed in the range of about 0.3 to 0.4 during the whole coupling strength. As can be seen from the Fig. 6, most values of synchronization indexes saw an increase at about  $C=0.2$ , while  $PS_{SE}$  and DET saw a sharp decrease. Particularly, DET had a high value (DET=0.9095) when  $C=0$  and it remained at high value during the whole range of coupling strength. By contrast, WTC had a low value (WTC=0.0511) when  $C=0$  and it stayed at low values, reaching 0.049 when  $C=2$ . In Fig. 7, a sharp rise appeared when  $C=1.15$  for most indexes. The KerMI and three PS indexes had a nonzero value when  $C=0$ , and three PS indexes showed more fluctuations. In terms of DET and WTC, fluctuating during the whole range of coupling strength, DET gained high values and WTC had low values as they were presented in the coupled Rössler systems (Fig. 6C).

“Fig. 5”

“Fig. 6”

“Fig. 7”

The values of DoM of the synchronization measures for the Hénon, Rössler and Lorenz systems were shown in Fig. 8. In terms of different model systems, almost all the highest value of DoM of each synchronization measure was obtained in Hénon and Rössler systems. The DoM values of the Lorenz system were smaller than that of the Hénon and Rössler systems, which was due to the fluctuations in Lorenz system. Regarding the different synchronization measures, PCMI had the highest DoM value in both Hénon system (DoM=0.985) and Lorenz system (DoM=0.770), and KerMI gained the highest DoM value in Rössler system (DoM=0.998). Also, we found that the higher DoM values were obtained for NI in Hénon (DoM=0.984) and Rössler (DoM=0.988) systems. These results illustrated that PCMI, KerMI and NI had a better ability to track the increasing coupling strength. By contrast, DET and WTC gained the negative DoM values which meant that they even had the monotonically decreasing trend with increasing coupling strength.

“Fig. 8”

### **9.5.2 Application to real EEG recordings**

FTC and WTC were analyzed with pairwise channels for each subjects in order to find a better coherence method to quantify the synchronization in frequency domain.

The EEG recordings of two channels from one subject were shown in Fig. 9 A and Fig. 9B. Fig. 9C and Fig. 9D showed the FTC and WTC spectrums during the whole period. In terms of FTC spectrum, two-channel EEG signals were divided into a series of 10-second epochs with an overlap of 75%. The epochs were windowed using a Hamming window and FFT length was set to be 128. As can be seen from the figure, FTC spectrum could not reflect the changes of coherence during the whole period (Fig. 9C). With similar results as the spectrogram analysis, the WTC spectrum in the  $\delta$ ,

$\alpha$  and  $\beta$  frequency bands increased obviously during unconscious state (Fig. 9(D)). Therefore, WTC index was extracted from WTC spectrum to quantify the synchronization during propofol-induced anesthesia period.

Then the synchronization indexes were computed during the whole anesthetic period for all subjects. Fig 10(A) gives an example of one subject from the left prefrontal and left primary motor cortex respectively.

Fig. 10(B) was the corresponding  $C_{eff}$  and BIS index. Fig. 10(D)-(K) showed the values of all synchronization indexes for the same subject. In each frequency bands ( $\delta$ ,  $\theta$ ,  $\alpha$ ,  $\beta$  and  $\gamma_1$ ), three PS indexes were calculated and results showed that the PSPLV and PSCP had similar results, which was consistent with previously reported results in [56], and the PSCP will be not further reported. It also can be seen that the PCMI, NI, PSPLV ( $\delta$ ,  $\theta$ ,  $\alpha$  and  $\gamma_1$ ), PSSE ( $\delta$ ,  $\beta$ ) saw a decreasing trend with the increasing  $C_{eff}$  value, whereas KerMI, DET and WTC ( $\delta$ ,  $\theta$  and  $\alpha$  frequency bands) showed an increasing trend which were consistent with the  $C_{eff}$ .

“Fig. 9”

“Fig. 10”

The statistical parameter  $P_k$  were used to quantify the ability of predicting BIS ( $P_{K\_BIS}$ ) and the  $C_{eff}$  ( $P_{K\_C_{eff}}$ ) of the synchronization measures. The box plots of  $P_k$  values of each synchronization indexes with BIS and  $C_{eff}$  were shown in Fig. 11. The median of  $P_k$  values of all measures were displayed in Table 2. It can be seen from Fig. 11 and Table 2 that PCMI had the highest  $P_k$  value with BIS ( $P_{K\_BIS}=0.855$ ) and ESPC ( $P_{K\_C_{eff}}=0.794$ ). DET ranked second with the value

$P_{K\_BIS}=0.823$  and  $P_{K\_C_{eff}}=0.781$ . These figures demonstrated that PCMI and DET could best predict the BIS and follow the ESPC. The  $P_k$  values of NI, KerMI and COR were smaller than PCMI and DET. Kolmogorov-Smirnov test showed that the PK values of each index were not normally distributed.

“Fig. 11”

“Table 2”

Furthermore, in order to evaluate the ability of the synchronization measures in distinguishing different anesthetic states which is essential for depth of anesthesia monitoring. We give the synchronization indexes and the box plots of the index values at three anesthetic states (awake, unconscious and recovery) in Fig. 12. It can be seen from Fig. 13 that KerMI, PCMI, NI and DET could significantly distinguish awake and unconscious states as well as unconscious and recovery states ( $p<0.001$ ), whereas COR could only distinguish awake and unconscious states ( $p<0.001$ ). As for WTC, there was a significant rise in unconscious state and a significant drop in recovery state for all frequency bands (Fig. 12 (B-F)). In terms of PSPLV, the phase synchronization dropped significantly in unconscious state for PSPLV ( $\delta$ ,  $\theta$ ,  $\alpha$  and  $\gamma_1$ ) and had no significant changes in recovery state, while PSPLV ( $\beta$ ) could not distinguish the three anesthetic states (Fig. 12 (G-K)). PSSE could only distinguish three states at  $\theta$  and  $\beta$  frequency bands (Fig. 12 L-P). There was an increase in unconscious state and a decrease in recovery state for KerMI and DET, while the trends were opposite for PCMI and NI.

It is crucial for the DoA monitoring that the index value should be stay stable during

each anesthetic states. Table 3 represents the CV values of synchronization indexes that calculated with all subjects at awake, unconscious and recovery states

As can be seen from Table 3, PCMI had the low CV in awake state (CV=0.085), unconscious state (CV=0.146) and recovery state (CV=0.105). The CV of NI, PS, PLV, PSSE and DET were lower than COR and KerMI, which were all smaller than WTC in awake and unconscious states. These results illustrated that PCMI, NI, PS and DET are more robust to noise during the propofol-induced anesthesia.

“Fig. 12”

“Table 3”

Although with various results for the synchronization measures, they also have somewhat relevance with the BIS and  $C_{eff}$ . Thus the correlation coefficients  $R$  was calculated.

BIS and ESPC of all subjects and the averaged  $R$  over all subjects were shown in Fig. 13. It can be seen that the PCMI had the highest correlation coefficient with BIS ( $R=0.846$ ) and  $C_{eff}$  ( $R=0.739$ ). DET ranked second with BIS ( $R=0.843$ ) and  $C_{eff}$  ( $R=0.703$ ). As for PS and WTC, PSPLV ( $\delta$ ) and WTC ( $\alpha$ ) correlated with BIS and  $C_{eff}$  higher than that of other frequency bands. In terms of the relation among different synchronization measures, PCMI correlated closely with DET ( $R=0.949$ ) and NI ( $R=0.838$ ).

“Fig. 13”

## 9.6 Conclusions

We considered nine synchrony measures, including cross correlation, cross coherence,

three phase synchronization measures, mutual information measures based on three different methods, nonlinear interdependence and cross recurrence analysis. These nine methods quantify synchronization based on different foundations. The cross correlation is based on the relationship of EEG magnitude between channels. As EEG magnitude increasing in one channel and at the same time (or within a preset time lag) it also occurs in the other channel, the cross correlation will be high. The cross coherence is a time-frequency domain method, and can separate the cross-channel associations within different frequency bands. In this study, we used two cross coherence evaluation methods (Fourier transform and wavelet transform) to quantify the coherence. It is generally thought that the wavelet decomposition have better time resolution than the Fourier based method. Phase synchronization analysis is a classic neuronal oscillation analysis method that is somewhat independent of the raw amplitude of the signal. The instantaneous phase extraction is based on the WHWT, which was proposed in our previous study <sup>[45]</sup>. Mutual information has been widely applied in EEG analysis as a way of estimating information integration between different EEG channels or brain regions for mechanism analysis and neurological disease diagnosis, such as epilepsy seizure, Alzheimer's disease and autism etc. <sup>[70-72]</sup>. It is based on the hypothesis that state information of one channel can be used to reduce the uncertainty for understanding the other channel if they are associated in some way. In practical terms, the probability density can be estimated in a number of different ways. We applied two different methods, kernel density estimation and permutation entropy to calculate the MI value. Nonlinear interdependence and cross

recurrence analysis are non-linear time series analysis methods based on reconstruction of the phase space of the signals. The nonlinear interdependence measure of  $S^{(k)}(X|Y)$  and the determinism measure can be used as indices to quantify synchrony. Although we considered a large variety of synchrony measure, it is impossible to include all existing measures in this study. Of the nine methods tested, each has their own representative features. The measures we have studied probe different aspects of the system or time series, such as phase, symbolic dynamics, time-frequency relationships, etc.

Neurophysiological signals are complex, nonlinear and nonstationary. The features of the coupling dynamics underlying these signals however are not well understood<sup>[73]</sup>, making the choice of evaluative measure somewhat arbitrary. At the very least, the measures to be used must be validated against a test standard. To evaluate the performance of the synchrony measures we utilized, three nonlinear coupling models were used, upon which each method was tested. The results show that the synchrony measures could track the changes of coupling strength in the models, but with differing, somewhat non-linear characteristics. All methods show an abrupt change at a certain coupling strength threshold.

The synchronization measures were able to distinguish the different anesthesia states (see Fig.12) with the exception of COR. Of all the measures, PCMI appears to be superior to the other methods, for the following reasons. Firstly, it is less sensitive to noise in the EEG signal during the awake state (seen in Fig. 9). Furthermore, PCMI correlated closely with propofol effect-site concentration and BIS index (a higher  $P_k$

and  $R_{ij}$  (see Table.2)) and is less affected by the amplitude of the EEG (the distribution probability calculation based on the permutation<sup>[74, 75]</sup>).

Interestingly, the WTC, KerMI and DET methods exhibit an opposite trend to changes in anesthetic levels compared with the other measures. This phenomenon is difficult to explain in the context of understanding anesthetic mechanisms. To some extent it can be explained on the basis of the simulation model analysis, which shows that WTC and DET change out of phase with the other methods. However, the KerMI index increases with increasing coupling strength in the simulations and appears to contradict the reductions seen with the other measures when applied to the EEG. Clearly, the EEG signal is more complex than simulated by simple nonlinear models and further insight is required into the underlying principles underpinning the different synchrony measures.

Although all synchrony measures could track this fundamental shift in EEG pattern, each algorithm responded in characteristic fashion. The WTC is a time-frequency measurement method, which characterizes the phase synchrony at each frequency point. It can be seen that the spectrum of the WTC is similar to the EEG spectrogram of the recordings computed using a short-time Fourier transform. WTC is based on the summation of the coherence of the frequency band at each time point. Because it takes signal amplitude into account, the value of WTC at  $\delta(1-4Hz)$  frequency band increases most obviously with the deepening of anesthesia. Among the three phase synchronization methods, which measure the phase difference of two EEG signals, only PS\_PLV and PS\_CP at the  $\delta(1-4Hz)$  frequency band clearly distinguished the

awake state from unconscious state. PCMI and KerMI are both mutual information measures, but their calculation principles are different. PCMI is related to the permutation pattern probability distribution. With deepening anesthesia the permutation pattern decreases because the EEG signals become more regular. On the other hand, the KerMI quantifies the difference in amplitude between time-domain neighboring signals. The high value of KerMI during anesthesia is on account of the small difference in signal magnitude between adjacent signals. The slower fluctuation of signal, the smaller the difference between adjacent points. So, when anesthesia deepens and the signals become regular, the KerMI will increase. The nonlinear method DET, which is based on the recurrence plot, describes the complexity of the nonlinear system. When anesthesia deepens, the EEG signal become more regular and the DET measure will increase with this trend. In our case we are looking at the cross-recurrence, i.e. the recurrence occurs when the trajectory in one channel becomes close to that of the other channel, thus reflecting the inner coupling changes during anesthesia.

It is not meaningful to attempt to quantify on the basis of one or other measure the extent to which synchronization either strengthens or weakens during anesthesia. Because each measure is derived from a different perspective, their outputs can be seen as complementary, not conflicting. Such as, we could say that coherence between two brain areas during anesthesia is increase based on the WTC. At the same time, mutual information based on the permutation measure decreases with deepening anesthesia. Further, PCMI, PS\_PLV ( $\delta(1-4Hz)$ ) and NI show a declining trend with

increasing propofol concentration, reflecting a reduction in long-range coupling. From the perspective of information theory, PCMI is based on the permutation pattern probability distribution, which decreases with the deepening of anesthesia. This decreasing pattern to some extent reflects the marked decrease in the mean firing rate in the cortex [75, 76]. Moreover, Lewis et al found that propofol-induced unconsciousness is associated with an increase in the low-frequency EEG (<1 Hz) band. Consistent with these observations, we found that PS\_PLV and PS\_CP values at the delta frequency band exhibit an abrupt change at the loss of consciousness point. This suggests that the appearance of low frequency activity might be a good proxy for loss of long distance coupling [19]. The NI index significant drop in unconsciousness state in our study, suggesting that disparate brain regions have weaker interdependence with increasing drug effect. This is consistent with the findings of previous studies [23, 77, 78]. The increase in wavelet coherence of the slow oscillation (<1Hz),  $\delta$  rhythm (1-4Hz) and  $\alpha$  rhythm (8-13Hz) during deep anesthesia suggests that propofol enhances corresponding band activity. We found that the high WTC values during deep anesthesia state is also consistent with the results of our previous study [34].

In conclusion, we found that most of the synchronization measures that we investigated can track the anesthetic effect on the EEG. However, each measure responded in distinctive fashion, on account of their corresponding characteristic principles. Each method may be seen to capture specific synchrony criteria. It is important to underscore that these issues need to be carefully taken into account when

formulating and verifying theories explaining anesthesia mechanisms. The different measures responded in characteristic fashion, suggesting that each may tell us something different about the mechanism by which anesthetic drugs disrupt cortical information processing and coupling. These in-depth analysis has an important implications for understanding of other neural mechanisms.

## Appendix

In order to evaluate the synchronization changes in different anesthetic states efficiently, we discussed the parameter selections of COR, PS, NI and DET. We calculated these synchronization indexes under different parameters of all subjects and chose three datasets from each synchronization index in awake, unconscious and recovery states which were according to the time points of each subjects. The values of synchronization indexes under different parameters were shown in Fig. S1-S5. All values were given by median

### A. COR

Fig.S1 shows the cross correlation values of different delay time  $\tau$  at different study periods (red: awake, green: unconsciousness, and blue: RoC) for all nine subjects under propofol anaesthesia. We chose two positive delay times, two negative delay times and the zero delay time. The cross correlation values are positive and higher when  $\tau = 0$  at both the awake state and recovery state. Besides, the COR value reveals quite large negative correlation at the deep anesthesia state when  $\tau = 0$ . For this reason, we choose the zero delay time.

“Fig. S1”

### B. PS

Fig. S2 and Fig. S3 showed the PSPLV ( $\delta, \theta, \alpha, \beta$  and  $\gamma_1$ ) and PSSE ( $\delta, \theta, \alpha, \beta$  and  $\gamma_1$ ) values at different epoch length  $T_e$  in awake state (red), unconscious state (green) and recovery state (blue) of all subjects. It can be seen from Fig. S2 that the PSPLV values of all frequency bands decreased with increasing  $T_e$ . The difference between awake

and unconscious states of PSPLV ( $\delta$ ) were larger than PSPLV in other frequency bands, which was also could be seen from Fig. 11(F). By contrast, PSSE had some fluctuation at different  $T_e$  (Fig. S3).  $T_e = 20$  was used in our study.

“Fig. S2”

“Fig. S3”

### C. NI

Fig. S4A showed the NI values with time lag  $\tau=1$ , nearest neighbors  $k=20$  in different embedding dimension  $m$  in awake state (red), unconscious state (green) and recovery state (blue) of all subjects. The NI values with  $\tau=2$ ,  $k=20$  in different  $m$  were shown in Fig. S4B. As can be seen from these two figures, NI increased monotonically with increasing  $m$  and the difference of NI values between awake, unconscious and recovery states became wider with increasing  $m$ . Therefore,  $m=5$  was selected in terms of calculation complexity. Fig. S4C showed NI values with  $m=5$ ,  $k=20$  in different  $\tau$ . The NI difference between awake and unconscious states became smaller with increasing  $\tau$ , so we chose  $\tau=1$ . The NI values with  $m=5$ ,  $\tau=1$  in different nearest neighbors  $k$  were shown in Fig. S4D and we selected  $k=20$ .

“Fig. S4”

### D. DET

Fig. S5A, Fig. S5B and Fig. S5C showed DET values with embedding dimension  $m=3$ ,  $m=4$  and  $m=3$  respectively in threshold of diagonal length  $l_{min}=2$  in different time lag  $\tau$  in awake state (red), unconscious state (green) and recovery state (blue) of all subjects.  $m=3$ ,  $\tau=2$  were selected because of the great DET difference between awake and unconscious states. DET values with  $m=3$ ,  $\tau=2$  in different  $l_{min}$  were shown in Fig. S5D and  $l_{min}=2$  was selected.

“Fig. S5”

## References

1. P R, R., et al., *Visuomotor integration is associated with zero time-lag synchronization among cortical areas*. Nature, 1997. **385**(6612): p. 157-161.
2. M, S., M. D A, and S. T J, *Thalamocortical oscillations in the sleeping and aroused brain*. Science, 1993. **262**(5134): p. 679-685.
3. Mizuhara, H. and Y. Yamaguchi, *Human cortical circuits for central executive function emerge by theta phase synchronization*. Neuroimage, 2007. **36**(1): p. 232-244.
4. Uhlhaas, P.J. and W. Singer, *Neural Synchrony in Brain Disorders: Relevance for Cognitive Dysfunctions and Pathophysiology*. Neuron, 2006. **52**(1): p. 155-168.
5. A K, E., F. P, and S. W, *Dynamic predictions: Oscillations and synchrony in top-down processing*. Nature Reviews Neuroscience, 2001. **2**(10): p. 704-716.
6. Li, X., et al., *Interaction dynamics of neuronal oscillations analysed using wavelet transforms*. Journal of Neuroscience Methods, 2007. **160**(1): p. 178-185.
7. Schnitzler, A. and J. Gross, *Normal and pathological oscillatory communication in the brain*. Nature Reiview Neuroscience, 2005. **6**(4): p. 285-296.
8. Aviyente, S., et al., *A phase synchrony measure for quantifying dynamic functional integration in the brain*. Hum Brain Mapp, 2011. **32**(1): p. 80-93.
9. Zheng, Y., et al., *Epileptic seizure prediction using phase synchronization based on bivariate empirical mode decomposition*. Clin Neurophysiol, 2014. **125**(6): p. 1104-11.
10. Mirowski, P., et al., *Classification of patterns of EEG synchronization for seizure prediction*. Clin Neurophysiol, 2009. **120**(11): p. 1927-40.
11. Slooter, A.J., et al., *Seizure detection in adult ICU patients based on changes in EEG synchronization likelihood*. Neurocrit Care, 2006. **5**(3): p. 186-92.
12. Koenig, T., et al., *Decreased EEG synchronization in Alzheimer's disease and mild cognitive impairment*. Neurobiology of Aging, 2005. **26**(7b): p. 165-171.
13. Stam, C.J., et al., *Disturbed fluctuations of resting state EEG synchronization in Alzheimer's disease*. Clinical Neurophysiology Official Journal of the International Federation of Clinical Neurophysiology, 2005. **116**(3): p. 708-15.
14. Mehran, A., A. Hojjat, and A. Amir, *Fuzzy Synchronization Likelihood-wavelet methodology for diagnosis of autism spectrum disorder*. Journal of Neuroscience Methods, 2012. **211**(2): p. 203-209.
15. Birchler-Pedross, A., et al., *Higher frontal EEG synchronization in young women with major depression: a marker for increased homeostatic sleep pressure?* Sleep, 2011. **34**(12): p. 1699-706.
16. Moroni, F., et al., *Slow EEG rhythms and inter-hemispheric synchronization across sleep and wakefulness in the human hippocampus*. Neuroimage, 2012. **60**(1): p. 497-504.
17. Koskinen, M., et al., *Propofol anesthesia induces phase synchronization changes in EEG*. Clin Neurophysiol, 2001. **112**(2): p. 386-92.
18. Shalbaf, R., et al., *Frontal-temporal synchronization of EEG signals quantified by order patterns cross recurrence analysis during propofol anesthesia*. IEEE Trans Neural Syst Rehabil Eng, 2015. **23**(3): p. 468-74.
19. Lewis, L.D., et al., *Rapid fragmentation of neuronal networks at the onset of propofol-induced*

- unconsciousness*. Proceedings of the National Academy of Sciences, 2012. **109**(49): p. E3377-E3386.
20. Voss, L. and J. Sleigh, *Monitoring consciousness: the current status of EEG-based depth of anaesthesia monitors*. Best Practice & Research Clinical Anaesthesiology, 2007. **21**(3): p. 313-325.
  21. Nallasamy, N. and D.Y. Tsao, *Functional connectivity in the brain: effects of anesthesia*. The Neuroscientist, 2011. **17**(1): p. 94-106.
  22. Lee, U., et al., *Propofol induction reduces the capacity for neural information integration: implications for the mechanism of consciousness and general anesthesia*. Consciousness and cognition, 2009. **18**(1): p. 56-64.
  23. Lee, U., et al., *The directionality and functional organization of frontoparietal connectivity during consciousness and anesthesia in humans*. Consciousness and cognition, 2009. **18**(4): p. 1069-1078.
  24. Pereda, E., R.Q. Quiroga, and J. Bhattacharya, *Nonlinear multivariate analysis of neurophysiological signals*. Progress in neurobiology, 2005. **77**(1): p. 1-37.
  25. Breakspear, M., "Dynamic" connectivity in neural systems. Neuroinformatics, 2004. **2**(2): p. 205-224.
  26. Kaminski, M. and H. Liang, *Causal influence: advances in neurosignal analysis*. Critical Reviews™ in Biomedical Engineering, 2005. **33**(4).
  27. Stam, C.J., *Nonlinear dynamical analysis of EEG and MEG: review of an emerging field*. Clinical Neurophysiology, 2005. **116**(10): p. 2266-2301.
  28. Dauwels, J., et al., *A comparative study of synchrony measures for the early diagnosis of Alzheimer's disease based on EEG*. Neuroimage, 2010. **49**(1): p. 668-693.
  29. Kreuz, T., et al., *Measuring synchronization in coupled model systems: A comparison of different approaches*. Physica D: Nonlinear Phenomena, 2007. **225**(1): p. 29-42.
  30. Zhou, D., W.K. Thompson, and G. Siegle, *MATLAB toolbox for functional connectivity*. Neuroimage, 2009. **47**(4): p. 1590-607.
  31. Thatcher, R.W., D.M. North, and C.J. Biver, *Development of cortical connections as measured by EEG coherence and phase delays*. Human brain mapping, 2008. **29**(12): p. 1400-1415.
  32. Nunez, P.L., *Electric fields of the brain: the neurophysics of EEG*. 2006: Oxford University Press.
  33. Li, X., et al., *Interaction dynamics of neuronal oscillations analysed using wavelet transforms*. Journal of neuroscience methods, 2007. **160**(1): p. 178-185.
  34. Li, D., et al., *Effects of volatile anesthetic agents on cerebral cortical synchronization in sheep*. Anesthesiology, 2013. **119**(1): p. 81-88.
  35. Lachaux, J.P., et al., *Measuring phase synchrony in brain signals*. Hum Brain Mapp, 1999. **8**(4): p. 194-208.
  36. Mormann, F., et al., *Mean phase coherence as a measure for phase synchronization and its application to the EEG of epilepsy patients*. Physica D: Nonlinear Phenomena, 2000. **144**(3): p. 358-369.
  37. Allefeld, C. and J. KURTHS, *Multivariate phase synchronization analysis of EEG data*. IEICE Transactions on Fundamentals of Electronics, Communications and Computer Sciences, 2003. **86**(9): p. 2218-2221.
  38. Allefeld, C. and J. Kurths, *An approach to multivariate phase synchronization analysis and its*

- application to event-related potentials*. International Journal of Bifurcation and Chaos, 2004. **14**(02): p. 417-426.
39. Rosenblum, M.G., A.S. Pikovsky, and J. Kurths, *Phase synchronization of chaotic oscillators*. Physical Review Letters, 1996. **76**(11): p. 1804.
  40. David, O., D. Cosmelli, and K.J. Friston, *Evaluation of different measures of functional connectivity using a neural mass model*. Neuroimage, 2004. **21**(2): p. 659-673.
  41. Engel, A.K., P. Fries, and W. Singer, *Dynamic predictions: oscillations and synchrony in top-down processing*. Nature Reviews Neuroscience, 2001. **2**(10): p. 704-716.
  42. David, O. and K.J. Friston, *A neural mass model for meg/eeg:: coupling and neuronal dynamics*. Neuroimage, 2003. **20**(3): p. 1743-1755.
  43. Le Van Quyen, M. and A. Bragin, *Analysis of dynamic brain oscillations: methodological advances*. Trends in neurosciences, 2007. **30**(7): p. 365-373.
  44. Aviyente, S., et al., *A phase synchrony measure for quantifying dynamic functional integration in the brain*. Human brain mapping, 2011. **32**(1): p. 80-93.
  45. Li, D., et al., *Phase synchronization with harmonic wavelet transform with application to neuronal populations*. Neurocomputing, 2011. **74**(17): p. 3389-3403.
  46. Park, H. and D.-S. Kim, *Evaluation of the dispersive phase and group velocities using harmonic wavelet transform*. NDT & E International, 2001. **34**(7): p. 457-467.
  47. Lachaux, J.-P., et al., *Studying single-trials of phase synchronous activity in the brain*. International Journal of Bifurcation and Chaos, 2000. **10**(10): p. 2429-2439.
  48. Silverman, B.W., *Density estimation for statistics and data analysis*. Vol. 26. 1986: CRC press.
  49. Beirlant, J., et al., *Nonparametric entropy estimation: An overview*. International Journal of Mathematical and Statistical Sciences, 1997. **6**: p. 17-40.
  50. Steuer, R., et al., *The mutual information: detecting and evaluating dependencies between variables*. Bioinformatics, 2002. **18 Suppl 2**: p. S231-40.
  51. Bandt, C. and B. Pompe, *Permutation entropy: a natural complexity measure for time series*. Phys Rev Lett, 2002. **88**(17): p. 174102.
  52. Liang, Z., et al., *Permutation auto-mutual information of electroencephalogram in anesthesia*. Journal of neural engineering, 2013. **10**(2): p. 026004.
  53. Quiroga, R.Q., J. Arnhold, and P. Grassberger, *Learning driver-response relationships from synchronization patterns*. Physical Review E, 2000. **61**(5): p. 5142.
  54. Breakspear, M. and J. Terry, *Topographic organization of nonlinear interdependence in multichannel human EEG*. Neuroimage, 2002. **16**(3): p. 822-835.
  55. Breakspear, M. and J. Terry, *Nonlinear interdependence in neural systems: motivation, theory, and relevance*. International Journal of Neuroscience, 2002. **112**(10): p. 1263-1284.
  56. Quiroga, R.Q., et al., *Performance of different synchronization measures in real data: a case study on electroencephalographic signals*. Physical Review E, 2002. **65**(4): p. 041903.
  57. Eckmann, J.-P., S.O. Kamphorst, and D. Ruelle, *Recurrence plots of dynamical systems*. Europhys. Lett, 1987. **4**(9): p. 973-977.
  58. Zbilut, J.P., A. Giuliani, and C.L. Webber, *Detecting deterministic signals in exceptionally noisy environments using cross-recurrence quantification*. Physics Letters A, 1998. **246**(1): p. 122-128.
  59. Marwan, N. and J. Kurths, *Nonlinear analysis of bivariate data with cross recurrence plots*.

- Physics Letters A, 2002. **302**(5): p. 299-307.
60. Schiff, S.J., et al., *Detecting dynamical interdependence and generalized synchrony through mutual prediction in a neural ensemble*. Physical Review E, 1996. **54**(6): p. 6708.
61. Palus, M. and A. Stefanovska, *Direction of coupling from phases of interacting oscillators: an information-theoretic approach*. Physical review. E, Statistical, nonlinear, and soft matter physics, 2003. **67**(5 Pt 2): p. 055201-055201.
62. Williams, M. and J. Sleigh, *Auditory recall and response to command during recovery from propofol anaesthesia*. Anaesthesia and intensive care, 1999. **27**(3): p. 265.
63. Delorme, A. and S. Makeig, *EEGLAB: an open source toolbox for analysis of single-trial EEG dynamics including independent component analysis*. Journal of neuroscience methods, 2004. **134**(1): p. 9-21.
64. Seo, S., *A review and comparison of methods for detecting outliers in univariate data sets*. 2006, University of Pittsburgh.
65. Li, X., S. Cui, and L.J. Voss, *Using permutation entropy to measure the electroencephalographic effects of sevoflurane*. Anesthesiology, 2008. **109**(3): p. 448.
66. Fatourehchi, M., et al., *EMG and EOG artifacts in brain computer interface systems: A survey*. Clinical Neurophysiology, 2007. **118**(3): p. 480-494.
67. Schlögl, A., *The electroencephalogram and the adaptive autoregressive model: theory and applications*. 2000: Shaker Germany.
68. Li, X., et al., *Analysis of depth of anesthesia with Hilbert-Huang spectral entropy*. Clinical Neurophysiology, 2008. **119**(11): p. 2465-2475.
69. !!! INVALID CITATION !!!
70. Abásolo, D., et al., *Approximate entropy and auto mutual information analysis of the electroencephalogram in Alzheimer's disease patients*. Medical & biological engineering & computing, 2008. **46**(10): p. 1019-1028.
71. Hall Jr, C.W. and A. Sarkar, *Mutual information in natural position order of electroencephalogram is significantly increased at seizure onset*. Medical & biological engineering & computing, 2011. **49**(2): p. 133-141.
72. Langen, M., et al., *Changes in the developmental trajectories of striatum in autism*. Biological psychiatry, 2009. **66**(4): p. 327-333.
73. Andrzejak, R.G., et al., *Bivariate surrogate techniques: Necessity, strengths, and caveats*. Physical Review E, 2003. **68**(6): p. 066202.
74. Li, X., S. Cui, and L. Voss, *Using permutation entropy to measure the electroencephalographic effects of sevoflurane*. Anesthesiology, 2008. **109**(3): p. 448.
75. Olofsen, E., J. Sleigh, and A. Dahan, *Permutation entropy of the electroencephalogram: a measure of anaesthetic drug effect*. British Journal of Anaesthesia, 2008. **101**(6): p. 810.
76. Hentschke, H., C. Schwarz, and B. Antkowiak, *Neocortex is the major target of sedative concentrations of volatile anaesthetics: strong depression of firing rates and increase of GABAA receptor-mediated inhibition*. European Journal of Neuroscience, 2005. **21**(1): p. 93-102.
77. Jameson, L.C. and T.B. Sloan, *Using EEG to monitor anesthesia drug effects during surgery*. Journal of clinical monitoring and computing, 2006. **20**(6): p. 445-472.
78. Schrouff, J., et al., *Brain functional integration decreases during propofol-induced loss of consciousness*. Neuroimage, 2011. **57**(1): p. 198-205.



## Figures

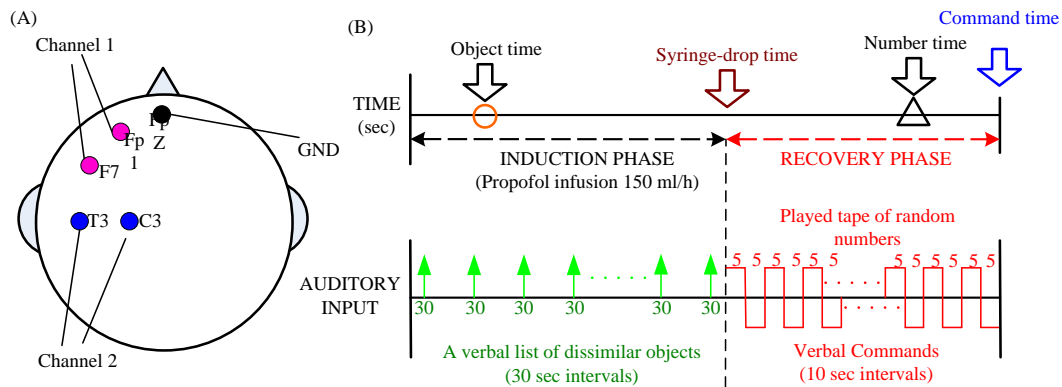


Fig.1. (A) Positions of scalp electrodes at Fp1-F7 and C3-T3. (B) The diagram of experimental sequence. The “Object time” (circle), “Syringe-drop time”, “Number time” (triangle) and “Command time” were marked in the diagram. A verbal list of dissimilar objects was executed in 30-second intervals in the induction phase. The tape of random numbers was played and verbal commands were given in 10-second intervals in the recovery phase.

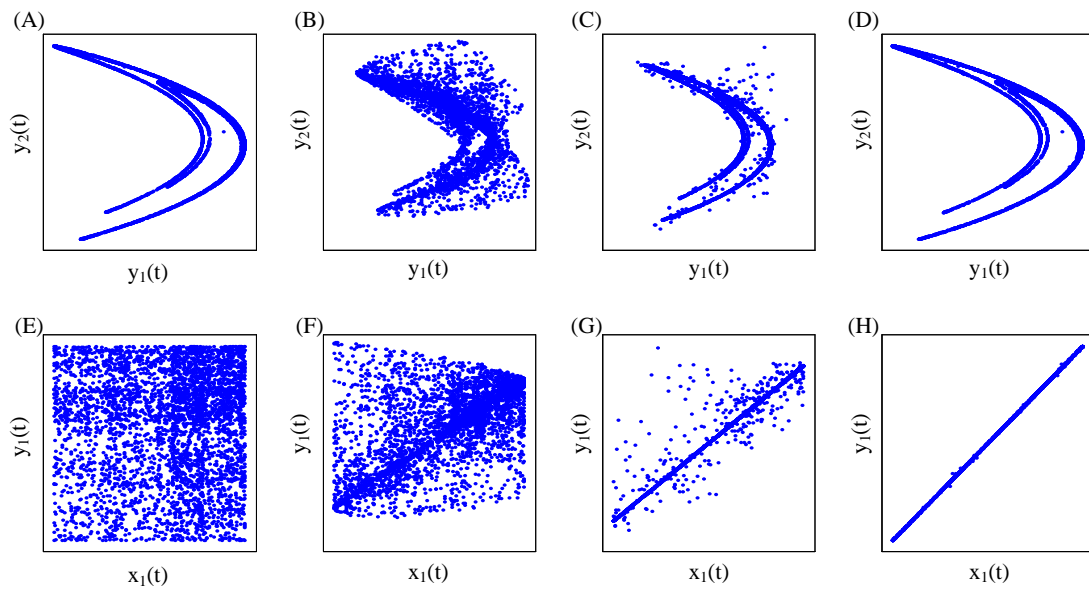


Fig.2. Coupled Hénon maps for different coupling strengths  $C$ . (A) and (E)  $C = 0$ , (B) and (F)  $C = 0.6$ , (C) and (G)  $C = 0.7$ , (D) and (H)  $C = 0.8$ .

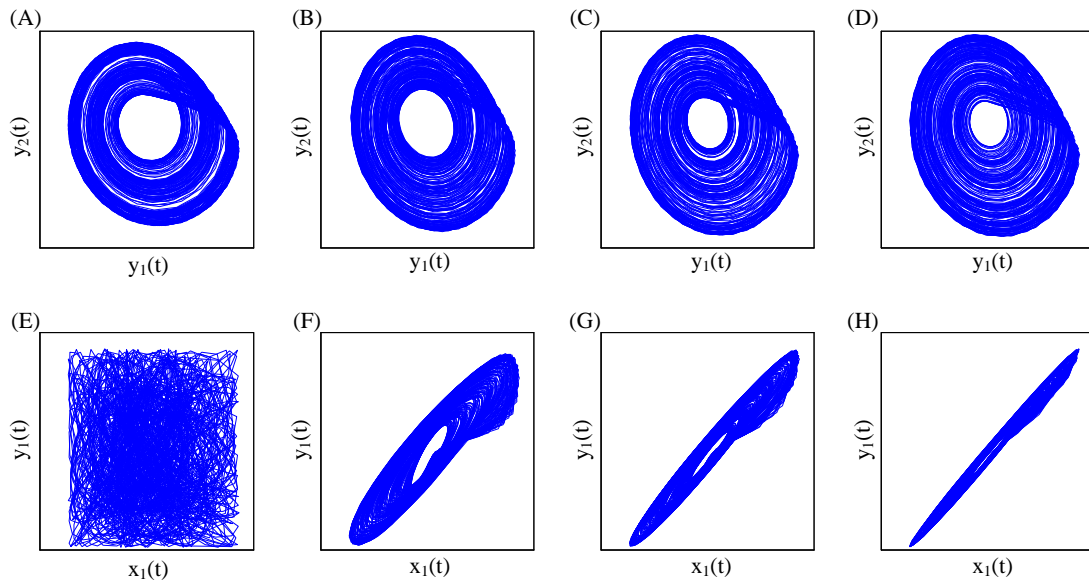


Fig.3. Coupled Rössler systems for different coupling strengths  $C$ . (A) and (E)  $C = 0$ , (B) and (F)  $C = 0.5$ , (C) and (G)  $C = 1$ , (D) and (H)  $C = 2$ .

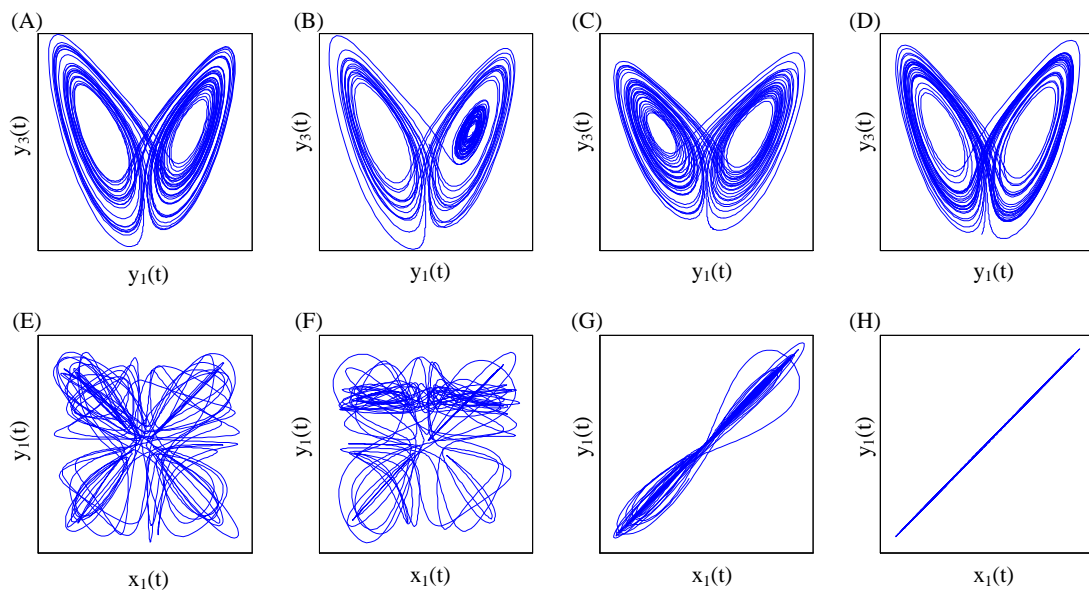


Fig.4. Coupled Lorenz systems for different coupling strengths  $C$ . (A) and (E)  $C = 0$ , (B) and (F)  $C = 0.4$ , (C) and (G)  $C = 1.15$ , (D) and (H)  $C = 2$ .

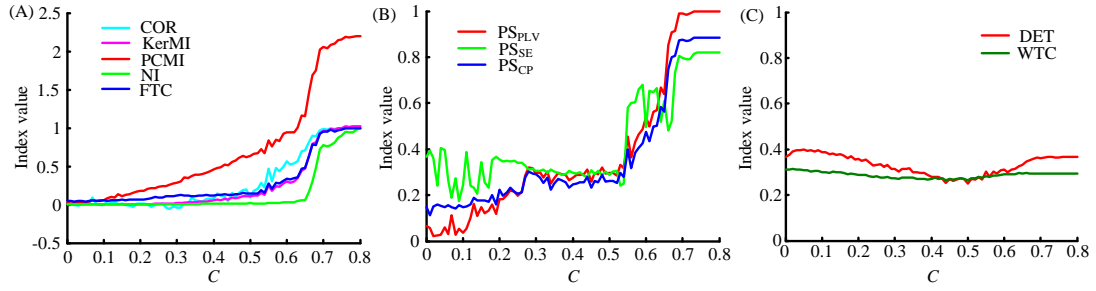


Fig.5. Synchronization measures applied to coupled Hénon systems. (A) COR, KerMI, PCMI, NI and FTC. (B) PS, PS\_SE, PS\_CP and PS\_FM. (C) DET and WTC.

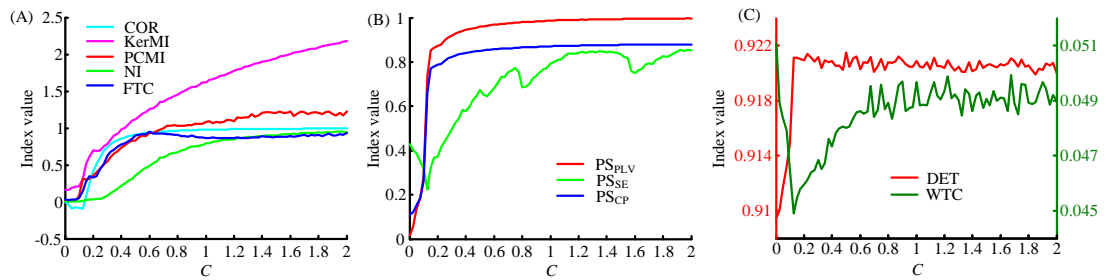


Fig.6. Synchronization measures applied to coupled Rössler systems. (A) COR, KerMI, PCMI, NI and FTC. (B) PS, PS\_SE, PS\_CP and PS\_FM. (C) DET and WTC.

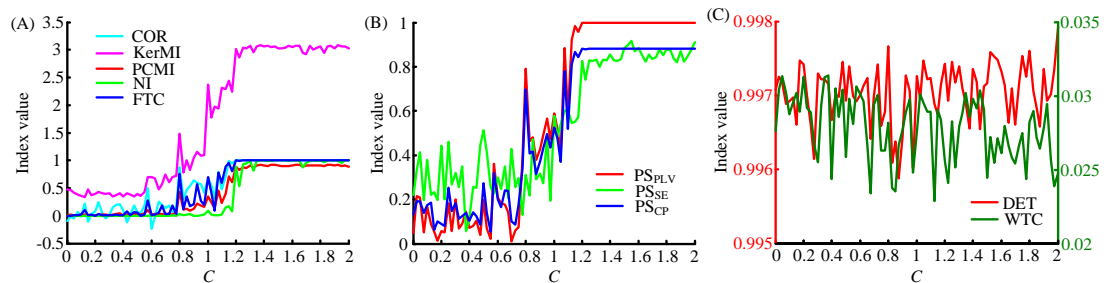


Fig.7. Synchronization measures applied to coupled Lorenz systems. (A) COR, KerMI, PCMI, NI and FTC. (B) PS, PS\_SE, PS\_CP and PS\_FM. (C) DET and WTC.

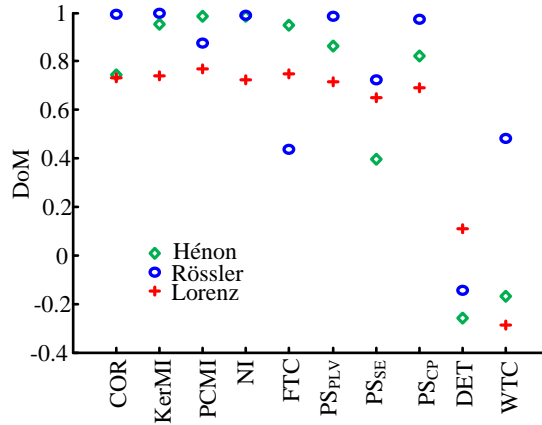


Fig. 8. Degree of monotonicity of synchronization indexes for the Hénon, Rössler and Lorenz systems.

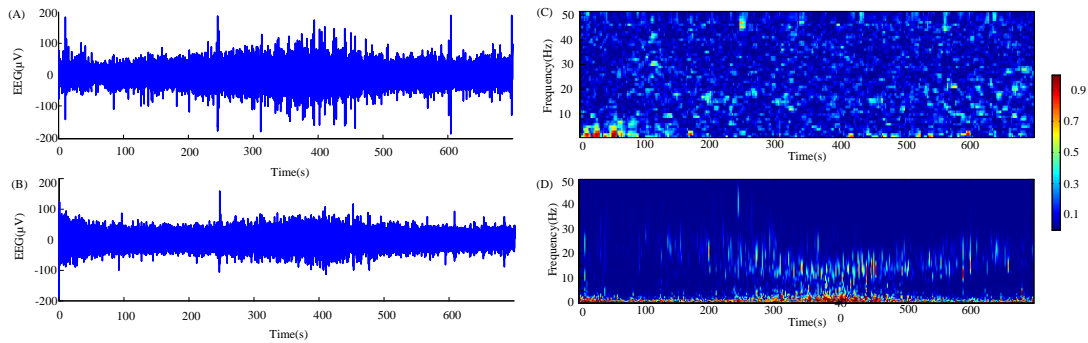


Fig.9. (A)-(B) Two-channel preprocessed EEG recordings of one subject over the whole experiment period. (C) The FTC spectrum of the two EEG recordings. (D) The WTC spectrum of the two EEG recordings.

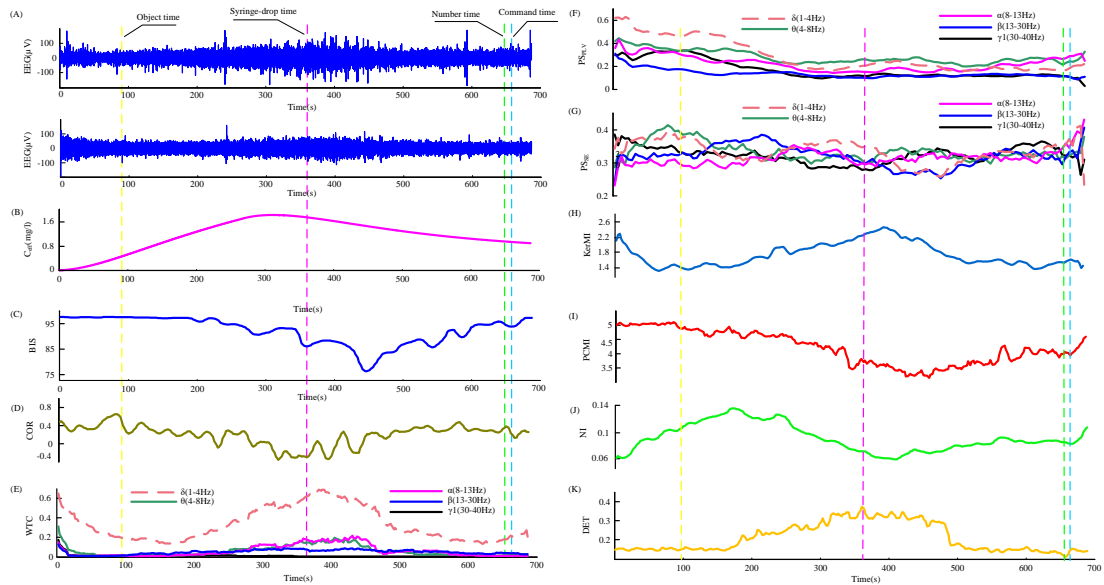


Fig.9. Two EEG recordings from one subject and corresponding synchrony measures versus time. (A) Two preprocessed EEG recordings from left prefrontal and left primary motor cortex recorded simultaneously at 256 Hz. The data were resampled to 100Hz for analysis. The recordings include the transitions from the conscious state to unconscious state and from unconsciousness to RoC. The four dashed gray lines are the time marks of the experiments. (B) Effect-site propofol concentration for the same subject. (C)-(K) Time course of synchrony measures, plotted with a time intervals of 10s with 75% overlap.

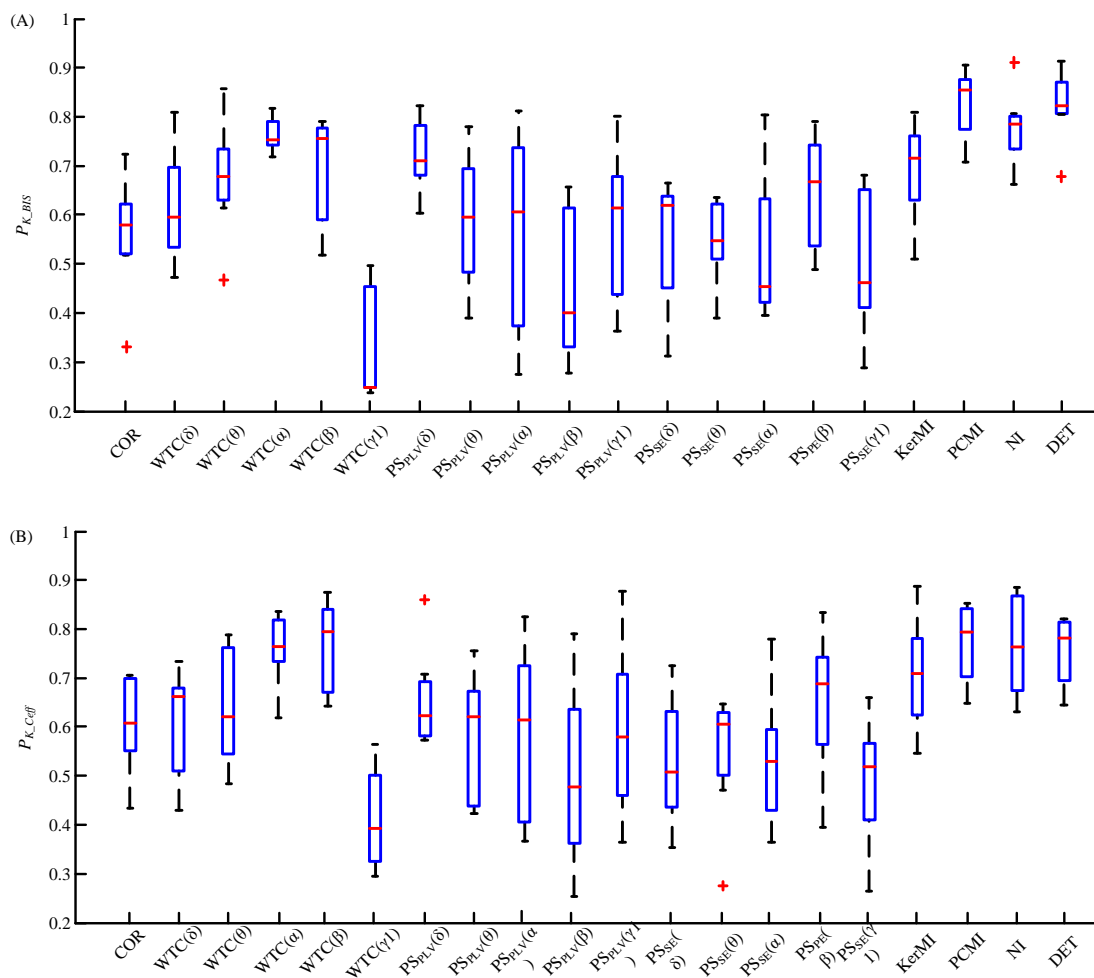


Fig.10. Statistical analysis of all subjects for each of the synchrony indices. (A) The

prediction probability value of the indices with the BIS as an independent variable. (B)

The prediction probability value of the synchrony measures with the ESPC index( $C_{eff}$ )

as the independent variable.

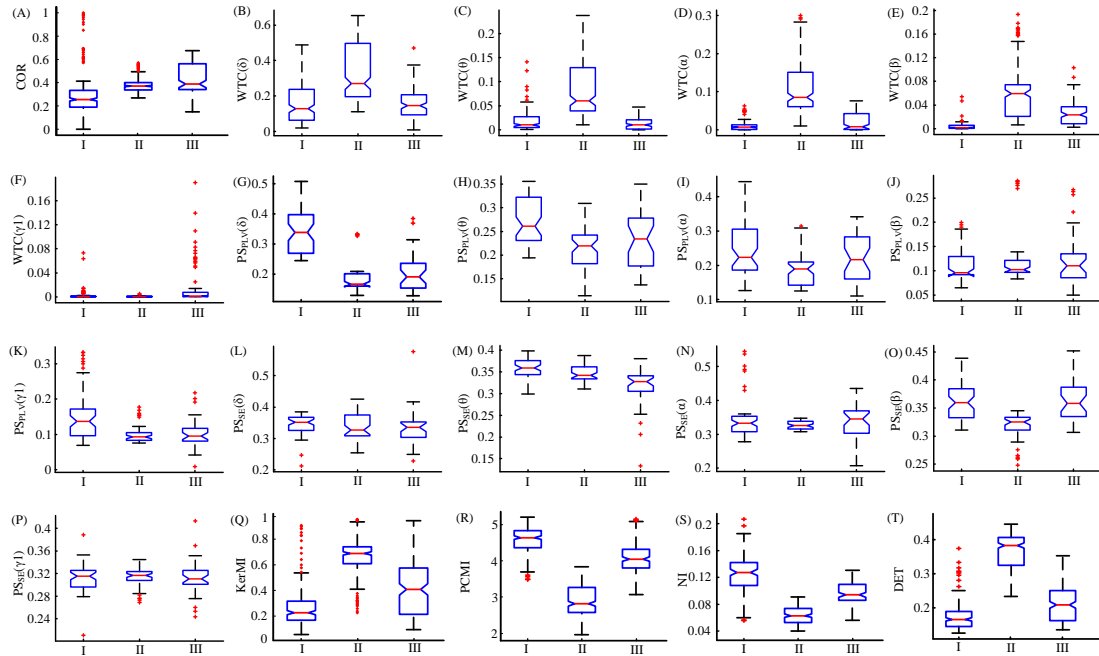


Fig. 11. Box plots of synchronization indexes in different studied periods (I: awake state, II: unconscious state, III: recovery state).

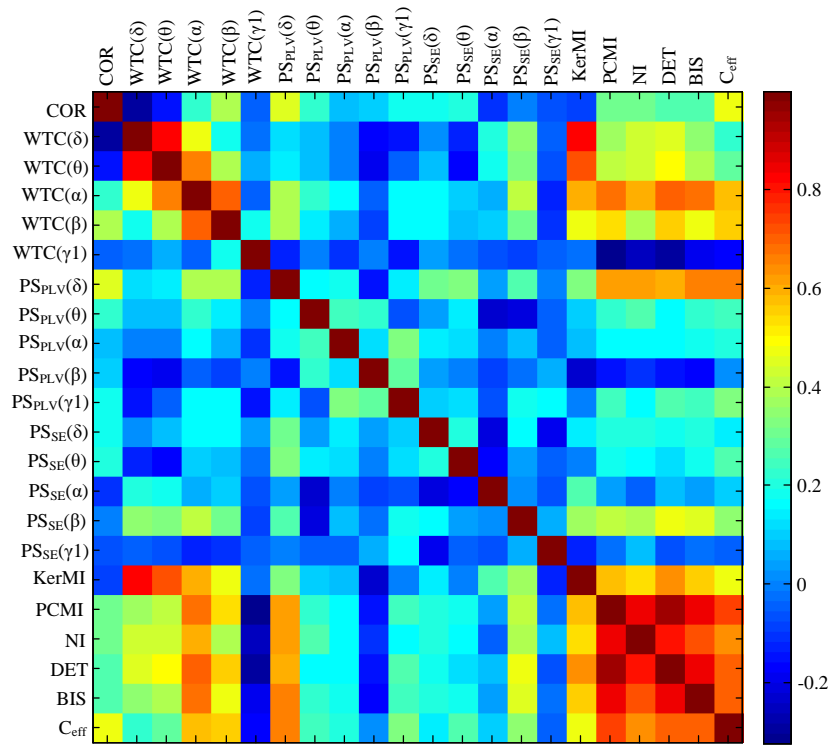


Fig.12. 13 Correlation coefficient  $R$  among synchronization indexes, BIS and  $C_{eff}$  averaged over all subjects.

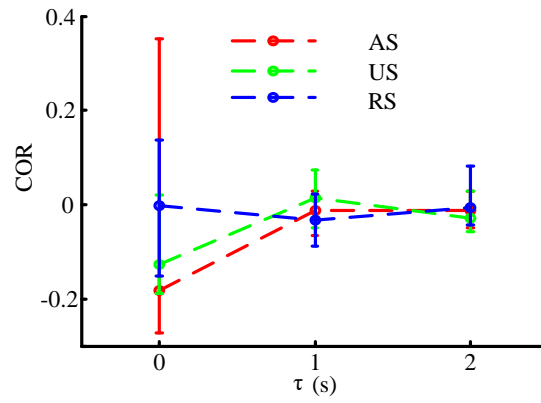


Fig. S1 COR values at different time lag  $\tau$  in awake state(AS) (red), unconscious state(US) (green) and recovery state(RS) (blue).

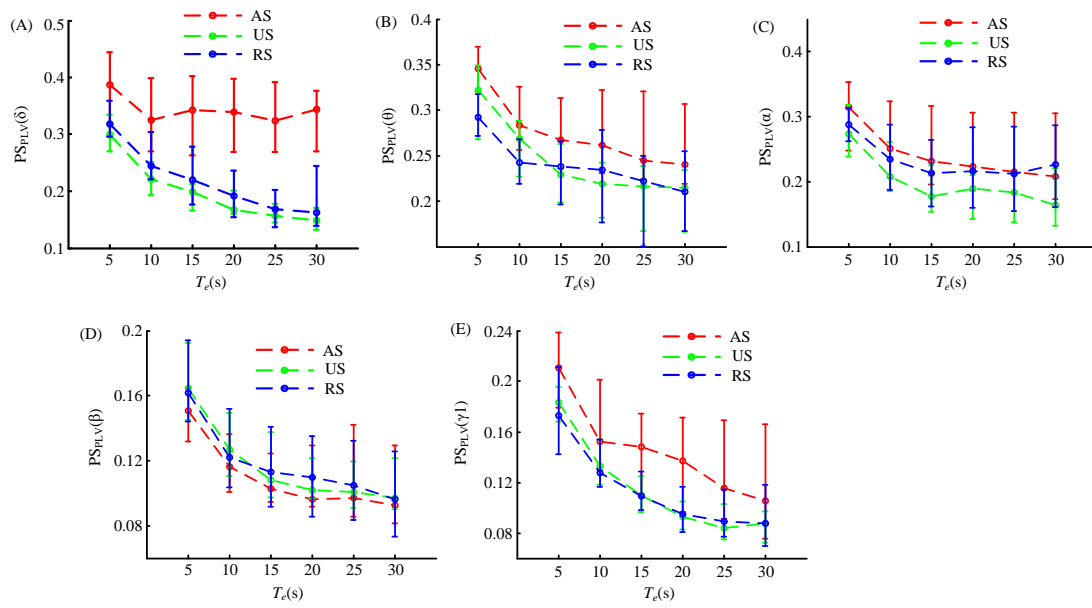


Fig. S2 PS<sub>PLV</sub> values of five frequency bands ( $\delta$ ,  $\theta$ ,  $\alpha$ ,  $\beta$  and  $\gamma_1$ ) of different epoch length  $T_e$  in AS (red), US (green) and RS (blue).

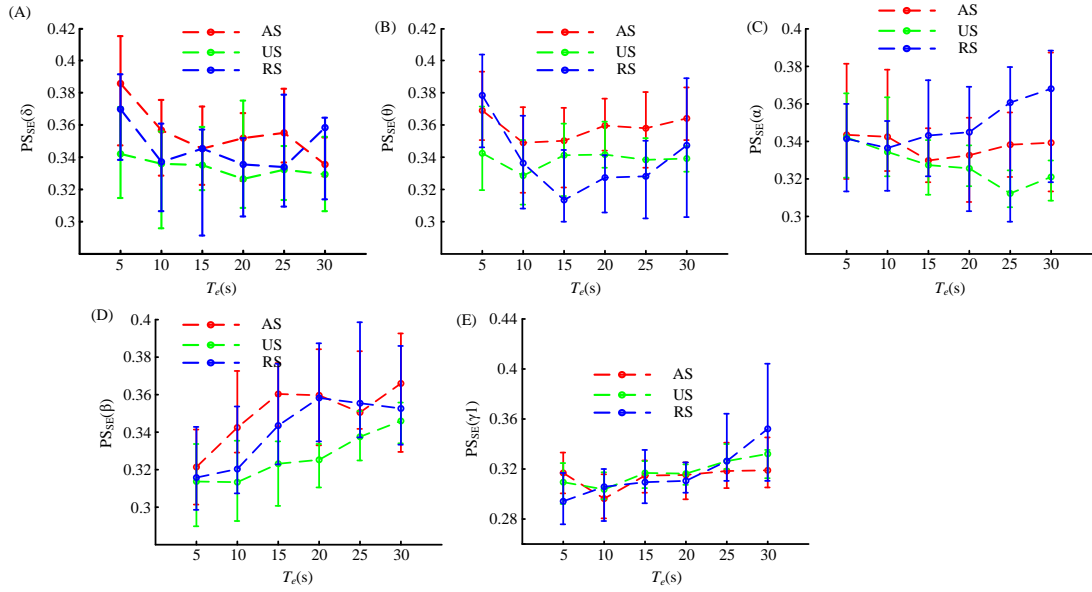


Fig. S3  $PS_{SE}$  values of five frequency bands ( $\delta$ ,  $\theta$ ,  $\alpha$ ,  $\beta$  and  $\gamma1$ ) of different epoch length  $T_e$  in AS (red), US (green) and RS (blue).

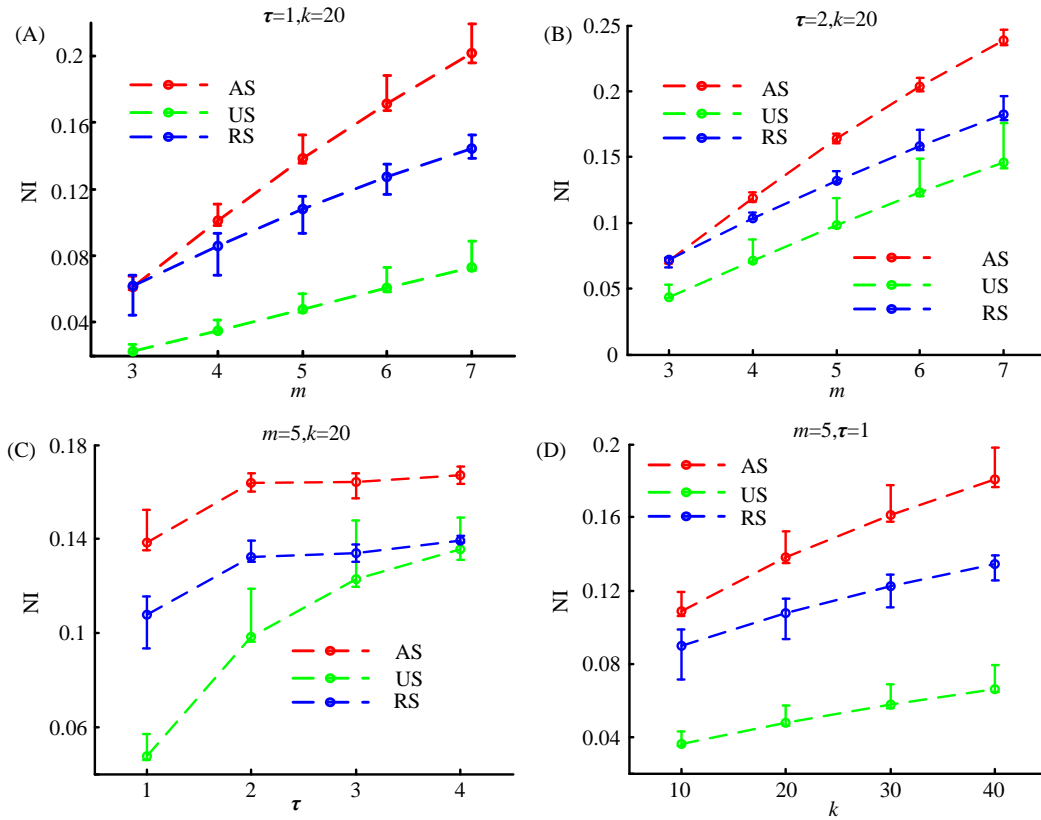


Fig. S4 NI values of different parameters embedding dimension  $m$ , time lag  $\tau$  and the number of nearest neighbors  $k$  in AS (red), US (green) and RS (blue).

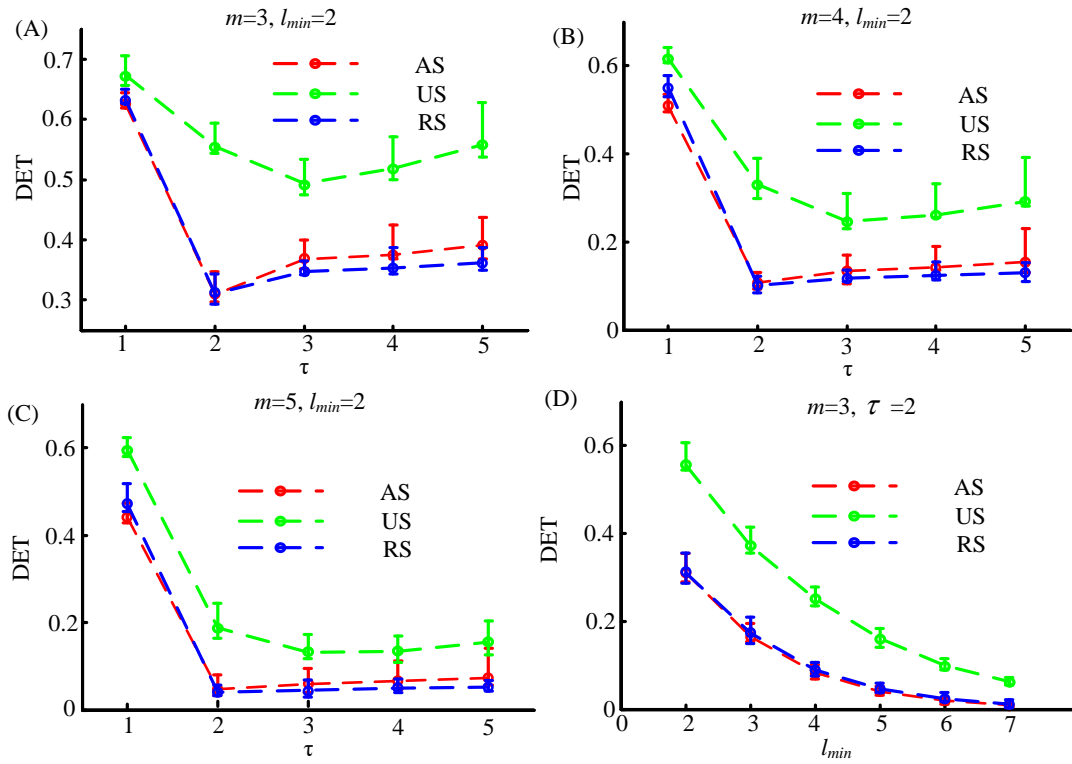


Fig. S5 DET values of different parameters embedding dimension  $m$ , time lag  $\tau$  and threshold of diagonal length  $l_{min}$  in AS (red), US (green) and RS (blue).

## Tables

Table.1. The event times for each subject (in seconds).

Subject	“Object time”	“Syringe-drop time”	“Number time”	“Command time”
#1	180	283	435	475
#2	150	379	732	757
#3	90	357	639	649
#4	90	421	792	802
#5	30	454	*	650
#6	120	289	360	380
#7	180	433	*	588
#8	90	202	*	545
#9	30	401	822	832
#10	90	355	560	570

“Object time” = the time point of the last object remembered for the subject during the induction phase.

“Syringe-drop time” = the time point that the subject dropped the syringe, denoting the end the induction and loss of consciousness.

“Number time” = the time point of the first number remembered during awakening.

\* Subjects who did not remember any number until responding to verbal command.

“Command time” = the time point corresponding to the subject’s correct response to verbal command.

Table 2 Median of  $P_K$  of different synchronization indexes with BIS and  $C_{eff}$

	COR	WTC( $\delta$ )	WTC( $\theta$ )	WTC( $\alpha$ )	WTC( $\beta$ )	WTC( $\gamma_1$ )	PS <sub>PLV</sub> ( $\delta$ )	PS <sub>PLV</sub> ( $\theta$ )	PS <sub>PLV</sub> ( $\alpha$ )	PS <sub>PLV</sub> ( $\beta$ )
BIS	0.579	0.594	0.677	0.753	0.755	0.248	0.711	0.595	0.605	0.399
$C_{eff}$	0.607	0.662	0.621	0.763	0.794	0.393	0.624	0.621	0.615	0.479
	PS <sub>PLV</sub> ( $\gamma_1$ )	PS <sub>SE</sub> ( $\delta$ )	PS <sub>SE</sub> ( $\theta$ )	PS <sub>SE</sub> ( $\alpha$ )	PS <sub>SE</sub> ( $\beta$ )	PS <sub>SE</sub> ( $\gamma_1$ )	KerMI	PCMI	NI	DET
BIS	0.613	0.619	0.545	0.453	0.667	0.460	0.714	0.855	0.783	0.823
$C_{eff}$	0.580	0.509	0.605	0.530	0.688	0.520	0.709	0.794	0.764	0.781

COR = cross correlation;

WTC = coherence based on wavelet transformation;

PS<sub>PLV</sub> = phase synchronization based on phase locking value;

PS<sub>SE</sub> = phase synchronization based on Shannon entropy;

KerMI = mutual information based on kernel estimation;

PCMI = permutation cross mutual information;

NI = nonlinear interdependence;

DET = determinism;

Table 3 CV of the studied indexes at different anesthetic states

	Awake	Unconscious	Recovery
COR	0.633	0.186	0.299
WTC( $\delta$ )	0.684	0.479	0.636
WTC( $\theta$ )	1.206	0.743	0.981
WTC( $\alpha$ )	1.334	0.705	1.118
WTC( $\beta$ )	1.595	0.733	0.822
WTC( $\gamma_1$ )	2.89	1.356	2.077
PS <sub>PLV</sub> ( $\delta$ )	0.243	0.280	0.323
PS <sub>PLV</sub> ( $\theta$ )	0.183	0.263	0.262
PS <sub>PLV</sub> ( $\alpha$ )	0.350	0.290	0.309
PS <sub>PLV</sub> ( $\beta$ )	0.326	0.490	0.480
PS <sub>PLV</sub> ( $\gamma_1$ )	0.491	0.255	0.427
PS <sub>SE</sub> ( $\delta$ )	0.095	0.141	0.185
PS <sub>SE</sub> ( $\theta$ )	0.064	0.059	0.177
PS <sub>SE</sub> ( $\alpha$ )	0.180	0.038	0.155
PS <sub>SE</sub> ( $\beta$ )	0.089	0.079	0.096
PS <sub>SE</sub> ( $\gamma_1$ )	0.082	0.0578	0.103
KerMI	0.627	0.227	0.548
PCMI	0.085	0.146	0.105
NI	0.220	0.165	0.209
DET	0.226	0.138	0.269

The meaning of the indexes refers to the legend of Table 2



### III

## **TEMPORAL-SPATIAL CHARACTERISTICS OF PHASE-AMPLITUDE COUPLING IN ELECTROCORFIGRAM FOR HUMAN TEMPORAL LOBE EPILEPSY**

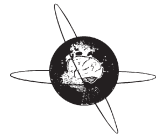
by

Ruihua Zhang, Ye Ren, Chunyan Liu, Na Xu, Xiaoli Li, Fengyu Cong, Tapani Ristanemi & Yuping Wang 2017

Clinical Neurophysiology, 128(9), 1707-1718

DOI: <https://doi.org/10.1016/j.clinph.2017.05.020>

Reproduced with kind permission by Elsevier.



## Temporal-spatial characteristics of phase-amplitude coupling in electrocorticogram for human temporal lobe epilepsy



Ruihua Zhang<sup>a,b,1</sup>, Ye Ren<sup>b,c,1</sup>, Chunyan Liu<sup>a</sup>, Na Xu<sup>b</sup>, Xiaoli Li<sup>d</sup>, Fengyu Cong<sup>c,e</sup>, Tapani Ristaniemi<sup>c</sup>, YuPing Wang<sup>a,f,g,\*</sup>

<sup>a</sup> Department of Neurology, Xuanwu Hospital, Capital Medical University, Beijing 100053, China

<sup>b</sup> Department of Geriatric Medicine, Beijing Luhe Hospital, Capital Medical University, Beijing 101149, China

<sup>c</sup> Department of Mathematical Information Technology, University of Jyväskylä, Jyväskylä 40014, Finland

<sup>d</sup> State Key Laboratory of Cognitive Neuroscience and Learning & IDG/McGovern Institute for Brain Research, Beijing Normal University, Beijing 100875, China

<sup>e</sup> Department of Biomedical Engineering, Faculty of Electronic Information and Electrical Engineering, Dalian University of Technology, Dalian 116024, China

<sup>f</sup> Beijing Key Laboratory of Neuromodulation, Beijing 100053, China

<sup>g</sup> Center of Epilepsy, Beijing Institute for Brain Disorders, Beijing 100053, China

### ARTICLE INFO

#### Article history:

Accepted 31 May 2017

Available online 28 June 2017

#### Keywords:

ECoG

Temporal lobe epilepsy

Cross-frequency coupling

Modulation index

Fall-max pattern

### HIGHLIGHTS

- Phase-amplitude coupling (PAC) can provide relevant information for the lateralization and localization of epileptic foci.
- The “fall-max” pattern was found to be a reliable biomarker in the mid-seizure period.
- Strong PAC appeared mainly between  $\delta$ ,  $\theta$ , and  $\alpha$  oscillations and  $\gamma$  and ripple oscillations.

### ABSTRACT

**Objective:** Neural activity of the epileptic human brain contains low- and high-frequency oscillations in different frequency bands, some of which have been used as reliable biomarkers of the epileptogenic brain areas. However, the relationship between the low- and high-frequency oscillations in different cortical areas during the period from pre-seizure to post-seizure has not been completely clarified.

**Methods:** We recorded electrocorticogram data from the temporal lobe and hippocampus of seven patients with temporal lobe epilepsy. The modulation index based on the Kullback-Leibler distance and the phase-amplitude coupling co-modulogram were adopted to quantify the coupling strength between the phase of low-frequency oscillations (0.2–10 Hz) and the amplitude of high-frequency oscillations (11–400 Hz) in different seizure epochs. The time-varying phase-amplitude modulogram was used to analyze the phase-amplitude coupling pattern during the entire period from pre-seizure to post-seizure in both the left and right temporal lobe and hippocampus. Channels with strong modulation index were compared with the seizure onset channels identified by the neurosurgeons and the resection channels in the clinical surgery.

**Results:** The phase-amplitude coupling strength (modulation index) increased significantly in the mid-seizure epoch and decrease significantly in seizure termination and post-seizure epochs ( $p < 0.001$ ). The strong phase-amplitude-modulating low- and high-frequency oscillations in the mid-seizure epoch were mainly  $\delta$ ,  $\theta$ , and  $\alpha$  oscillations and  $\gamma$  and ripple oscillations, respectively. The phase-amplitude modulation and strength varied among channels and was asymmetrical in the left and right temporal cortex and hippocampus. The “fall-max” phase-amplitude modulation pattern, i.e., high-frequency amplitudes were largest in the low-frequency phase range  $[-\pi, 0]$ , which corresponded to the falling edges of low-frequency oscillations, appeared in the middle period of the seizures at epileptic focus channels. Channels with strong modulation index appeared on the corresponding left or right temporal cortex of surgical resection and overlapped with the clinical resection zones in all patients.

**Conclusions:** The “fall-max” pattern between the phase of low-frequency oscillation and amplitude of high-frequency oscillation that appeared in the middle period of the seizures is a reliable biomarker in

\* Corresponding author at: No. 45, Changchun Street, Xicheng District, Beijing 100053, China. Fax: +86 10 69543901 1051.

E-mail address: [wangyupingcn@163.com](mailto:wangyupingcn@163.com) (Y. Wang).

<sup>1</sup> These authors contributed equally to this work.

epileptogenic cortical areas. The modulation index can be used as a good tool for lateralization and localization for the epileptic focus in patients with epilepsy.

**Significance:** Phase-amplitude coupling can provide meaningful reference for accurate resection of epileptogenic focus and provide insight into the underlying neural dynamics of the epileptic seizure in patients with temporal lobe epilepsy.

© 2017 International Federation of Clinical Neurophysiology. Published by Elsevier Ireland Ltd. All rights reserved.

## 1. Introduction

Abnormal discharge of neurons in the epileptic human brain causes the specificity of the neural oscillations of the cerebral cortex. The low- and high-frequency neural oscillations of some frequency bands have been known as the essential biomarkers of epileptogenicity and epileptic seizure onset zones. The dynamic process of very low-frequency oscillations (LFOs) in the intracranial electroencephalographic recordings has been found to occur during the preictal state in patients with refractory epilepsy (Ren et al., 2011). Ictal infraslow activity and ictal high-frequency oscillations (HFOs) both represent the core of the tissue generating seizures in patients with epilepsy (Imamura et al., 2011; Kanazawa et al., 2015). Moreover, Crépon et al. used the semi-automatic detection procedure of wavelet decomposition to confirm the generation of interictal HFOs of over 200 Hz in medial and polar temporal lobes, which was regarded as a reliable marker of the seizure onset zone (Crépon et al., 2010). Resection of cortical areas generating fast ripples (>200 Hz) and ripples on a flat background activity has also been found to show a significant correlation with seizure-free outcome (Kerber et al., 2014). Moreover, temporal changes in ripples (100–250 Hz) and fast ripples (250–500 Hz) during different seizure periods have been found to vary greatly between individual patients with epilepsy (Pearce et al., 2013). These LFOs and HFOs that occur in patients with epilepsy have been considered potential biomarkers of epileptogenesis. However, they offered limited insight into the features of neural oscillations during the epileptic seizures because the complex neural activities in the epileptic cerebral cortex are constituted by simultaneous neural oscillations in different frequency bands.

The interactions between neural oscillations in different frequency bands, which are termed as cross-frequency coupling (CFC), play an important role in investigating the mechanisms of the communication and connectivity in neural networks. Phase-amplitude coupling (PAC), a form of CFC in which the phase of LFO modulates the amplitude of HFO, has become a rising concern in recent studies. Alvarado-Rojas et al. used cross-frequency PAC in ECoG of patients with partial epilepsy to predict the seizures (Alvarado-Rojas et al., 2011). CFC between the amplitude of pathological HFOs and the phase of  $\theta$  and  $\alpha$  rhythms was found to be significantly elevated in the seizure onset zone compared to non-epileptic regions in patients with partial epilepsy (Ibrahim et al., 2014). Moreover, Guirgis et al. adopted the measures of modulation index (MI) and eigenvalue decomposition to confirm that  $\delta$ -modulated HFOs could provide more accurate localization of epileptogenic zones in patients with extratemporal lobe epilepsy (Guirgis et al., 2015a). Recently, MI was also used to determine the predictive accuracy of seizure onset sites and eloquent areas in children with focal epilepsy, which suggested that epileptogenic HFOs might be coupled with slow waves of 3–4 Hz more preferentially than slow waves of 0.5–1 Hz (Nonoda et al., 2016). In addition, PAC was estimated from the synchronization index for ECoG from patients with refractory temporal lobe epilepsy and accurately distinguished the ictal state from interictal state with strong

coupling between the phase of  $\beta$  oscillation and the amplitude of high  $\gamma$  oscillation (Edakawa et al., 2016).

Previous studies concentrated more on the coupling strength, coupling frequency bands, or coupling areas of the brain between the phase of LFO and amplitude of HFO. However, the coupling patterns of phase-amplitude interaction in different brain areas during non-seizure and seizure periods remain unclear. Therefore, this study aimed to investigate whether PAC differs in different seizure periods and in what forms do the low-frequency phase and high-frequency amplitude couple. Moreover, we aimed to estimate whether PAC differs in the left and right temporal cortex and hippocampi of patients with temporal lobe epilepsy.

To address and better understand these issues, we collected the ECoG data from the left and right temporal cortex and hippocampi of seven patients with temporal lobe epilepsy. We adopted the MI based on the Kullback-Leibler distance (Tort et al., 2010), PAC comodulogram, and time-varying phase-amplitude modulogram (Mukamel et al., 2011) to explore the temporal-spatial characterization of PAC strength and patterns during the period from pre-seizure to post-seizure in both sides of the cortex (see Materials and methods for details).

## 2. Materials and methods

### 2.1. Data recordings and preprocessing

We obtained ECoG recordings from subdural strip electrodes implanted in seven patients. Six patients presented with suspected bilateral temporal lobe epilepsy, and one presented with right temporal lobe epilepsy. All patients provided written informed consent, and the study was approved by the ethics committees of Xuanwu Hospital (Patient A, B, C, and D) and Luhe Hospital (Patient E, F, and G). All seven patients had pathologically focal cortical dysplasia (FCD). The clinical characteristics of each patient are summarized in Table 1. The cortical electrode strip (2.5 mm diameter platinum electrodes positioned 10 mm apart center-to-center) and depth electrode strip (1.2 mm diameter platinum electrodes positioned 10 mm apart center-to-center) were implanted on the temporal lobes and hippocampi of each patient, respectively. All electrode strips were placed symmetrically on the left and right cerebral cortex, except for patient E. The strips of patient E were placed only on the right cerebral cortex. The spatial distribution of preoperative intracranial electrode strips of patient A is shown in Fig. 1A. The top panel shows the left and right views of cerebral cortex, while the bottom panel shows the top and upward views of cerebral cortex. We arranged all the electrode strips in a plane (Fig. 1B) to allow for easy observation.

ECoG signals were continuously recorded day and night for the preoperative assessment of all patients using a video-EEG monitoring system (PN-NET, Beijing Yunshen Technology, China). An electrode located far from the epileptic focus was used as the reference electrode. The sampling frequency of the ECoG data was 2048 Hz. The ECoG data were exported as European Data Format Plus (EDF+) files and imported into EEGLAB for changing the file format

**Table 1**  
Clinical characteristics of seven patients.

Patients/seizure number	Sex	Age (years)	Epilepsy duration (years)	Seizure semiology	MRI findings	MEG abnormal current source	Interictal EEG	Pathology	Strip electrode placement/ Electrode contacts	Resection side	Follow-up period (months)/ Surgical outcome (Engel Class)
A/1, 2, 3	F	24	6	LoC, Bilateral hand automatism, Automatism of right leg; Convulsions of the limbs	RHS	Mainly in LTL	Left posterior temporal sharp waves	HS+FCD IIIa	LH, LTP, LTB, RH, RTP, RTB/44	R	26/I
B/4	F	46	28	LoC, Bilateral hand automatism	No abnormalities	Mainly in LTL, occasionally in RTL	Bilateral sphenoid spikes	FCD I	LTP, LTB, RTP, RTB/32	L	53/II
C/5	M	22	18	Convulsions of the limbs	LHS	–	Bilateral frontal and sphenoid spikes and sharp waves	HS+FCD I	LH, LTB, LPTB, RH, RTB, RPTB/48	L	55/II
D/6, 7	M	33	11	Convulsions of the limbs	LHS	Mainly in LTL, occasionally in RTL	–	Severe HS	LH, LTP, LTB, RH, RTP, RTB/38	L	54/I
E/8, 9	F	28	19	LoC, Involuntary movements; Convulsions of the limbs	No abnormalities	RTL	Right frontal and central sharp waves	FCD I	RH, RTP, RTB, RPTL, RFPL/64	R	27/I
F/10, 11	F	28	23	LoC, Bilateral hand automatism; Eyes on the turn accompanied by nausea; Convulsions of the limbs	Suspected bilateral HS	–	Bilateral sphenoid spikes	FCD I+Gray matter heterotopia	LTP, LTB, LTO, RTP, RTB, RTO/48	R	34/III
G/12	M	21	18	LoC, Convulsions of the limbs	No abnormalities	–	Bilateral sphenoid sharp waves	HS+FCD IIIa	LTP, LTB, LTO, RTP, RTB, RTO/48	R	29/III

F: female, M: male, L: left, R: right, H: hippocampus, TL: temporal lobe, TP: temporal pole, TB: temporal base, PTL: posterior temporal lobe, PTB: posterior temporal base, FPL: frontal-parietal lobe, TO: temporal-occipital, LoC: loss of consciousness, HS: hippocampal sclerosis, FCD: focal cortical dysplasia.

to MAT. We recorded the ECoG data of 16 seizures across 7 patients in total and selected 12 seizures for analysis, which included complete spontaneous epileptic seizures from each patient. The data of other four seizures were not used for analysis because of incomplete data recording, which did not contain the data from the pre-seizure or post-seizure period. All ECoG data segments were selected from about 1 min before seizure onset time to about 1 min after seizure termination time. The ECoG data segments were down-sampled to 1024 Hz first and then filtered with a 0.2 Hz high-pass filter for removing baseline interference. Power frequency noise (50 Hz) and harmonic noises were then removed by the notch filter. We also removed large-amplitude artifacts in the ECoG data of each patient and rejected the bad channels by visual inspection. Fig. 2A shows the preprocessed ECoG data of channel 38 from patient A. Both the seizure onset time ( $t_{SO}$ ) and the seizure termination time ( $t_{ST}$ ) were determined by neurologists clinically and labeled on the time coordinate. The seizure onset channels were also clinically defined as electrodes with earliest ictal activity, named focal fast waves.

## 2.2. Phase-amplitude coupling analysis

MI based on the Kullback-Leibler distance (Tort et al., 2010) was adopted to quantify the strength of PAC. Time-varying phase-amplitude modulogram (Mukamel et al., 2011) was used to characterize the PAC pattern between two specific frequency bands during the period from pre-seizure to post-seizure.

The computing process for PAC is described in Fig. 3 and includes the following steps:

- (i) Filter the ECoG data  $X(t)$  using a bandpass filter (*eegfilt.m* in EEGLAB toolbox) to construct a narrow-band low-frequency signal  $X_L(t)$  and a high-frequency signal  $X_H(t)$ .
- (ii) Extract the instantaneous phase  $\varphi_L(t)$  and instantaneous amplitude  $A_H(t)$  from  $X_L(t)$  and  $X_H(t)$ , respectively, by using the Hilbert transform.
- (iii) Segment  $\varphi_L(t)$  and  $A_H(t)$  into 10-s epochs with an overlap of 90%. The phase and amplitude in each epoch  $k$  is denoted as  $\varphi_{L_k}(t)$  and  $A_{H_k}(t)$  ( $k = 1, 2, \dots, K$ ). Divide the phase range

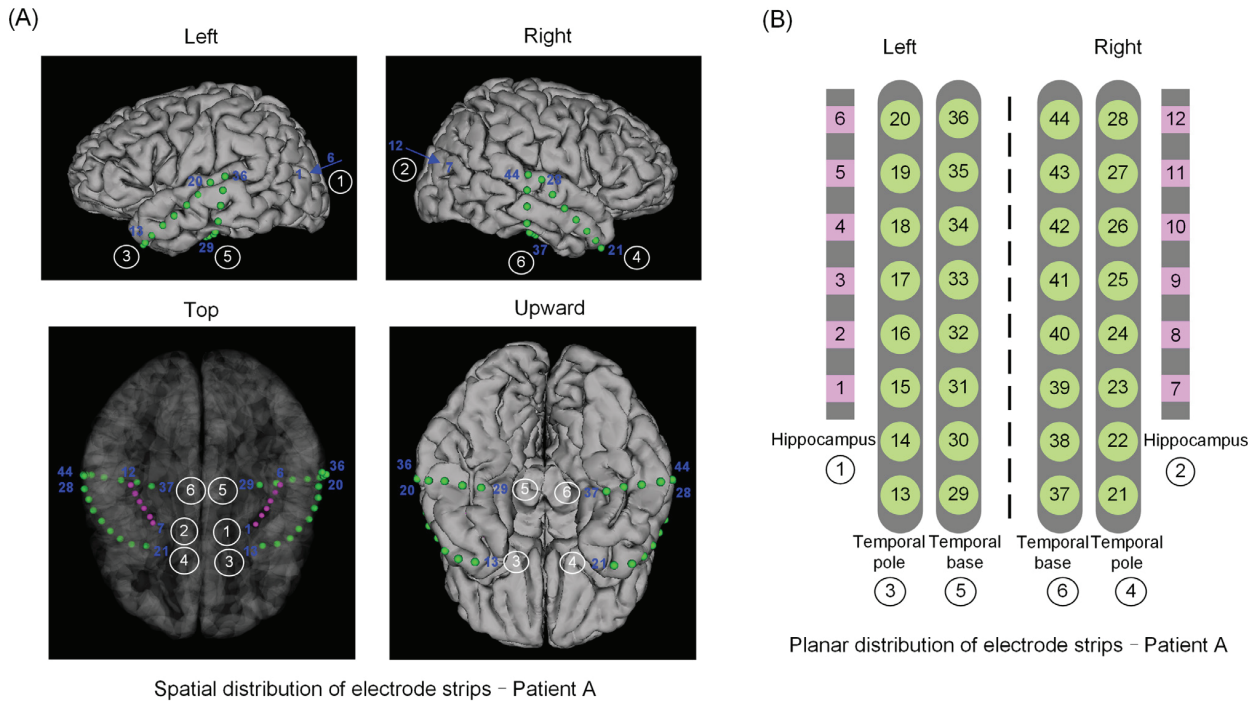


**Fig. 1.** (A) Three-dimensional distribution of the electrode strips of patient A. The electrode strip ① and ② with purple color were implanted in both left (6 × 1, channel 1–6) and right (6 × 1, channel 7–12) hippocampi. The electrode strips ③, ④, ⑤, and ⑥ with green color were implanted in the left (8 × 1, channel 13–20) and right (8 × 1, channel 21–28) temporal pole and in the left (8 × 1, channel 29–36) and right (8 × 1, channel 37–44) temporal base. The blue numbers marked beside the electrode strips denote the channel number on the strips. (B) Planar distribution of all arranged electrode strips of patient A. (For interpretation of the references to color in this figure legend, the reader is referred to the web version of this article.)

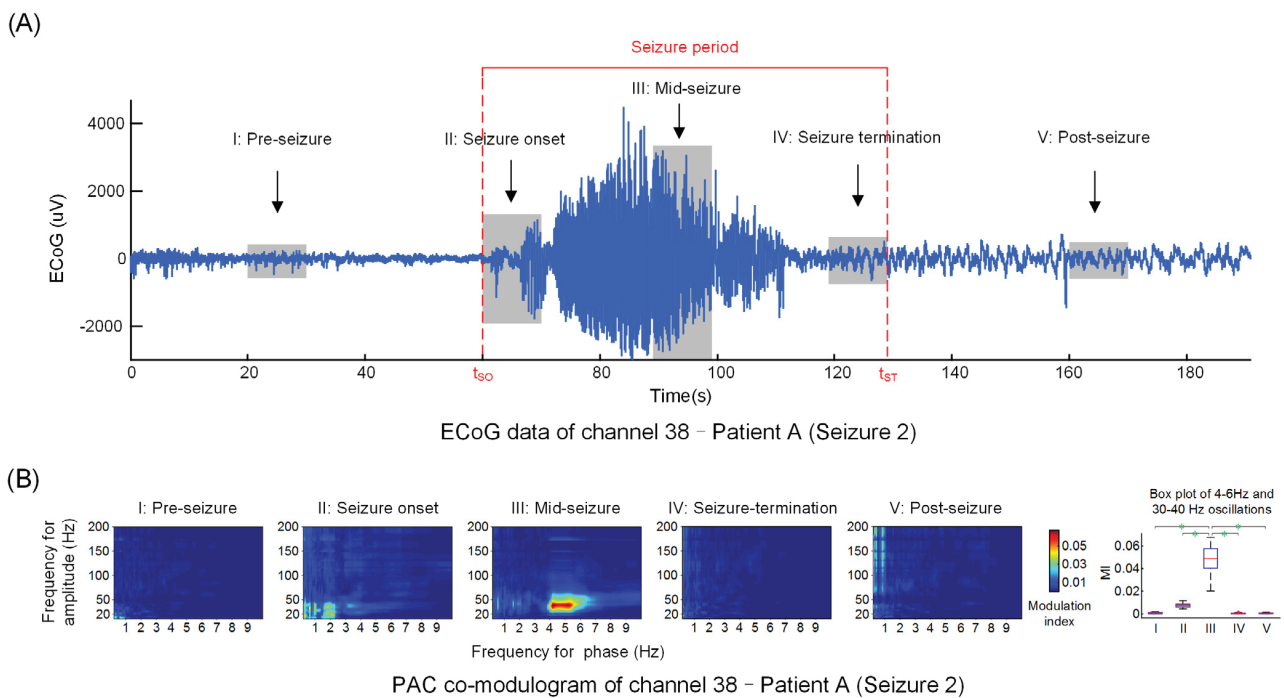


**Fig. 2.** (A) Preprocessed ECoG data of channel 38 from patient A during the period from pre-seizure to post-seizure. Two red dotted lines denote the seizure onset time  $t_{s0}$  and seizure termination time  $t_{sT}$ , respectively. The gray rectangles indicate the five selected 10-s seizure epochs, i.e., pre-seizure (I), seizure onset (II), mid-seizure (III), seizure termination (IV), and post-seizure (V). (B) PAC co-modulograms set between the phase of 0.2–10 Hz in steps of 0.1 Hz and the amplitude of 11–200 Hz in steps of 1 Hz of five seizure epochs and corresponding box plots of  $MI$  values in the co-modulograms between 4–6-Hz and 30–40-Hz oscillations among the five epochs. The notation \* indicates significant difference in  $MI$  values at  $p < 0.001$ . (For interpretation of the references to color in this figure legend, the reader is referred to the web version of this article.)

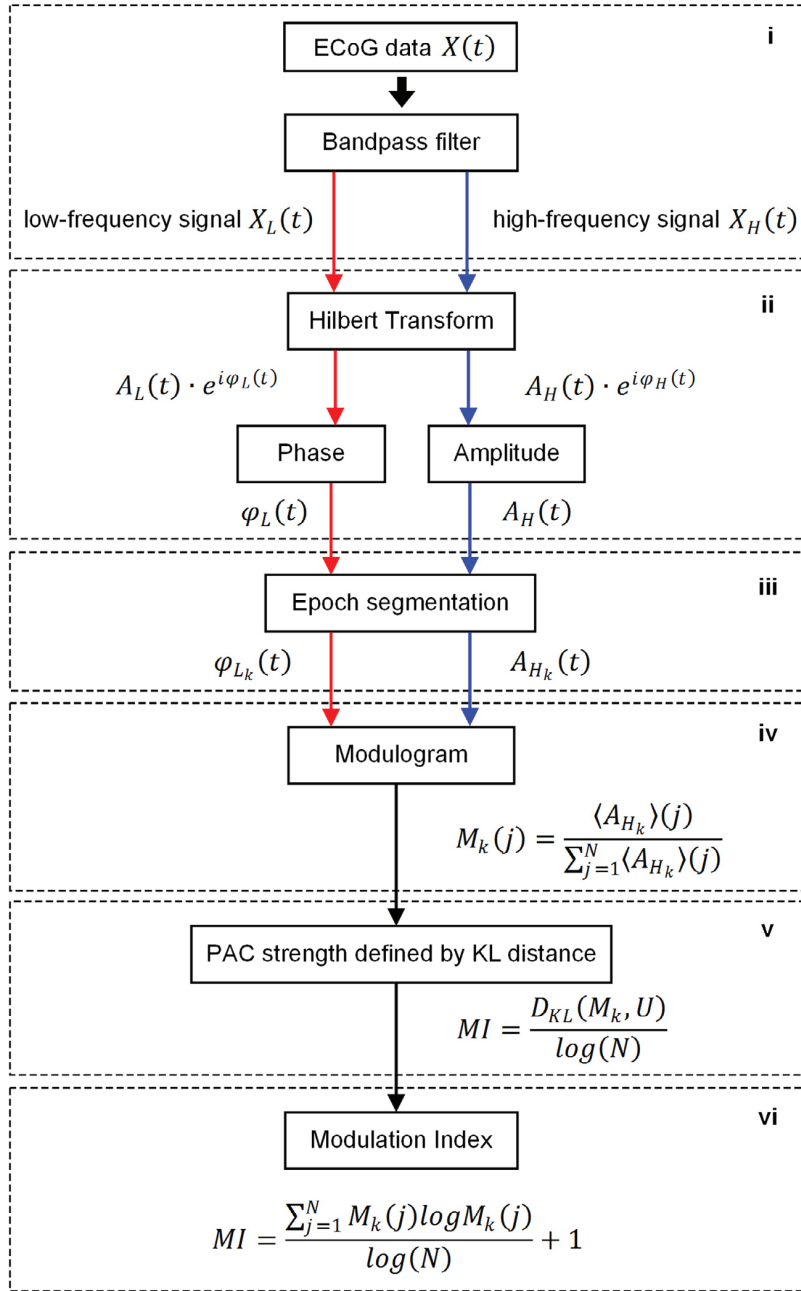


Fig. 3. Schematic presentation of the phase-amplitude analysis procedures.

$[-\pi, +\pi]$  into 18 equal intervals (the length of each interval is  $\pi/9$ ,  $N = 18$ ).

- (iv) In each epoch  $k$ , assign all instantaneous phases of  $\phi_{L_k}(t)$  to one of the 18 phase bins  $j$ ,  $j = 1, 2, \dots, N$ . The instantaneous phase and the corresponding instantaneous amplitude are denoted as  $\phi_{L_{kj}}(t)$  and  $A_{H_{kj}}(t)$ , respectively. The mean amplitude in each phase bin  $j$  is denoted  $\langle A_{H_k} \rangle(j)$ . Then we normalize the mean amplitudes over the 18 phase bins  $M_k(j) = \frac{\langle A_{H_k} \rangle(j)}{\sum_{j=1}^N \langle A_{H_k} \rangle(j)}$  to obtain the time-varying phase-amplitude modulogram.

- (v) The  $MI$  is defined by dividing the KL distance of the modulogram distribution  $M_k(j)$  from the uniform distribution  $U(j)$  by  $\log(N)$ . The  $MI$  is denoted as  $MI = \frac{D_{KL}(M_k, U)}{\log(N)}$ , where the  $D_{KL}(M_k, U) = \sum_{j=1}^N M_k(j) \log \left[ \frac{M_k(j)}{U(j)} \right]$ .
- (vi) Considering  $U(j) = 1/N, j = 1, 2, \dots, N$ , the  $MI$  can be denoted as  $MI = \frac{\sum_{j=1}^N M_k(j) \log M_k(j)}{\log(N)} + 1$ , which quantifies the strength of PAC between LFOs and HFOs. The  $MI$  ranges from 0 to 1, where an  $MI$  value of 0 represents lack of PAC and  $MI$  of 1 reflects strong PAC.

Narrow-band low-frequency and high-frequency ECoG data were filtered at 0.2–10 Hz in steps of 0.1 Hz and 11–400 Hz in steps of 1 Hz, respectively. The *MI* was computed between the narrow-band low-frequency and high-frequency data in 10-s windows with an overlap of 90%.

### 2.3. Statistical analysis

We assessed the statistical significance of *MI* by permutation test (Mukamel et al., 2014). Two hundred random time shifts were generated from a uniform distribution on the interval [−5 s, 5 s]. We computed the permuted *MI*  $MI_{perm}$  using the original phase and the shifted amplitude. Then, the *MI* was considered significant if it was larger than 95% of the 200 permuted values  $MI_{perm}$ . Matlab Statistics Toolbox was also applied for statistics. To assess the changes in PAC strength during the period from pre-seizure to post-seizure, we compared the *MI* values between specific LFOs and HFOs in five seizure epochs (pre-seizure, seizure onset, mid-seizure, seizure termination, and post-seizure epoch) of each patient. We used the Kruskal-Wallis test (*kruskalwallis.m*) and multiple comparison test (*multcompare.m*) to determine significant differences in the *MI* among different seizure epochs. The *MI* values were presented using a box plot. In addition, *MI* values between seizure-specific LFOs and HFOs in the mid-seizure epoch of all electrode channels of each patients were compared using the Kruskal-Wallis test (*kruskalwallis.m*) and multiple comparison test (*multcompare.m*) to determine a significant difference of PAC strength cross all channels.  $p < 0.01$  was considered significant and marked with the notation \*.

## 3. Results

### 3.1. Time-varying phase-amplitude modulation during temporal seizure

To quantify the strength of PAC of ECoG signals during seizure period for all patients, we computed the *MI* value along the entire period of all channels for each patient. To investigate the specificity of PAC in different time periods of temporal seizure, 10-s pre-seizure, seizure onset, mid-seizure, seizure termination and post-seizure epochs were selected from all channels for each patient. Five seizure epochs in Patient A are shown with the gray rectangles marked on one channel's ECoG signal in Fig. 2A. The seizure onset epoch was selected from  $t_{SO}$  to 10 s afterward, and the seizure termination epoch was selected from  $t_{ST}$  to 10 s forward. The mid-seizure epoch was chosen from 5 s before and after the middle time point of seizure period (from  $t_{SO}$  to  $t_{ST}$ ). Pre-seizure and post-seizure epochs were selected approximately 30 s before and after the seizure onset and seizure termination epoch, respectively.

Then, we computed the *MI* between each low-frequency (0.2–10 Hz in steps of 0.1 Hz) phase and high-frequency (11–400 Hz in steps of 1 Hz) amplitude in five selected epochs from all channels of each patient, which constructed the PAC co-modulogram. The co-modulogram in each epoch from channel 38 (at right temporal base) of patient A (seizure 2) is shown in Fig. 2B. The frequency for the amplitude was set at 11–200 Hz in the figure, which enlarged the displayed *MI* values. It can be seen from Fig. 2B that the *MI* values from various epochs of seizure differed, which demonstrated the temporal specificity of PAC along the entire period. Obviously, there is a strong coupling between the phase of 4–6-Hz oscillations and amplitude of 30–40-Hz oscillations in the mid-seizure epoch.

To further determine the significant difference of *MI* in different co-modulograms, we compared the *MI* values of 4–6-Hz and 30–40-Hz oscillations among the five seizure epochs. Box plots of *MI*

values of the five epochs are shown in the right panel of Fig. 2B. All *MI* values in the box plot were statistically significant ( $p < 0.05$ , permutation test). As can be seen from the box plot, the *MI* significantly increased in the mid-seizure epoch and significantly decreased in the seizure termination and post-seizure epochs ( $p < 0.001$ , Kruskal-Wallis test).

The co-modulograms in five seizure epochs and their corresponding box plots in one selected channel of seven patients (12 recorded seizures in total) are illustrated in Fig. 4. As can be seen from the figure, a strong *MI* appeared in the mid-seizure epoch in all 12 recorded seizures from all patients. For patient A, strong phase-amplitude modulation was observed between 4–6-Hz and 30–40-Hz or 30–50-Hz oscillations in three seizures (seizures 1, 2, and 3), which belonged to the  $\theta$  oscillation in LFO and  $\gamma$  oscillation in HFO. For patient B (seizure 4), strong modulation existed in 6–8-Hz and 60–100-Hz oscillations, i.e., the  $\theta$  oscillation in LFO and  $\gamma$  and ripple oscillations in HFO. Similarly, patient C (seizure 5) had a strong modulation in 4–5-Hz and 30–80-Hz oscillations, which were in the range of the  $\theta$  oscillation in LFO and  $\gamma$  oscillation in HFO. Unlike patient A, B, and C, the LFOs of patient D (seizures 6 and 7) remained in  $\alpha$  oscillation modulating the  $\gamma$  and ripple oscillations in HFO. The LFOs of patient E (seizures 8 and 9) and F (seizures 10 and 11) were observed in  $\delta$  oscillation modulating the  $\gamma$  or ripple oscillation in HFO. For patient G (seizure 12),  $\gamma$  and ripple oscillations were modulated by the 7–9-Hz oscillations in LFO. The LFOs and HFOs of strong phase-amplitude modulation in the mid-seizure epoch of each patient are illustrated in Table 2. The strong phase-amplitude modulating LFOs and HFOs in the mid-seizure epoch of 12 seizures (seven patients) were mainly  $\delta$ ,  $\theta$ , and  $\alpha$  oscillations and  $\gamma$  and ripple oscillations, respectively. In addition, *MI* values of seizure-specific frequency oscillations in five seizure epochs were compared and showed significant difference by box plots (right panel of Fig. 4). All *MI* values in the box plots had statistical significance ( $p < 0.05$ , permutation test). It can be seen from all box plots that the *MI* values in the mid-seizure epoch were significantly larger than those in other four seizure epochs (pre-seizure, seizure onset, seizure termination, and post-seizure epochs) ( $p < 0.001$ , Kruskal-Wallis test). These results demonstrate that the modulation between the phase of LFOs and amplitude of HFOs differs during different epochs of temporal seizures. Temporal seizures make the low-frequency phase and high-frequency amplitude have a strong modulation between  $\delta$ ,  $\theta$ , and  $\alpha$  oscillations and  $\gamma$  and ripple oscillations in the middle seizure period rather than during other seizure epochs and non-seizure period.

### 3.2. Spatial specificity of phase-amplitude modulation in the mid-seizure epoch

As can be seen from the co-modulograms in seizure epochs in the selected channel of 12 recorded seizures, mid-seizure epoch exhibited significantly strong phase-amplitude modulation (Fig. 4). We considered the hypotheses that whether phase-amplitude modulation in the mid-seizure epoch differed in different regions of left and right temporal cortex and whether the spatial specificity of phase-amplitude modulation was related to the location of the epilepsy lesions. Therefore, we computed the co-modulogram in the mid-seizure epoch in all channels from the 12 seizures from 7 patients. Fig. 5A shows the co-modulograms in the mid-seizure epoch of 43 channels of patient A (seizure 2). The bad channel 12 on the electrode strip ② implanted in the right hippocampus was rejected. The distribution of the co-modulogram in each channel was same as that of the electrodes on the arranged strips in Fig. 1B. Co-modulograms in the left hippocampus, left temporal pole, and left temporal base and in the right hippocampus, right temporal pole, and right temporal base are in the left and right panel of the figure, respectively. *MI* values in the

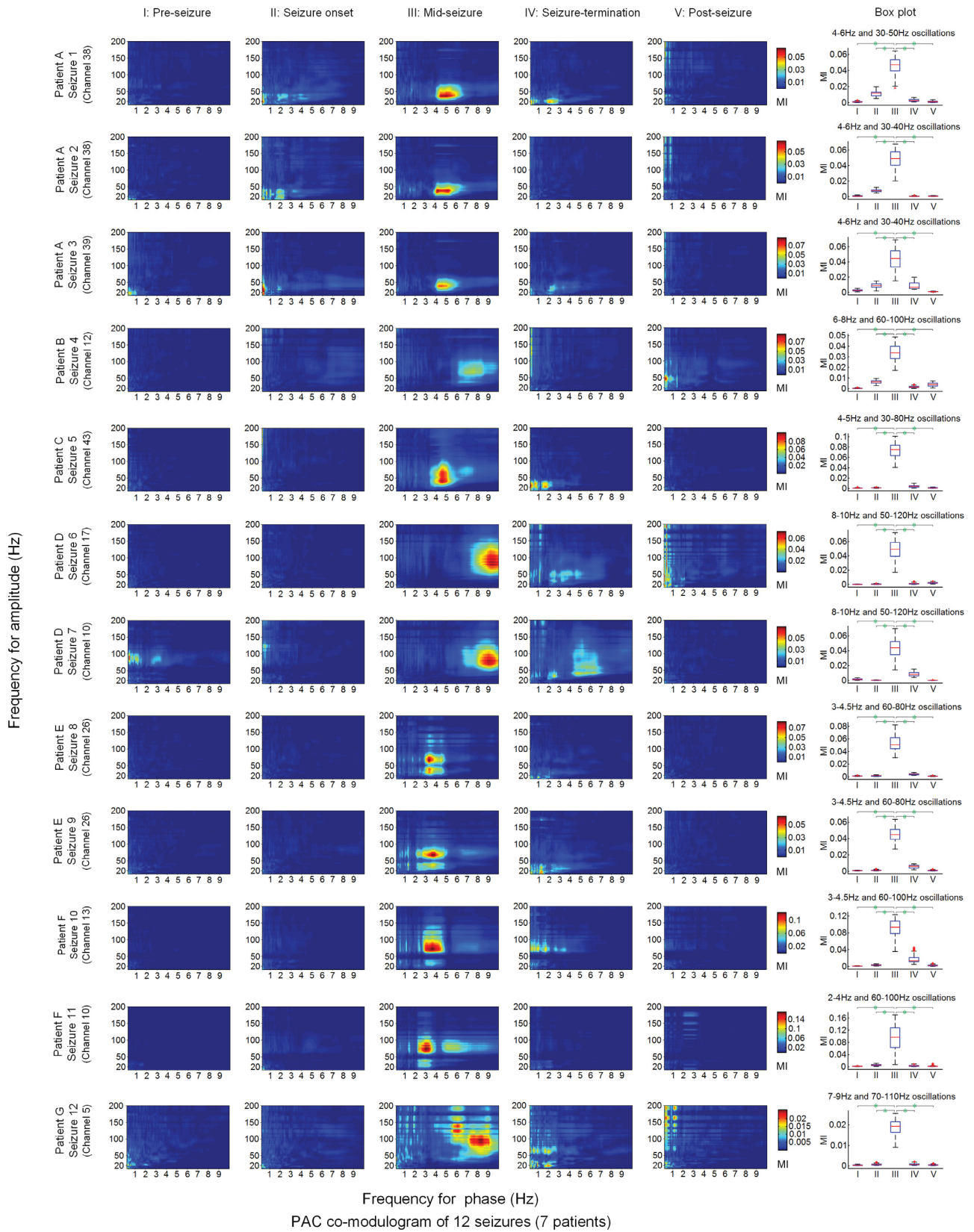


**Fig. 4.** PAC co-modulograms in five seizure epochs and the corresponding box plots of *MI* values of one selected channel from total 12 recorded seizures from 7 patients. Frequency for phase (0.2–10 Hz in steps of 0.1 Hz) and amplitude (11–200 Hz in steps of 1 Hz) are indicated on the horizontal and vertical axes, respectively.

**Table 2**  
Frequency band of oscillation of strong MI in the mid-seizure epoch of the selected channel in 12 seizures from seven patients.

Seizure/Patient	1/A	2/A	3/A	4/B	5/C	6/D	7/D	8/E	9/E	10/F	11/F	12/G
LFO	θ	θ	θ	θ	θ	A	α	δ	δ	δ	δ	θ and α
HFO	γ	γ	γ	γ and ripple	γ	γ and ripple	γ and ripple	γ	γ	γ and ripple	γ and ripple	γ and ripple

LFO: low-frequency oscillation, HFO: high-frequency oscillation.

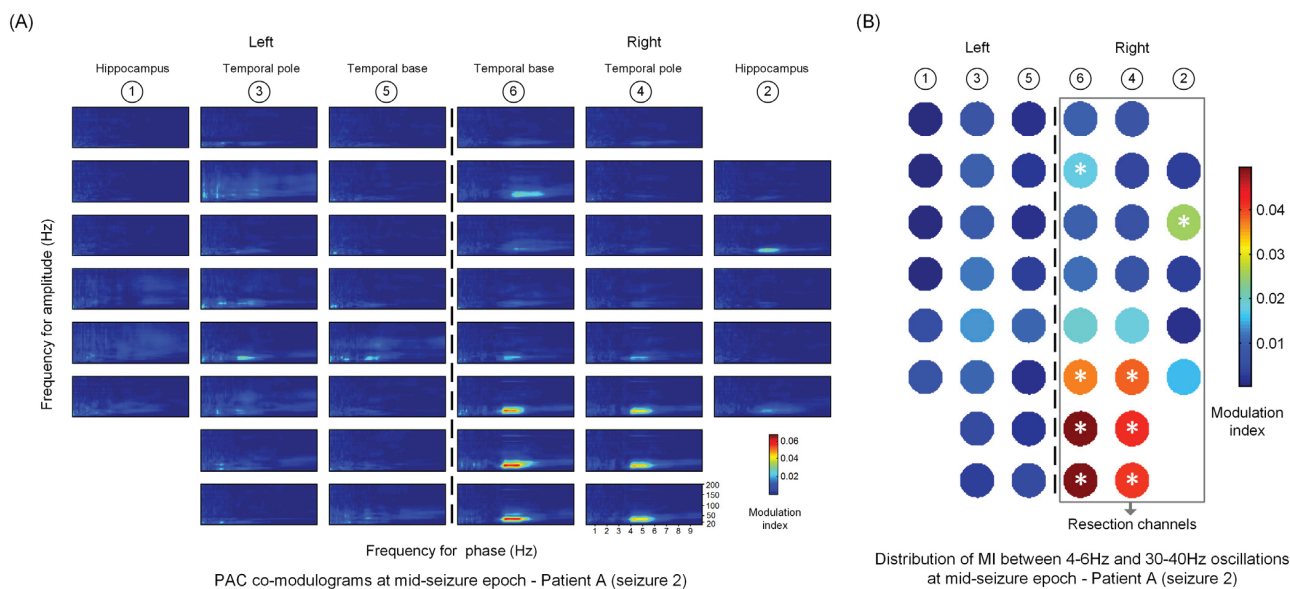


**Fig. 5.** (A) PAC co-modulograms in the mid-seizure epoch from all channels of patient A (seizure 2). Frequency for phase (0.2–10 Hz in steps of 0.1 Hz) and amplitude (11–200 Hz in steps of 1 Hz) are indicated on the horizontal and vertical axes, respectively. (B) MI values between 4–6 Hz and 30–40 Hz in the mid-seizure epoch from all channels of patient A (seizure 2). Strong MI channels are marked with white asterisk.

co-modulograms were computed between the phase of low-frequency 0.2–10 Hz in steps of 0.1 Hz and the amplitude of high-frequency 11–200 Hz in steps of 1 Hz.

It can be seen from Fig. 5A that the phase-amplitude modulation was notably different and asymmetrical on the left and right sides. In the right temporal pole (electrode strip ④) and right temporal base (electrode strip ⑥), strong phase-amplitude modulation appeared in channels 21–23, 37–39 and 43. Moreover, channel 10 in the right hippocampus (electrode strip ②) also showed a strong modulation. The strong phase-amplitude modulations in these channels were all between the θ and γ oscillations. In contrast, there was no strong phase-amplitude modulation in the left temporal cortex and hippocampus. Co-modulograms of mid-seizure epoch for all channels of other patients were distinct in different regions of the temporal cortex and hippocampus. These results illustrated that the modulation between HFOs and LFOs varied among channels in the mid-seizure epoch, which implies the spatial specificity of phase-amplitude modulation in temporal lobe epilepsy.

In addition, to determine whether the PAC modulation strength varies across different electrode channels, we computed the median values of MI between seizure-specific LFOs and HFOs in the mid-seizure epoch in each seizure for all patients. Fig. 5B shows the median values of MI between LFO of 4–6 Hz and HFO of 30–40 Hz of all 43 channels on both left and right hippocampi and temporal lobes of patient A (seizure 2). This patient underwent right temporal lobe resection, whose resected channels are marked with a light gray rectangle in the figure. As can be seen in Fig. 5B,

high MI values were noted in channels 10, 21–23, 37–39, and 43 (white asterisk \*), and the MI values of these channels were significantly greater than those of other ipsilateral and contralateral channels ( $p < 0.001$ , Kruskal-Wallis test). The MI values of epileptic focus in the mid-seizure epoch were also significantly greater than those of other channels in other patients. These results demonstrated the spatial specificity of PAC strength in the mid-seizure period. That is, strong PAC appears in the epileptic focus rather than in the normal cortex in temporal lobe epilepsy.

To further evaluate the relationship between the spatial specificity of phase-amplitude modulation in the mid-seizure epoch and epilepsy lesion, we compared channels with strong MI in co-modulogram, seizure onset channels identified by the neurosurgeons, and resection channels in the clinical surgery of all 12 recorded seizures. Channels with different features of each patient were marked with various symbols on their corresponding electrode strips, which are illustrated in Fig. 6. Asterisk (\*) denotes strong MI channels, and different colors (green, red and blue) of the asterisk denote different recorded seizures of each patient. Pound sign (#) indicates seizure onset channels. Channels filled with gray color indicate the clinical resection zones.

As can be seen from Fig. 6, almost all the channels with strong MI appeared on the corresponding left or right temporal cortex of surgical resection and overlapped with the clinical resection zones in all seven patients. It is important to note that neurosurgeons generally avoid the functional cortex and resect tissue slightly outside the defined epileptogenic region to minimize the risk of a secondary surgery. These results illustrate that strong MI in the

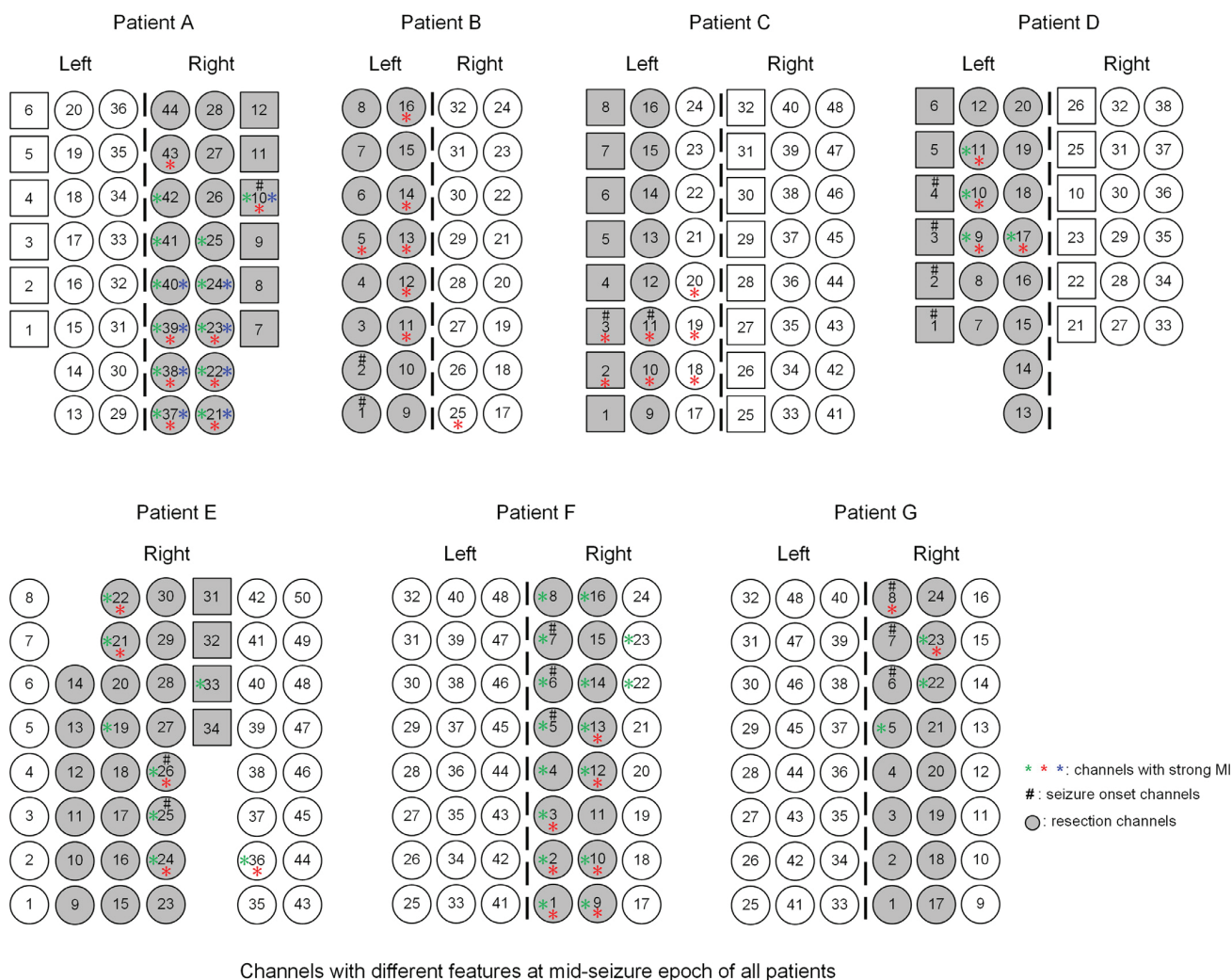


**Fig. 6.** Channels marked with different symbols represent strong MI channels in co-modulogram (\*), seizure onset channels identified by the neurosurgeons (#), and the resection channels in the clinical surgery (gray electrode) of all 12 recorded seizures from 7 patients.

mid-seizure period can be the biomarker of epileptogenic cortex area, and PAC is a potential measure for the lateralization and localization of epileptic focus in temporal lobe epilepsy.

### 3.3. Fall-max pattern of phase-amplitude modulation on epileptic foci

Because the MI only quantifies the coupling strength of low-frequency phase and high-frequency amplitude, the pattern of PAC remains unclear. Therefore, we investigated the PAC pattern using time-varying phase-amplitude modulograms during the entire period from pre-seizure to post-seizure. We analyzed the modulogram between the phase of LFOs and the amplitude of HFOs of ECoG data from all channels for each patient, where the calculated LFOs and HFOs were patient specific.

Fig. 7 shows the time-varying modulograms between low-frequency 4–6-Hz and high-frequency 30–40-Hz oscillations of patient A. The time and low-frequency phases (from  $-\pi$  to  $+\pi$  in steps of  $\pi/9$ ) are indicated on the horizontal and vertical axes, respectively. Two vertical solid lines represent the seizure onset time and seizure termination time. As can be seen in Fig. 7, in the modulograms of almost all channels in the right temporal pole (electrode strip ④) and right temporal base (electrode strip ⑥), the high-frequency (30–40 Hz) amplitudes were the largest at the

low-frequency (4–6 Hz) phase range  $[-\pi, 0]$  that corresponded to the falling edges of LFOs during the middle period of seizure, which was called the “fall-max” pattern. Moreover, this pattern was relatively obvious in the modulograms of channels 21–23 and channels 37–39, in which the co-modulograms had strong MI values (Fig. 5). In contrast, there was no obvious “fall-max” pattern in the left temporal cortex and left hippocampus. In addition, this “fall-max” pattern also appeared in the middle period of seizure of channels with strong MI values in co-modulograms in patients C (seizure 5) and D (seizures 6 and 7) rather than in all the 12 studied seizures. These results demonstrated that the “fall-max” pattern was a remarkable PAC pattern in the epileptic focus during the period of seizures and also a notable feature of neural oscillations in patients with temporal lobe epilepsy.

To further determine the “fall-max” pattern in the epileptic focus (i.e., how the low-frequency phase and high-frequency amplitude couple in the ECoG signal) and the difference in the oscillation features between epileptic cortex and normal cortex, we selected 3-s ECoG data of low-frequency 4–6-Hz and high-frequency 30–40-Hz oscillations in the mid-seizure epoch from a channel in the epileptic cortex (channel 38) and in the normal cortex (channel 6) of patient A (seizure 2), respectively. The ECoG data (black line), 4–6-Hz oscillation (dark green line) and its

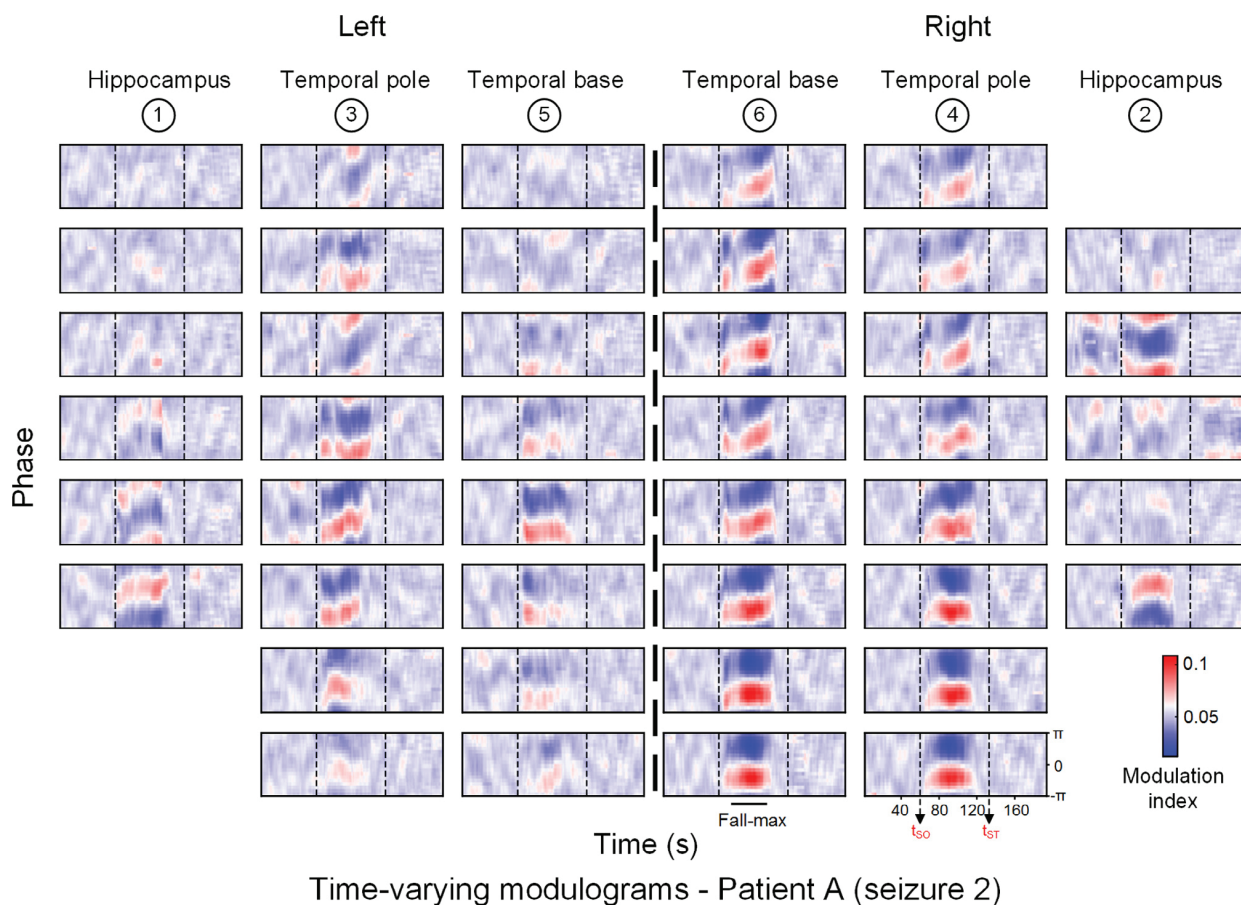


**Fig. 7.** Time-varying phase-amplitude modulograms during the period from pre-seizure to post-seizure from all channels of patient A (seizure 2). The seizure onset time ( $t_{so}$ ) and seizure termination time ( $t_{st}$ ) are demarcated by black vertical lines in each modulogram.

corresponding instantaneous phase (light green line), and 30–40-Hz oscillation (light red line) and its corresponding instantaneous amplitude (dark red line) are shown in the left panel of Fig. 8A and B. It can be seen from Fig. 8A that the high-frequency amplitudes were the largest only at the falling edges of the LFO where the gray arrows point to, i.e., the large high-frequency amplitudes distributed in the low-frequency phase range  $[-\pi, 0]$ , which could be seen in the mid-seizure period of time-varying modulograms in Fig. 7. Moreover, the distribution of normalized mean high-frequency amplitudes in the low-frequency phase range  $[-\pi, \pi]$  of a mid-seizure epoch of the “fall-max” pattern is given in the right panel of Fig. 8A. The large mean amplitudes were also distributed in the phase range  $[-\pi, 0]$ . In contrast, in Fig. 8B, the high-frequency amplitudes were the largest at the peaks, troughs, rising edges, and falling edges of the LFO, which implies that the large high-frequency amplitudes are distributed evenly in the low-frequency phase range  $[-\pi, \pi]$ . These results illustrated that in the mid-seizure period, the LFO and HFO of the epileptic cortex evolved into a specific coupling pattern, whereas they presented without any synchronous features in the normal cortex.

#### 4. Discussion

Interictal and ictal ECoG recordings are essential for preoperative assessment of localization of the epilepsy focus for patients with refractory focal seizures. Neurologists sometimes cannot completely determine the seizure onset zones clinically from the

interictal and ictal ECoG recordings, and they are trying to discover a more efficient and reliable biomarker for assessing epileptogenic zones. In this study, we investigated the temporal and spatial coupling difference between low-frequency phase and high-frequency amplitude of ECoG signals collected from seven patients with temporal lobe epilepsy by using the measure of PAC, which described the characteristics of neural oscillations during different periods of seizures. This enabled PAC to be a significant measure for lateralization and localization of the epileptic focus.

To quantify the strength of PAC during the period from pre-seizure to post-seizure in all patients, we adopted the *MI* to analyze the coupling intensity change between the low-frequency phase (0.2–10 Hz in steps of 0.1 Hz) and high-frequency amplitude (11–400 Hz in steps of 1 Hz). In addition, we determined a significant difference of *MI* value in five representative seizure epochs (pre-seizure, seizure onset, mid-seizure, seizure termination, and post-seizure epoch). The *MI* in co-modulogram in the mid-seizure epoch was significantly stronger than that of other seizure epochs in the 12 seizures from all patients (Figs. 3 and 4). In fact, in the interictal period, there was no phase-amplitude synchronization feature between LFOs and HFOs. Gradually, the LFOs and HFOs tended to present a synchronous oscillation mode after seizure onset. When the seizure developed to the mid-seizure period, the neural oscillations between low frequency and high frequency showed a specific and regular synchronization feature, which caused the strong PAC. After that, this particular synchronization oscillation weakened gradually. It is this regular phase-amplitude synchronous mode between LFOs and HFOs in the middle period

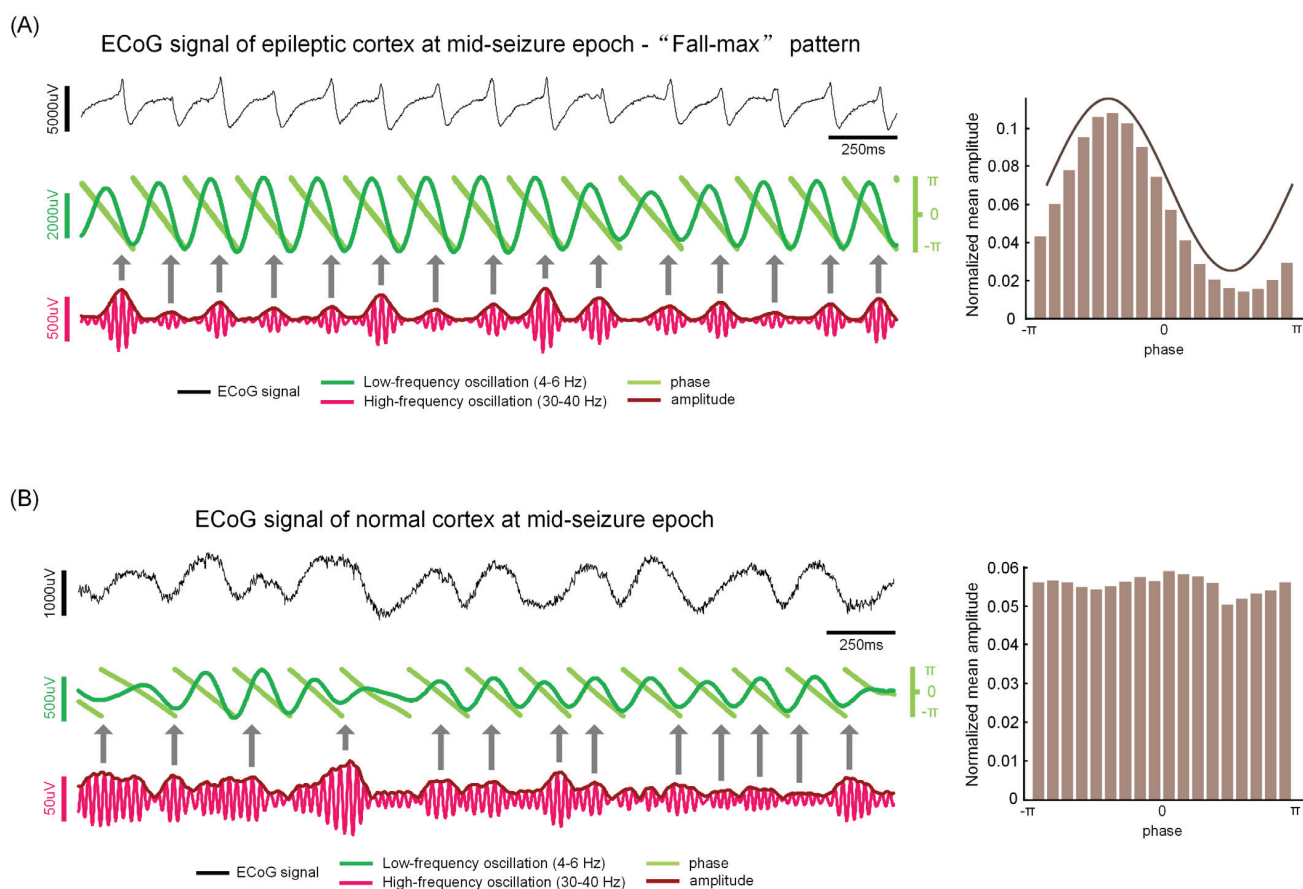


**Fig. 8.** ECoG signals of epileptic cortex (A) and normal cortex (B) in the mid-seizure epoch (left panel) and their corresponding distribution of normalized mean amplitudes of HFO in the low-frequency phase range  $[-\pi, \pi]$  (right panel).

of seizures that gave a high *MI* value compared to other seizure periods. This significantly strong coupling between low-frequency phase and high-frequency amplitude, which appeared in the middle period of the entire seizure, is an important characteristic and could be a biomarker for temporal lobe epilepsy. However, in a previous study, Guirgis et al. used the *MI* to compute the PAC strength at seizure onset, mid-seizure, and seizure termination periods and found the modulation in all three seizure periods (Guirgis et al., 2015b). Moreover, phase-amplitude modulation was observed in the low-frequency  $\delta$  and  $\theta$  rhythms in their study, while the strong PAC in our study appeared mainly between the low-frequency  $\delta$ ,  $\theta$ , and  $\alpha$  oscillations and high-frequency  $\gamma$  and ripple oscillations. Therefore, the LFO and HFO modulation frequency bands vary among patients, and the strong PAC did not just appear in the middle period of seizures, which may be related to patients' different conscious states when neurosurgeons record the epileptic seizures or the different types of epilepsy.

In addition, we investigated the spatial distribution of PAC strength in the mid-seizure epoch of all recorded seizures to find the difference across all channels in the left and right hippocampus and temporal cortex. The co-modulograms and *MI* between seizure-specific LFOs and HFOs of all channels were calculated to assess the spatial distribution of PAC strength and to assess the relationship between the spatial phase-amplitude modulation and epilepsy lesion location. The spatial modulation and strength of PAC in the mid-seizure epoch showed differences and asymmetry between LFOs and HFOs of the epileptic cortex and normal cortex (Fig. 5). Obvious phase-amplitude modulation appeared in the

specific channels of each patient. Moreover, channels with strong *MI* overlapped with the seizure onset channels identified by the neurosurgeons and the resection cortex areas in the clinical surgery (Fig. 6). This spatial specificity of phase-amplitude modulation and PAC strength demonstrate that the epileptic foci cause the strong and specific PAC compared to the normal cortex. This provides the neurologists important reference point for the lateralization and localization of the epilepsy lesion in the patients with temporal lobe epilepsy.

To further determine the pattern of PAC during the entire period from pre-seizure to post-seizure, especially the mid-seizure epoch, time-varying modulogram was used to describe the PAC pattern of seizure-specific LFOs and HFOs (Fig. 7). An obvious "fall-max" pattern was observed in three of the seven patients (six of 12 recorded seizures) in the middle period of the seizures. Although this "fall-max" pattern does not appeared in all the 12 studied seizures from all patients, we speculate this phase-amplitude pattern may be discovered in other recorded epileptic seizures. Moreover, channels with this "fall-max" pattern in modulograms were the ones with strong *MI* values in co-modulograms. These results illustrate that low-frequency phase modulates the high-frequency amplitude in a particular way in the middle period of seizures, which also varies among different cortical areas. There is no PAC pattern at the seizure onset time, while the epileptic foci make the LFOs and HFOs form a pattern of coupling ("fall-max" pattern) after several seconds. However, this "fall-max" pattern vanishes before the seizure termination time rather than continue to the end of the seizure. Moreover, the ECoG data, LFO and its corresponding instantaneous

phase, and HFO and its corresponding instantaneous amplitude were elaborated to illustrate the difference in neural oscillations between epileptic cortex and normal cortex (Fig. 8). The specific phase-amplitude synchronization between low-frequency phase and high-frequency amplitude in the epileptic cortex led to a strong PAC and high *MI* value directly, while the irregular PAC in the normal cortex resulted in the low *MI* value. The “fall-max” PAC pattern, which has not been mentioned in previous studies, caused by the epileptic foci in the seizure period may be an important biomarker of epileptogenicity. Neurosurgeons can determine the lateralization and localization of the epilepsy lesion by observing the synchronization modes and characteristics between LFOs and HFOs. The neuropathological mechanisms for the appearance and disappearance of the “fall-max” pattern during the period from pre-seizure to post-seizure needs further investigation.

Nevertheless, our study has some limitations. Only 12 recorded seizures from seven patients were studied. More ECoG data segments of recorded spontaneous seizures from more number of patients with epilepsy can provide more sufficient and worthy information regarding the characteristics of PAC during seizure and non-seizure periods. Future studies on different genders, different age groups, and different time periods of the day are required. Epileptic foci located in various cortical areas may have different influences on the pattern of PAC during the seizure period. Moreover, the data lengths of the ECoG data segments we selected are limited, which only included the data period from pre-seizure to post-seizure for all the patients with epilepsy. Data of interictal periods, which have longer time interval than that of the seizure period may contain some neurophysiological information about the phase-amplitude modulation of the epileptic foci.

Overall, the PAC during the entire period from pre-seizure to post-seizure exhibits different features in patients with temporal lobe epilepsy. In addition, the modulation between low-frequency phase and high-frequency amplitude has spatial specificity in different cortical areas. The spatial specificity of phase-amplitude modulation and the newfound “fall-max” phase-amplitude pattern in the middle period of seizure are the important neurophysiological characteristic and biomarker, respectively, which may be a good tool for the lateralization and localization of the epileptic foci and provide insight into the underlying neural dynamics of the epileptic seizure.

## Acknowledgments

This work was supported by National High-tech R&D Program (863 Program) (2015AA020514); Beijing Municipal Science

and Technology Project (No. Z121107001012007 and No. Z131107002813039); Beijing Municipal Administration of Hospitals Clinical Medicine Development for special funding support (XM201401).

*Conflict of interest:* None of the authors have potential conflicts of interest to be disclosed.

## References

- Alvarado-Rojas C, Valderrama M, Witon A, Navarro V, Le Van Quyen M. Probing cortical excitability using cross-frequency coupling in intracranial EEG recordings: a new method for seizure prediction. In: 2011 Annual international conference of the IEEE engineering in medicine and biology society. IEEE; 2011. p. 1632–5.
- Crépon B, Navarro V, Hasboun D, Clemenceau S, Martinerie J, Baulac M, et al. Mapping interictal oscillations greater than 200 Hz recorded with intracranial macroelectrodes in human epilepsy. *Brain* 2010;133:33–45.
- Edakawa K, Yanagisawa T, Kishima H, Fukuma R, Oshino S, Khoo HM, et al. Detection of epileptic seizures using phase-amplitude coupling in intracranial electroencephalography. *Sci Rep* 2016;6:25422.
- Guirgis M, Chinvarun Y, del Campo M, Carlen PL, Bardakjian BL. Defining regions of interest using cross-frequency coupling in extratemporal lobe epilepsy patients. *J Neural Eng* 2015a;12:026011.
- Guirgis M, Chinvarun Y, Del Campo M, Carlen PL, Bardakjian BL. Defining regions of interest using cross-frequency coupling in extratemporal lobe epilepsy patients. *J Neural Eng* 2015b;12:026011.
- Ibrahim GM, Wong SM, Anderson RA, Singh-Cadieux G, Akiyama T, Ochi A, et al. Ictal wideband ECoG: direct comparison between ictal slow shifts and high frequency oscillations. *Clin Neurophysiol* 2011;122:1500–4.
- Imamura H, Matsumoto R, Inouchi M, Matsuhashi M, Mikuni N, Takahashi R, et al. Intracranially recorded ictal direct current shifts may precede high frequency oscillations in human epilepsy. *Clin Neurophys* 2015;126:47–59.
- Kanazawa K, Matsumoto R, Imamura H, Matsuhashi M, Kikuchi T, Kunieda T, et al. Intracranially recorded ictal direct current shifts may precede high frequency oscillations in human epilepsy. *Clin Neurophys* 2015;126:47–59.
- Kerber K, Dümpelmann M, Schelter B, Le Van P, Korinthenberg R, Schulze-Bonhage A, et al. Differentiation of specific ripple patterns helps to identify epileptogenic areas for surgical procedures. *Clin Neurophysiol* 2014;125:1339–45.
- Mukamel EA, Pirondini E, Babadi B, Wong KF, Pierce ET, Harrell PG, et al. A transition in brain state during propofol-induced unconsciousness. *J Neurosci* 2014;34:839–45.
- Mukamel EA, Wong KF, Prerau MJ, Brown EN, Purdon PL. Phase-based measures of cross-frequency coupling in brain electrical dynamics under general anesthesia. *Conf Proc IEEE Eng Med Biol Soc* 2011;2011:1981–4.
- Nonoda Y, Miyakoshi M, Ojeda A, Makeig S, Juhász C, Sood S, et al. Interictal high-frequency oscillations generated by seizure onset and eloquent areas may be differentially coupled with different slow waves. *Clin Neurophysiol* 2016;127:2489–99.
- Pearce A, Wulsin D, Blanco JA, Krieger A, Litt B, Stacey WC. Temporal changes of neocortical high-frequency oscillations in epilepsy. *J Neurophysiol* 2013;110:1167–79.
- Ren L, Terada K, Baba K, Usui N, Umeoka S, Usui K, et al. Ictal very low frequency oscillation in human epilepsy patients. *Ann Neurol* 2011;69:201–6.
- Tort AB, Komorowski R, Eichenbaum H, Kopell N. Measuring phase-amplitude coupling between neuronal oscillations of different frequencies. *J Neurophysiol* 2010;104:1195–210.



## IV

# **TRANSIENT SEIZURE ONSET NETWORK FOR LOCALIZATION OF EPILEPTOGENIC ZONE: EFFECTIVE CONNECTIVITY AND GRAPH THEORY-BASED ANALYSES OF ECOG DATA IN TEMPORAL LOBE EPILEPSY**

by

Ye Ren, Fengyu Cong, Tapani Ristaniemi, Yuping Wang, Xiaoli Li & Ruihua Zhang  
2019

Journal of Neurology, 266(4), 844-859

DOI: <https://doi.org/10.1007/s00415-019-09204-4>

Reproduced with kind permission by Springer Nature.

**Transient seizure onset network for localization of epileptogenic zone:  
Effective connectivity and graph theory-based analyses of ECoG data in  
temporal lobe epilepsy**

Ye Ren<sup>1,2</sup>, Fengyu Cong<sup>2,3</sup>, Tapani Ristaniemi<sup>2</sup>, Yuping Wang<sup>4,5,6</sup>, Xiaoli Li<sup>7,\*</sup>, Ruihua  
Zhang<sup>1,\*</sup>

<sup>1</sup> Department of Geriatric Medicine, Beijing Luhe Hospital, Capital Medical University, Beijing, 101149, China

<sup>2</sup> Faculty of Information Technology, University of Jyväskylä, Jyväskylä, 40014, Finland

<sup>3</sup> School of Biomedical Engineering, Faculty of Electronic Information and Electrical Engineering, Dalian University of Technology, Dalian, 116024, China

<sup>4</sup> Department of Neurology, Xuanwu Hospital, Capital Medical University, Beijing, 100053, China

<sup>5</sup> Beijing Key Laboratory of Neuromodulation, Beijing, 100053, China

<sup>6</sup> Center of Epilepsy, Beijing Institute for Brain Disorders, Beijing, 100053, China

<sup>7</sup> State Key Laboratory of Cognitive Neuroscience and Learning & IDG/McGovern Institute for Brain Research, Beijing Normal University, Beijing, 100875, China

**\* Corresponding authors:**

Xiaoli Li

Address: No. 19 Xijiekou Street, Haidian District, Beijing, 100875, China

Email: xiaoli@bnu.edu.cn

Ruihua Zhang

Address: No. 82, Xinhua South Street, Tongzhou District, Beijing, 101149, China

Email: ruihua.zhang@ccmu.edu.cn

## Highlights

- ✧ Origination and propagation of epileptic activities could be observed with the high temporal resolution of the full-frequency adaptive directed transfer function (ffADTF) effective connectivity networks.
- ✧ The seizure-specific transient seizure onset ffADTF network remained for approximately 20-50 ms with strong connections generated from both the seizure onset zone (SOZ) and epileptogenic zone (EZ).
- ✧ The ffADTF combined with the graph metrics in the transient seizure onset network can provide a more precise localization of the SOZ and EZ.
- ✧ Out-degree and clustering coefficient were found to be more closely correlated with the clinically determined SOZ and EZ than closeness centrality, betweenness centrality and local efficiency in the low-frequency  $\delta$  and  $\theta$  bands than in the  $\alpha$ ,  $\beta$  and  $\gamma$  frequency bands in seizure-free patients postoperatively.

## **Abstract**

**Objective:** Abnormal and dynamic epileptogenic networks cause difficulties for clinical epileptologists in the localization of the seizure onset zone (SOZ) and the epileptogenic zone (EZ) in preoperative assessments of patients with refractory epilepsy. The aim of this study is to investigate the characteristics of time-varying effective connectivity networks in various non-seizure and seizure periods and to propose a quantitative approach for accurate localization of SOZ and EZ.

**Methods:** We used electrocorticogram recordings in the temporal lobe and hippocampus from seven patients with temporal lobe epilepsy to characterize the effective connectivity dynamics at a high temporal resolution using the full-frequency adaptive directed transfer function (ffADTF) measure and five graph metrics, i.e., the out-degree (OD), closeness centrality (CC), betweenness centrality (BC), clustering coefficient (C), and local efficiency (LE). The ffADTF effective connectivity network was calculated and described in five frequency bands ( $\delta$ ,  $\theta$ ,  $\alpha$ ,  $\beta$ , and  $\gamma$ ) and five seizure periods (pre-seizure, early seizure, mid-seizure, late seizure, and post-seizure). The cortical areas with high values of graph metrics in the transient seizure onset network were compared with the SOZ and EZ identified by clinical epileptologists and the results of epilepsy resection surgeries.

**Results:** Origination and propagation of epileptic activity were observed in the high time resolution ffADTF effective connectivity network throughout the entire seizure period. The seizure-specific transient seizure onset ffADTF network that emerged at seizure onset time remained for approximately 20-50 ms with strong connections generated from both SOZ and EZ. The values of graph metrics in the SOZ and EZ were significantly larger than that in the

other cortical areas. More cortical areas with the highest mean of graph metrics were the same as the clinically determined SOZ in the low-frequency  $\delta$  and  $\theta$  bands and in Engel Class I patients than in higher frequency  $\alpha$ ,  $\beta$ , and  $\gamma$  bands and in Engel Class II and III patients. The OD and C were more likely to localize the SOZ and EZ than CC, BC, and LE in the transient seizure onset network.

**Conclusion:** The high temporal resolution ffADTF effective connectivity analysis combined with the graph theoretical analysis helps us to understand how epileptic activity is generated and propagated during the seizure period. The newly discovered seizure-specific transient seizure onset network could be an important biomarker and a promising tool for more precise localization of the SOZ and EZ in preoperative evaluations.

**Keywords:** adaptive directed transfer function; graph metric; brain connectivity; seizure onset zone; epileptogenic zone

## 1. Introduction

Temporal lobe epilepsy (TLE) is the most common form of medically intractable epilepsy, which is increasingly seen as a disorder of the epileptogenic networks that lead to connectivity disturbances [3, 5, 10]. Abnormal activity in the epileptic connectivity network makes it difficult for epileptologists to locate the seizure onset zone (SOZ), epileptogenic zone (EZ), and resective region, which may lead to the failure of resection surgery or various degrees of postoperative seizures in these drug-resistant epilepsy patients. Accurate localization of SOZ and EZ during preoperative assessment and precise resection of these cortical areas during epilepsy surgery are vital for patients with TLE. The aim of this paper is to investigate the characteristics of time-varying effective connectivity networks in patients with TLE, and to

propose a quantitative approach for more accurate localization of SOZ and EZ using the effective connectivity and graph theoretical analyses.

Effective connectivity [8] refers to causal interactions among the neural elements [36], thus describing the directed connections in the brain network. Granger-causality (GC) is one of the prototypical data-driven effective connectivity techniques [19]. Directed transfer function (DTF), a GC-based effective connectivity measure, was proposed by Kaminski and Blinowska in 1991 [11] to reveal the direction of the information flow between multiple signals in the frequency domain of the brain. DTF has been used to assess interictal and preictal activity to indicate an upcoming seizure [37], and to assess ictal activity to localize the EZ in medically intractable epilepsy patients [33, 35]. However, DTF assumes the stationarity of neural signals and the time invariance of network connectivity in a short time window. That is, the connectivity pattern obtained by DTF is unchanged over the analyzed time period.

Wilke et al. proposed an adaptive DTF (ADTF) measure using an adaptive multivariate autoregressive (AMVAR) model for detecting the dynamic changes of the information interactions [31] and used ADTF to study the time-variant connectivity of seizures and interictal spikes [32]. Having high temporal resolution, this effective connectivity measure is able to address non-stationary signals, thus capturing the temporal dynamics of network connectivity at specified frequencies, which the DTF measure cannot. The ADTF has been used to reveal dynamic brain network patterns and to detect EZ during the interictal electroencephalography (EEG) [38]. In addition, the full-frequency ADTF (ffADTF) that measures the effective connectivity in a specific frequency band has been used to describe the propagation patterns of electrocorticogram (ECoG) recordings of seizure onsets across brain

areas and proved that it outperforms the other normalizations of ADTF in locating the EZ [26]. Graph theory allows a network-based representation of TLE brain networks, which has the potential to illuminate the characteristics of brain topology [1]. Different electrophysiologic and neuroimaging modalities have used graph theory to identify EZ, predict seizures, and assess cognitive performance in TLE [10]. In terms of localization, graph theoretical measures, including out-degree (OD), betweenness centrality (BC) and graph index complexity have shown the most potential [10]. It was found through simulation data and ictal or interictal patient data that the ADTF and normalizations of the ADTF measures combined with the OD resulted in correct SOZ and EZ localization [25, 27, 38]. In addition, ADTF combined with BC was applied to ictal and interictal ECoG, and was found to correlate with the resected cortical regions [34]. It was also used to assess interictal spikes on EEG recording, confirming that this combination was effective at detecting the focal regions and characterizing the dynamics of the spike propagation [23]. Closeness centrality (CC) has been used to predict an upcoming seizure [37] and describe the change of network topology at seizure onset [13]. ECoG studies have determined the increase in clustering coefficient (C) during the ictal compared to interictal phase [12, 16]. Local efficiency (LE) has been found to be correlated positively with the epilepsy duration in the resting-state fMRI data of TLE patients [29]. However, effective connectivity features of epileptic activity in different frequency bands during non-seizure and various seizure periods in the epileptic network have not been clearly elaborated in these previous studies. A few studies have compared the performance of different graph theoretical measures for localization of the SOZ and EZ in TLE.

In this study, we investigated the time-varying characteristics of effective connectivity network

using the ffADTF measure and five graph metrics (OD, CC, BC, C, and LE) in 14 seizures of seven patients with TLE. The ffADTF effective connectivity network was compared in five frequency bands ( $\delta$ ,  $\theta$ ,  $\alpha$ ,  $\beta$ , and  $\gamma$ ), five representative seizure periods (pre-seizure, early seizure, mid-seizure, late seizure, and post-seizure), as well as the SOZ and resected regions that were identified by the clinical epileptologists and the results of epilepsy surgery. The results showed that the high temporal resolution ffADTF could provide more information about the origination and propagation of seizures. More cortical areas with the highest mean of OD and C were the same as the clinically determined SOZ in the low-frequency  $\delta$  and  $\theta$  bands. The seizure-specific transient seizure onset network could lead to a more accurate localization of SOZ and EZ, helping us to understand the neuroelectrophysiological mechanism of epileptic seizures and improving the accuracy of preoperative evaluations of patients with refractory epilepsy.

## **2. Materials and methods**

### **2.1 Data recording and preprocessing**

We obtained multichannel ECoG data from subdural electrode strips implanted in seven patients with TLE before resective epilepsy surgery. All patients were provided with written informed consent. The clinical information regarding these patients is illustrated in Table 1. Surgical outcomes were classified according to Engel's classification [4] into Class I: Free of disabling seizures, Class II: Rare disabling seizures ("almost seizure-free"), Class III: Worthwhile improvement, and Class IV: No worthwhile improvement. Cortical electrode strips (2.5-mm-diameter platinum electrodes positioned 10-mm apart centre-to-centre) were placed on the temporal lobe and other cortical areas. Depth electrodes (1.2-mm-diameter platinum electrodes positioned 10 mm apart centre-to-centre) were implanted in the hippocampus.

ECoG was continuously recorded day and night for the preoperative assessments of all patients using a video-EEG monitoring system (PN-NET, Beijing Yunshen Technology, China). Electrode contacts, which were located far from the epileptogenic lesion, were used as the reference electrode contact. The sampling frequency of the ECoG data was 2048 Hz. The ECoG data of 14 seizures from seven patients, which included complete spontaneous epileptic seizures, were selected for analysis. An ECoG data segment was cut from approximately 1 min before seizure onset to approximately 1 minute after seizure termination. These data were first exported as European Data Format Plus (EDF+) files and then imported into EEGLAB to convert the file format to MAT. Then, the files were down-sampled to 256 Hz and filtered with a 0.2-Hz high-pass filter to remove baseline interference. Standardized z-scores were also used to normalize the variance of the ECoG data in each channel. Power frequency noise (50 Hz) and harmonic noises were removed by a notch filter. Large-amplitude artifacts were removed, and bad channels were rejected by visual inspection.

### [Table 1]

## 2.2 Effective connectivity analysis

The ADTF measure was adopted to quantify the causal connection feature among different cortical areas. The ADTF developed by Wilke et al. [32] is based on the concept of GC [9], which can capture the temporal dynamics of the models. According to GC, if a signal  $x_1$  can be predicted by the past information from a signal  $x_2$  better than the past information from its own signal, then the signal  $x_2$  can be considered causal to the signal  $x_1$  [19]. A common way to model GC is using the autoregressive modelling technique. The pre-processed ECoG data epoch is modelled using the AMVAR model and is represented as a combination of its own

past as follows:

$$\mathbf{X}(t) = \sum_{m=1}^p \mathbf{A}_m(t) \mathbf{X}(t-m) + \mathbf{E}(t) \quad (1)$$

where  $\mathbf{X}(t)$  is the signal matrix,  $\mathbf{A}_m(t)$  is the  $K \times K$  model coefficient matrix for delay  $m$ ,  $K$  is the number of signal channels,  $p$  is the model order, and  $\mathbf{E}(t)$  is the uncorrelated white noise matrix. Eq. (1) can be given by the following:

$$\begin{bmatrix} x_1(t) \\ \vdots \\ x_K(t) \end{bmatrix} = \sum_{m=1}^p \begin{bmatrix} a_{m,11}(t) & \cdots & a_{m,1K}(t) \\ \vdots & \ddots & \vdots \\ a_{m,K1}(t) & \cdots & a_{m,KK}(t) \end{bmatrix} \begin{bmatrix} x_1(t-m) \\ \vdots \\ x_K(t-m) \end{bmatrix} + \begin{bmatrix} e_1(t) \\ \vdots \\ e_K(t) \end{bmatrix} \quad (2)$$

MATLAB module ARfit [14, 21] was used (<http://climate-dynamics.org/software/#arfit>) to estimate the parameters of the model.

A lower bound  $p_{min}$  and an upper bound  $p_{max}$  were first given on the model order. For the estimation of the parameters coefficient matrices of the model  $\mathbf{A}_1, \mathbf{A}_2, \dots, \mathbf{A}_p$  and  $K \times K$  noise covariance matrix  $C_p$  of the zero-mean white noise  $\mathbf{E}(t)$ , the stepwise least-squares algorithm is implemented for the models of successive orders  $p_{min}, \dots, p_{max}$  in ARfit. The optimal model order  $p_{opt}$  was selected according to the Schwarz' Bayesian Criterion (SBC) [22]. The SBC can be calculated as follows:

$$\text{SBC}(p) = \ln|C_p| + \frac{\ln(N)pK^2}{N} \quad (3)$$

where  $C_p$  is the covariance matrix of the noises,  $N$  is the number of time points.  $p_{opt}$  corresponds with the minimum of the SBC function. The parameters  $\mathbf{A}_1, \mathbf{A}_2, \dots, \mathbf{A}_{opt}$  were then computed for a model of the optimal order  $p_{opt}$ .  $p_{min}=1, p_{max}=5$  were set in our study and the  $p_{opt}$  was estimated for each data epoch, which ranged from 1 to 2.

To investigate the causality between the signals in the spectral domain, the Fourier transform was applied to Eq. (1):

$$\mathbf{E}(f) = \mathbf{A}(f) \mathbf{X}(f) \quad (4)$$

where the coefficient matrix is as follows:

$$\mathbf{A}(f) = \mathbf{I} - \sum_{m=1}^p \mathbf{A}_m e^{-i2\pi f m} \quad (5)$$

where  $\mathbf{I}$  is the  $K \times K$  identity matrix.  $\mathbf{E}(f)$ ,  $\mathbf{A}(f)$  and  $\mathbf{X}(f)$  are the Fourier transformation of the noise, the coefficient matrix, and the signal matrix, respectively. Under the assumption that the matrix  $\mathbf{A}(f)$  is nonsingular and thus invertible, Eq. (2) can be written as follows:

$$\mathbf{X}(f) = \mathbf{A}^{-1}(f)\mathbf{E}(f) = \mathbf{H}(f)\mathbf{E}(f) \quad (6)$$

where  $\mathbf{H}(f)$  is the  $K \times K$  transfer matrix, which is the inverse of the Fourier transform of the coefficient matrix  $\mathbf{A}(f)$ .

$$\mathbf{H}(f) = \mathbf{A}(f)^{-1} \quad (7)$$

The element  $H_{ij}(f)$  contains information about the causality from the signal  $x_j$  to signal  $x_i$  at frequency  $f$ .

The AMVAR model, i.e., time-variant multivariate autoregressive (TVAR) model allows us to obtain the time-varying model coefficients  $\mathbf{A}(f, t)$  at each time point  $t$ , which was estimated by the standard Kalman algorithm [20, 26].

The time-variant effective connectivity measures ADTF and normalized ADTF (nADTF) at each time point were then defined as follows:

$$ADTF_{ij}(f, t) = |\mathbf{H}_{ij}(f, t)|^2 \quad (8)$$

$$nADTF_{ij}(f, t) = \frac{|\mathbf{H}_{ij}(f, t)|^2}{\sum_{k=1}^K |\mathbf{H}_{ik}(f, t)|^2} \quad (9)$$

The ffADTF in the specific frequency band  $[f_1, f_2]$  from signal  $x_j$  to signal  $x_i$  was defined as follows:

$$ffADTF_{ij}(t) = \frac{\sum_{f=f_1}^{f_2} |\mathbf{H}_{ij}(f, t)|^2}{\sum_{k=1}^K \sum_{f=f_1}^{f_2} |\mathbf{H}_{ik}(f, t)|^2} \quad (10)$$

ffADTF is a normalization of ADTF, which incorporates the frequency information of all the frequencies in the defined frequency band  $[f_1, f_2]$  at each time point. The value of ffADTF is an interval  $[0, 1]$ , which is used as edge weight and represents the connection strength in the network. The sum of the incoming information flow into a channel at each time point is equal to 1.

$$\sum_{k=1}^K ffADTF_{ik}(t) = 1 \quad (11)$$

To investigate the features of the effective connectivity network during epileptic seizures, we calculated the ffADTF in the  $\delta$  (1-4 Hz),  $\theta$  (4-8 Hz),  $\alpha$  (8-13 Hz),  $\beta$  (13-30 Hz) and  $\gamma$  (30-50 Hz) frequency bands in five representative 5-second seizure epochs (I: pre-seizure, II: early seizure, III: mid-seizure, IV: late seizure, and V: post-seizure) of all 14 seizures across all patients. The pre-seizure and early seizure epochs were selected 5 s before and after the seizure onset time ( $t_{SO}$ ), respectively. The late seizure and post-seizure epochs were selected 5 s before and after the seizure termination time ( $t_{ST}$ ), respectively. The  $t_{SO}$  and the  $t_{ST}$  were determined by the neurologists. The mid-seizure epoch was chosen from 2.5 s before and after the middle time point of the whole seizure period.

### 2.3 Graph theoretical analysis

Topological properties of the brain network were evaluated by the graph metrics at the small scale of single regions, i.e. graph metrics on single nodes. In the brain network, each electrical channel denotes a node. Each value in the weighted directed connectivity matrix  $ffADTF_{ij}$  represents the connection weights from node  $j$  to node  $i$ , i.e., the edge weight of the network. Transpose  $ffADTF_{ij}$  and use  $a_{ij}$  to indicate the weights from node  $i$  to node  $j$ . In directed networks,  $a_{ij}$  does not necessarily equal  $a_{ji}$ .  $K$  is the number of ECoG channels. Five graph metrics were used in the study: out-degree, closeness centrality, betweenness centrality,

clustering coefficient, and local efficiency. All graph metrics were computed using the Brain Connectivity Toolbox (brain-connectivity-toolbox.net) [18].

To investigate the topological properties of the ffADTF effective connectivity network during different seizure periods, we calculated the graph metrics of five frequency bands in five seizure epochs of all seizures.

### 2.3.1 Out-degree

The out-degree  $OD_i$  quantified the information outflow of a node  $i$ :

$$OD_i = \sum_{j=1, j \neq i}^K a_{ij} \quad (12)$$

Nodes with high OD values output more information to other nodes in a network.

### 2.3.2 Closeness centrality

The closeness centrality  $CC_i$  of a node  $i$  was defined as the reciprocal of the sum of the shortest path length between the node  $i$  with all other nodes [7]:

$$CC_i = \frac{K-1}{\sum_{j=1, j \neq i}^K d_{ij}} \quad (13)$$

where  $d_{ij}$  is the directed shortest path length from node  $i$  to node  $j$

$$d_{ij} = \sum_{a_{ij} \in g_{i \rightarrow j}} f(a_{ij}) \quad (14)$$

In the weighted correlation network, higher correlations are interpreted as shorter distances.

$f(a_{ij}) = \frac{1}{a_{ij}}$  is a mapping from weight matrix to length matrix and  $g_{i \rightarrow j}$  is the shortest path

from node  $i$  to node  $j$ .

Nodes with high values of CC communicate the information with the other nodes faster than the others.

### 2.3.3 Betweenness centrality

The betweenness centrality  $BC_i$  of a node  $i$  was defined as follows [7]:

$$BC_i = \frac{1}{(K-1)(K-2)} \sum_{h=1, h \neq j, h \neq i}^K \sum_{j=1, j \neq i}^K \frac{\rho_{hj}(i)}{\rho_{hj}} \quad (15)$$

where  $\rho_{hj}$  is the number of directed shortest paths from node  $h$  to node  $j$ , and  $\rho_{hj}(i)$  is the

number of directed shortest paths from  $h$  to  $j$  that pass through  $i$ .

Nodes with high values of BC participate in a larger number of shortest paths and act as hubs in a network.

### 2.3.4 Clustering coefficient

The clustering coefficient  $C_i$  of a node  $i$  was defined as follows [6]:

$$C_i = \frac{t_i}{(OD_i + ID_i)(OD_i + ID_i - 1) - 2 \sum_{j=1, j \neq i}^K a_{ij} a_{ji}} \quad (16)$$

where  $t_i$  is the number of directed triangles around a node  $i$

$$t_i = \frac{1}{2} \sum_{h=1, h \neq j, h \neq i}^K \sum_{j=1, j \neq i}^K (a_{ij} + a_{ji})(a_{ih} + a_{hi})(a_{jh} + a_{hj}) \quad (17)$$

and  $ID_i$  is the in-degree of a node  $i$

$$ID_i = \sum_{j=1, j \neq i}^K a_{ji} \quad (18)$$

The clustering coefficient quantifies the number of connections that exist between the nearest neighbours of a node as a proportion of the maximum number of possible connections [30].

Nodes with high values of C tend to cluster together with more nearest neighbours in a network.

### 2.3.5 Local efficiency

As an alternative to the clustering coefficient, the local efficiency  $LE_i$  of a node  $i$  was defined as follows [18]:

$$LE_i = \frac{1}{2} \frac{\sum_{h=1, h \neq j, j \neq i}^K \sum_{j=1, j \neq i}^K (a_{ij} + a_{ji})(a_{ih} + a_{hi}) \left( \frac{1}{d_{jh}(N_i)} + \frac{1}{d_{hj}(N_i)} \right)}{(OD_i + ID_i)(OD_i + ID_i - 1) - 2 \sum_{j=1, j \neq i}^K a_{ij} a_{ji}} \quad (19)$$

where  $d_{jh}(N_i)$  is the length of the directed shortest path from node  $j$  to node  $h$  that contains only neighbours of  $i$ .

## 2.4 Statistical analysis

Since there is a highly nonlinear relation between the ADTF and the time series from which it is derived, the traditional parametric statistical methods cannot be applied [32]. Instead, random phases surrogate data testing [15, 24], a nonparametric method, is used to assess the statistical significance of the ffADTF. The null hypothesis was proposed, stating that there exists no

causal relationship among different channels of the ECoG signals. Phases and amplitudes of the ECoG data were first obtained by Fourier transform. We randomly shuffled the phases and used the new phases and the original amplitudes to generate the surrogate ECoG data using inverse Fourier transform. This phase shuffling process destroys the causality among ECoG signals, while preserving the spectral structure of the ECoG data, which is critical, since the ffADTF is a frequency-dependent measure. Then, the surrogate ECoG data were used to calculate the surrogate ffADTF. We implemented this procedure 100 times. If 95% of the time, the original ffADTF was greater than the surrogate ffADTF, we rejected the null hypothesis, and the ffADTF was considered statistically significant.

Kruskal-Wallis test (*kruskalwallis.m*) and multiple comparison test (*multcompare.m*) in the Matlab Statistics Toolbox were used to assess the significant difference of the graph metrics among different cortical regions in the transient seizure onset network. The graph metric values were presented using the boxplot.  $p < 0.05$ ,  $p < 0.01$ ,  $p < 0.001$  were considered significant difference and marked with the notation \*, \*\*, \*\*\*, respectively.

An illustration of the main steps of the effective connectivity and graph theoretical analyses of the epileptic brain is presented in Fig. 1.

[Fig. 1]

### 3. Results

#### 3.1 Dynamic effective connectivity networks during epileptic seizures

The z-scored ECoG data of all channels for a representative patient (patient A, seizure #1), containing a complete epileptic seizure, and the data of pre- and post- seizures are shown in Fig. 2A. The seizure period is indicated by two blue dashed lines delineating the  $t_{SO}$  to the  $t_{ST}$ . Five seizure epochs were marked with light grey rectangles. Due to the time-variant ffADTF of each sample point, the ffADTF effective connectivity matrices and corresponding effective

connectivity networks in the  $\theta$  frequency band of five representative time points of each epoch are selected and shown in Fig. 2B and Fig. 2C. The top 5% of strong connections were presented in the effective connectivity network. Depth electrodes were implanted in the left hippocampus (LH) and right hippocampus (RH) in this patient. Cortical electrode strips were placed on the left temporal pole (LTP), left temporal base (LTB), right temporal pole (RTP) and right temporal base (RTB). The SOZ, i.e., RH and the seizure onset channel (SOC), i.e., channel 10 (white asterisk) determined by clinical epileptologists are marked in the figure.

Because of the high temporal resolution, the ffADTF is able to characterize the dynamic epileptic connectivity network during the whole seizure. The asymmetrical effective connectivity ffADTF matrix was weighted and directed, thus quantifying the connection strength and detecting the connection direction. The effective connectivity matrices and its corresponding networks varied during the different seizure periods. Before the seizure onset time, a uniform network was presented during all seizures. As shown in Fig. 2B and Fig. 2C, the effective connectivity among all channels was uniform, and there was no obvious source activity. Particularly, some strong connections from the SOCs occasionally emerged during this period in the low-frequency bands of seizure #3 ( $\delta$  and  $\theta$ ) in patient A, seizure #4 ( $\delta$ ,  $\theta$  and  $\alpha$ ) in patient B, and seizure #10 ( $\theta$  and  $\alpha$ ) and seizure #11 ( $\delta$ ,  $\theta$  and  $\alpha$ ) of patient F, and even from the side contralateral to the SOZ of seizure # 12 ( $\theta$  and  $\alpha$ ) of patient G. At the seizure onset time, the strong epileptic sources were mainly derived from the regions where the SOZ was located and some other ipsilateral regions involved in epileptogenic activity in the  $\delta$ ,  $\theta$  and  $\alpha$  frequency bands in most seizures. In the effective connectivity results of seizure #1 in patient A, strong connections from the RH, RTP, and RTB to the other channels appeared in both the right and left hemispheres, particularly on the ipsilateral side (Fig. 2B and Fig. 2C). This effective connectivity network that emerged at the seizure onset time remained for approximately 43 ms. However, the strong epileptic sources were found not only on side

ipsilateral to the SOZ but also on side contralateral to the SOZ in the seizure #5 ( $\delta$ ) in patient C, seizure #10 ( $\delta$ ) and seizure #11 ( $\delta$ ,  $\theta$ , and  $\alpha$ ) of patient F, seizure #12 ( $\delta$ ,  $\theta$ ,  $\alpha$ , and  $\beta$ ), seizure #13 ( $\delta$ ,  $\theta$ ,  $\alpha$ , and  $\beta$ ) and seizure #14 ( $\delta$ ,  $\theta$ ,  $\alpha$ , and  $\beta$ ) of patient G when the seizures began. The durations of the transient seizure onset network in all seizures are illustrated in Table 2. The seizure-specific durations ranged from 19 ms to 54 ms, with a mean value of 42 ms. Compared with the clinical epilepsy surgery results, the channels with strong connections in the transient seizure onset ffADTF network were included in the resection regions identified by the epileptologists in the Engel Class I (patient A, D and E) and Engel Class II (patient B) patients, and they were also located in some other regions on the ipsilateral or contralateral side of the resection regions in the Engel Class II (patient C) and Engel Class III (patient F and G) patients. Then, the epileptic network changed to networks with irregular features. Strong epileptic sources were generated from the side ipsilateral or contralateral to the SOZ or from both sides of the cortex. The networks of the two time points in the mid-seizure and late seizure epochs of seizure #1 in patient A were selected as the examples of the time-varying effective connectivity networks, where the strong connections originated only from the RTP in the mid-seizure epoch and from both the RH and the contralateral LTB as the seizure approached its termination. Interestingly, at the post-seizure time, just after the seizure termination, clear, strong connections from the SOZ RH to other areas were established again, remaining for approximately 300 ms and converting to an irregular connectivity network afterwards. However, this special post-seizure network only appeared in the  $\delta$  and  $\theta$  frequency bands of seizure #1 in patient A and seizure #8 in patient E (the average duration of the post-seizure networks was 400 ms) rather than in all patients.

[Fig. 2]

### **3.2 High values of graph metrics in the transient seizure onset network localize the seizure onset zone and epileptogenic zones**

The distributions of the graph metrics across all channels in the  $\theta$  frequency band at the five seizure time points presented in Fig. 2A are shown in Fig. 3. Typically, neurosurgeons avoid functional brain areas and resect the tissue slightly outside the defined EZ to minimize the risk of a secondary surgery. It can be seen in Fig. 3 that the distribution of the graph metrics differed across the seizure epochs. In the pre-seizure epoch, the high values of OD, CC, C, and LE appeared in both the left and right hemispheres, i.e., the distribution was relatively uniform. However, only a few channels with high BC were found on both sides. Conversely, almost all the high values of graph metrics were on the right side at seizure onset time. In addition, the highest OD and CC (marked with max on the channel) at the seizure onset time appeared in the RH, which was the SOZ determined by clinical epileptologists. The highest BC, C, and LE appeared in the RTB which was included in the clinical resection areas. Subsequently, all the highest graph metrics were in the RTP at the selected time of the mid-seizure period. As the seizure reached its termination, high values of graph metrics were located in both the RH and the contralateral side. After the seizure termination, high values of OD, BC, C, and LE were found only in a few channels in the RH, while a high value of CC appeared on many channels in both hemispheres.

### [Fig. 3]

Moreover, due to the emergence of the transient seizure onset network and its high relevance to the SOZ and the EZ, we generated a hypothesis, stating that the graph metrics in the SOZ and the EZ were higher than that in the other areas in the transient seizure onset network. We first calculated the total graph metric, i.e., the sum of the graph metric at all time points, of each channel in the seizure-specific transient seizure onset network in each frequency band of all seizures. The total OD, CC, BC, C and LE of the 43-ms seizure onset network in an Engel Class I patient (seizure #1,  $\theta$  frequency band) are shown in Fig. 4, depicted using bars. As seen in Fig. 4, high values of graph metrics appeared mainly in the right temporal lobe, especially

in the RH and RTB. In Fig. 4A, 4B, 4D, 4E, the highest OD, CC, C, and LE were generated by channel 9 which was located in the RH and was the neighbouring contact of the clinically identified SOC (marked with a white asterisk). In Fig. 4C, the highest BC appeared in channel 41, which was located in the RTB and included in the clinical resection areas. Moreover, the BC of most channels were found to be equal to zero, which means that these channels participate in none of the shortest paths in the transient seizure network. Channel 9 in the RH and channel 41 in the RTB acted as the essential hubs in the network and removal of areas where these two channels were located will have the most significant effect on the seizure onset network performance.

**[Fig. 4]**

Then, the graph metrics of the seizure-specific transient seizure onset network in each frequency band of all seizures in each electrode strip, i.e., each involved cortical region, are described by boxplots. Fig. 5 presents the boxplots of OD, CC, BC, C, and LE of the transient seizure onset network (Engel Class I patient A, seizure #1,  $\theta$  frequency band). The OD, BC, CC, and LE in the RH were significantly higher than the graph metric values in the other two regions on the ipsilateral side (RTP and RTB) and in all regions on the contralateral side (LH, LTP and LTB) (Kruskal-Wallis test). The CC in the RH was significantly higher than that in RTB and all regions on the contralateral side (Kruskal-Wallis test). These results demonstrated that the RH region, the SOZ identified by clinical epileptologists, communicated the most information to the other regions at the fastest speed, clustered together with the most numbers of nearest neighbours and acted as the most essential hub in the transient seizure onset network. Moreover, the OD, CC, C, and LE in RTB and RTP regions were significantly higher than the values in some regions on the contralateral hemisphere, which means that RTB and RTP regions also worked as the important cortical areas in the transient seizure onset network.

**[Fig. 5]**

The cortical regions with highest means of graph metrics in the seizure-specific transient seizure onset network in each frequency band of all seizures are presented in Table 2. The same cortical region as the clinically identified SOZ is indicated in bold font and with a border. The cortical region that belongs to the clinical resected regions is only indicated in bold.

In terms of the Engel Class I, patient A, the highest means were found in RH in almost all frequency bands and graph metrics of seizure #1 and #2, while they were found in the contralateral side LTB and LH of seizure #3. The durations of the transient seizure onset networks of these three seizures were almost the same. Another Engel Class I, patient D, the locations with the highest means were the LH in all the frequency bands and graph metrics of seizure #6, which were consistent with the clinical identified SOZ. However, in seizure #7, the same locations appeared in almost all frequency bands in OD and BC, while in none frequency bands in CC and only in high-frequency bands ( $\beta$  and  $\gamma$ ) in C and LE. The duration of the transient seizure onset network of these two seizures exhibited a substantial difference, i.e., the duration of seizure #6 (51 ms) was more than 2.5 times than that of seizure #7 (19 ms), which was unique for patient A. Unlike the patients A and D, the Engel Class I patient E had no same highest mean values of graph metric as the clinical identified SOZ. Only in the seizure #8, the low-frequency bands  $\delta$ ,  $\theta$ , and  $\alpha$  of OD, CC, C, and LE, the area RTB with the highest mean belonged to the clinical resected regions. Regarding the Engel Class II, patient B, the locations with the highest means were the LTB in all frequency bands and graph metrics, which was the neighbouring cortical area of the SOZ, i.e., LTP that with the second highest means. Another Engel Class II patient C, the LH that is the same as the clinical identified SOZ, was the highest mean in  $\delta$  and  $\theta$  frequency bands of all graph metrics and in higher frequency bands of OD, BC, C and LE. In the case of Engel Class III, patient F, the highest means were found in the  $\delta$ ,  $\theta$ ,  $\alpha$ , and  $\beta$  frequency bands of OD and BC, in the  $\delta$ ,  $\theta$ , and  $\alpha$  frequency bands of CC, and  $\delta$ ,  $\theta$  frequency bands of C and LE in seizure #10. In seizure #11, the cortical area with the highest

means was the RTO in all the frequency bands and graph metrics, which was neither consistent with the SOZ nor included in the resected regions. The duration of seizure #10 (51 ms) was twice that of seizure #11 (27 ms). In Engel Class III patient G, no results were the same as the clinical identified SOZ. Only RTB in  $\gamma$  frequency band of OD, C, and LE in seizure #12, RTB in  $\gamma$  frequency band of C and LE in seizure #13, RTB in  $\delta$ ,  $\theta$ ,  $\alpha$ , and  $\beta$  frequency bands of OD, CC, C, and LE in seizure #14, were belong to the resected regions. The durations of these three seizures were more than 40 ms.

### [Table 2]

The proportions of the same cortical regions with the highest mean of graph metrics as the clinical identified SOZ of each graph metric in three different Engel Classes and in five different frequency bands are illustrated in Table3. In terms of different Engel Classes, the proportion of Engel Class I was greater than the proportion of Engel Class II and the proportion of Engel Class II was greater than the proportion of Engel Class III in all the graph metrics. The mean proportions of Engel Class I, II, and III were 46.4%, 34%, and 12%, respectively. It was also found that the OD was the largest in all Engel Classes compared with the other four graph metrics. In Engel Class I patients, the proportion rank was  $OD > C > BC = LE > CC$ , which means that the out-degree and clustering coefficient are more likely to localize the cortical areas that are the same as the clinical identified SOZ. Regarding different frequency bands, the mean proportions of  $\delta$  and  $\theta$  frequency bands were larger than the proportions of the higher frequency bands. The OD had the same proportion (43%) in  $\delta$ ,  $\theta$ ,  $\alpha$ , and  $\beta$  frequency bands, and the BC had the same proportion (43%) in  $\delta$  and  $\theta$  frequency bands, which was the largest value among the five graph metrics. The proportion of CC in  $\delta$  band was larger than that in the other four higher frequency bands. C had the same proportions in  $\delta$ ,  $\theta$ ,  $\beta$ , and  $\gamma$  frequency bands (36%), which was larger than that in the  $\alpha$  frequency bands. LE had the same values in the  $\delta$  and  $\theta$  frequency bands (36%) as well as in the  $\beta$  and  $\gamma$  frequency bands (29%), which were larger

than the values in  $\alpha$  frequency bands.

[Table 3]

#### 4. Discussion

This study investigated the time-varying characteristics of effective connectivity in the epileptic brain networks in 14 seizures of seven patients with TLE, using the measure of the ffADTF combined with five graph metrics. The effective connectivity was evaluated and compared across five frequency bands and five representative seizure periods. The locations of the strong epileptic sources found using these measures were compared with the SOZ and EZ identified by epileptologists, as well as with the results of epilepsy surgery.

The main difference between DTF and ADTF is the ‘adaptive’ which can be explained as ‘time-variant’. Given a data epoch, we can get only one connectivity matrix DTF using the multivariate autoregressive (MVAR) model. However, the connectivity matrices ADTF at each sample point can be obtained using the AMVAR model which is also called a TVAR model. The ADTF-based measure ffADTF can detect the dynamic change of the effective connectivity, with a high temporal resolution at specific frequency bands. This allows us to gain useful information in terms of dynamic causality from the non-stationary signals in the epileptic brain. From the effective connectivity network results, the ffADTF connectivity networks were time-dependent throughout the entire period of the seizure. Before the seizure onset, uniform networks were observed most of the time across all five frequency bands of all patients, with some strong connections occasionally appearing in the low-frequency bands ( $\delta$ ,  $\theta$ ,  $\alpha$ ) from the SOC of two Engel Class I and II patients and from side contralateral to the SOZ of one Engel Class III patient. These results illustrated that some strong low-frequency epileptogenic activity may emerge before a seizure, but they do not trigger seizures. The location of this strong activity is just within the region of the SOZ, as identified by epileptologists, or the region that is not identified as the EZ. These findings lead us to suspect that the location of strong

information communication before a seizure might be the potential SOZ or EZ.

At the seizure onset time, strong connections were observed between the regions where the SOZ was located and some ipsilateral EZ mainly on the side where the SOZ was located in all Engel Class I patients and one Engel Class II patient. However, strong epileptic activity was generated on both the ipsilateral and contralateral sides of the SOZ in one Engel Class II patient and all Engel Class III patients. In regard to the Engel II and III patients, there still existed varying degrees of seizures after their first resection surgeries, meaning that there were some regions with abnormal epileptic discharge in the cerebral cortex that were not resected. These regions are likely to be the regions where the strong activity is generated outside the surgical resection areas in the ffADTF effectivity connectivity network. Therefore, the seizure onset network based on the ffADTF may detect potential EZ other than the ones identified by the epileptologists. Furthermore, the locations that the strong connections were generated from in the seizure onset network in the low-frequency  $\delta$ ,  $\theta$  and  $\alpha$  bands were found to be more closely correlated with the SOZ and the EZ than those in the  $\beta$  and  $\gamma$  bands. However, high-frequency  $\beta$  and  $\gamma$  band activities demonstrated significantly more overlap with the SOZ than the low-frequency  $\theta$  and  $\alpha$  band activities in Wilke's studies [34, 35], which was inconsistent with our findings. This finding may have been due to the different seizure types and the large individual differences among the epileptic patients. Another important finding was that the seizure onset network that emerged at seizure onset time remained for approximately 20-50 ms with strong connections generated from both the SOZ and other EZ, rather than rapidly changing to the other network patterns. This newly discovered transient seizure onset network is an important biomarker during the seizure period and could be a promising tool for the localization of the SOZ and the EZ.

In subsequent epileptic networks, the effectivity connectivity presented irregular features, which indicated that the strong epileptic activity was not only restricted in the ipsilateral

hemisphere of the SOZ but was also propagated to the hemisphere contralateral to the SOZ. Finally, a special phenomenon was observed in the low-frequency  $\delta$  and  $\theta$  bands in two seizures of two Engel Class I patients at the seizure termination time. Strong connections from the SOZ to other areas were established again in a similar to that of the transient seizure onset network. A possible interpretation could be that the neurons in the SOZ in these two patients may, sometimes, serve as main controllers in both seizure onset and seizure termination.

In terms of the results of the distribution of graph metrics, high values of graph metrics corresponded to the channels that generated the strong connections in the effective connectivity networks. The information communication strength of each channel could be seen more intuitively, such that we are able to estimate which channels were the epileptogenic sources and played important roles in the epileptic network. In addition, in the transient seizure onset network as discussed above, the channels with high values of total graph metrics were located in the clinically identified SOZ and ipsilateral EZ in most Engel Class I and II patients and even in some contralateral areas in a few Engel Class II or III patients. Also, the values of graph metrics of SOZ were found to be the largest among the cortical areas and the values of all EZs were significantly larger than other cortical areas in seizure-free patients. The SOZ is the area of the cortex from which abnormal rhythm of seizures are actually generated, and EZ is the area of the cortex that is indispensable for the generation of epileptic seizures [17]. In the process of the origination and propagation of epileptic information, SOZ and EZ involve more information generation and transfer than other cortical areas in the epileptic brain network. Different graph metrics evaluate the characteristics of the cortical areas in the epileptic brain from different aspects. The OD quantifies how much information is output, CC measures how long it will take to spread information, BC indicates how important the node is in the information transfer path, C and LE describe how much the node is clustered with other neighbours, which make it possible to detect the SOZ and EZ in the epileptic brain. In particular,

the BC could locate the most important channels which acted as the essential hubs in the seizure onset network. These results illustrate that high values of graph metrics in the transient seizure onset network could provide a more accurate localization of the SOZ and the EZ for epileptologists in the preoperative assessment.

Furthermore, with regard to the seizure-specific results of cortical area with highest mean of graph metrics in the transient seizure onset network across the five frequency bands, more cortical areas with the highest mean of graph metrics were the same as the clinically determined SOZ existed in the low-frequency  $\delta$  and  $\theta$  bands and in Engel Class I patients than in higher frequency  $\alpha$ ,  $\beta$  and  $\gamma$  bands and in Engel Class II and III patients. This result demonstrates that the SOZs in the Engel Class I patients are relatively centralized. Conversely, the SOZs in Engel Class II and III patients are relatively scattered. Some SOZs and EZs that were not resected in the first surgeries still exist, that is why these patients have varying degrees of seizures after the resection surgeries. On the other hand, out-degree and clustering coefficient are more likely to localize the SOZ and EZ than closeness centrality, betweenness centrality, and local efficiency, illustrating that SOZ and EZ have a higher correlation with the amount of information output and the degree of clustering with the surrounding cortex in the seizure onset network. Moreover, the different durations of the transient seizure onset networks were probably due to the large individual differences among the patients and the different physiological statuses within the same patient.

However, our study had some limitations. Only 14 recorded seizures in seven patients were included. The same numbers of seizure in each Engel Class would be better to make a comparison. More patients with different Engel Classes will be included in our future work to further verify the findings. Depth electrodes and cortical electrode strips cannot completely ensure coverage of the entire SOZ and EZ. If some EZ located outside the regions are covered by the electrode strips, some locations of EZ would be omitted in both clinical visual analysis

and effective connectivity analysis. In addition, invasive electrode strips or grids cannot be implanted in healthy individuals, so it is not possible to compare the differences in effective connectivity networks between epileptic patients and healthy subjects. High-density EEG recordings could be applied to effective connectivity analyses in future studies, which could provide more information on the connectivity features of the whole brain and obtain contrastive connectivity networks from a healthy control group. Other effective connectivity measures, such as the integrated ADTF [26, 27], masked ADTF [26], and spectrum-weighted ADTF [25], and measures of adaptive partial directed coherence [2, 28] can be used and compared. Although accurate localization of EZ using the ffADTF and graph metrics may lead to small resection regions, this still needs to be further verified in clinical preoperative evaluation and postoperative follow-up results in a large group of epileptic patients before this brain connectivity method can be applied in clinical practice.

In conclusion, the ffADTF combined with OD, CC, BC, C, and LE were used to investigate the time-varying effective connectivity of ECoG signals at a high temporal resolution in patients with temporal lobe epilepsy, which was evaluated and compared across different frequency bands and different seizure periods. Generation and propagation of strong epileptic activities can be observed from the ffADTF effective connectivity networks, and the location of the SOZ and EZ can be found using the high values of graph metrics in the newfound transient seizure onset effective connectivity network. Different graph metrics reflect the different characteristics of epileptic information communication among the cortical areas. Overall, our study proved that the high temporal resolution effective connectivity measure ffADTF combined with different graph metrics is able to provide a more precise localization of the SOZ and EZ, contributing to clinical preoperative assessments and reducing both the number of postoperative seizures and the probability of secondary surgeries.

## **Acknowledgments**

This research is supported by the Ph.D. grant of the Faculty of Information Technology in the University of Jyväskylä, Beijing Science & Technology Commission in Tongzhou District No. KJ2015CX004 and Beijing Municipal Science & Technology Commission No. Z161100002616001.

### **Conflicts of interest**

On behalf of all authors, the corresponding author states that there is no conflict of interest.

### **Ethical approval**

This research has been approved by the Ethics Committees of Xuanwu Hospital, Capital Medical University and Luhe Hospital, Capital Medical University, and it has been performed in accordance with the ethical standards laid down in the 1964 Declaration of Helsinki and its later amendments.

### **References**

1. Chiang S, Haneef Z (2014) Graph theory findings in the pathophysiology of temporal lobe epilepsy. *Clin Neurophysiol* 125:1295-1305
2. Coito A, Plomp G, Genetti M, Abela E, Wiest R, Seeck M, Michel CM, Vulliemoz S (2015) Dynamic directed interictal connectivity in left and right temporal lobe epilepsy. *Epilepsia* 56:207-217
3. Engel J, Jr., Thompson PM, Stern JM, Staba RJ, Bragin A, Mody I (2013) Connectomics and epilepsy. *Curr Opin Neurol* 26:186-194
4. Engel Jr J (1993) Outcome with respect to epileptic seizures. *Surgical treatment of the epilepsies*:609-621
5. Englot DJ, D'Haese PF, Konrad PE, Jacobs ML, Gore JC, Abou-Khalil BW, Morgan VL

- (2017) Functional connectivity disturbances of the ascending reticular activating system in temporal lobe epilepsy. *J Neurol Neurosurg Psychiatry* 88:925-932
6. Fagiolo G (2007) Clustering in complex directed networks. *Phys Rev E Stat Nonlin Soft Matter Phys* 76:026107
  7. Freeman LC (1978) Centrality in social networks conceptual clarification. *Social networks* 1:215-239
  8. Friston K, Frith C, Frackowiak R (1993) Time - dependent changes in effective connectivity measured with PET. *Human Brain Mapping* 1:69-79
  9. Granger CW (1969) Investigating causal relations by econometric models and cross-spectral methods. *Econometrica: Journal of the Econometric Society* 37:424-438
  10. Haneef Z, Chiang S (2014) Clinical correlates of graph theory findings in temporal lobe epilepsy. *Seizure* 23:809-818
  11. Kaminski MJ, Blinowska KJ (1991) A new method of the description of the information flow in the brain structures. *Biol Cybern* 65:203-210
  12. Kramer MA, Cash SS (2012) Epilepsy as a disorder of cortical network organization. *The Neuroscientist* 18:360-372
  13. Kramer MA, Kolaczyk ED, Kirsch HE (2008) Emergent network topology at seizure onset in humans. *Epilepsy Res* 79:173-186
  14. Neumaier A, Schneider T (2001) Estimation of parameters and eigenmodes of multivariate autoregressive models. *ACM Transactions on Mathematical Software (TOMS)* 27:27-57
  15. Palus M, Hoyer D (1998) Detecting nonlinearity and phase synchronization with surrogate

- data. *IEEE Eng Med Biol Mag* 17:40-45
16. Ponten SC, Bartolomei F, Stam CJ (2007) Small-world networks and epilepsy: graph theoretical analysis of intracerebrally recorded mesial temporal lobe seizures. *Clin Neurophysiol* 118:918-927
  17. Rosenow F, Luders H (2001) Presurgical evaluation of epilepsy. *Brain* 124:1683-1700
  18. Rubinov M, Sporns O (2010) Complex network measures of brain connectivity: uses and interpretations. *Neuroimage* 52:1059-1069
  19. Sakkalis V (2011) Review of advanced techniques for the estimation of brain connectivity measured with EEG/MEG. *Comput Biol Med* 41:1110-1117
  20. Schlogl A, Roberts SJ, Pfurtscheller G (2000) A criterion for adaptive autoregressive models. In: *Proceedings of the 22nd Annual International Conference of the IEEE Engineering in Medicine and Biology Society* (Cat. No. 00CH37143). IEEE, pp 1581-1582
  21. Schneider T, Neumaier A (2001) Algorithm 808: ARfit—A Matlab package for the estimation of parameters and eigenmodes of multivariate autoregressive models. *ACM Transactions on Mathematical Software (TOMS)* 27:58-65
  22. Schwarz G (1978) Estimating the dimension of a model. *The annals of statistics* 6:461-464
  23. Storti SF, Galazzo IB, Khan S, Manganotti P, Menegaz G (2017) Exploring the Epileptic Brain Network Using Time-Variant Effective Connectivity and Graph Theory. *IEEE J Biomed Health Inform* 21:1411-1421
  24. Theiler J, Eubank S, Longtin A, Galdrikian B, Farmer JD (1992) Testing for nonlinearity

- in time series: the method of surrogate data. *Physica D: Nonlinear Phenomena* 58:77-94
25. van Mierlo P, Carrette E, Hallez H, Raedt R, Meurs A, Vandenberghe S, Van Roost D, Boon P, Staelens S, Vonck K (2013) Ictal-onset localization through connectivity analysis of intracranial EEG signals in patients with refractory epilepsy. *Epilepsia* 54:1409-1418
  26. van Mierlo P, Carrette E, Hallez H, Vonck K, Van Roost D, Boon P, Staelens S (2011) Accurate epileptogenic focus localization through time-variant functional connectivity analysis of intracranial electroencephalographic signals. *Neuroimage* 56:1122-1133
  27. van Mierlo P, Coito A, Vulliémoz S, Lie O (2016) Seizure onset zone localization from many invasive EEG channels using directed functional connectivity. In: *Signal Processing Conference (EUSIPCO), 2016 24th European*. IEEE, pp 255-259
  28. Wang G, Sun Z, Tao R, Li K, Bao G, Yan X (2016) Epileptic Seizure Detection Based on Partial Directed Coherence Analysis. *IEEE J Biomed Health Inform* 20:873-879
  29. Wang J, Qiu S, Xu Y, Liu Z, Wen X, Hu X, Zhang R, Li M, Wang W, Huang R (2014) Graph theoretical analysis reveals disrupted topological properties of whole brain functional networks in temporal lobe epilepsy. *Clin Neurophysiol* 125:1744-1756
  30. Watts DJ, Strogatz SH (1998) Collective dynamics of 'small-world' networks. *Nature* 393:440-442
  31. Wilke C, Ding L, He B (2007) An adaptive directed transfer function approach for detecting dynamic causal interactions. In: *Engineering in Medicine and Biology Society, 2007. EMBS 2007. 29th Annual International Conference of the IEEE*. IEEE, pp 4949-4952
  32. Wilke C, Ding L, He B (2008) Estimation of time-varying connectivity patterns through

- the use of an adaptive directed transfer function. *IEEE Trans Biomed Eng* 55:2557-2564
33. Wilke C, van Drongelen W, Kohrman M, He B (2010) Neocortical seizure foci localization by means of a directed transfer function method. *Epilepsia* 51:564-572
  34. Wilke C, Worrell G, He B (2011) Graph analysis of epileptogenic networks in human partial epilepsy. *Epilepsia* 52:84-93
  35. Wilke C, Worrell GA, He B (2009) Analysis of epileptogenic network properties during ictal activity. *Conf Proc IEEE Eng Med Biol Soc* 2009:2220-2223
  36. Yaffe RB, Borger P, Megevand P, Groppe DM, Kramer MA, Chu CJ, Santaniello S, Meisel C, Mehta AD, Sarma SV (2015) Physiology of functional and effective networks in epilepsy. *Clin Neurophysiol* 126:227-236
  37. Zhang H, Lai D, Xie C, Zhang H, Chen W (2016) Directed-transfer-function based analysis for epileptic prediction. In: *Image and Signal Processing, BioMedical Engineering and Informatics (CISP-BMEI), International Congress on*. IEEE, pp 1487-1491
  38. Zhang L, Liang Y, Li F, Sun H, Peng W, Du P, Si Y, Song L, Yu L, Xu P (2017) Time-Varying Networks of Inter-Ictal Discharging Reveal Epileptogenic Zone. *Front Comput Neurosci* 11:77

## Figures

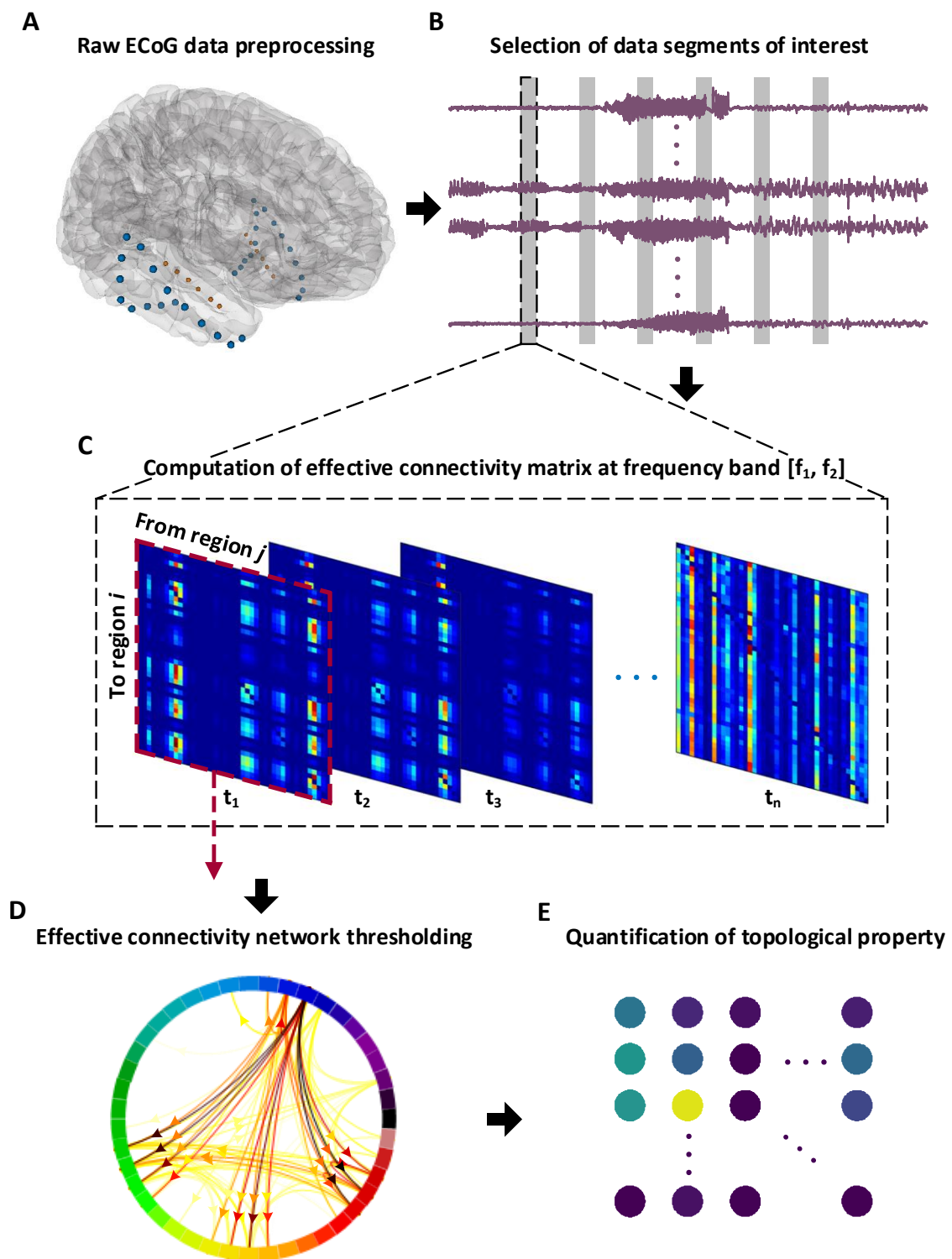


Fig. 1 Illustration of the main steps of the effective connectivity and graph theoretical analyses.

(A) Preprocessing of the raw ECoG data: down-sampling to 256 Hz and 0.2-Hz high-pass filter,

standardized z-scores, and removal of power frequency noise (50 Hz), harmonic noises, large-amplitude artifacts and bad channels. (B) Select the data segments of interest: five representative 5-second data epochs, i.e., pre-seizure, early seizure, mid-seizure, late seizure and post-seizure. (C) Calculate the directed and weighted effective connectivity matrix in the frequency band  $[f_1, f_2]$ : the ffADTF was calculated in the  $\delta$  (1-4 Hz),  $\theta$  (4-8 Hz),  $\alpha$  (8-13 Hz),  $\beta$  (13-30 Hz) and  $\gamma$  (30-50 Hz) frequency bands of each epoch. (D) Effective connectivity thresholding: the top 5% of the strong connections were displayed in the ffADTF connectivity networks. (E) Quantify the topological properties using graph metrics (out-degree, closeness centrality, betweenness centrality, clustering coefficient and local efficiency): the graph metrics were calculated at the small scale of single nodes and the total graph metrics in each cortical regions were evaluated and compared with the clinical SOZ and resected regions.

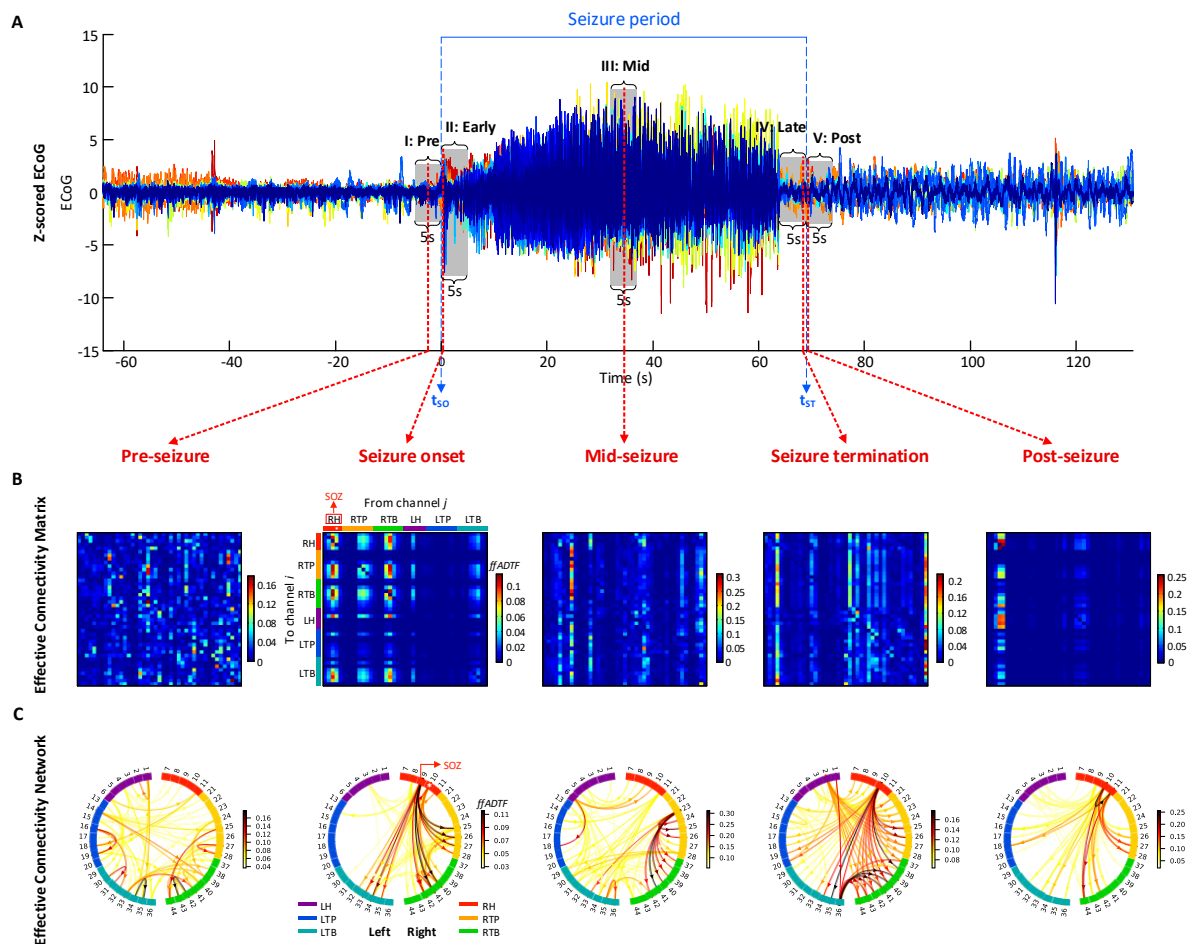


Fig. 2 Effective connectivity analysis results of the  $\theta$  frequency band in seizure #1 of patient A.

(A) Z-scored ECoG data of 43 channels in patient A, including a complete epileptic seizure, which is indicated by two blue dashed lines delineating the seizure onset time  $t_{SO}$  to the seizure termination time  $t_{ST}$ . Five representative 5-second seizure epochs were selected for the effective connectivity analysis (I: pre-seizure, II: early seizure, III: mid-seizure, IV: late seizure, and V: post-seizure), which are marked with light grey rectangles. In addition, five representative time points (pre-seizure, seizure onset, mid-seizure, seizure termination, and post-seizure) in these epochs were chosen to present the effective connectivity results in different time periods of temporal lobe epileptic seizures. (B) The ffADTF effective connectivity matrix from channel  $j$  to channel  $i$ . Channels with the same colour belong to the same electrode trip (red: right

hippocampus, yellow: right temporal pole, green: right temporal base, purple: left hippocampus, blue: left temporal pole, and cyan: left temporal base). The right hippocampus and the channel marked with a white asterisk are the SOZ and SOC identified by clinical neurologists, respectively. (C) The ffADTF effective connectivity network at five representative time points of an epileptic seizure.

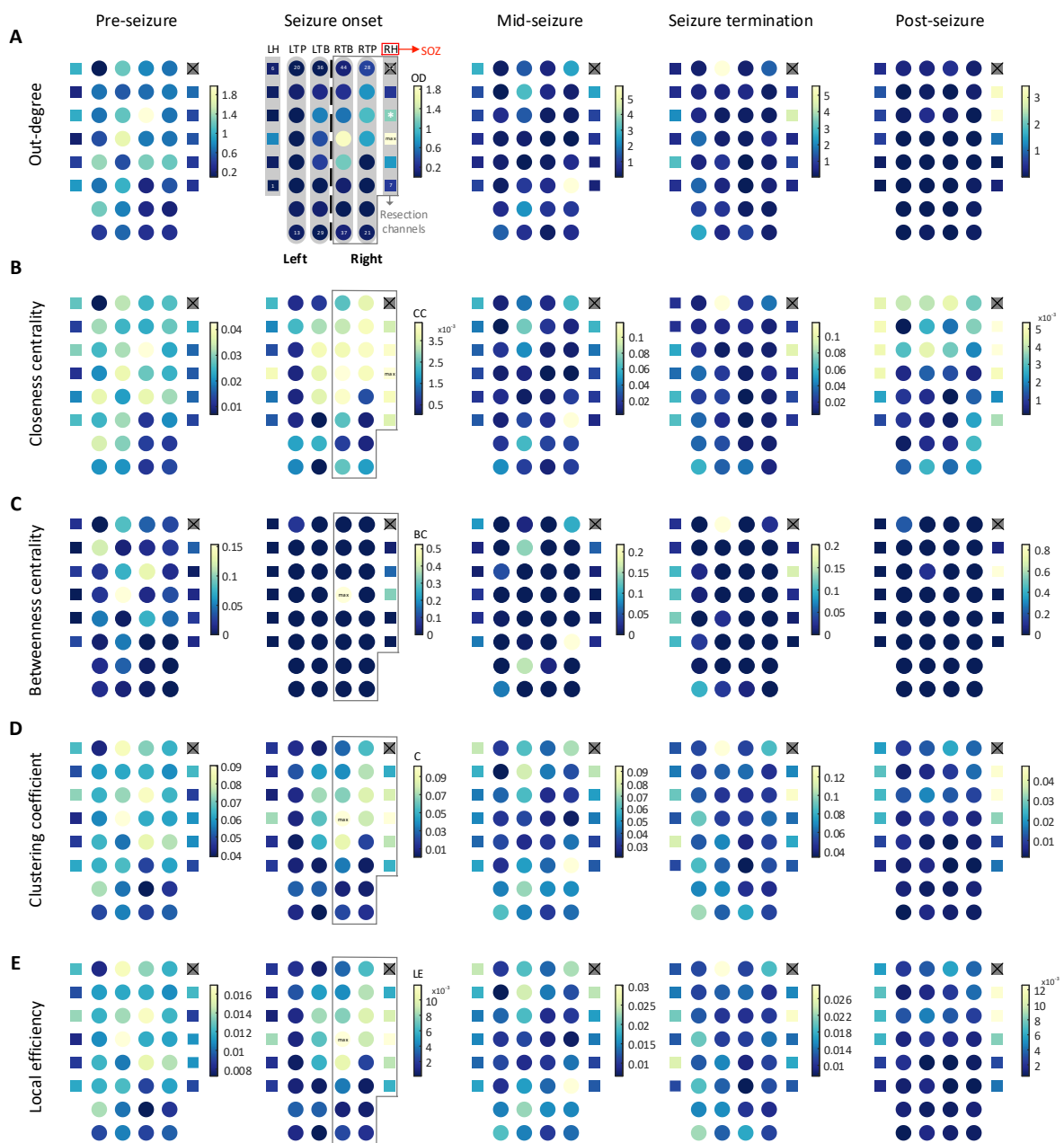


Fig. 3 Distribution of the graph metrics across all channels at five representative seizure time points is presented in Fig. 2. Depth electrodes (RH and LH) and cortical electrode strips (RTP,

RTB, LTP, and LTB) are denoted by squares and circles, respectively. Channels in the grey rectangle were included in the resection areas in the clinical surgery. Channel 12 was the bad channel, as assessed by visual inspection. Channel 10 with a white asterisk was the SOC determined by clinical epileptologists.

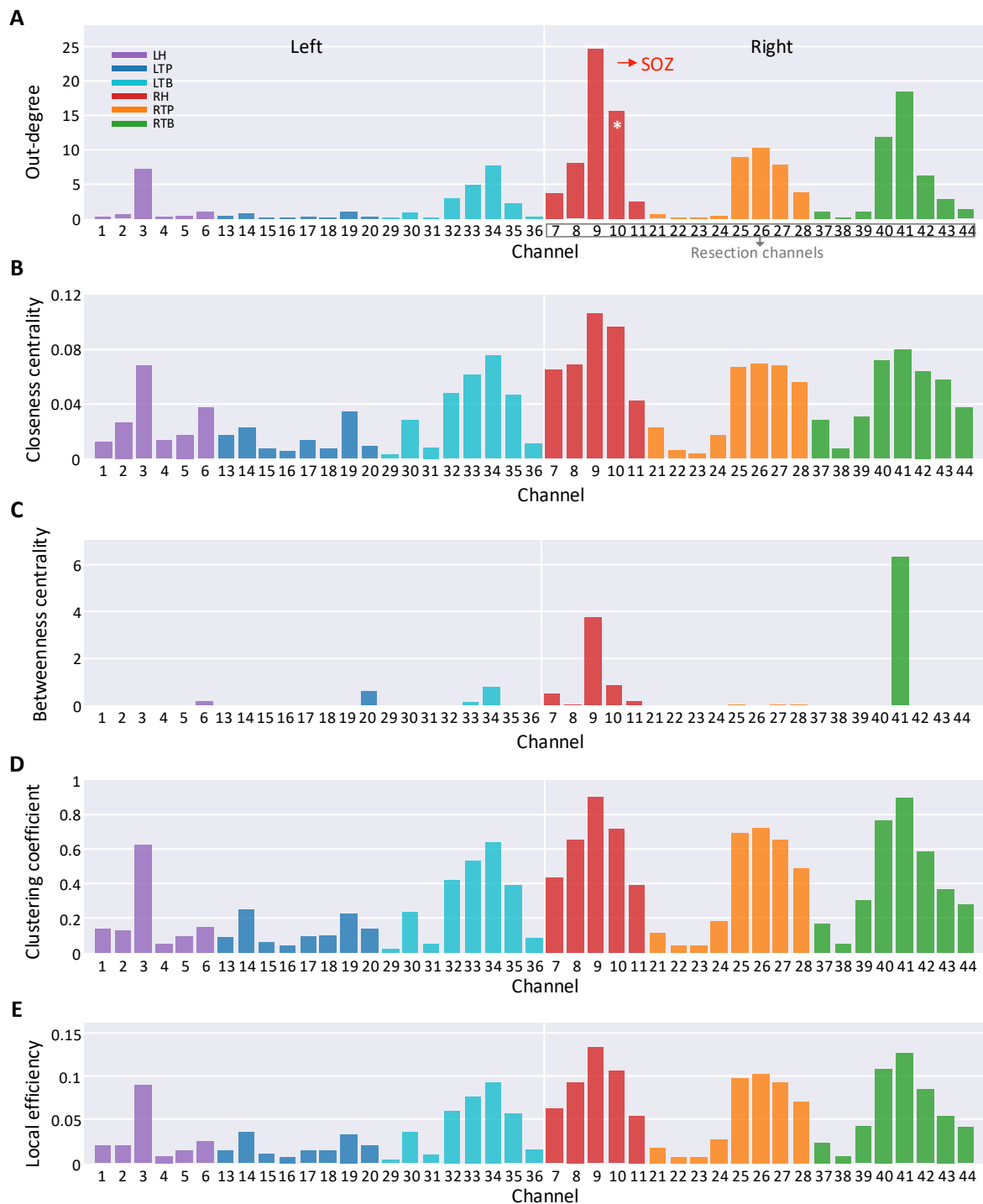


Fig. 4 Total graph metrics of each channel in the transient seizure onset network of the  $\theta$  frequency band in seizure #1 of patient A.

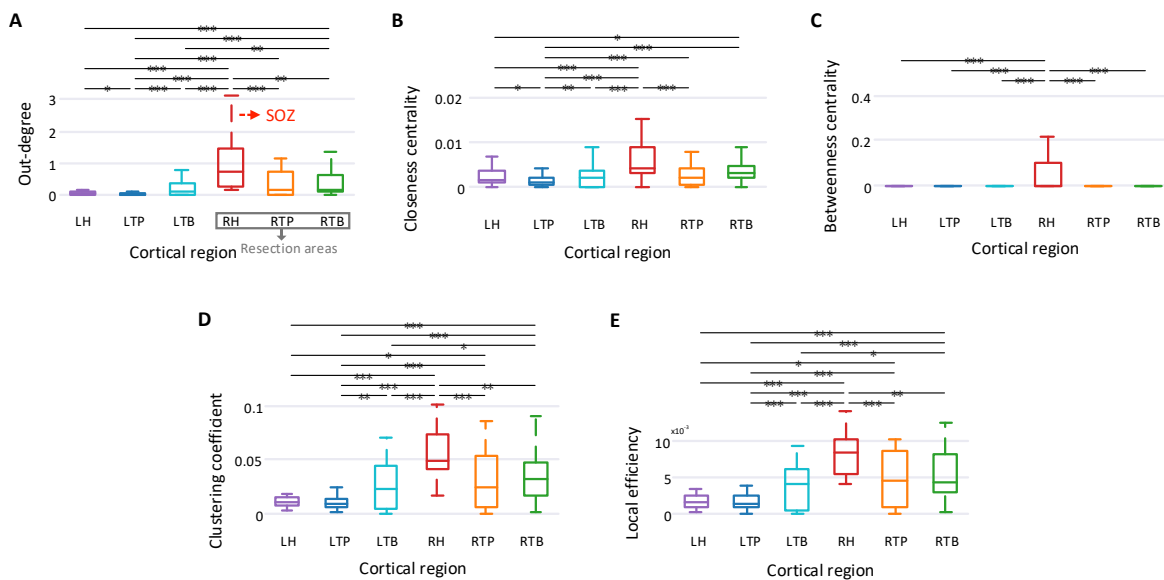


Fig. 5 Boxplot of the graph metrics in each cortical area in the transient seizure onset network of the  $\theta$  frequency band in seizure #1 of patient A.

## Tables

Table 1 Clinical information of the patients with temporal lobe epilepsy

Patient/ Sex/Age (years)	Electrode strip placement/ Total number of electrode contacts	SOC	SOZ	Resected regions	Follow-up (months)/ Surgical outcome (Engel Class)
A/F/24	LH (6×1), LTP (8×1), LTB (8×1) RH (6×1), RTP (8×1), RTB (8×1)/44	10	RH	RH, RTP, RTB	26/I
B/F/46	LTP (8×1), LTB (8×1) RTP (8×1), RTB (8×1)/32	1, 2	LTP	LTP, LTB	53/II
C/M/22	LH (8×1), LTB (8×1), LPTB (8×1) RH (8×1), RTB (8×1), RPTB (8×1)/48	3, 11	LH, LTB	LH, LTB	55/II
D/M/33	LH (6×1), LTP (6×1), LTB (8×1) RH (6×1), RTP (6×1), RTB (6×1)/38	1, 2, 3, 4	LH	LH, LTP, LTB	54/I
E/F/28	RH (4×1), RTP (8×2), RTB (6×1), RPTL (8×1), RFPL (8×2)/50	25, 26	RTP	RH, RTP, RTB	27/I
F/F/28	LTP (8×1), LTB (8×1), LTO (8×1) RTP (8×1), RTB (8×1), RTO (8×1)/48	5, 6, 7	RTP	RTP, RTB	34/III
G/M/21	LTP (8×1), LTB (8×1), LTO (8×1) RTP (8×1), RTB (8×1), RTO (8×1)/48	6, 7, 8	RTP	RTP, RTB	29/III

F: female, M: male, L: left, R: right, H: hippocampus, TL: temporal lobe, TP: temporal pole, TB: temporal base, PTL: posterior temporal lobe, PTB: posterior temporal base, FPL: frontal-parietal lobe, TO: temporal-occipital, SOC: seizure onset channel, SOZ: seizure onset zone

Table 2 Seizure-specific results of cortical area with highest mean of graph metrics in the transient seizure onset network

Engel class	I	I	I	I	I	I	I	II	II	III	III	III	III	III	
Seizure/ Patient	#1/A	#2/A	#3/A	#6/D	#7/D	#8/E	#9/E	#4/B	#5/C	#10/F	#11/F	#12/G	#13/G	#14/G	
Duration (ms)	43	40	40	51	19	43	40	54	39	51	27	52	43	41	
OD	$\delta$	<b>RH</b>	<b>RH</b>	LTB	<b>LH</b>	<b>LH</b>	<b>RTB</b>	RFPL	<b>LTB</b>	<b>LH</b>	<b>RTP</b>	RTO	LTP	LTO	<b>RTB</b>
	$\theta$	<b>RH</b>	<b>RH</b>	LTB	<b>LH</b>	<b>LH</b>	<b>RTB</b>	RFPL	<b>LTB</b>	<b>LH</b>	<b>RTP</b>	RTO	LTP	LTO	<b>RTB</b>
	$\alpha$	<b>RH</b>	<b>RH</b>	LTB	<b>LH</b>	<b>LH</b>	<b>RTB</b>	RFPL	<b>LTB</b>	<b>LH</b>	<b>RTP</b>	RTO	LTP	LTO	<b>RTB</b>
	$\beta$	<b>RH</b>	<b>RH</b>	LTB	<b>LH</b>	<b>LH</b>	RPTL	RPTL	<b>LTB</b>	<b>LH</b>	<b>RTP</b>	RTO	LTP	LTO	<b>RTB</b>
	$\gamma$	<b>RH</b>	<b>RH</b>	LTB	<b>LH</b>	<b>LH</b>	RPTL	RPTL	<b>LTB</b>	LTPB	<b>RTB</b>	RTO	<b>RTB</b>	LTO	RTO
CC	$\delta$	<b>RH</b>	<b>RH</b>	LTB	<b>LH</b>	<b>LTB</b>	<b>RTB</b>	RFPL	<b>LTB</b>	<b>LH</b>	<b>RTP</b>	RTO	LTP	LTO	<b>RTB</b>
	$\theta$	<b>RH</b>	LH	LTB	<b>LH</b>	RTB	<b>RTB</b>	RFPL	<b>LTB</b>	<b>LH</b>	<b>RTP</b>	RTO	LTP	RTO	<b>RTB</b>
	$\alpha$	<b>RH</b>	LH	LH	<b>LH</b>	RTB	RPTL	RFPL	<b>LTB</b>	RH	<b>RTP</b>	RTO	LTP	RTO	<b>RTB</b>
	$\beta$	<b>RH</b>	LH	LH	<b>LH</b>	RTB	RPTL	RPTL	<b>LTB</b>	RH	<b>RTB</b>	RTO	LTP	RTO	<b>RTB</b>
	$\gamma$	<b>RH</b>	<b>RH</b>	LH	<b>LH</b>	RTB	RPTL	RFPL	<b>LTB</b>	LTPB	<b>RTB</b>	RTO	RTO	RTO	RTO
BC	$\delta$	<b>RH</b>	<b>RH</b>	LTB	<b>LH</b>	<b>LH</b>	RPTL	RFPL	<b>LTB</b>	<b>LH</b>	<b>RTP</b>	RTO	LTP	LTO	RTO
	$\theta$	<b>RH</b>	<b>RH</b>	LTB	<b>LH</b>	<b>LH</b>	RPTL	RFPL	<b>LTB</b>	<b>LH</b>	<b>RTP</b>	RTO	LTP	LTO	RTO
	$\alpha$	<b>RTB</b>	<b>RH</b>	LTB	<b>LH</b>	RH	RPTL	RFPL	<b>LTB</b>	<b>LH</b>	<b>RTP</b>	RTO	LTP	LTO	RTO
	$\beta$	<b>RTB</b>	<b>RH</b>	LTB	<b>LH</b>	<b>LH</b>	RPTL	RFPL	<b>LTB</b>	<b>LH</b>	<b>RTP</b>	RTO	LTP	LTO	RTO
	$\gamma$	<b>RTB</b>	<b>RH</b>	LTB	<b>LH</b>	<b>LH</b>	RPTL	RFPL	<b>LTB</b>	LTPB	LTO	RTO	LTP	LTO	RTO
C	$\delta$	<b>RH</b>	<b>RH</b>	LTB	<b>LH</b>	RTB	<b>RTB</b>	RFPL	<b>LTB</b>	<b>LH</b>	<b>RTP</b>	RTO	LTP	LTO	<b>RTB</b>
	$\theta$	<b>RH</b>	<b>RH</b>	LTB	<b>LH</b>	RTB	<b>RTB</b>	RFPL	<b>LTB</b>	<b>LH</b>	<b>RTP</b>	RTO	LTP	LTO	<b>RTB</b>
	$\alpha$	<b>RH</b>	<b>RH</b>	LTB	<b>LH</b>	RTB	<b>RTB</b>	RFPL	<b>LTB</b>	RH	LTO	RTO	LTP	LTO	<b>RTB</b>
	$\beta$	<b>RH</b>	<b>RH</b>	LTB	<b>LH</b>	<b>LH</b>	<b>RTB</b>	RFPL	<b>LTB</b>	<b>LH</b>	LTO	RTO	LTP	LTO	<b>RTB</b>
	$\gamma$	<b>RH</b>	<b>RH</b>	LTB	<b>LH</b>	<b>LH</b>	RPTL	RFPL	<b>LTB</b>	<b>LH</b>	LTO	RTO	<b>RTB</b>	<b>RTB</b>	RTO
LE	$\delta$	<b>RH</b>	<b>RH</b>	LTB	<b>LH</b>	RTB	<b>RTB</b>	RFPL	<b>LTB</b>	<b>LH</b>	<b>RTP</b>	RTO	LTP	LTO	<b>RTB</b>
	$\theta$	<b>RH</b>	<b>RH</b>	LTB	<b>LH</b>	RTB	<b>RTB</b>	RFPL	<b>LTB</b>	<b>LH</b>	<b>RTP</b>	RTO	LTP	LTO	<b>RTB</b>
	$\alpha$	<b>RH</b>	<b>RH</b>	LTB	<b>LH</b>	RTB	<b>RTB</b>	RFPL	<b>LTB</b>	RH	LTO	RTO	LTP	LTO	<b>RTB</b>
	$\beta$	<b>RH</b>	<b>RH</b>	LTB	<b>LH</b>	RH	RPTL	RFPL	<b>LTB</b>	<b>LH</b>	LTO	RTO	LTP	LTO	<b>RTB</b>
	$\gamma$	<b>RH</b>	<b>RH</b>	LTB	<b>LH</b>	<b>LH</b>	RPTL	RFPL	<b>LTB</b>	LTPB	LTO	RTO	<b>RTB</b>	<b>RTB</b>	RTO

The same cortical region as the clinically identified SOZ is indicated in bold font and with a border. The cortical region that belongs to the clinical resected regions is only indicated in bold.

L: left, R: right, H: hippocampus, TL: temporal lobe, TP: temporal pole, TB: temporal base, PTL: posterior temporal lobe, PTB: posterior temporal base, FPL: frontal-parietal lobe, TO: temporal-occipital, OD: out-degree, CC: closeness centrality, BC: betweenness centrality, C: clustering coefficient, LE: local efficiency

Table 3 Proportion of the same cortical area with highest mean of graph metrics as the clinical identified SOZ

Graph metric	Engel Class			Frequency band				
	I	II	III	$\delta$	$\theta$	$\alpha$	$\beta$	$\gamma$
OD	57%	40%	16%	43%	43%	43%	43%	29%
CC	34%	20%	12%	36%	29%	21%	14%	21%
BC	46%	40%	16%	43%	43%	29%	36%	21%
C	49%	40%	8%	36%	36%	21%	36%	36%
LE	46%	30%	8%	36%	36%	21%	29%	29%
<b>Mean</b>	<b>46.4%</b>	<b>34.0%</b>	<b>12.0%</b>	<b>38.8%</b>	<b>37.4%</b>	<b>27.0%</b>	<b>31.6%</b>	<b>27.2%</b>

OD: out-degree, CC: closeness centrality, BC: betweenness centrality, C: clustering coefficient, LE: local efficiency



V

**EEG SOURCE LOCALIZATION AND FUNCTIONAL  
CONNECTIVITY IN A RARE PATIENT WITH COLD-  
INDUCED REFLEX EPILEPSY**

by

Ye Ren, Xiaoli Li, Fengyu Cong, Shuying Xiao, Qin Zhang, Ting Ao, Jun Zhang,  
Yup-ing Wang, Tapani Ristaniemi, Ruihua Zhang 2019

Under Review

Reproduced with kind permission by the authors.

Request a copy from author.